PROPERTIES OF DIRTY BOSONS IN DISORDERED OPTICAL LATTICES

BY

USHNISH RAY

DISSERTATION

Submitted in partial fulfillment of the requirements
for the degree of Doctor of Philosophy in Physics
in the Graduate College of the
University of Illinois at Urbana-Champaign, 2015

Urbana, Illinois

Doctoral Committee:

Professor Anthony Leggett, Chair
Professor David Ceperley, Director of Research
Professor Brian DeMarco
Professor Paul Kwiat

Abstract

The study of the disordered Bose-Hubbard model is key to understanding the interplay of disorder and interactions. Despite many studies with uniform diagonal disorder, few have inquired into experimental realizations with an additional correlated off-diagonal disorder. The presence of a trap and finite temperature effects in experiments lead to multiple domains of the Superfluid, Mott-Insulator/normal and the Bose-Glass phase. Previous studies using approximate theories produced results that are not in accordance with experiments. Stochastic Series Expansion is a finite temperature technique that can solve Bosonic lattice Hamiltonians exactly for large systems. Here, studies are performed for an extensive range of parameters using disorder distributions that are similar to experiments. Insights are first acquired by studying trap-free situations. Constant density calculations show that, although the qualitative features of the phase diagram remain robust between speckle disorder and uniform box disorder, there are quantitative differences. Studies of the Bose-glass phase explicitly show that it is composed of superfluid puddles that are stable to finite temperature effects for large temperature ranges. Finite temperature behavior of a strongly correlated system reveals that at unit filling, the transition temperature of the superfluid is increased due to the addition of disorder. Inquires are then extended to discern the properties of trapped systems. Extensive calculations show that domain-like structures that develop can be rigorously demarcated using the single-particle eigenstates extracted from the single-particle density matrix. Observables are calculated for the system at the single-site and global scales, showing that intermediate length scales provide the correct description of the physics of the domains in these systems. These techniques are used to conclusively show the possibility of the re-entrant superfluid that should be accessible to experiments. The temperature dependence of the re-entrant domain is explicitly calculated to be within experimental limits provided interactions are not too large. Comparisons with the local density approximation show reasonable agreement at low disorder strengths. At large disorder strengths there can be quantitative errors and can also result in qualitative errors. The phase diagram due to speckle disorder is presented for a range of values that are readily accessible to experiments. It is quantitatively shown that the effects of off-diagonal disorder are minimal. The superfluid remains unaffected despite large disorder in the tunneling term. Full scale *ab initio* calculations of the largest trapped disordered systems to date are performed in order to identify the superfluid-Bose-glass phase boundary in collaboration with experiments. Results show remarkable agreement, but there are open questions with regards to the possibility of glassy dynamics.

Acknowledgements

This doctoral work would not have been possible without the help of my advisor, Professor David Ceperley. I would like to thank him for the generous support he gave me throughout my tenure as a graduate student. My work with David also made it possible to meet outstanding collaborators who contributed a great deal to my development. Among these scholars, I would especially like to thank Professor Brian DeMarco for the opportunity to work with him and his group. Brian was exceptionally generous to me with his time and guidance. I thoroughly enjoyed the numerous hours we spent discussing physics, academia, and life. I have had the distinct pleasure of learning from these pioneers of physics, both of whom played important roles in showing me that it was indeed possible to be a good scientist and a good human being.

Numerous other individuals contributed to my intellectual growth and graduate career. I would like to thank my collaborators and colleagues, Carolyn Meldgin, Stefan Natu, David McKay, Philip Russ, Norm Tubman, Jeremy McMinis, Hitesh Changlani, Fei Lin, Sheng-Quan Zhou, Stanomir Kondov, Matthew Pasienski, Matthew White, Mingwu Lu, Seo-Ho Youn, Ethan Brown, Raymond Clay, Ilka Kylanpaa, and Victor Chua. I would especially like to thank ChangMo Yang for encouraging me to talk to David Ceperley for a possible position in his group (in 2010). Also, special thanks to Professors Anthony Leggett, Paul Kwiat, Vito Scarola, Bryan Clark, Lucas Wagner, Bryce Gadway, Nigel Goldenfeld, and Paul Goldbart for taking the time to listen to my (hopefully only) occasional ramblings, dissertation and defense preparations, and coursework. Also thank you to Professor Benjamin Lev for kickstarting my graduate career at the University of Illinois, Urbana-Champaign.

Physics research is one part of graduate school, the other part involves social aspects without which my graduate career would have been impossible. My father has been a role model and exemplar of benevolence, wisdom, and fortitude in my life. I would like to thank him for his constant guidance and support in pursuing my interests. A big thank you also to my mother. My earnest gratitude and regards to Mr. Sudipta Sinha (uncle, as I call him) for helping me start my journey to the US for higher education, and also for being an indomitable force and advocate of my interests. Mrs. Durga Sinha (aunty) was also a guiding light in this regard; my sincere gratitude to her, as well.

Throughout the highs and lows of graduate school, one companion was a constant source of love, amusement and support: my dog Zero. I must admit that I am perpetually amazed

at his ability to perceive my moods and react in ways that always makes me “lighter” and not take life too seriously. Friends were of great help in this regard as well, and I am lucky to have so many that I couldn’t possibly list them all here – but a big thank you to them all. Special thanks to Zsuzsánna Magdó, Brendan Pavlow, Brandon Lansche, David Coonan, Giovanni Fiorre, and Frank Filippi who took the brunt of my personality on a regular basis. Finally, my warmest regards and gratitude to the staff at Bacaro for keeping my spirits up with the excellent food, wine, and atmosphere of congeniality.

Contents

Part I

Introduction

Chapter 1

Overview

This chapter is intended to present a preview of the upcoming attractions pertaining to effects of disorder in 3D optical lattice systems. As such, the discussion here will be restricted to qualitative descriptions that will be expanded upon through the discussions in upcoming chapters. It starts with a discussion of synthetic materials realized through ultra-cold atomic gases. One such system, the disordered Bose-Hubbard model – the topic of this dissertation, has recently been synthesized with cold atoms and offers the unique possibility of gaining insight into phenomenology that results from the interaction of disorder with strong correlations. However, such systems are not easy to probe or manipulate, and indeed its properties are a subject of intense research today. Towards this end, general numerical techniques are incredibly useful and it will be shown that quantum Monte-Carlo (QMC), in particular, can be used to both explain the behavior of such systems and to guide experiments in developing novel tools to systematically expand the frontiers of research in the effects of disorder.

1.1 Synthetic Materials with Ultra-Cold Atomic Gases

The physical understanding of systems progresses via a cyclical process by which theoretical expectation guides experiment, following which experimental insight guides expansion of theory. However, direct comparisons between theory and experiment is not straightforward. Real systems can be extremely complicated and it may be impossible to diagnose and extricate the essential ingredients that contribute to phenomena of interest. It would thus be extremely useful to be able to construct materials from scratch with only the bare ingredients that are suspected to contribute. The emerging field of synthetic materials combines techniques of atomic-molecular-optical (AMO) physics to study systems more traditionally associated with condensed matter (CM). Indeed, AMO systems have been extremely successful in studying a variety of novel phenomena; prominent examples include the realization of Bose-Einstein condensation (BEC) [1, 2, 3], degenerate Fermi gases [4, 5, 6, 7], and the Bardeen-Cooper Schrieffer (BCS) to BEC crossover [8, 9], among others. These techniques have been extended in innovative ways that allow for fantastic new possibilities. For instance, by constructing artificial lattices with tunable parameters such as interaction strength, particle number and even characterizable disordered potentials – the system of interest in this dissertation, it is possible to access fundamental models of CM physics. Interesting CM phenomena that have been probed in this way include the Superfluid to Mott-Insulating phase transition [10], superfluid to Bose-Glass transition in 1D and 3D [11, 12]. Further advances with synthetic Gauge fields [13], multi-species gases [14] will open the frontiers into topological phases, composite fermion and other exotic strongly correlated phenomena [15, 16].

1.2 Bosons in Lattices

Bosons constitute one half of the Universe (the other half being made of Fermions) and in the Standard Model correspond to fundamental particles such as the Gauge Bosons (gluons, photons, Z boson and the W boson) and the Higgs Boson. The former are known as force carriers and mediate the strong, weak and electromagnetic fundamental interactions. The Higgs Boson, which has been recently confirmed to exist [17], is responsible for making all the elementary particles (except the photon and gluon) massive. A full discussion of such particles is beyond the scope of this work but an excellent introduction can be found in [18]. Aside from such fundamental particles, Bosons can also arise in the form of collective modes or quasi-particles (phonons), compositions of elementary Fermions – atoms, superconducting Cooper pairs [19] and so forth. Provided that the long wavelength features are being probed, such collective entities behave like Bosons and possess their fundamental property, *viz.* that the wavefunction used to describe the physical content of a collection of such particles remains symmetric under exchange of particle coordinates. In simple terms this also implies that Bosons "like" to be near one another (compared to distinguishable particles there is a statistical pressure for non-interacting Bosons that brings them closer together). In non-interacting systems with Bosons, for instance this leads to the Bose-Einstein condensate below a certain *critical* temperature. Interactions complicate affairs, but the basic phenomena still holds. In the CM setting, Bosons in a lattice is thus arguably one of the simplest ways of studying interaction-mediated effects – the Bose-Hubbard model (BHM) does precisely this.

In 3D systems, Bose condensation is synonymous with the concept of superfluidity. Superfluids are remarkable states of matter that can flow with zero viscosity. Superconductivity is a specific realization of superfluids and can arise via various mechanisms, the most ubiquitous of which is the formation of Cooper pairs due to attractive interactions induced by lattice vibrations (phonons). The microscopic description of this fundamental form of superconductivity was given by the celebrated Bardeen-Cooper-Schrieffer (BCS) theory [20].

The phenomenology of interacting superfluids leads to the a novel type of insulating state called the Mott-insulator (MI) when interaction strength is sufficiently large. This was demonstrated in the ultra-cold atomic setting by Greiner et al. at a qualitative level [10]. The quantitative aspects of such systems, especially at finite temperatures, however, are still unclear. In the presence of strong interactions such Bosonic systems quickly enter a parameter regime that is not describable by conventional theoretical approaches owing to strong correlations among the particles; these are discussed in Chapter 6. Recently a collaborative effort between theory and experiment purportedly showed excellent agreement at the quantitative level for all temperatures [21]. However, an even more recent study presented in this dissertation in collaboration with experiments suggests that there may be strong non-equilibrium effects owing to lack of adibaticity in such systems. As a result, the condensate that develops in the superfluid regime can exhibit long-lived metastability – it persists at temperature values much larger than the critical temperature. The basic framework to understand this is encapsulated within the theory of Landau damping, also discussed in Chapter 6.

1.3 The Dirty Boson Problem

The basic ideas discussed above motivate the need for a rigorous approach to understanding equilibrium properties of systems made possible with ultra-cold gases. It is only by first understanding such behavior at both qualitative and quantitative levels can aberrant behavior be deemed "exotic". After all, non-universal phenomena that are sensitive to initial conditions, while interesting, can reveal very little about general phenomenology. A systematic approach demands that exotic behavior be at the very least reproducible and, if possible, explainable in terms of universal principles that are applicable to a variety of systems. The absence of explanations motivates further inquiries and development of novel universal principles. The phenomena associated with disordered systems fits well into this paradigm.

Although disorder is ubiquitous in nature, very little is actually known about it and how it modifies behavior of conventional universal phenomena. The little that is known points to an exotic landscape of phenomena such as Anderson Localization [22] and it can have far reaching consequences such as Many-body localization that can halt equilibration in closed quantum systems [23, 24]. Additionally, disorder can lead to unconventional behavior in phases and phase transitions, for instance leading to destruction of first-order phase transitions, smearing out of continuous phase transitions and so forth [25].

The "Dirty Boson" problem is one example of such a system, where the conventional picture of interacting Bosons in a lattice gets modified by the addition of disorder. A seminal paper by Fisher et al. [26] studied this problem, realized via the disordered Bose-Hubbard model (DBHM), using renormalization group (RG) techniques and reported the fantastic possibility of a novel state of matter - the "Bose glass". Since then, a variety of attempts have been made analytically, numerically and experimentally to identify the properties of this phase and the other phases –superfluid and Mott-Insulator – as they are modified by disorder (references and discussions of which are given in Chapters 7-9).

However, quantitative comparison between theory and experiment in disordered systems is exceptionally hard. This is primarily because the properties of the disorder being introduced in experiments are notoriously difficult to characterize. It is only recently through the use of AMO techniques that completely characterizable disorder has been made possible, via the use of speckle fields, multi-chromatic lattices and so forth [27]. These innovations have led to a novel realization of a system with tunable disorder and interactions in optical lattices, which is the main subject of interest in this dissertation. Concurrently, owing to the breakdown or inapplicability of existing analytical frameworks over the full range of accessible parameters, an appropriate course of action is to use Quantum Monte-Carlo (QMC) techniques that for the DBHM suffer from no approximations. The results obtained from QMC can be used to gain insights into this model, and to check experimental findings.

1.4 Methodology

The primary method of theoretical inquiry in this dissertation is quantum Monte-Carlo (QMC). It is applied to a range of lattice systems that is constructed from the continuum Hamiltonian via coarse-graining procedure that integrates out high energy components of the dynamics. Part II of this dissertation describes the details of these methods. Chapter 2 discusses the basics of Monte-Carlo sampling techniques that is the corner stone of modern QMC methods. The ideas of Monte-Carlo sampling and integration are presented at a fundamental level and should be accessible to the general audience. Following this, the main QMC algorithm used to study the DBHM, Stochastics Series Expansion (SSE) is discussed in detail in Chapter 3. This technique is based on the path Integral formulation of quantum mechanics [28] that was used to develop a numerical method known as path integral Monte-Carlo (PIMC) [29]. In PIMC the quantum statistical problem is mapped to a classical counterpart in which particles are described in spatial and imaginary time landscapes. The configuration of particles in this landscape correspond to paths that describe the physics of equilibrium systems. For example, the phenomenon of superfluids manifests as multiple particles connected over imaginary time and space. This global connectivity leads to long-range correlation in space and time that, in turn, results in superfluidity and Bose-Einstein condensation (BEC). Using these techniques it is possible to calculate a variety of theoretically well established observables that can be extended to understand experimental probes.

One such observable that is of tremendous importance throughout the rest of the dissertation is the single-particle density matrix (ρ_1). Manipulations of ρ_1 are outlined in Chapter 4, and lead to the possibility of extracting the single-particle eigenstates of the system. These states correspond to the way single particles behave when the system is probed at the single-particle level. The technical aspects of extracting such modes is discussed together with a systematic characterization of possible sources of error and ways to avoid them.

As discussed earlier, the main limitation of disordered systems is the difficulty in characterizing the specific form of the disorder that is present in the system. Not accounting for this makes it almost impossible to conclusively identify effects and phenomena that arise in experiments. Fortunately the use of speckle fields alleviate this problem greatly. However, despite the fact that all properties of the disorder are known, the way in which a low-temperature effective Hamiltonian can be constructed is not simple. It is possible to use the potential as is, i.e., handle the full problem in the continuum, but this severely constrains the ability to handle large systems. Consequently, an effective coarse-grained Hamiltonian such as the DBHM must be used. Such a model has all the essential features of the low-temperature system. In the clean case, the coarse-graining procedure uses localized basis states called Wannier functions of the lattice potential to arrive at the BHM. For the disordered system a similar approach, discussed in Chapter 5, is used to generalize the notion of Wannier functions to aperiodic systems and construct the DBHM for optical lattices with speckle disorder. This system has disorder in all terms of the Hamiltonian – unlike conventional theoretical models of disorder, where disorder is only present as a local potential shift. The tools and techniques developed in this part of the dissertation are applied to study the DBHM in part III.

1.5 Applications

The final part of this work concerns studying the properties of the DBHM. Previously, it was mentioned that the starting point of the work is concerned with the clean BHM in Chapter 6. The systematic study between theory and experimental techniques involves one of the largest QMC calculation done to date, accessing system sizes of $\sim$ 200,000 particles at temperatures much lower than those accessed in experiments. This was done in order to be able to calculate the entropy per particle. Unlike conventional CM systems, experiments with ultra-cold atomic gases suffer from a limitation that there are no external temperature probes available. However, using certain basic approximations experiments can estimate the entropy in the systems. Together with another probe, the peak fraction that estimates the quantity of condensed atoms, it is thus possible to perform thermometry in these systems. Additionally, the BHM is one of the few systems for which there exists a range of analytical theories. Therefore, a straightforward comparison between such theories, QMC and experiment is possible. Results of these have been discussed in Chapter 6 following [12]. As mentioned earlier, there appears to be a possibile lack of equilibration that leads to the metastability of the condensate. The theory of Landau damping provides some insight into such out-of-equilibrium phenomena, which is discussed also in Chapter 6.

The following chapters are concerned with the DBHM. Chapter 7 handles the preliminaries of the DBHM in trap-free systems. In this chapter the basic scaling theory, known as the Harris criteria, that describes a wide class of disordered problem is discussed. According to this theory, the effects of disorder on a system is dictated by its correlation length critical exponent ν. These aspects derive from the theory of continuous phase transition and critical phenomena [30].

In basic terms the change of the parameters of the system such as temperature and parameters of the Hamiltonian, lead to fundamental changes in the state of the system. Each such state corresponds to a phase and the full parametric landscape defines a phase diagram. The set of particular values of parameters at which the system undergoes a phase transition is called a critical point. According to the theory of critical phenomena, when a system approaches a critical point the correlation length – the distance over which particle motion is correlated – starts to diverge, and observables of the system scale according to some universal scaling functional forms that are characterized by parameters called critical exponents. For instance, ν characterizes the way the correlation length scales. At the critical point all systems possessing the same set of exponents – called a Universality class – behave identically! Additionally, the critical point dictates how the system proceeds through the transition, i.e., it dictates what the resulting phases are. When disorder is present the phase diagram gets modified in non-trivial ways.

The Harris criteria states that if $\nu d > 2$, where d is the dimensionally of the system, then the system is unstable to disorder and the phase diagram will change at the qualitative level. This is precisely what happens for the DBHM. The conventional superfluid-Mott-Insulator (SF-MI) phase diagram for the clean system gets qualitatively modified by the appearance of the Bose-glass (BG), which is a novel quantum state of matter, and there are two new critical points that dictates SF-BG and BG-MI transition. These are discussed in some detail in Chapter 7 together with general phase transition mechanisms between different phases and so forth. The BG differs from SF via the fact that it has zero global superfluid fraction. On the other hand it differs from a MI due to its finite compressibility.

The main point of Chapter 7 is to establish the properties of the BG – its qualitative properties and the key aspects that make it different from other phases. QMC results are used to explicitly show that the BG is composed of puddles of SF that are uncorrelated with each other. The paths of particles in these puddles tend to be local to the puddles and exchange rarely with he incoherent background in which the puddles are embedded. The physics of these puddles is fascinating. Unlike ordered domains in regular disordered phases the way they grow is not within the regular framework of phases and phase transitions. These properties point to remarkable physics that should be observable in dynamical aspects of the system, for instance. These will be discussed later.

Result also illustrate the basic features of the phase diagram at constant density and how they compare between two different types of disorder distributions. Qualitatively, features of the phase diagram appear to be robust; however, there are large quantitive differences due to the speckle form of disorder that is used in experimental settings. Finally, finite temperature effects are illustrated via the superfluid fraction and compressibility observables that are of prime importance in these systems. Intriguingly the BG itself has two distinct flavors ranging from ultra-low to large finite compressibility. These regions are connected via a cross-over. Finite temperature effects also show that disorder can stabilize order: at filling factor larger than 0.5, the transition temperature for the SF phase is increased for increasing values of disorder (up to a point).

Chapter 8-9 discuss the aspects of trapped disordered systems. The discussions are concerned with parameters that are readily accessible to experiments. In fact, direct comparisons are made with experimental systems. The first few sections of Chapter 8, describe the properties of domains that develop in these systems due to the trap. It is shown that both short length scales (of the order of lattice distances) and global length scales are inadequate to describe the rich phenomena in these systems. Instead, using the single-particle eigenstates, it is possible to identify intermediate length scales that correspond to the typical sizes of the domains. Calculations of observables conclusively show that these domains correspond well to phases of the trap-free system. Thus, these trapped system can simultaneously possess multi-phase properties of the BG, SF and MI. Using quantitative comparisons it is shown that the local density approximation that is frequently used to explain clean trapped systems, cannot account for the properties of the system and, in certain cases, can even fail qualitatively. The expansion of the gas that result from the addition of disorder is a key contributor to many of its properties in the trap. Finally, the tools developed in this chapter is used to conclusively demonstrate the existence of SF domains that correspond to a reentrant phenomena that has remained elusive to experiments. Results are discussed for an experimentally realizable system and shown to be well within the limits of current cooling schemes for experiments.

In order to facilitate experiments in accessing and interpreting the range of possible behavior with speckle disorder, full scale phase diagrams are presented at the end of Chapter 8. Also, the aspects of disorder averaging and the break down of self-averaging (SA) due to disorder is discussed. It seems that observables show large deviations (between disorder realizations) near phase boundaries, whereas within respective phases there are only small quantitative changes. Finally, the effects of tunneling disorder in these systems are discussed at ultra-low temperatures. The SF phase remains remarkably robust, even quantitatively, despite large disorder values. The condensate on the other hand exhibits minor differences.

The final Chapter 9 delineates the results of a collaborative effort between experiments and theoretical work done in this dissertation [31]. In this novel study, experiments utilize a quantum quenching protocol to exploit the Kibble-Zurek (KZ) mechanism as a means of identifying parameters for which a BG exists in the gas. Comparisons with QMC estimates of the SF-BG reveal a remarkable agreement between the two boundaries. However, the time-scale of dynamics are found to vary very weakly with time scales of the experiment, pointing to a lack of relaxation of the excitations generated during the quench whenever there is a BG present. Although it is unclear at the moment, there are good reasons for believing that this form of slow relaxation is a quintessential example of glassy dynamics that might be similar to phenomena in classical systems such as Spin glasses, and quantum glasses such as the disordered transverse-field Ising model. The DBHM might be one of the few other examples of quantum glasses that are accessible to theoretical and experimental inquiries. The work presented in this dissertation will hopefully contribute to future studies in this exciting field.

Part II

Methods

This part of the dissertation focuses on the methods used to study specific systems outlined later. In Chapter 2 the basics of Monte Carlo methods are briefly discussed. These will be needed to understand the notation used in later chapters. Chapter 3 describes the Stochastic Series Expansion method in detail, since it is the main Quantum Monte Carlo tool used in this dissertation. All discussions in this part is kept as general as possible. Specific instances discussed in the context of systems covered in part III, are also applicable to a wide variety of situations. For instance, measurements of correlation functions in imaginary time are of great interest for studying equilibrium properties of Many-body systems. Chapter 4 covers extraction of eigenmodes from the single-particle density matrix, but the details are applicable to any reduced density matrix extracted via Monte Carlo schemes. Algorithmic details pertaining to Arnoldi Iterative methods used to diagonalize noisy matrices are also discussed. The eigenfunctions of the respective reduced density matrices can be used in a variety of ways to study systems – for instance, the macroscopic occupation of an eigenmode of the single-particle density matrix signals Bose-Einstein condensation. Additionally, the spatial distribution of the condensate conveys important information about the domains that develop in trapped systems. Finally, Chapter 5 handles the mechanics of coarse-graining continuum Hamiltonians to produce low energy effective lattice models. The general method outlined therein is used extensively to study disordered systems that corroborate closely to experiments with ultra-cold atomic gases.

Chapter 2

Monte Carlo Techniques

Monte Carlo methods applicable to this dissertation are concerned with studying physical systems which obey laws of Quantum Mechanics. These methods, however, are much more general and can be used in many different ways. It is remarkable that such a simple idea involving i.e., "random" generation of samples – effectively tossing the dice – can lead to deep insights into what would otherwise be intractable problems. As a full discussion of this old and rich subject is beyond the scope of a dissertation, the focus in this chapter will be only the essentials that will be needed for later chapters. For more refer to [32, 33].

2.1 Random Variables and Probability Distributions

The most fundamental constituent of a Monte Carlo sampling involves a *random variable* X drawn from some *probability distribution function (pdf)* $P\{X\}$ such that in the long sampling limit, the frequency with which $X = x_i$ occurs is proportional to $p_i \equiv P[X = x_i]$. The symbols carry the following meaning: $\{x_i\}$ are different permitted values characterizing the probability distribution P, written as $P[X]$. X symbolizes one possible value from among the set $\{x_i\}$. For real physical systems, the drawing or generation of a sample is associated with a real (or virtual) event – i.e., it is a consequence of how the system evolves. Computationally, the process has to be defined, which will be done shortly. For the moment assume such a process is possible.

Given that a sequence of values $x_1, x_2, x_3, ...$ can be drawn from a pdf, such that $X \in \{x_i\}$, it is possible to define the *expectation value* of the random variable X as:

$$E[X] \equiv \sum_i P[X = x_i]x_i = \sum_i p_i x_i \equiv \langle X \rangle, \tag{2.1}$$

where $\langle X\rangle$ is called the expected or mean value. For any function $g(X)$ the expectation value of the function is given by:

$$E[g(X)] = \langle g(X)\rangle = \sum_i p_i g(x_i). \tag{2.2}$$

Additionally the *variance* of any function is given by:

$$\begin{aligned} var\{g(X)\} &\equiv \langle (g(X) - \langle g(X)\rangle)^2\rangle \\ &= \langle g(X)^2\rangle - \langle g(X)\rangle^2 \\ &= E[g^2(X)] - (E[g(X)])^2. \end{aligned} \tag{2.3}$$

2.2 Monte Carlo Quadrature: Estimators

Let $X_1, X_2, X_3, \cdots, X_i, \cdots, X_N$ be random variables drawn from the same pdf (say $P(x)$), not necessarily independently. Let g be some function, that needs to be estimated. Using the *estimator*,

$$G \equiv \frac{1}{N}\sum_{i=1}^{N} g(X_i). \tag{2.4}$$

The expectation value of G is given by:

$$\begin{aligned} E[G] = \langle G\rangle &= E\left[\frac{1}{N}\sum_{i=1}^{N} g(X_i)\right] \\ &= \frac{1}{N}\sum_{i=1}^{N} E\left[g(X_i)\right] \\ &= \frac{1}{N}\sum_{i=1}^{N}\int g(x_i)P(x_i)dx_i \\ &= \frac{1}{N}\sum_{i=1}^{N}\langle g(X)\rangle \\ &= \langle g(X)\rangle. \end{aligned} \tag{2.5}$$

So the expectation value or mean of G is equal to the mean of $g(x)$. This is why G is called an estimator of $\langle g(X)\rangle$. Additionally the variance of G is given by:

$$\begin{aligned}
var\{G\} &= var\left\{\frac{1}{N}\sum_{i=1}^{N} g(X_i)\right\} \\
&= \frac{1}{N^2}\left\{E\left[\left(\sum_{i=1}^{N} g(X_i)\right)^2\right] - \left(E\left[\sum_{i=1}^{N} g(X_i)\right]\right)^2\right\} \\
&= \frac{1}{N^2}\left\{\sum_{i,j=1}^{N} E\left[(g(X_i)g(X_j))\right] - \left(\sum_{i=1}^{N} E\left[g(X_i)\right]\right)^2\right\} \\
&= \frac{1}{N^2}\left\{\sum_{i,j=1}^{N} E\left[(g(X_i)g(X_j))\right] - \sum_{i,j=1}^{N}\left(E\left[g(X_i)\right]E\left[g(X_j)\right]\right)\right\} \\
&= \frac{1}{N^2}\left\{\sum_{i=1}^{N} E\left[(g(X_i)g(X_j))\right] - \left(E\left[g(X_i)\right]E\left[g(X_j)\right]\right)\right. \\
&\quad \left. + \sum_{i\neq j}^{N} E\left[(g(X_i)g(X_j))\right] - \left(E\left[g(X_i)\right]E\left[g(X_j)\right]\right)\right\}. \qquad (2.6)
\end{aligned}$$

For independent observables $Cov\{X_i, X_j\} = E[g(X_i)g(X_j)] - E(g(X_i)]E(g(X_j)] = 0$, so that

$$\begin{aligned}
var\{G\} &= \frac{1}{N^2}\left\{\sum_{i=1}^{N} E\left[(g(X_i)g(X_j))\right] - \left(E\left[g(X_i)\right]E\left[g(X_j)\right]\right)\right\} \\
&= \frac{1}{N} var\{g(X)\}. \qquad (2.7)
\end{aligned}$$

This is an extremely important result. It explicitly shows that for increasing number of samples, the estimator G becomes increasingly accurate. The equation of the estimator (2.5) together with variance reduction relation (2.7) are the central ideas of Monte Carlo sampling.

2.3 Sampling Distributions via Transformation of Random Variables

Using Monte Carlo to sample distributions and obtain estimators of different observables relies on the ability *to sample*. Somehow one must be able to generate a sequence of samples (e.g., simple ones such as numbers or a complex object such as configurations in N-dimension phase-space) that correspond to some pdf of interest. This is not straightforward, but several techniques have been developed that are especially suited for computers. The cornerstone of all sampling techniques on modern computers is the use of *pseudo-random* numbers that are random within some large periodicity (a popular choice for Monte Carlo is the Mersenne twister algorithm that has a periodicity of $2^{19937} - 1$ [34]).[1] Such numbers are generated uniformly so that any number in the sequence is equally likely to be generated. Using these numbers it is possible to draw samples from a different pdf by the transformation of random variables so that the desired pdf is sampled despite the random numbers being drawn from another (well understood and simple) pdf.

The idea of transformation of variables can be illustrated as follows [32]. Let X be a random variable to be sampled from the pdf $f(x)$. The associated *cumulative distribution function* (cdf) is given by:

$$F(x) = \int_{-\infty}^{x} f(x')dx'. \tag{2.8}$$

Let the random variable Y be related to X given by a continuous monotonically increasing function of X given by $Y = y(X)$. Then by the monotonic relationship:

$$y(X) \leq y(x) \text{ iff } X \leq x,$$

so that the probabilities transform as

$$\begin{aligned} P\{y(X) = Y \leq y(x)\} &= P\{X \leq x\} \\ \text{i.e., } F(y) &= F(x) \\ \text{and,} \frac{dF}{dy}\frac{dy}{dx} &= \frac{dF}{dx} \\ f(y)\frac{dy}{dx} &= f(x). \end{aligned} \tag{2.9}$$

The same analysis can be extended to a monotonically decreasing function of X so that

$$\begin{aligned} P\{y(X) = Y \leq y(x)\} &= P\{X \geq x\} \\ \text{i.e., } F(y) &= 1 - F(x) \\ f(y)\frac{dy}{dx} &= -f(x). \end{aligned} \tag{2.10}$$

Combining 2.9 and 2.10, the connection between the pdf's resulting from the transformation

---

[1] More recently the computer industry is looking into generating true random numbers.

of variables $Y = y(X)$ is:

$$\begin{aligned} f(y)|\frac{dy}{dx}| &= f(x) \\ |f(y)dy| &= |f(x)dx|. \end{aligned} \tag{2.11}$$

Thus, given the knowledge of $f(x)$ and a desired $g(x)$ it is possible to tailor the transformation function $y(x)$ so that:

$$f(y(x)) = g(x) \tag{2.12}$$

$$f(x)\frac{dx}{dy} = g(x) \tag{2.13}$$

$$y(x) = \int \frac{f(x)}{g(x)}dx. \tag{2.14}$$

Frequently, however, such straightforward transformations are not possible and alternative strategies are needed. Once class of such methods is known as *Rejection Techniques*, discussed next.

2.4 Rejection Techniques

The idea behind rejection technique is to generate a random variable (X) of a desired distribution $(f(x))$ by exploiting two random variables and corresponding distribution functions. Let Z be the random variable from the pdf $g(z)$ that is called the *proposal probability distribution function*. Another variable ξ is drawn from the *acceptance or rejection probability distribution function* $h(z)$ to test if Z is to be accepted or rejected. The strategy is to propose a Z and accept it with probability $h(Z)$, in which case $X \leftarrow Z$ otherwise another Z is proposed and the process is continued. By tailoring $h(z)$ correctly, $f(x)$ can be sampled. To see how this is achieved, consider the joint probability that a Z is proposed and accepted:

$$P\{Z < x \ and \ \xi \leq h(Z)\} = \int_{-\infty}^{x} h(z)g(z)dz. \tag{2.15}$$

Note that the acceptance is signaled by generating a random number ξ from $h(z)$ and checking for $\xi \leq h(Z)$. This equation simply states, that the probability of a random number Z drawn from the pdf $g(z)$ being less than some number x and that number Z being accepted is given by the integral of the probability of success $h(z)$ times the probability of occurrence of z in dz, i.e., $g(z)dz$. If we qualify success as the assignment $X \leftarrow Z$, for the full range of values of Z, i.e., from $-\infty$ to ∞, then:

$$\begin{aligned} P\{Z < \infty \text{ and } \xi \leq h(Z)\} &= \int_{-\infty}^{\infty} h(z)g(z)dz \\ P\{\xi \leq h(Z)|Z < \infty\}P\{Z < \infty\} &= \int_{-\infty}^{\infty} h(z)g(z)dz \\ P\{\xi \leq h(Z)|Z < \infty\} &= \int_{-\infty}^{\infty} h(z)g(z)dz. \end{aligned} \tag{2.16}$$

Since, $P\{Z < \infty\} = 1$, this indicates the probability of success no matter what the value of Z. Following [32], let $P\{success\} \equiv P\{\xi \leq h(Z)|Z < \infty\}$. Then:

$$\begin{aligned} P\{Z < x and \xi \leq h(Z)\} &= P\{success\}P\{Z < x|success\} \\ \therefore P\{Z < x|success\} &= \frac{P\{Z < x \text{ and } \xi \leq h(Z)\}}{P\{success\}} \\ &= \frac{\int_{-\infty}^{x} h(z)g(z)dz}{\int_{-\infty}^{\infty} h(z)g(z)dz}. \end{aligned} \tag{2.17}$$

Thus the resulting pdf due to the use of rejection technique is given by:

$$t(z) = \frac{h(z)g(z)dz}{\int_{-\infty}^{\infty} h(z)g(z)dz}. \tag{2.18}$$

In order to generate $f(x)$, a good choice is:

$$h(z) = \frac{f(z)/g(z)}{\left\lceil \frac{f(z)}{g(z)} \right\rceil}. \tag{2.19}$$

The *a priori* success probability, i.e, $P\{success\}$ becomes:

$$\begin{aligned} P\{success\} &= \int_{-\infty}^{\infty} h(z)g(z)dz \\ &= \frac{1}{\left\lceil \frac{f(z)}{g(z)} \right\rceil} \int_{-\infty}^{\infty} \left[\frac{f(z)}{g(z)}\right] g(z)dz \\ &= \frac{1}{\left\lceil \frac{f(z)}{g(z)} \right\rceil}. \end{aligned} \tag{2.20}$$

So that in order maximize the success probability, $\lceil \frac{f(z)}{g(z)} \rceil = \vee \left\{ \frac{f(z)}{g(z)} \right\}$ should be used, where $\vee$ indicates the *supremum* or least upper bound.

2.5 The $M(RT)^2$ Algorithm

Possibly the primary work-horse of most modern Monte Carlo methods is the $M(RT)^2$ or Metropolis algorithm [35]. This is a type of rejection technique that relies on the idea of detailed balance, *viz.*, that the probability of a system to evolve from a state X to another state Y, given by $K(X \to Y)$ together with the probability of occurrence of the state X given by $f(X)$ must be equal to the reverse process. More succinctly:

$$K(X \to Y)f(X) = K(Y \to X)f(Y). \tag{2.21}$$

Monte Carlo techniques typically use the $f(X)$ – the *a priori* chance of finding the system near the configuration X to determine the kinetic transition probability $K(X \to Y)$, by which the system evolves to other states. Incidentally the principle of detailed balance is intimately linked to equilibrium Statistical Mechanics [33]. Additionally, the use of the kinetic transition probability encoded in $K(X \to Y)$ follows from the idea of Markov processes, which have no memory. Notice, that the only thing that matters in the determination of the next state, is the current state and not the history of all prior states. For a full discussion refer to [32, 33]. Normally $K(X \to Y)$ is determined indirectly via the idea of rejection technique discussed in the previous section so that $K(X \to Y)$ can be decomposed as $K(X \to Y) = T(Y|X)A(Y|X).T(Y|X)$ gives the probability with which the configuration Y is proposed (given X) from any distribution. $A(Y|X)$ is the acceptance probability of configuration Y given the current configuration X. Then detailed balance is given by:

$$A(Y|X)T(Y|X)f(X) = A(X|Y)T(X|Y)f(Y). \tag{2.22}$$

Using $q(X|Y) \equiv \frac{T(Y|X)f(X)}{T(X|Y)f(Y)}$, a usable form of the acceptance probability that maintains detailed balance is given by:

$$A(X|Y) = min(1, q(X|Y)). \tag{2.23}$$

The Metropolis method proceeds as follows:

1. A random configuration that is valid is used as the initial state of the system $X \leftarrow X_0$.
2. Using X_0 and some easy to access $T(x)$, a new configuration is proposed, say X_1.
3. This new state is accepted or rejected using 2.23.
4. If it is accepted then $X \leftarrow X_1$ otherwise $X = X_0$.

5. Repeat from step 2.

The method guarantees that in the asymptotic limit of large number of samples $n \to \infty$, the probability with which X_n is sampled is given by $f(X)$. The problem is that generally there is no *a priori* way to know the appropriate n, and has to be found by running the simulation and monitoring the observable that needs to be computed. This phase is called the equilibration phase and can be very costly. After equilibration, when the system has settled down to sampling the distribution that is needed, the necessary observable may be computed. Each observable has its own equilibration time. Also, subsequent samples may be correlated (and frequently is), so the autocorrelation time must be found so that the variance of the estimator is computed correctly. The efficiency of any algorithm is therefore controlled by good choices of T in connection with the distribution being sampled.

Chapter 3

Stochastic Series Expansion

The primary QMC technique used in this work is the Stochastics Series Expansion (SSE) method together with algorithmic modifications such as the directed loop algorithm [36, 37]. It is an extremely robust finite-temperature method that aims to calculate properties of lattice Hamiltonians. The method is exact for Bosons as well as other sign-problem free systems such as spins.[1] Unlike most documentation the discussions below will be centered around a single species of Bosons, as it is very general and can be easily extended to cover other types of systems. In this section the general method is outlined.

Since the aim is to solve finite temperature systems, the starting point is the thermal thermal density matrix $\hat{\rho} \equiv \frac{e^{-\beta\hat{\mathscr{H}}}}{\mathcal{Z}}$ where the partition function Z is given by,

$$\mathcal{Z} = Tr[e^{-\beta\hat{\mathscr{H}}}]. \tag{3.1}$$

$\hat{\mathscr{H}}$ is the Hamiltonian, β is the inverse temperature, and Tr denotes the trace operator.[2] Note that the chemical potential term has been implicitly included ($\mu\hat{N}$) in $\hat{\mathscr{H}}$ - for particle systems (as opposed to spins) SSE works with the Grand Canonical ensemble.

SSE works by expanding the exponential to a power series and taking a trace over all possible states $\{|\alpha\rangle\}$ described by some basis:

$$\mathcal{Z} = Tr\left[\sum_{p=0} \frac{\beta^p}{p!}(-\hat{\mathscr{H}})^p\right] = \sum_{\alpha}\sum_{p=0}^{\infty} \frac{\beta^p}{p!}\langle\alpha|(-\hat{\mathscr{H}})^p|\alpha\rangle. \tag{3.2}$$

---

[1] The sign problem arises in QMC from sampling an anti-symmetric wavefunction. Essentially the kinetic component introduces negative off-diagonal elements in the Hamiltonian that cannot be removed via some general procedure. For a full discussion refer to [38].

[2] See appendix A for a brief discussion on Density Matrices.

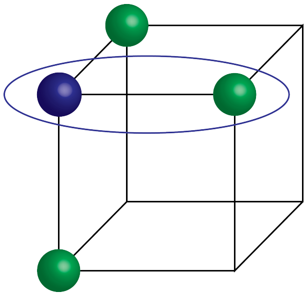

$$\begin{aligned}\hat{\mathscr{H}} &= -t\sum_{\langle ij\rangle} + \frac{U}{2}\sum_{i}\hat{n}_i(\hat{n}_i - 1)\\ &= \sum_{\langle ij\rangle}\left[-t(\hat{b}_i^\dagger\hat{b}_j + \hat{b}_i\hat{b}_j^\dagger)\right] + \left[\frac{U}{4D}\{\hat{n}_i(\hat{n}_i-1) + \hat{n}_j(\hat{n}_j-1)\}\right]\\ &= \sum_{b\in\{\langle ij\rangle\}} \hat{H}_b^o + \hat{H}_b^d\end{aligned}$$

Figure 3.1: Illustration of bonds and bond decomposition made to obtain local bond operators. For a ($D = 3$) system any lattice site (shown in blue) is connected to 3 nearest neighbors (shown in green) for a nearest-neighbor type of model. A bond is made up of 2 such sites (encapsulated within the elliptical region). The corresponding Hamiltonian can be broken up into diagonal ($\hat{H}_b^d$) and off-diagonal ($\hat{H}_b^o$) terms. Notice how the diagonal operator that typically acts on a single site is expanded D (dimensionality) times in order to accommodate the bond picture. It should be clear that bonds can easily be made to accommodate more than nearest neighbors.

Usually the basis of choice is the occupation number basis $\{|n\rangle\}$, where n is the particle number, so that $|\alpha\rangle = |n_1\rangle \bigotimes |n_2\rangle ... \bigotimes |n_{N_s}\rangle$ and N_s is the number of sites in the lattice. For lattice systems the Hamiltonian can be decomposed into a sum over all possible bonds of the system, i.e., $\hat{\mathscr{H}} = -\sum_{b=1}^{N_b}\hat{H}_b$. Here N_b denotes the total number of bonds, b is the bond number, and $\hat{H}_b$ is the local Hamiltonian operator defined locally for the bond. $\hat{H}_b$ can be further decomposed into off-diagonal ($\hat{H}_b^o$) and diagonal components ($\hat{H}_b^d$), via $\hat{H}_b = \hat{H}_b^o + \hat{H}_b^d$. An illustration of this decomposition is shown in Fig. (3.1). $\hat{H}_b^o$ must be a positive term so that there is no sign problem. The diagonal term can be made positive by adding a large enough constant term, which is cancelled out since for observables $\mathscr{Z}$ appears in the denominator as well (more later on measuring observables). Using these definitions:

$$\mathscr{Z} = \sum_{\alpha}\sum_{p=0}^{\infty}\frac{\beta^p}{p!}\langle\alpha|\left(\sum_{b=1}^{N_b}\hat{H}_b\right)^p|\alpha\rangle \tag{3.3}$$

$$= \sum_{\alpha}\sum_{p=0}^{\infty}\sum_{S_p}\frac{\beta^p}{p!}\langle\alpha|\hat{H}_{s_p}\hat{H}_{s_{p-1}}...\hat{H}_{s_1}|\alpha\rangle \tag{3.4}$$

Here $\left(\sum_{b=1}^{N_b}\hat{H}_b\right)^p = \sum_{S_p}\hat{H}_{s_p}\hat{H}_{s_{p-1}}...\hat{H}_{s_1}$ is used, where S_p denotes a sum over all possible strings of length p composed of bond operators $\hat{H}_{s_i} = \hat{H}_b^o$ or $\hat{H}_b^d$. Additionally a complete set of states $\{|\alpha(p)\rangle\}$ is introduced between the individual bond operators to get the final form:

$$
\begin{aligned}
\mathcal{Z} = \sum_{p=0}^{\infty} \sum_{S_p} \sum_{\alpha(0),\alpha(1)...} & \frac{\beta^p}{p!} \langle \alpha(0)|\hat{H}_{s_p}|\alpha(p-1)\rangle \langle \alpha(p-1)|\hat{H}_{s_{p-1}}|\alpha(p-2)\rangle \\
& \langle \alpha(p-2)|...|\alpha(1)\rangle \langle \alpha(1)|\hat{H}_{s_1}|\alpha(0)\rangle. \qquad (3.5)
\end{aligned}
$$

Due to the trace operation $|\alpha(p)\rangle \equiv |\alpha(0)\rangle$ is required. Also note that due to the trace, all cyclic permutations of the string of operators are identical. This form allows us to visualize a *configuration space* – the so called World Line picture that will be useful to explain measurement procedures needed for many types of observables (see. fig.(3.2)). Quite generally an observable is measured using,

$$
\langle O \rangle = \sum_{p=0}^{\infty} \sum_{S_p} \sum_{\alpha(0),\alpha(1)...} \frac{\beta^p}{p!} O(p, S_p, \{\alpha(0), \alpha(1)...\alpha(p-1)\}) \mathcal{P}(p, S_p, \{\alpha(0), \alpha(1)...\alpha(p-1)\}), \qquad (3.6)
$$

with $\mathcal{P}(p, S_p, \{\alpha(0), \alpha(1)...\alpha(p-1)\}) \equiv \frac{\beta^p}{p!}[\langle \alpha(0)|\hat{H}_{s_p}|\alpha(p-1)\rangle \langle \alpha(p-1)|\hat{H}_{s_{p-1}}|\alpha(p-2)\rangle ...]/\mathcal{Z}$ – a weight or probability function. The only thing left to estimate O is to generate configurations using $\mathcal{P}$ using Monte Carlo techniques discussed in the previous chapter.

There is one final modification that is generally made for numerical convenience. Although it is possible to allow the number of operators in the operator string to change during the sampling procedure, it is generally easier to fix the operator string length to some appropriately chosen large constant (Λ) and introduce a number of unit operators. So, the $\{H_{s_i}\}$ can now also be $\hat{1}$. Since every operator string of length p can be produced by the insertion of $(\Lambda - p)$ unit operators distributed in ${}^{\Lambda}C_p$ ways, we have to re-weight the expression by $1/{}^{\Lambda}C_p$. So the final partition function that we sample is given by:

$$
\begin{aligned}
\mathcal{Z} = \sum_{p=0}^{\Lambda} \sum_{S_\Lambda} \sum_{\alpha(0),\alpha(1)...} & \frac{\beta^p(\Lambda-p)!}{\Lambda!} \langle \alpha(0)|\hat{H}_{s_\Lambda}|\alpha(\Lambda-1)\rangle \langle \alpha(\Lambda-1)|\hat{H}_{s_{\Lambda-1}}|\alpha(\Lambda-2)\rangle \\
& \langle \alpha(\Lambda-2)|...|\alpha(1)\rangle \langle \alpha(1)|\hat{H}_{s_1}|\alpha(0)\rangle. \qquad (3.7)
\end{aligned}
$$

During equilibration Λ is adjusted so that the truncation in the series produces no errors. Equilibration is achieved following the Metropolis sampling strategy discussed in the previous chapter – achieved via two different types of update procedures called diagonal and loop update. These two updates constitute a single Monte Carlo sweep. The procedure is started with some initial state, which is updated using the SSE sweeps, so that asymptotically the

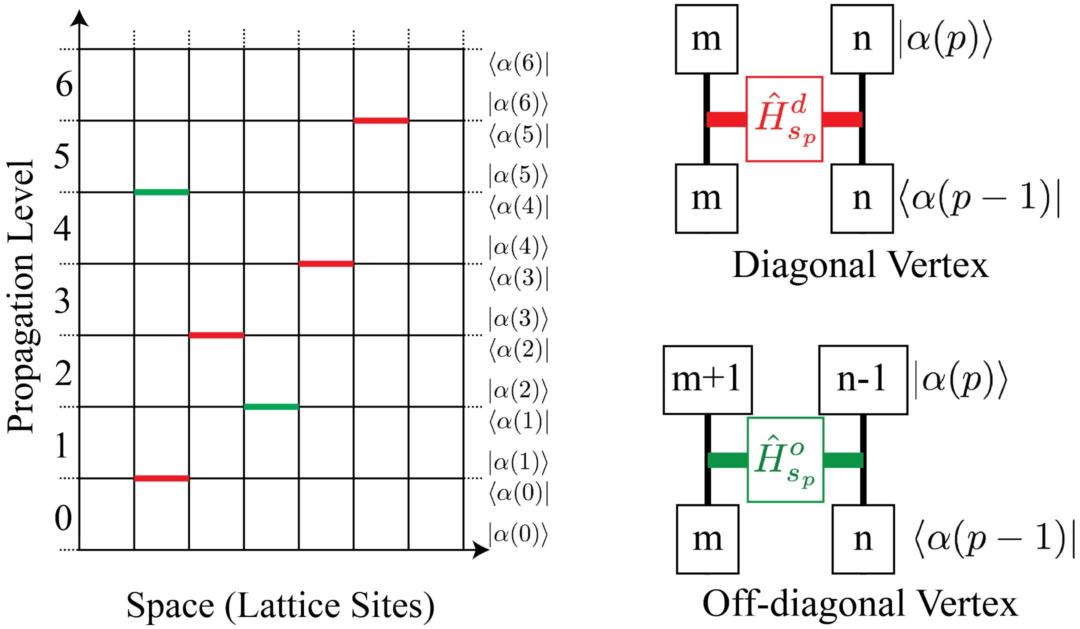

(a) (b)

Figure 3.2: (a) Shows the *World Line* picture corresponding to an operator string. Each bond operator is shown in different colors based on whether it is a diagonal or off-diagonal operator. The bonds connect sites as well as propagation levels (p). The associated state with a level is given by $|\alpha(p)\rangle$. (b) A bond together with the associated states on the incoming and outgoing legs represent a *vertex*. So there can be diagonal and off-diagonal vertices based on the bond operator.

system reaches equilibrium. After equilibration, it is possible to measure observables using configurations that can be generated using the same update procedures, discussed in detail below.

3.1 Diagonal Update

The first update procedure is about sampling p that controls the expansion order. This means a bond operator is either introduced by replacing a unit operator in the operator string or removed by the reverse procedure. The transition probabilities are give by:

$$\mathscr{P}(p \to p+1) = \frac{N_b \beta \langle\alpha(p)|\hat{H}_{s_p}|\alpha(p-1)\rangle}{\Lambda - p} \tag{3.8}$$

$$\mathscr{P}(p+1 \to p) = \frac{\Lambda - p + 1}{N_b \beta \langle\alpha(p)|\hat{H}_{s_p}|\alpha(p-1)\rangle} \tag{3.9}$$

The operator that is inserted or removed must be a diagonal type of operator. Note that an increase in operator order (p) is the same as replacing a unit operator with a new bond

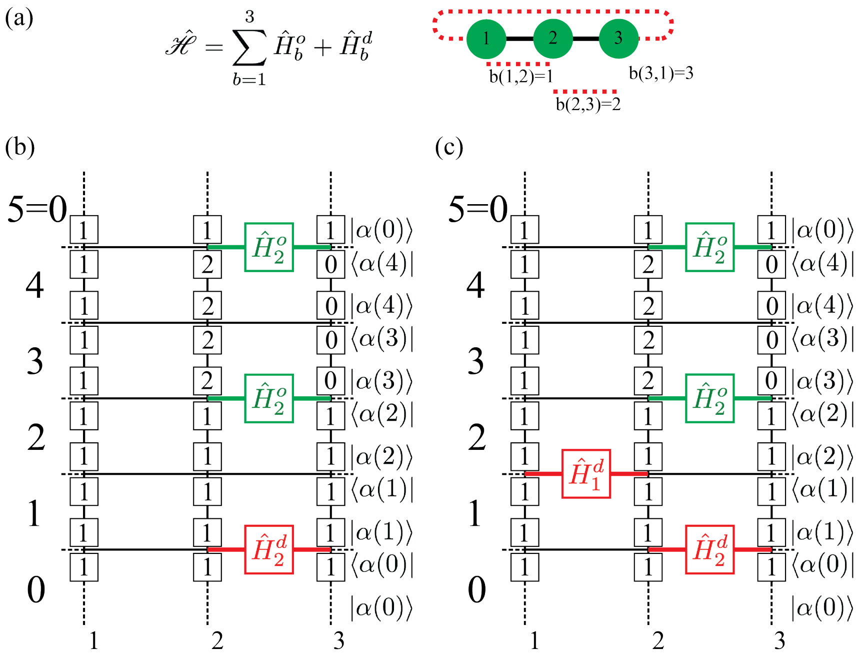

Figure 3.3: Illustration of Diagonal Update. a) Shows the system we consider. There are 3 sites with periodic boundary conditions. Bonds 1,2 and 3 connect sites (1,2), (2,3) and (3,1) respectively. b) Shows the world line and operator string representation of the configuration space before diagonal update starts. During the update, each vertex, starting with vertex 0, is checked sequentially for a possible transition using equations 3.8-3.9. In this example, the steps proceed as follows: **1.** The vertex connecting level 0 and 1 given by the term $\langle\alpha(0)|\hat{H}_2^d|\alpha(1)\rangle$ is checked for possible removal, which fails. **2.** The second vertex is located between levels 1 and 2, but is a unit operator so it doesn't have any specific sites to connect. In this case a random bond is chosen and checked for insertion, which in this case succeeds. Thus the operator string gets updated as shown in (c). **3.** The third vertex connecting level 2 and 3 is an off-diagonal operator, and is left unchanged but the state is propagated forward using $\hat{H}_2^o = \hat{b}_2^\dagger \hat{b}_3$ so that $|\alpha(2)\rangle = |1,1,1\rangle$ becomes $|\alpha(3)\rangle = |1,2,0\rangle$. **4.** The fourth vertex is another unit operator, but in this case insertion fails and the operator string is left unchanged. **5.** Finally the fifth vertex is another off-diagonal operator that causes the state to return to the original state at $|\alpha(0)\rangle$, ensuring the periodic condition due to the trace operation.

operator. In this case a bond location is randomly chosen and tested for possible update using 3.8. Similarly, reduction of operator order is the same as replacing a bond operator by an unit operator using 3.9. The general procedure is to iterate through the vertices (starting with vertex connecting level 0 and level 1). Off-diagonal operators are left unchanged, but the state is propagated forward using the off-diagonal operators. An example of this update is shown in fig. (3.3). Note that diagonal update does not change the particle number, nor does it sample the states in the configuration space $\{|\alpha(p)\rangle\}$.

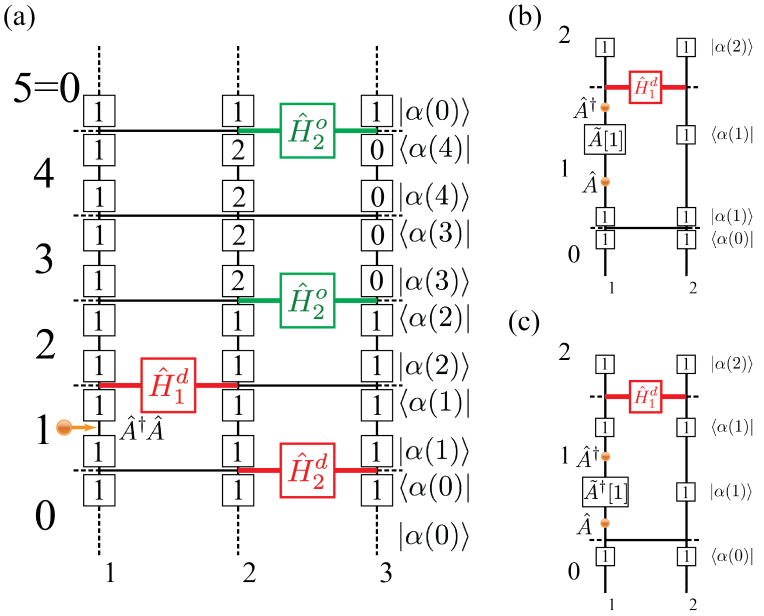

Figure 3.4: Illustration of Loop Update. At the start of every operator loop creation, a random insertion point in space-time is chosen together with transition operators $\hat{A}^\dagger\hat{A}$. (a) For this example, let the insertion point be at site 1 and propagation level 1, between vertices 1 and 2 with $\hat{A} = \hat{b}_1$. Now for the vertex and leg there are two possible directions: either leg 0 on vertex 1 i.e., forward in imaginary time or leg 1 on vertex 1 i.e., backward in imaginary time. (b) If the former is chosen then the head of the worm carries operator $\hat{A}^\dagger = \hat{b}_1^\dagger$ while the fixed tail carries $\hat{A} = \hat{b}_1$. The movement of the head will bring about a change in the state of site 1 from $|1\rangle$ to $|0\rangle$ so that the net state remains unchanged ($\hat{b}_1^\dagger|0\rangle = |1\rangle$). In operator string language the following transformation happened: $...\langle\alpha(2)|\hat{H}_1^d|\alpha(1)\rangle\hat{b}_1^\dagger\hat{b}_1\langle\alpha(1)|... = ...\langle\alpha(2)|\hat{H}_1^d\hat{b}_1^\dagger|\tilde{b}_1[\alpha(1)]\rangle\hat{b}_1\langle\alpha(1)|...$ (c) On the other hand, if the worm moves backward in imaginary time then the head of the worm carries $\hat{A} = \hat{b}_1$, while the fixed tail carries $\hat{A}^\dagger = \hat{b}_1^\dagger$. Again, the movement of the head will bring about a change in the state of site 1 from $\langle 1|$ to $\langle 0|$ so that the net state remains unchanged ($\langle 0|\hat{b}_1 = \langle 1|$). The resulting transformation is given by the operator string transformation: $...|\alpha(1)\rangle\hat{b}_1^\dagger\hat{b}_1\langle\alpha(1)|\hat{H}_2^d|\alpha(0)\rangle = ...|\alpha(1)\rangle\hat{b}_1^\dagger\langle\tilde{b}_1^\dagger[\alpha(1)]|\hat{b}\hat{H}_2^d|\alpha(0)\rangle$.

3.2 Loop Update

Once the expansion order of the configuration space is set, the states in the configuration space need to be sampled. This is the same as transforming diagonal operators to off-diagonal operators or vice-versa. After diagonal update the configuration space is composed of interconnected bond operators spanning lattice sites (space) and propagation levels or imaginary time.[3] Every bond operator connects sites from a level i to level $i+1$ - called a *vertex*, shown in fig. (3.2b). In this step, all unit operators are ignored and the expansion order remains unchanged. Although there are many ways to sample the off-diagonal operators, arguably the most efficient procedure for Bosons (or spins) entails the use of *worms* to construct closed

---

[3] Propagation level and imaginary time is used interchangeably throughout these discussions, but the exact connection will be explored later in greater detail when imaginary time correlation functions are discussed.

operator loops.

To start, a random insertion point on a leg between two vertices is chosen from the entire vertex list (see fig. 3.4a) together with a direction for the motion of the worm. This basically means a point in space-time is chosen, since the leg of the vertex maps to a site (say i) at some propagation level which is defined as the origin in time, $\tau = 0$.[4] Next a pair of operators ($\hat{A_i}^\dagger \hat{A}_i = \hat{b_i}^\dagger \hat{b}_i$ or $\hat{b}_i \hat{b_i}^\dagger$ – with $\hat{b}^\dagger$ ($\hat{b}$) being the Boson creation (annihilation) operator) is inserted with probability $\mathscr{P}_{insert} = \frac{1}{2}$ at that point.[5] Depending on the direction the worm propagates, the head will either carry $\hat{A}_i^\dagger$ (forward propagation) or $\hat{A}_i$ (backward propagation). As it enters the chosen leg (which without loss of generality let's say forward), the state on that site changes so that net state remains unchanged. In terms of operator strings the transformation is:

$$...|\alpha(\tau)\rangle \hat{A}_i^\dagger \hat{A}_i \langle\alpha(\tau)|... = ...\hat{A}_i^\dagger |\tilde{T}_i[\alpha(\tau)]\rangle \hat{A}_i \langle\alpha(\tau)|... \tag{3.10}$$

Here $|\tilde{T}_i[\alpha(\tau)]\rangle$ indicates the *transformation* operation due to the passage of the worm's head with operator $\hat{A}^\dagger$. The transformation is dependent on the direction of propagation. If the worm propagates forward in time then $\tilde{T} = \hat{A}$ otherwise $\tilde{T} = \hat{A}^\dagger$. The reason behind this is that the transformation must preserve the original state since it is not a Monte Carlo update. Thus, if $|\alpha(\tau)\rangle \equiv |n_i\rangle \bigotimes |n_j\rangle$, then for forward propagation $|\tilde{T}_i[\alpha(\tau)]\rangle = \tilde{T}_i|n_i\rangle \bigotimes |n_j\rangle = \tilde{A}_i|n_i\rangle \bigotimes |n_j\rangle$, whereas for backward propagation $\langle\tilde{T}_i[\alpha(\tau)]| \equiv \langle n_i| \bigotimes \langle n_j|\tilde{A}_i^\dagger$. The '$\sim$' on the operator indicates that the transformation is normalized, i.e., $\tilde{b}^\dagger|n\rangle \equiv \frac{|n+1\rangle}{\sqrt{n+1}}$ and $\tilde{b}|n\rangle \equiv \frac{|n-1\rangle}{\sqrt{n}}$. This procedure is illustrated in fig. (3.4) for a specific system. The worm can move unimpeded until the head reaches a vertex that has a bond operator involving site i.

On reaching a scattering vertex there are multiple ways in which the worm can proceed. Each of these options involve a Monte Carlo move that satisfies the detailed balance condition given by:

$$\mathscr{P}(l \to l', \Sigma, \hat{A}_l \to \hat{A}_{l'}) W(l, \Sigma, \hat{A}_l) = \mathscr{P}(l' \to l, \Sigma', \hat{A}_{l'} \to \hat{A}_l) W(l', \Sigma', \hat{A}_{l'}). \tag{3.11}$$

Here l is the entrance leg, l' is the exit leg, Σ is current state of the vertex, $\hat{A}_l$ is the current operator at entrance leg l, Σ' is state of the vertex after the movement of the worm and

---

[4] Due to the equivalence of cyclic permutations this is always allowed.

[5] Recalling that $\hat{b}|n = 0\rangle = 0$ and $\hat{b}^\dagger|n = M\rangle = 0$. M is the maximum number of particles allowed for the Boson basis – a numerical convenience. M is adjusted during equilibration so that max(n)< M for all sites in the lattice.

$\hat{A}_{l'}$ is the transition operator after the movement of the worm. W is the weight function proportional to the local Hamiltonian operator e.g. $\langle\alpha(i-1)|H_{s_i}|\alpha(i)\rangle$. $\mathscr{P}$ is the transition probability from one configuration to another configuration resulting from the passage of the worm. There are many ways to set $\mathscr{P}$ so that detailed balance is fulfilled; the simplest of these is to set:

$$\mathscr{P}(l \to l', \Sigma, \hat{A}_l \to \hat{A}_{l'}) = W(l', \Sigma', \hat{A}_{l'}) \tag{3.12}$$

$$\mathscr{P}(l' \to l, \Sigma', \hat{A}_{l'} \to \hat{A}_l) = W(l, \Sigma, \hat{A}_l). \tag{3.13}$$

However, this is not the optimal choice and alternate strategies exist that maximizes the efficiency of the algorithm [39].

For a vertex composed of four sites (true for all systems reported this dissertation) there are four possible moves, which have been presented in fig. (3.5a-d). Corresponding to the moves (a)-(d), below are the equivalent operator string representations:

$$\langle\alpha(q+1)|\hat{H}_{s_q}\hat{A}_i^{\dagger}|\tilde{A}_i[\alpha(q)]\rangle\hat{A}_i \to \hat{A}_i^{\dagger}\langle\tilde{A}_i[\alpha(q+1)]|\hat{H}_{s_q}|\tilde{A}_i[\alpha(q)]\rangle \tag{3.14}$$

$$\langle\alpha(q+1)|\hat{H}_{s_q}\hat{A}_i^{\dagger}|\tilde{A}_i[\alpha(q)]\rangle\hat{A}_i \to \hat{A}_j^{\dagger}\langle\tilde{A}_j[\alpha(q+1)]|\hat{H}_{s_q}|\tilde{A}_i[\alpha(q)]\rangle \tag{3.15}$$

$$\langle\alpha(q+1)|\hat{H}_{s_q}\hat{A}_i^{\dagger}|\tilde{A}_i[\alpha(q)]\rangle\hat{A}_i \to \langle\alpha(q+1)|\hat{H}_{s_q}|\tilde{A}_i\tilde{A}_j^{\dagger}[\alpha(q)]\rangle\hat{A}_i\hat{A}_j^{\dagger} \tag{3.16}$$

$$\langle\alpha(q+1)|\hat{H}_{s_q}\hat{A}_i^{\dagger}|\tilde{A}_i[\alpha(q)]\rangle\hat{A}_i \to \langle\alpha(q+1)|\hat{H}_{s_q}|\alpha(q)\rangle\hat{A}_i^{\dagger}\hat{A}_i \tag{3.17}$$

Note that for diagonal vertices the switch-jump-forward and switch-jump-backward moves (fig. 3.5b and c, respectively) lead to replacement of the diagonal Hamiltonian operator to an off-diagonal operator. Additionally, if the worm changes direction it carries the same operator but the transformation is flipped $\tilde{T} \to \tilde{T}^{\dagger}$ in order to conserve particle number across all time slices. Fig. (3.5d) shows a bounce move which undoes any change made locally in configuration space. In general, minimizing such bounce moves will greatly improve the updating efficiency. Notice that the introduction of the worm leads to the creation of a discontinuity in the World line that is propagated along by the worm's head. This propagation process terminates once the worm returns to the insertion point at the tail and we end one iteration of the loop update.

Generally multiple iterations are needed to ensure that subsequent states are uncorrelated. Occasionally it may also be the case that worm length is prohibitively large, in which case the iteration is terminated and we discard all changes. Following this a new iteration is started. The appropriate length can be found during equilibration, but generally simulations show

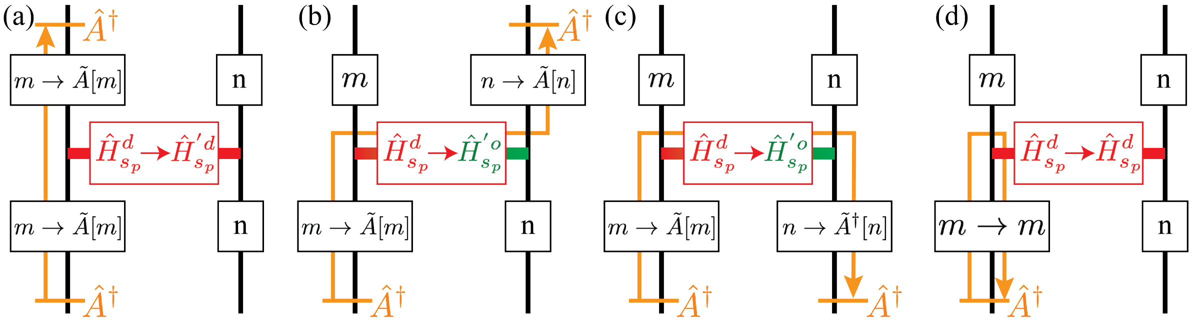

Figure 3.5: Update moves once the worm head enters the vertex.

that ~ 100 times $\langle p \rangle$, the average number of operators in the operator string is appropriate. Also, the number of iterations that compose a loop update has to be set. The criteria used to select this number is to reduce the number of Monte Carlo sweeps needed to de-correlate the observable of interest. For systems studied in this dissertation, the number of iterations during equilibration is adjusted such that the number of vertices visited is 20 to 40 times $\langle p \rangle$. At the end of equilibration, the number of iterations is fixed otherwise the normalization factor needed for observables is unknown.

3.3 Observables

Having described the procedure used to sample the partition function, the discussion will now be on the method by which observables are measured in the SSE algorithm. In SSE, it makes practical sense to distinguish observables into two categories: Z-sector and G-sector observables. The former is named after the fact that the observables are of the form $O = \frac{1}{\mathcal{Z}} \sum_\alpha \langle \alpha | \hat{O} e^{-\beta \mathscr{H}} | \alpha \rangle$; i.e., in the diagonal sector of configuration space. It encapsulates most thermodynamic measurables – measurements made in configuration space when there are no discontinuities present in it. Practically this means measurements are made using states in the configuration space after loop update ends. On the other hand G-sector observables include correlation functions in imaginary time when there is a discontinuity present in configuration space - often called the *extended* configuration space.[6] Operators in this sector are of the form $O = \frac{1}{\mathcal{Z}} \sum_\alpha \langle \tilde{\alpha} | \hat{O} e^{-\beta \mathscr{H}} | \alpha \rangle$, where $|\tilde{\alpha}\rangle \equiv \hat{O} |\alpha\rangle$ ($|\tilde{\alpha}\rangle$ is not necessarily equal to $|\alpha\rangle$). Such measurements are made during the passage of the worm during the loop update procedure.

---

[6] The nomenclature will become clearer in section 3.3.2

3.3.1 Z-sector Observables

Important observables in the Z-sector class of observables include observables such as the internal energy (U), the heat capacity (C_v), density (N), local density ($n(r)$), compressibility (κ) and local compressibility ($\kappa(r)$). Other more exotic observables include the superfluid fraction (ρ_s) and local superfluid density ($\rho_s(r)$). Since all of these observables are used to study the physical systems we describe later, they are derived below.

1. *Internal Energy* (U) of a system is arguably one of the most important observables of interest. For most ground state QMC methods the quality of wave functions is determined by the U. For experimental systems U is generally not measurable, but other derived observables might be available. For instance, in cold atomic systems the entropy (S) in some contexts is measurable and can be used to characterize the state of a system - discussed later in part III.

$$\begin{aligned} U = \frac{Tr[\hat{\mathscr{H}} e^{-\beta\hat{\mathscr{H}}}]}{\mathcal{Z}} &= \frac{1}{\mathcal{Z}} \sum_{p=0}^{\infty} \sum_{\alpha} \frac{(-\beta)^p}{p!} \langle\alpha|\hat{\mathscr{H}}(\hat{\mathscr{H}})^p|\alpha\rangle \\ &= \frac{1}{\mathcal{Z}} \sum_{p=0}^{\infty} \sum_{\alpha} \frac{(-\beta)^{p+1}}{(p+1)!} \frac{p+1}{-\beta} \langle\alpha|\hat{\mathscr{H}}^{p+1}|\alpha\rangle \\ &= \frac{1}{\mathcal{Z}} \sum_{p=0}^{\infty} \sum_{\alpha} \frac{(-\beta)^p}{p!} \frac{-p}{\beta} \langle\alpha|\hat{\mathscr{H}}^{p}|\alpha\rangle \\ &\equiv -\frac{\langle p\rangle}{\beta} \end{aligned} \tag{3.18}$$

   So just the average number of operators need to be measured and multiplied by $\frac{-1}{\beta}$ where the inverse temperature is a known parameter.

2. *Heat Capacity* (C_v) of the system is generally calculated by obtaining U for a range of temperatures and then using numeric differentiation. However, SSE allows for an alternate formulation using the fluctuations of number of operators in the system.

Noting that $C_v \equiv \langle \mathscr{H}^2 \rangle - \langle \mathscr{H} \rangle^2$, consider the first term:

$$\begin{aligned}
\langle \hat{\mathscr{H}}^2 \rangle = \frac{Tr[\hat{\mathscr{H}} e^{-\beta\hat{\mathscr{H}}}]}{\mathcal{Z}} &= \frac{1}{\mathcal{Z}} \sum_{p=0}^{\infty} \sum_{\alpha} \frac{(-\beta)^p}{p!} \langle \alpha | \hat{\mathscr{H}}^2 (\hat{\mathscr{H}})^p | \alpha \rangle \\
&= \frac{1}{\mathcal{Z}} \sum_{p=0}^{\infty} \sum_{\alpha} \frac{(-\beta)^{p+2}}{(p+2)!} \frac{(p+2)(p+1)}{\beta^2} \langle \alpha | \hat{\mathscr{H}}^{p+2} | \alpha \rangle \\
&= \frac{1}{\mathcal{Z}} \sum_{p=0}^{\infty} \sum_{\alpha} \frac{(-\beta)^p}{p!} \frac{p(p-1)}{\beta^2} \langle \alpha | \hat{\mathscr{H}}^{p} | \alpha \rangle \\
&= -\frac{\langle p(p-1) \rangle}{\beta^2}
\end{aligned}$$

Finally then using 3.18 we get:

$$C_v = \frac{1}{\beta^2} (\langle p^2 \rangle - \langle p \rangle^2 - \langle p \rangle) \tag{3.19}$$

3. *Density* (N) of the system can be directly measured by simply counting the number of particles at a particular site. This is straightforward since the chosen basis is the particle number basis. Using $\hat{N} = \sum_i \hat{n}_i$,

$$\langle N \rangle = \frac{Tr[\hat{N} e^{-\beta\hat{\mathscr{H}}}]}{\mathcal{Z}} = \frac{1}{\mathcal{Z}} \sum_{p=0}^{\infty} \sum_{\alpha} \frac{(-\beta)^p}{p!} \langle \alpha | [\sum_i \hat{n}_i] (\hat{\mathscr{H}})^p | \alpha \rangle \tag{3.20}$$

Recall that $\alpha \equiv |n_1\rangle \bigotimes |n_2\rangle \bigotimes ... |n_{N_s}\rangle$, where N_s is total number of sites in the system.

4. *Local Density* (n_i) where i indicates the site or position is given by:

$$\langle n_i \rangle = \frac{Tr[\hat{N} e^{-\beta\hat{\mathscr{H}}}]}{\mathcal{Z}} = \frac{1}{\mathcal{Z}} \sum_{p=0}^{\infty} \sum_{\alpha} \frac{(-\beta)^p}{p!} \langle \alpha | \hat{n}_i (\hat{\mathscr{H}})^p | \alpha \rangle \tag{3.21}$$

5. *Compressibility* (κ) is given by

$$\kappa \equiv \frac{\partial \langle N \rangle}{\partial \mu} = \beta [\langle N^2 \rangle - \langle N \rangle^2] \tag{3.22}$$

that can be measured following the same method described in 3.20.

6. *Local Compressibility* $(\kappa(i))$ is similarly given by

$$\kappa(i) \equiv \beta [\langle N(i)^2 \rangle - \langle N(i) \rangle^2]. \tag{3.23}$$

It is worth noting that there many alternate definitions possible for the local compressibility. However, this particular definition in terms of the variance of the local density could be readily measured in AMO systems such as the quantum gas microscope.

7. *Superfluid Fraction* (ρ_s) can be calculated using the winding number prescription defined for path integrals [40, 41]. For the purposes of measuring this observable, all that is needed is the winding number subtended by the paths. Basically in the World line configuration with periodic boundary conditions, whenever a particle crosses a boundary it means a winding has occurred. This is particularly easy to measure in SSE as all that is need is to check for off-diagonal terms that connect two sites across the (periodic) boundary. The fluctuations of the net winding W can be used to define the superfluid fraction:
$$\rho_s = \frac{m\langle W^2\rangle L^2}{\hbar^2 \beta N}, \tag{3.24}$$
where L is the one dimensional length of the periodic cell and N is the total particle number. In the presence of a lattice potential, the mass m gets changed to the effective mass m^*.

   In situations where, periodic cells cannot be employed for instance in the presence of traps extensively employed in cold atom experiments, the global superfluid fraction cannot be measured using the winding number prescription discussed above. In such cases, the only alternative is to use the rotational formulation of superfluidity according to which the total superfluid density is given by:
$$\rho_s^T|_u = \frac{4m\langle A_u^2\rangle}{\hbar^2\beta}, \tag{3.25}$$
   where ρ_s is measured around a principal axis of rotation $\hat{u}$, and
$$A_u \equiv \int d^D\vec{r} A_u(\vec{r}) = \int d^D\vec{r}\frac{1}{2}\sum_{i=1}^{N}\sum_{k}[(\vec{r}^{\,i}_k \times \vec{r}^{\,i}_{k+1})\cdot\hat{u}]\delta(\vec{r}-\vec{r}^{\,i}_k). \tag{3.26}$$
   $A(r)$ is the sum of areas of paths projected out in imaginary time that contribute to a differential volume dr^3 at r [42]. Once the total superfluid density is calculated, the superfluid fraction (ρ_s) can be calculated by normalizing via the classical momentum of inertia $I_c = m\sum_{ij}\vec{r}^{\,i}_{k\perp}\cdot\vec{r}^{\,i}_{k+1\perp}$. Here $\vec{r}_\perp$ indicates the perpendicular vector between $\vec{r}$ and the axis direction $\hat{u}$.

8. *Local Superfluid Density* The rotational formalism discussed above, can be extended to

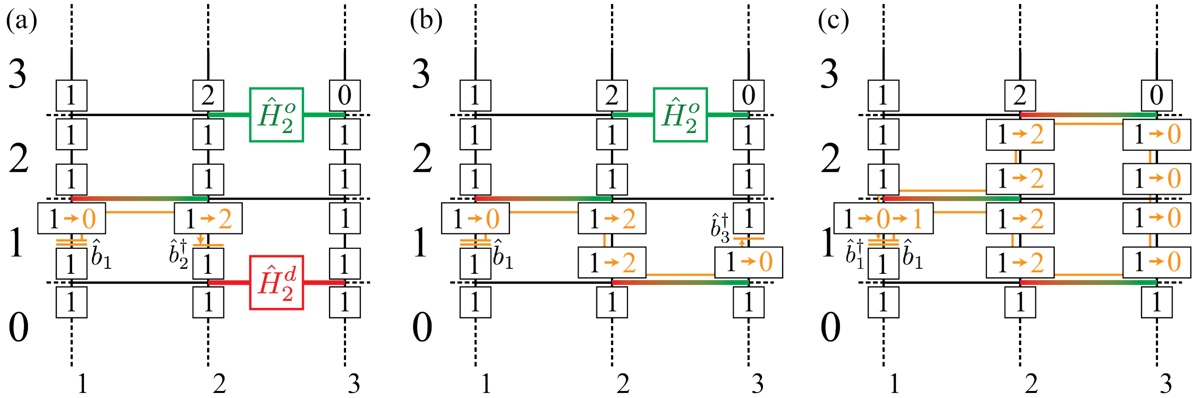

Figure 3.6: Measurement of the Elements of the Single Particle Density Matrix. (See text for discussion)

measure the density of paths about a point in space. Such a breakup is not unique but it can lend important information about the way winding paths develop in confined systems. Using this formulation it is possible to measure the local superfluid density:

$$\rho_s(\vec{r})|_u = \frac{4m\langle A_a A_a(\vec{r})\rangle}{\hbar^2 \beta r_\perp^2}, \tag{3.27}$$

such that the total superfluid density in a region $\mathcal{R}$ is given by:

$$\rho_s^{\mathcal{R}}|_u \equiv \int_{\mathcal{R}} d^D\vec{r}\rho_s(\vec{r})|_u r_\perp^2 \tag{3.28}$$

and the superfluid fraction in the region ($\mathcal{R}$) is given as usual by diving with the classical momentum of inertia I_{cl}.

3.3.2 G-sector Observables

The second class of observables involve measurements made in the extended configuration space that was defined earlier (the nomenclature will be clarified shorty). Observables in this sector are in the form of correlation functions that can be used to obtain a wide class of useful measurements such as n-particle Green's function, n-particle reduced density matrix etc. The SSE formalism allows for these measurements but it can be challenging for newcomers. Some of the algorithmic aspects have been described in [43], but they are discussed in greater detail below.

1. *Single-Particle Density Matrix* given by $\hat{\rho}_1 \equiv \sum_{ij} |i\rangle\langle \hat{b}_i^\dagger \hat{b}_j\rangle\langle j|$ is a single-particle correlation function measured at equal (imaginary) times. It is a particularly useful measurement since it can be used to yield the momentum distribution that can be compared

with corresponding measurements in experiments. Additionally ρ_1 can be further used to measure the occupation number of single-particle modes which is further connected to Bose-Einstein condensation. The diagonalization of ρ_1 followed by extraction of occupation numbers and single-particle distributions will be discussed in detail in the next section.

As mentioned earlier, the measurement process utilizes the worm propagation during loop update. Starting with the introduction of the worm operators at some insertion location in the World line we track the states of the system as the discontinuity is propagated. Every time the head of the worm returns to the same location in time, equal time correlation functions can be measured. The procedure is best illustrated via an example shown in fig. (3.6). The procedure starts with the insertion at ($\tau = 1$,site $i = 1$) of the operator pair $\hat{b}_1\hat{b}_1^\dagger$. In terms of operator strings the process is:

$$...|\alpha(2)\rangle\langle\alpha(2)|\hat{H}_1^d|\alpha(1)\rangle\hat{b}_1^\dagger\hat{b}_1\langle\alpha(1)|... = ...|1,1,1\rangle\langle 1,1,1|\hat{H}_1^d|1,1,1\rangle\hat{b}_1^\dagger\hat{b}_1\langle 1,1,1|... \tag{3.29}$$

The notation is as follows: $|\alpha(\tau)\rangle$ indicates the state of the system at time (τ). $|\alpha(\tau)\rangle \equiv |n_1\rangle \bigotimes |n_2\rangle ... \bigotimes |n_i\rangle \bigotimes ...|n_{N_s}\rangle$ where $|n_i\rangle$ indicates the number of particles n_i on site i. Next suppose the worm propagates forward in time and enters leg 0 on site 1 so that the transformation is:

$$...|1,1,1\rangle\langle 1,1,1|\hat{H}_1^d|1,1,1\rangle\hat{b}_1^\dagger\hat{b}_1\langle 1,1,1|... = ...|1,1,1\rangle\langle 1,1,1|\hat{H}_1^d\hat{b}_1^\dagger|0,1,1\rangle\hat{b}_1\langle 1,1,1|... \tag{3.30}$$

Next supposing that probabilistically via a QMC move, the worm exits at (1,2), which in term of operator strings is given by:

$$...|1,1,1\rangle\langle 1,1,1|\hat{H}_1^d\hat{b}_1^\dagger|0,1,1\rangle\hat{b}_1\langle 1,1,1|... \rightarrow ...|1,1,1\rangle\langle 1,1,1|\hat{H}_1^o|0,2,1\rangle\hat{b}_2^\dagger\hat{b}_1\langle 1,1,1|... \tag{3.31}$$

This situation is illustrated in fig. (3.6a). The form of the operator sequence at ($\tau = 1$) is given by $|021\rangle\hat{b}_2^\dagger\hat{b}_1\langle 111|$, which shows the current location of the discontinuity. Note that the current form of the operator string is *not* in $\mathcal{Z}$ space, since the trace condition is not fulfilled. The entire operator sequence thus looks like:

$$\frac{1}{\mathcal{Z}}\sum_{n=0}^{\infty}\sum_{S_n}\sum_{\{\alpha\}}\frac{\beta^n}{n!}\hat{b}_2^{\dagger}\hat{b}_1\langle 1,1,1|H^n|0,2,1\rangle \rightarrow$$
$$\frac{1}{\mathcal{Z}}\sum_{n=0}^{\infty}\sum_{S_n}\sum_{\{\alpha\}}\frac{\beta^n}{n!}\langle 0,2,1|\hat{b}_2^{\dagger}\hat{b}_1|1,1,1\rangle\langle 1,1,1|H^n|0,2,1\rangle \equiv \langle \hat{b}_2^{\dagger}\hat{b}_1\rangle \tag{3.32}$$

The right hand side corresponds to what an equivalent simulation in would like like if $\langle 0,2,1|$ and $|1,1,1\rangle$ is introduced before and after the worm operators and, by definition, it is the measurement $\langle \hat{b}_2^{\dagger}\hat{b}_1\rangle$. More generally, the right hand side would look like:

$$\frac{1}{\mathcal{Z}}\sum_{n=0}\sum_{S_n}\sum_{\alpha(\tau),\alpha'(\tau)}\frac{\beta^n}{n!}\langle\alpha'(\tau)|\hat{A}_i^{\dagger}\hat{A}_j|\alpha(\tau)\rangle\langle\alpha(\tau)|\hat{H}^n|\alpha'(\tau)\rangle \equiv \langle\hat{A}_i^{\dagger}\hat{A}_j\rangle \tag{3.33}$$

Thus, the discontinuous space that the worm creates during propagation is the same as the space needed to measure correlation functions. This is why the propagation space is called an *extended configuration* space that leads to measurements of *G-sector* observables.

The worm continues, onward to enter (1,2) so that

$$...\hat{H}_1^o|0,2,1\rangle\hat{b}_2^{\dagger}\hat{b}_1\langle 1,1,1|... \rightarrow ...\hat{H}_1^o|0,2,1\rangle\hat{b}_1\langle 1,2,1|\hat{b}_2^{\dagger}\hat{H}_0^d|1,1,1\rangle... \tag{3.34}$$

Following which again via a QMC move, the worm exits at (1,3), which in terms of operator strings is given by:

$$...\hat{H}_1^o|0,2,1\rangle\hat{b}_1\langle 1,2,1|\hat{b}_2^{\dagger}\hat{H}_0^d|1,1,1\rangle... \rightarrow ...\hat{H}_1^o|0,2,1\rangle\hat{b}_1\hat{b}_3^{\dagger}\langle 1,2,0|\hat{H}_0^d|1,1,1\rangle... \tag{3.35}$$

As before this allows the measurement of $\langle \hat{b}_3^{\dagger}\hat{b}_1\rangle$. An example of the following set of moves that leads to the head returning to the tail is shown in fig. (3.6c). These final set of moves (apart from the termination move) do not involve the head crossing the propagation level at which the the tail is located, so no further equal time measurements are possible. (However, imaginary time correlation measurements are possible, which is outlined later.) Following the ideas discussed above, note that the insertion and termination of the passage of the worm allows for the measurement of the diagonal component $\langle \hat{b}_1\hat{b}_1^{\dagger}\rangle$. However, the most efficient way to measure the diagonal density is using the prescriptions outlined above under **Z-sector Observables**.

2. *Momentum Distribution* is obtained directly from $\hat{\rho}_1$. The derivation follows from the definition of fundamental real space and corresponding momentum space operators:

$$n(\vec{k}) \equiv \langle \hat{\phi}^\dagger(k)\hat{\phi}(k)\rangle = \frac{1}{V}\int d^3r d^3r' e^{i\vec{k}\cdot(\vec{r}-\vec{r}')}\langle \hat{\psi}^\dagger(r)\hat{\psi}(r')\rangle \tag{3.36}$$

From the general coarse-graining procedure used in setting up lattice Hamiltonians that will be discussed in detail later, we use $\hat{\psi}(r) \equiv \sum_i w(\vec{r}-\vec{r_i})\hat{b}_i \equiv \sum_i w_i(\vec{r})\hat{b}_i$, so that

$$n(\vec{k}) = \sum_{ij} e^{i\vec{k}\cdot(\vec{r}_i-\vec{r}_j)} w_i^*(\vec{k}) w_j(\vec{k}) \langle \hat{b}_i^\dagger \hat{b}_j\rangle \tag{3.37}$$

where, $w_i(\vec{k}) \equiv \frac{1}{\sqrt{V}}\int d^3\vec{r} e^{-i\vec{k}\cdot(\vec{r}-\vec{r}_i)} w_i(\vec{r})$. For clean systems $w_i(\vec{k}) = w(\vec{k})$ and we obtain the simpler well known form:

$$n(\vec{k}) = |w(\vec{k})|^2 \sum_{ij} e^{i\vec{k}\cdot(\vec{r}_i-\vec{r}_j)}\langle \hat{b}_i^\dagger \hat{b}_j\rangle \tag{3.38}$$

3. *Single-Particle Imaginary Time Correlation Function* is given by

$$\hat{G}(\tau,0) = \sum_{ij} |i\rangle\langle \hat{b}_i^\dagger(\tau)\hat{b}_j(0)\rangle\langle j|. \tag{3.39}$$

The measurement ideas follow directly from the ideas involved in measuring $\hat{\rho}_1$, however there is one modification that is needed. Up until now propagation level and imaginary time has been used interchangeably, but there is a weighting factor that is needed in order to obtain the exact mapping. The relationship follows by using the Heisenberg notion of time evolving operators, $\hat{A}(\tau) \equiv e^{\tau \mathscr{H}} \hat{A} e^{-\tau \mathscr{H}}$. Using which,

$$\begin{aligned}
\langle \hat{A}(\tau)\hat{B}(0)\rangle &\equiv \langle e^{\tau\mathscr{H}}\hat{A}e^{-\tau\mathscr{H}}\hat{B}\rangle \\
&= \frac{1}{\mathcal{Z}}\sum_{n=0}^{\infty}\frac{(\tau-\beta)^n}{n!}\sum_{m=0}^{\infty}\frac{(-\tau)^m}{m!}\sum_{\alpha}\langle\alpha|\hat{\mathscr{H}}^n\hat{A}\hat{\mathscr{H}}^m\hat{B}|\alpha\rangle \\
&= \frac{1}{\mathcal{Z}}\sum_{n=0}^{\infty}\sum_{m=0}^{\infty}\frac{(\tau-\beta)^n}{n!}\frac{(-\tau)^m}{m!}\sum_{S_{n+m}}\sum_{\{\alpha\}}\prod_{i=m+1}^{n+m}H_iA\prod_{j=1}^{m}H_jB
\end{aligned}$$

Relabel n $\rightarrow n-m$

$$\begin{aligned}
&= \frac{1}{\mathcal{Z}}\sum_{n=0}^{\infty}\sum_{m=0}^{n}\frac{(\tau-\beta)^{n-m}}{(n-m)!}\frac{(-\tau)^m}{m!}\sum_{S_n}\sum_{\{\alpha\}}\prod_{i=m+1}^{n}H_iA\prod_{j=1}^{m}H_jB \\
&= \frac{1}{\mathcal{Z}}\sum_{n=0}^{\infty}\sum_{m=0}^{n}\binom{n}{m}\left(1-\frac{\tau}{\beta}\right)^{n-m}\left(\frac{\tau}{\beta}\right)^m \\
&\qquad \sum_{S_n}\sum_{\{\alpha\}}\frac{(-\beta)^n}{n!}\prod_{i=m+1}^{n}H_iA\prod_{j=1}^{m}H_jB
\end{aligned}$$

As a quick aside note that the relabeling is done by using the identity:

$$\begin{aligned}
e^{(a+b)\hat{H}} &= e^{a\hat{H}}e^{b\hat{H}} \\
\sum_{n=0}^{\infty}\frac{(a+b)^n}{n!}\hat{H}^n &= \sum_{n=0}^{\infty}\sum_{m=0}^{\infty}\frac{a^n}{n!}\frac{b^m}{m!}\hat{H}^{n+m} \\
\sum_{n=0}^{\infty}\sum_{m=0}^{n}\binom{n}{m}\frac{a^{n-m}b^m}{n!}\hat{H}^n &= \sum_{n=0}^{\infty}\sum_{m=0}^{\infty}\frac{a^n}{n!}\frac{b^m}{m!}\hat{H}^{n+m} \\
\sum_{n=0}^{\infty}\sum_{m=0}^{n}\frac{a^{n-m}}{(n-m)!}\frac{b^m}{m!}\hat{H}^n &= \sum_{n=0}^{\infty}\sum_{m=0}^{\infty}\frac{a^n}{n!}\frac{b^m}{m!}\hat{H}^{n+m} \qquad (3.40)
\end{aligned}$$

For $\hat{A} = \hat{b}_i^\dagger$, $\hat{B} = \hat{b}_j$ and setting $m = \Delta l$ as the difference in propagation level between the insertion point and the measuring point,

$$\langle \hat{b}_i^\dagger(\tau)\hat{b}_j(0)\rangle = \sum_{\Delta l=0}^{n}\binom{n}{\Delta l}\left(1-\frac{\tau}{\beta}\right)^{n-\Delta l}\left(\frac{\tau}{\beta}\right)^{\Delta l}G(i,j;\Delta l)$$

with

$$G(i,j;\Delta l) \equiv \frac{1}{\mathcal{Z}}\sum_{n=0}^{\infty}\sum_{S_n}\sum_{\{\alpha\}}\frac{(-\beta)^n}{n!}\prod_{i=\Delta l+1}^{n}H_ib_i^\dagger\prod_{j=1}^{\Delta l}H_jb_j$$

These measurements can be taken in the fixed operator string representation by introducing unit operators as explained above. There is a minor caveat needed for measuring G. In the variable length scheme the measurement is sandwiched between Δl operators that range from $[0, n]$. However, in the fixed length scheme the Δl operators include unit operators and ranges from $[0, L]$ so the weights need to account for this:

$$\langle \hat{b}_i^\dagger(\tau)\hat{b}_j(0)\rangle = \sum_{\Delta l=0}^{L} \binom{L}{\Delta l} \left(1-\frac{\tau}{\beta}\right)^{L-\Delta l} \left(\frac{\tau}{\beta}\right)^{\Delta l} G(i,j;\Delta l) \equiv \sum_{\Delta l=0}^{L} w(\Delta l, \tau/\beta) F(i,j;\Delta_l) \tag{3.41}$$

with

$$F(i,j;\Delta l) \equiv \frac{1}{\mathcal{Z}} \sum_{n=0}^{\infty} \sum_{S_L} \sum_{\{\alpha\}} \frac{(-\beta)^n (L-n)!}{L!} \prod_{i=\Delta l+1}^{L} H_i b_i^\dagger \prod_{j=1}^{\Delta l} H_j b_j. \tag{3.42}$$

The weighing function $w(\Delta l, \tau/\beta)$ is a binomial distribution function which on convolution with $F(i,j;\Delta_l)$ yields the correlation values at a particular imaginary time. Before discussing some useful transformations and storage strategies for this observable, it's worth illustrating the measurement of $F(i,j,\Delta l)$ via the example discussed above – see fig. 3.7a-b.

The storage and convolution needed to obtain $G(i,j;\tau)$ is greatly benefited by using certain properties of the World line structure formed during loop update. The first property of note is that during loop update the location of all operators is fixed. This means that between consecutive operators on a particular site the number of levels are fixed. So as the worm travels on a site from one bond operator to another, we end up measuring the same value for propagation levels between them. As a result $F(i,j;\Delta l)$ has a block like structure with the function taking a constant value over the interval, as shown in fig. (3.8). Consequently it's better to store $F(i,j;\Delta l)$ as $F(i,j;I)$ where $I(l_{lb}, l_{ub})$ is the set of all propagation levels in the interval $]l_{lb}, l_{ub}]$ At the end of loop update we proceed to transform $F(i,j;I)$ to $G(i,j;\tau)$.

Now since, the value of F is constant over an interval, (3.41) can be massaged to the following convenient format:

$$G(i,j;\tau) = \sum_I F(i,j;I)[\mathcal{W}(\tau/\beta, I_{ub}) - \mathcal{W}(\tau/\beta, I_{lb})] \tag{3.43}$$

where, $\mathcal{W}(\tau/\beta, l) \equiv \sum_{m=0}^{l} w(\tau/\beta, m)$, w was defined earlier as the Binomial distri-

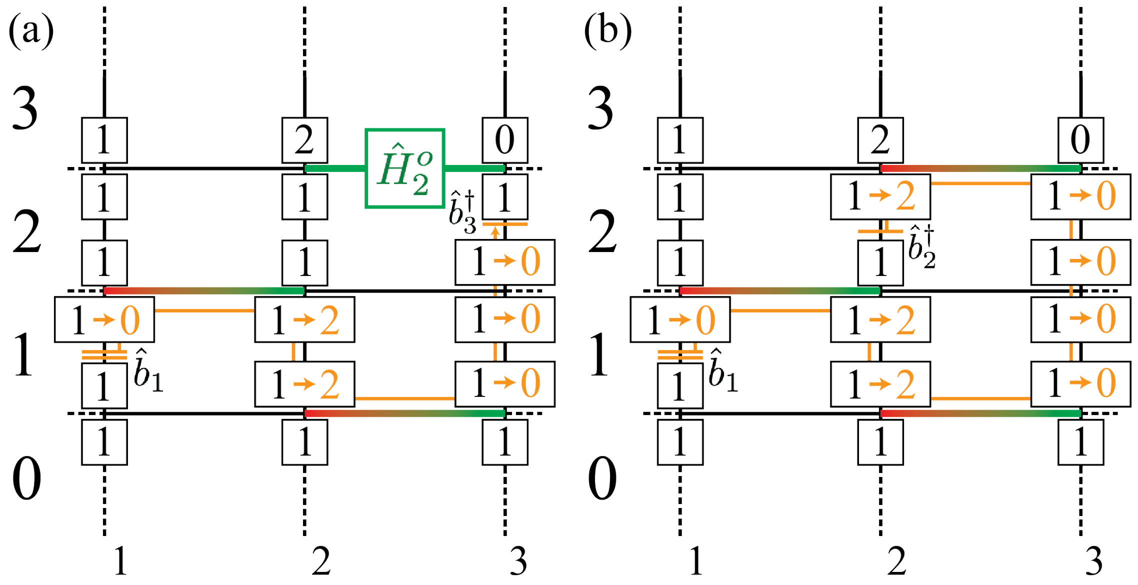

Figure 3.7: Measurement of Imaginary Time Green's Function. (a) Shows that the worm head move into propagation level 2 from propagation level 1 on site 3 so that $\Delta l = 1$ while having transformed states along the way. At this point the worm head is located at level 2 below the scattering vertex. The operator string looks like $...|1,1,1\rangle \hat{b}_3^\dagger \langle 1,1,0|\hat{H}_1^o|0,2,0\rangle \hat{b}_1 \langle 1,2,0|...$, which is the same as a simulation state in the extended configuration space with the operator string $...|1,1,1\rangle\langle 1,1,1|\hat{b}_3^\dagger|1,1,0\rangle\langle 1,1,0|\hat{H}_1^o|0,2,0\rangle\langle 0,2,0|\hat{b}_1|1,2,0\rangle\langle 1,2,0|...$ So we end up measuring $\langle \hat{b}_3^\dagger(2)\hat{b}_1(1)\rangle = \langle \hat{b}_3^\dagger(1)\hat{b}_1(0)\rangle$. The latter arises from the fact that the dynamical properties of the system does not change in time or translation invariance in imaginary time. (b) Shows the next step where the head returns to level 1 but now on a different site. Following our earlier discussion, this allows the measurement of $\langle \hat{b}_2^\dagger(2)\hat{b}_1(1)\rangle = \langle \hat{b}_2^\dagger(1)\hat{b}_1(0)\rangle$.

bution function. This of-course makes $\mathcal{W}(\tau, l)$ the cumulative Binomial distribution function. Generally there are only a few intervals worth of data gathered per site so the sum is not usually prohibitively expensive. However, another set of facts can be used to reduce the cost of evaluating the sum over intervals. Typically, values in imaginary time $\{\tau\}$ at which G needs to be measured is specified before the simulation starts. For any time τ/β the average value of $w(\tau/\beta)$ is located at $L\tau/\beta$ with a standard deviation $\sigma = \sqrt{L\tau/\beta(1-\tau/\beta)}$. Outside of some reasonably chosen width (say $\sim 5\sigma$) centered around the mean, $w = 0$ which means that intervals $I \notin \{L\tau/\beta \pm 5\sigma\}$ will not contribute to (3.43) and can be ignored (see fig. 3.8). This can reduce the effort needed to calculate $G(i,j;\tau)$ considerably and should be exploited. Additionally for low temperatures when L is large, $\mathcal{W}$ can be expensive to store. In such case interpolating functions can be used to represent it [43].

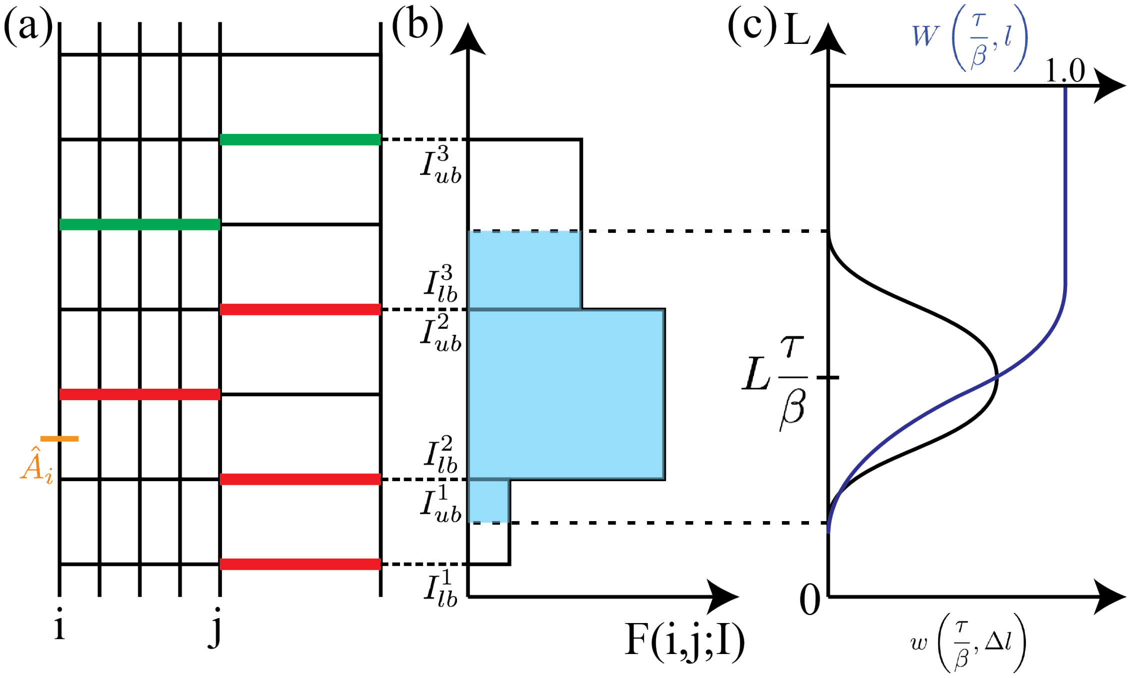

Figure 3.8: (a) For a particular loop update, the operators are fixed. This leads to a block like structure in imaginary time that defines intervals $\{I\}$ so that any particular interval is define by propagation levels $I \in]I_{lb}, I_{ub}]$. Here, the measurements are taking place with the tail fixed at site i so all measurements are with respect to this site. (b) Shows typical block structure that develops in the fixed interval space when $F(i,j;J)$ is measured. (c) Binomial distribution values $w(\tau/\beta, \Delta l)$ and corresponding integrated value $W(\tau/\beta, l)$. Only those blocks within the shaded region contributes to the calculation of $G(i,j;\tau)$.

Chapter 4

Calculating Single-Particle Modes

In the previous chapter, the general method used to measure correlation functions was discussed in some detail. Such functions are of great importance in probing the properties of a many-body system, since handling the full density matrix of a system is very challenging; typically calculating and storing the full density matrix of a system is rarely possible. However, as it turns out, for many systems interesting properties are accessible via reduced density matrices. Perhaps the most important of such matrices are the single-particle ($\hat{\rho}_1$) and two-particle ($\hat{\rho}_2$) density matrix that capture the single-particle and two-particle correlations in the many-body system. Although it is in principle possible to measure n-particle reduced density matrix using QMC, for large system such as those considered in this dissertation the statistical noise is significant and requires a lot of resources to obtain reasonable results. The discussion below will focus on manipulating $\hat{\rho}_1$, but the general techniques discussed here are applicable to higher order correlation functions.

As discussed earlier, $\hat{\rho}_1 \equiv \sum_{i,j} |i\rangle\langle\hat{b}_i^\dagger\hat{b}_j\rangle\langle j|$ captures spatial correlations at the single-particle level. It is possible to acquire some physical insight into this observable by considering its calculation in the SSE formalism. Essentially, the measurement entails studying the effects of introducing a particle or hole into a system characterized by the Hamiltonian $\hat{\mathscr{H}}$ (which is what the worm does). As the worm propagates in imaginary time it introduces fluctuations in the system that spread across the system, giving us access to properties such as the correlation length in space (ξ) and time (ξ_τ), which are of interest in characterizing phase transitions and studying critical phenomena. Additionally, as shown earlier $\hat{\rho}_1$ also gives access to momentum distribution that is of key importance in optical lattice experiments. Most of these properties involve linear transformations of $\hat{\rho}_1$. For instance, its Fourier transform yields the momentum distribution. However, non-linear transformations such as diagonalization of $\hat{\rho}_1$ is incredibly important as it gives access to the single-particle or natural modes of the system that will be used extensively in studying Bose systems. The rest of this chapter is concerned with extracting such modes.

4.1 Non-linear Transformations of the Single-Particle Density Matrix: Important Aspects of Diagonalization

Formally the main interest is diagonalizing $\hat{\rho}_1$ because the eigenvalues correspond to the occupation number of the single-particle modes:

$$\hat{\rho}_1|\psi_\alpha\rangle = N_\alpha|\psi_\alpha\rangle \tag{4.1}$$

where $(\{N_\alpha, \psi_\alpha\})$ is an eigenpair of the single-particle density matrix with N_i is the occupation number and $|\psi_i\rangle$ is the corresponding single-particle eigenvector. Such eigenpairs are important for Many-body systems as they provide insights into the nature of the single-particle properties of the systems mediated by the interaction effects. For instance in case of Bose systems, which will be discussed in more detail in part III, the macroscopic occupation of such a mode signals the presence of a Bose-Einstein condensate (BEC). Therefore it can be used as an order parameter to study phase transitions [44, 19, 45]. Additionally, most experimental probes in modern optical lattice experiments can access the behavior of systems at this single-particle level and therefore understanding it serves the important purpose of bridging experimental observation with theory.

The extraction of single-particle modes using QMC can be broken into two sub problems that can be treated independently. The first one is concerned with effects of approximating the true $\hat{\rho}_1$ (obtained in the infinite sample limit, where the statistical noise is reduced to zero) with one that has statistical noise present in the elements. The issue here is that non-linear transformations may transform the statistical noise in complicated ways. The second problem is concerned with applying non-linear transformations to large systems, which will be tackled later. Unfortunately, the first problem might not have a general answer and so starting with some specific situation of interest might be more useful and perhaps may lead to understanding more general and widely applicable properties. For the purposes of this dissertation, therefore it will be useful to focus on Bose systems and to ascertain the consequences of statistical noise in $\hat{\rho}_1$. In the following discussion, it will be assumed that a non-linear transformation exists that could in principle be used to extract the eigenmodes.

As discussed earlier, for Bose systems, the presence of a BEC is indicated by the macroscopic occupation of an eigenmode of $\hat{\rho}_1$ (say) with N_0 particles (here N_0 is $\sim O(N)$, with N being the total particle number in the system). Then the condensate fraction is defined as $n_0 = N_0/N$. For the purposes of the discussion assume that the elements of ρ_1 measured during the passage of the worm is over N_l loops and averaged over N_s samples to construct a single block that can be represented as:

$$\rho_1^k(i,j) = \frac{1}{N_s} \sum_{q=1}^{N_s} \frac{\sum_{S(q)} \hat{b}_i^\dagger \hat{b}_j}{N_l}. \tag{4.2}$$

Here ρ_1^k is $\hat{\rho}_1$ calculated for the k^{th} block, $b_i^\dagger b_j$ is the correlation measurement operator and $S(q)$ denotes the configuration space that the worm sampled to generate sample q. The average n_0 is calculated by transforming each ρ_1^k and extracting the corresponding condensate number:

$$\left\langle \frac{N_0}{N} \right\rangle = \frac{1}{B} \sum_{k=1}^{B} \frac{\hat{\mathfrak{T}}[\rho_1^k]}{N}. \tag{4.3}$$

The transformation operator $\hat{\mathfrak{T}}$ computes and extracts the largest eigenvalue of $\hat{\rho}_1$ via some exact diagonalization (ED) procedure. The n_0 calculated in this manner depends on both the number of measured elements in $\hat{\rho}_1$ and their fluctuations. The sparsity of ρ_1 is defined as the fraction of elements in ρ_1 that are not measured.[1] It should be noted that in due course of measurement the Hermitian property, viz. $\rho_1(i,j) = \rho_1(j,i)$, is not guaranteed.[2] An obvious question pertains to ascertaining the quality of the extracted eigenpairs. For well behaved transformations an expected property of the result should be that the quality of results should improve as the accuracy of measurements increase. However, the criteria for overall accuracy might not be straightforward.

For simulations of large systems – the subject matter of interest in this dissertation – estimating the values of the large number of off-diagonal elements of $\hat{\rho}_1$ may require a prohibitively large number of QMC sweeps. In such cases it seems reasonable to impose exact properties of observables as constraints on QMC estimators designed to compute them as a means to reduce the computational effort. Therefore, since the exact $\hat{\rho}_1$ is Hermitian and has

---

[1] The sparsity is scaled based on the actual number of sites occupied by the particles as opposed to the size of the grid in which simulations are being carried out. The scaling factor is estimated from the density of the system and we eliminate sites where the occupation number is zero.

[2] In the infinite sample limit it *is* guaranteed but not so for finite samples due to the presence of statistical noise that renders the matrix asymmetric.

the same symmetries as the Hamiltonian, it might seem like a good idea to symmetrize it to reduce statistical noise and increase the known number of elements in $\hat{\rho}_1$. However, enforcing symmetry this way results in biased eigenvalues and a corresponding overestimation of n_0. This causes n_0 to converge slowly with respect to QMC sweeps. For illustrative purposes consider the example below.

Example 4.1.1. Let $\hat{M} = \begin{pmatrix} m_{00} & m_{01} \\ m_{10} & m_{11} \end{pmatrix}$ be the exact matrix of interest which is Hermitian with $m_{01} = m_{10} = m$. Then the solution to the eigenvalue problem is,

$$\lambda_{\pm} = \frac{m_{00} + m_{11}}{2} \pm \frac{1}{2}\sqrt{(m_{00} + m_{11})^2 + 4m^2}$$

Now on addition of an asymmetric noise matrix $\hat{E}_{us} = \begin{pmatrix} \epsilon_{00} & \epsilon_{01} \\ \epsilon_{10} & \epsilon_{11} \end{pmatrix}$, the solution becomes,

$$\begin{aligned} \lambda^*_{\pm} &= \frac{m_{00} + m_{11}}{2} + \frac{\epsilon_{00} + \epsilon_{11}}{2} \pm \frac{1}{2}\sqrt{(m_{00} + m_{11})^2 + 4m^2 + \varepsilon} \\ &\approx \frac{m_{00} + m_{11}}{2} \pm \frac{1}{2}\sqrt{(m_{00} + m_{11})^2 + 4m^2} + \left[\frac{\epsilon_{00} + \epsilon_{11}}{2} \pm \frac{1}{4}\frac{\varepsilon}{\sqrt{(m_{00} + m_{11})^2 + 4m^2}}\right] \\ &\approx \lambda_{\pm} + \text{Bias}_{\pm}(\hat{E}_{us}) \end{aligned}$$

with

$$\begin{aligned} \text{Bias}_{\pm}(\hat{E}_{us}) = &\left[\frac{\epsilon_{00} + \epsilon_{11}}{2} \pm \frac{1}{4}\left\{\frac{[(\epsilon_{00} - \epsilon_{11})^2 + 2(m_{00} - m_{11})(\epsilon_{00} + \epsilon_{11})]}{\sqrt{(m_{00} + m_{11})^2 + 4m^2}}\right.\right. \qquad (4.4) \\ &\left.\left. + \frac{\varepsilon_{us}}{\sqrt{(m_{00} + m_{11})^2 + 4m^2}}\right\}\right] \\ \varepsilon_{us} = &\ 4m(\epsilon_{01} + \epsilon_{10}) + 4\epsilon_{01}\epsilon_{10} \qquad (4.5) \end{aligned}$$

For symmetrized matrix $\hat{E}_s = \begin{pmatrix} \epsilon_{00} & \frac{(\epsilon_{01}+\epsilon_{10})}{2} \\ \frac{(\epsilon_{01}+\epsilon_{10})}{2} & \epsilon_{11} \end{pmatrix}$ the bias becomes $\epsilon_{us} \to \epsilon_s$, with

$$\varepsilon_s = 4m(\epsilon_{01} + \epsilon_{10}) + (\epsilon_{01} + \epsilon_{10})^2 \qquad (4.6)$$

So the difference between the symmetrized and the unsymmetrized case is given by:

$$\text{Bias}_{\pm}(\hat{E}_s) - \text{Bias}_{\pm}(\hat{E}_{us}) \propto \pm(\epsilon_{01} - \epsilon_{10})^2 \qquad (4.7)$$

and averaging over a Gaussian noise distribution the difference is:

$$\langle \mathrm{Bias}_{\pm}(\hat{E}_s)\rangle - \langle \mathrm{Bias}_{\pm}(\hat{E}_{us})\rangle \propto \pm[\sigma^2(\epsilon_{01}) + \sigma^2(\epsilon_{10})] \tag{4.8}$$

Therefore, for either of the two eigenvalues symmetrization leads to biasing the eigenvalue *away* from the true value by a factor proportional to the variance of the noise distributions. This property transfers quite generally to the larger matrices and has been discussed in Appendix B. Irrespective of symmetrization, clearly the reduction of the variance in the noise terms does play an important role and in this regard using other symmetries might be very useful. However, the latter is problem dependent and the specific case of trapped particles is considered later. There is another aspect of the symmetric *vis-a-vis* unsymmetric problem that needs to be discussed.

When the noise in ρ_1 or its sparsity is large, the unsymmetrized matrix may be far away from the true ρ_1, despite there being minimal bias with respect to the symmetrize matrix. As such, it is possible for it to possess properties that do not correspond to the physical situation. In particular, it is possible for the eigenvectors of non-Hermitian matrices to be non-orthogonal, linearly dependent and the eigenvalues to be complex. These properties can never arise in Hermitian matrices composed of elements with (non-negative) real terms. It is, thus, very important to check that the eigenpair from non-symmetrized calculations do not suffer from these problems. In other words care must be taken to ensure that despite convergence of the eigenvalue problem the solutions actually are physical. Experience with the systems considered in this dissertation shows that these problems can arise for smaller non-dominant eigenvalues. In many cases there might be no choice other than to take a large number of samples. Alternate strategies to compute bounds would be extremely useful. Fortunately, such a strategy is possible for the dominant eigenvalue via a variational calculation that will be discussed next.

4.1.1 Variational Estimate of The Dominant Eigenvalue

The variational (VR) method discussed here can be used to calculate n_0. This method could be useful in cases where obvious symmetries may not be available, such as disordered systems. Using $|\Psi\rangle$, the system's single-particle ground state wave function, and substituting its expansion, $|\Psi\rangle = \sum_i c_i|\phi_i\rangle$, with variational parameters c_i, and basis wavefunctions $|\phi_i\rangle$

into the the equation for the number of particles residing in the single-particle ground state,

$$N_0 = \frac{\langle\Psi|\hat{\rho}_1|\Psi\rangle}{\langle\Psi|\Psi\rangle} \tag{4.9}$$

$$= \frac{\sum_{i,j} c_i c_j \langle\phi_i|\hat{\rho}_1|\phi_j\rangle}{\sum_{i,j} c_i c_j \langle\phi_i|\phi_j\rangle}, \tag{4.10}$$

yields an equation that can be computed variationally. Maximizing N_0 with respect to parameter c_i yields,

$$\sum_j \langle\phi_i|\hat{\rho}_1|\phi_j\rangle c_j = N_0 \sum_j \langle\phi_i|\phi_j\rangle c_j, \tag{4.11}$$

a general eigenvalue equation. The choice of the variational basis set $(\{|\phi\rangle\})$ is problem specific and a good choice will undoubtedly yield better estimates. Additionally if $r\hat{h}o_1$ is symmetric then the estimate is guaranteed to be an upper bound. This method will be tested in the context of the trapped system below.

4.1.2 Ultra-Cold Atomic Gases in Traps

Since one of the main systems of interest in this dissertation is trapped ultra-cold atoms in optical lattices, the symmetries of the trap are an important case to consider. Therefore, the symmetrization of ρ_1 involves several different schemes:

1. *No Symmetrization* (NS) indicates that ρ_1 is left as is. No symmetries are used.

2. *Off-diagonal Symmetrization* (ODS) indicates enforcing only the Hermitian symmetry by setting $\rho(i,j) = \frac{1}{2}[\rho(i,j) + \rho(j,i)]$

3. *Spherical Symmetrization with No Hermitian Symmetry* (SSNHS) exploits the symmetry of the trapped system to map $\tilde{\rho}(i,j) \mapsto \tilde{\rho}(R(i), R(j), |\theta|)$ where $R(i)$ $(R(j))$ are the radial distances from the center of the trap to the lattice points at $i(j)$ and θ is the angle between the two vectors i and j. Notice that Hermitian symmetry is not guaranteed in general but if the two points are located on the same sphere i.e., $R(i) = R(j)$ then the only way to distinguish between the two points is putting a sign in front of $|\theta|$. This procedure is leads to not enforcing Hermitian symmetry on points on the same sphere.

4. *Spherical Symmetrization with Hermitian Symmetry* (SSHS) enforces Hermitian symmetry on the points on the same sphere by removing the sign in front of $|\theta|$.

5. *Full Symmeterization* is a combination of ODS together with SSHS.

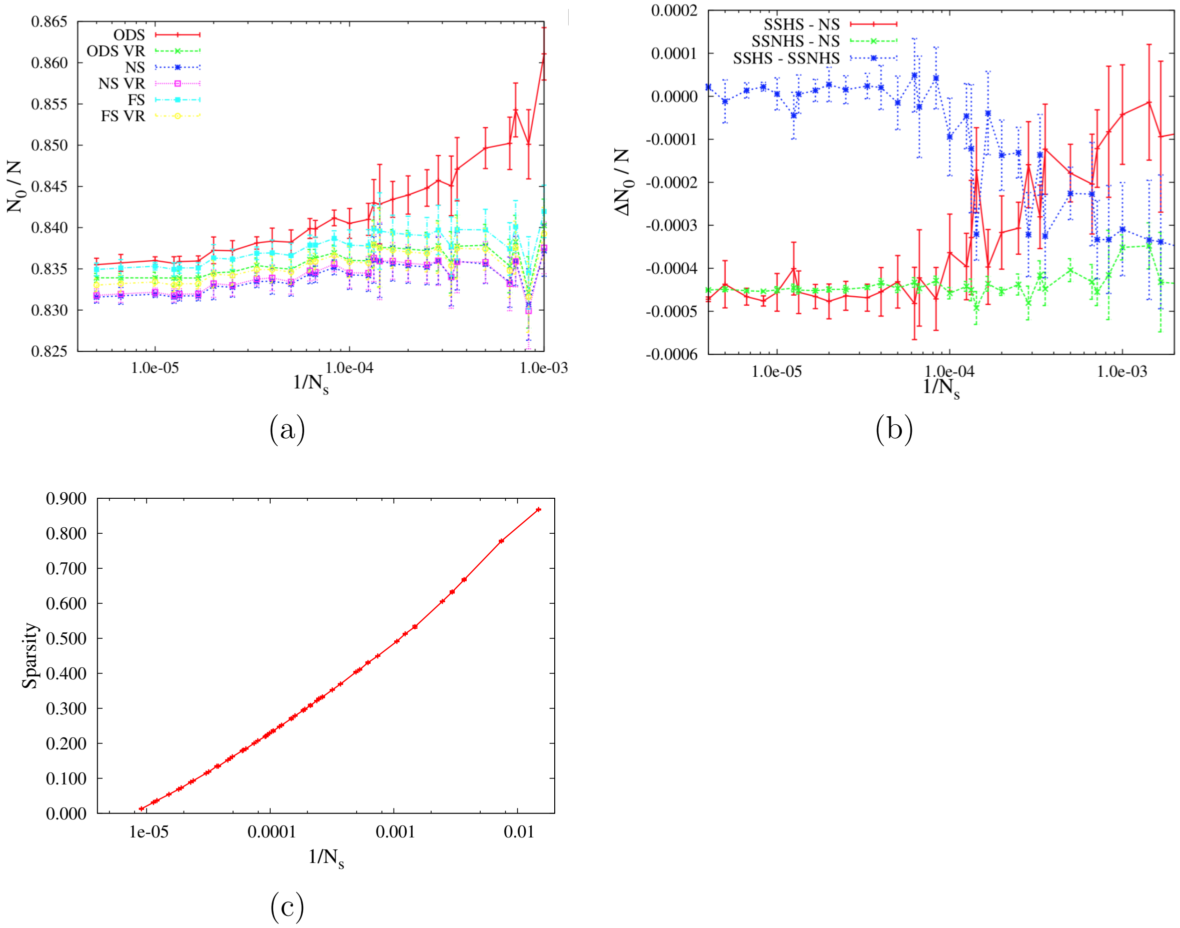

(a)

(b)

(c)

Figure 4.1: (a) Convergence of condensate fraction N_0/N as a function of number of samples N_s for VR and ED calculations on different symmetrized versions of $\hat{\rho}_1$. The system is a trapped 10^3 optical lattice with strength $s = 1$, temperature $T = 0.25$. Comparisons between Spherical symmetrizations have not been shown here since they overlap with unsymmetrized data. (b) Comparisons for difference in N_0/N estimates as a function of number of samples N_s for ED calculations on spherically symmetrized $\hat{\rho}_1$e. Similar behavior is expected for results with VR since the bias introduction mechanism is the same. (c) Sparsity as a function of number of samples N_s

The last three types of symmetrization specifically use the symmetries available due to the trap. For other systems similar studies should be performed using available symmetries to devise the best measurement strategy during QMC simulations.

In order to test the VR method, an appropriate basis is needed. Taking into account the spherical symmetry of the trap, a useful basis function is obtained by defining it to depend only on its distance to the center of the optical trap. Furthermore the trap radius can be divided into sections so that for $1 \leq i \leq M$,

$$\phi_i(|r|) = \{ \begin{array}{cc} \sqrt{n(|r|)} & , |r_{i-1}| \leq |r| < |r_i|, \\ 0 & , \text{otherwise}, \end{array} \tag{4.12}$$

where $n(|r|)$ is average particle density at radius $|r|$. By this construction, a trivially orthogonal basis set is obtained. M is carefully chosen to be the largest possible value for which $\phi_i \neq 0$, $\forall i$. Note that density profile $n(|r|)$ can be obtained from the diagonal matrix elements of $\hat{\rho}_1$ after QMC simulations. This is expected to be a good choice, since at low temperatures ground state wavefunction should overlap with the density profile.

In Fig. (4.1a-c) results for $\hat{\rho}_1$ from simulations done on a 10^3 lattice in a trap is used to illustrate key features of the different methods discussed above. Simulations done for other un-trapped and trapped systems showed similar behaviors. QMC calculations were done using 1000 equilibration sweeps during which N_l is calibrated to ensure that the average number of vertices visited during a loop update was about 10 times the average number of operators. Fig. 4.1a illustrates the n_0 convergence as the number of samples, N_s, increases. It is evident that n_0 calculations done using ODS converges rapidly compared to other estimators. The difference in convergence rates can be explained by the shifts in the eigenvalue spectrum due to noisy matrix elements.

As derived in appendix B, correlations in the off-diagonal elements leads to a biased n_0 estimate [46]. Although off-diagonal correlations always exist due to the diagonalization process, they are usually small. When $\hat{\rho}_1$ is symmetrized by hand, a trade off is made between correlating the off-diagonal noise terms and reducing their variance. Of these symmetrization procedures only symmetrizing off-diagonal pairs, i.e., $\rho(i, j) = \rho(j, i)$, results in the smallest variance reduction and the largest increase in bias. For highly symmetric matrices the resulting variance reduction in elements due to symmetrization may offset the bias due to matrix element correlations if all symmetry operations are used. Note that explicit off-diagonal symmetrization leads to a large addition of noise, consequently the variance reduction due to FS is not enough to be able to reduce the effect of the bias. This explains why NS, SSHS and SSNHS performs better than FS.

In Fig. 4.1b the differences in n_0 calculations for the three estimators viz. NS, SSHS and SSNHS that leads to nearly overlapping n_0 estimates, is presented. Although, enforcing Hermitian symmetry explicitly introduces correlations for points lying on the same sphere, the net variance reduction can offset it, and consequently, SSHS performs better than SSNHS.

The reason is that the sampling procedure leads to distance dependent noise that increases with distance between two points. The symmetrization procedure involved in SSHS only introduces noise correlations for points on the same sphere. Also, the NS data has a small bias due to implicit correlations that are not reduced due to insufficient variance reduction. On the other hand the bias is effectively removed for SSHS and SSNHS for large N_s.

A good theoretical basis is provided for fitting the n_0 results to a second order polynomial for extrapolation to the zero noise limit (Eq. B.6) (See Appendix B). As N_s increases, the sampled state space, $S(k)$, approaches the full configuration space S. In this case both symmetrized and unsymmetrized $\hat{\rho}_1$ are the same and must yield the same n_0 value from ED. The quality of estimates from VR calculation increases because $\hat{\rho}_1$ is more accurate, though it is still limited by the basis. For small N_s, VR calculations done on the symmetrized $\hat{\rho}_1$ shows the same converging behavior as ED calculations. The VR method is less sensitive to the effects of the bias due to symmetrization because it fits blocks of elements which are generally minimally correlated. Many elements contribute to the noise in a single expansion parameter and the variance in their estimated values is reduced. Consequently, symmetrized VR is better than its ED counterpart. Although the variational n_0 calculations using the unsymmetrized $\hat{\rho}_1$ is not bounded, since $\hat{\rho}_1$ is not Hermitian, the n_0 values from VR are well within the error bars of ED. Experience has shown that one important advantage of VR calculation is in the estimation of n_0 for very small N_s. In such regimes, large fluctuations in $\hat{\rho}_1$ elements and sparsity can combine to generate spurious n_0 values that are greater than 1.0 for ED calculations. However, coarse graining effects on $\hat{\rho}_1$ in VR calculations can reduce the fluctuations and give n_0 values that are still reasonable.

Another feature observable in Fig. 4.1a and 4.1c is that n_0 values are not necessarily correlated with the sparsity values. Both n_0 value and sparsity decrease initially as N_s is increased. However, after a modest N_s value, n_0 curve flattens out while sparsity curve continues to decrease. This behavior is due to the sampling of the dominant superfluid puddle in the system which happens within a modest N_s. Further sampling of smaller puddles do not contribute significantly. This means that even with low sparsity due to modest N_s for large realistic systems, it is still possible to obtain reasonable n_0 estimates.

4.2 Diagonalization Strategies for Large Systems

In the discussion so far the non-linear transformation operation used to extract n_0 is assumed to be achievable through exact diagonalization (ED). However, for large systems ED is prohibitively expensive and also unnecessary, unless a large number of single-particle modes need to be accessed. Even if ED was possible, the presence of statistical noise would severely constrain the accuracy of eigenmodes with small occupation numbers. Fortunately, for the systems of interest, only a few of the largest eigenmodes are needed. In what follows, the discussion starts by considering the diagonalization problem of the sparse matrix independent of the noise related properties of $\hat{\rho}_1$.

A well known solution to such sparse matrix problems is to use iterative algorithms such as the Lanczos procedure for Hermitian matrices, or more generally the Arnoldi Iterative algorithm applicable to non-Hermitian matrices as well. From the analysis earlier it is clear that enforcing Hermitian symmetries is generally not a good idea since it requires large number of sweeps to reduce the statistical noise. So the primary mode of enquiry is going to be Arnoldi iteration, but there are certain caveats discussed later that will require us to consider symmetric matrices.

In the following sections, the Arnoldi Iteration method will be discussed in some detail because it will be a major component of our analysis of physical systems. A full discussion of *Eigespaces* and other associated topics are beyond the scope of this work. Instead, only those properties that will enable the study of the systems of interest will be highlighted below. For an excellent and detailed discussion see [47], which will be extensively referenced below.

4.2.1 Krylov Subspace

A good starting point is the Krylov subspace, which is not a topic regularly encountered in physics. Consider the matrix of interest ($\hat{A}$) and apply it successively to a random vector ($|u\rangle \neq 0$) to obtain a sequence $\{|u\rangle, \hat{A}|u\rangle, \hat{A}^2|u\rangle, \hat{A}^3|u\rangle, ..., \hat{A}^{k-1}|u\rangle\}$. Using this sequence define,

$$K_k(\hat{A}, |u\rangle) \equiv (|u\rangle \; \hat{A}|u\rangle \; \hat{A}^2|u\rangle \; \hat{A}^3|u\rangle \; ... \; \hat{A}^{k-1}|u\rangle), \tag{4.13}$$

which is called the kth Krylov matrix and the column space of $\mathcal{K}_k$ is called the kth Krylov subspace $\mathcal{K}_k$. General experience has shown that $\mathcal{K}_k$ can be used to rapidly converge to the dominant eigenvector in the sub space spanned by $\{|u\rangle, \hat{A}|u\rangle, \hat{A}^2|u\rangle, \hat{A}^3|u\rangle, ..., \hat{A}^{k-1}|u\rangle\}$ [47]. Some definitions that are important for our calculations are:

1. **Termination**

   A Krylov sequence is said to terminate at l *iff* l is the smallest integer for which

$\mathcal{K}_{l+1}(\hat{A}, |u\rangle) = \mathcal{K}_l(\hat{A}, |u\rangle)$. In this case $\mathcal{K}_l$ is an eigenspace of $\hat{A}$ of dimension l. If $|u\rangle$ lies in an eigenspace of dimension m, then for some $l \leq m$ the sequence terminates at l. Notice that the termination of the sequence indicates that the Krylov sequence contains exact eigenvectors of $\hat{A}$. However, it also means that the Krylov sequence can't furnish any further information about other eigenvectors.

2. **Convergence**
The Krylov subspace is said to converge if the sequence yields accurate approximations of some of the eigenvectors of $\hat{A}$. An illustrative way to see convergence is via the polynomial connection of Krylov subspaces. Consider a subspace $\mathcal{K}_k(\hat{A}, |u\rangle)$ and some vector v in the subspace, then

$$|v\rangle = \gamma_1|u\rangle + \gamma_2\hat{A}|u\rangle + \gamma_3\hat{A}^2|u\rangle + \ ... \ + \gamma_{k-1}\hat{A}^{k-1}|u\rangle.$$

So we can define the matrix polynomial $p(\hat{A})$:

$$p(\hat{A}) = \gamma_1 I + \gamma_2\hat{A} + \gamma_3\hat{A}^2 + \ ... \ + \gamma_{k-1}\hat{A}^{k-1}.$$

Now suppose $\hat{A}$ is Hermitian and has an orthonormal system of eigenpairs $(\lambda_i, |x_i\rangle)$ for $i = 1, ..., n$. So if u is a starting vector of the Krylov sequence then:

$$|u\rangle = \langle x_1|u\rangle|x_1\rangle + \langle x_2|u\rangle|x_2\rangle + \ ... \ + \langle x_n|u\rangle|x_n\rangle$$

So applying $p(\hat{A})$ to u, where $p(y)$ is a polynomial of degree less than or equal to k, we get:

$$p(\hat{A})|u\rangle = \langle x_1|u\rangle p(\lambda_1)|x_1\rangle + \langle x_2|u\rangle p(\lambda_2)|x_2\rangle + \ ... \ + \langle x_n|u\rangle p(\lambda_n)|x_n\rangle$$

Therefore by choosing an appropriate polynomial, with $p(\lambda_i) > p(\lambda_j)$ for $j \neq i$ we can obtain a good approximation to $|x_i\rangle$ using $p(\hat{A})|u\rangle$. In fact for Hermitian matrices it is possible to obtain bounds on the approximation of the eigenvector:

$$\tan\angle(p(\hat{A})|u\rangle, |x_i\rangle) \leq \max_{j\neq i}\frac{|p(\lambda_j)|}{|p(\lambda_i)|} \cdot \tan\angle(|u\rangle, |x_i\rangle) \tag{4.14}$$

4.2.2 Rayleigh-Ritz Approximation

From the definition of Krylov subspaces based on the matrix $\hat{A}$ it is, therefore, clear that it can contain increasingly accurate approximations of the eigenspace of $\hat{A}$. However, it is still not evident how to obtain an accurate approximation. Towards this end, the Rayleigh-Ritz method is a commonly used method of extracting approximate eigenspace from a larger subspace. The Ritz procedure uses the idea of a *Rayleigh quotient*,

$$\hat{B} \equiv \hat{V}^{-1}\hat{A}\hat{U} \tag{4.15}$$

where $\hat{U}$ is a basis for the subspace $\mathcal{U}$ containing the approximate eigenspace of $\hat{A}$, and $\hat{V}^{-1}$ is the left inverse of $\hat{U}$ with $\hat{V}^{-1}\hat{U} = \hat{I}$.

Consider $(\hat{L}, \hat{X})$ be an eigenpair corresponding to $\mathcal{X} \subset \mathcal{U}$ and let $\hat{X} = \hat{U}\hat{W}$ then,

$$\begin{aligned} \hat{A}\hat{X} &= \hat{X}\hat{L} \\ \hat{A}\hat{U}\hat{W} &= \hat{U}\hat{W}\hat{L} \\ \hat{B}\hat{W} &= \hat{V}^{-1}\hat{U}\hat{W}\hat{L} \\ &= \hat{W}\hat{L} \end{aligned} \tag{4.16}$$

So that $(\hat{L}, \hat{W})$ is an eigenpair of $\hat{B}$. This means that if we have an approximate representation of the eigenspace $\mathcal{U}$ and an eigenpair $(\hat{L}, \hat{W})$ then we construct a *Ritz pair* of $\hat{A}$: $(\hat{L}, \hat{U}\hat{W})$. $\hat{L}$ is called the *Ritz block*, $\hat{U}\hat{W}$ is its *Ritz basis* and the associated space is called the *Ritz space*. Additionally, $\hat{W}$ is called the primitive *primitive Ritz basis*. For a particular eigenvalue and eigenvector pair of B say $(\lambda, |w\rangle)$, the corresponding pair for $\hat{A}$ is $(\lambda, \hat{U}|w\rangle)$. λ is a *Ritz value*, $\hat{U}|w\rangle$ is a *Ritz vector* and $|w\rangle$ is a *primitive Ritz vector*. Unfortunately, it is not clear what is the procedure to choose $(\hat{L}, \hat{W})$ and, furthermore, there is no way to guarantee that it approximates the desired eigenpair of $\hat{A}$. However, by choosing an appropriate part of the spectrum of $\hat{B}$ such that the eigenvalue of $\hat{B}$ are close to the desired eigenvalues $\hat{A}$, it is possible to obtain suitable approximations. For large eigenvalue problems it is possible to construct the $\hat{B}$ from $\hat{K}$ that yields extremal eigenpairs – this forms the basis of the Arnoldi decomposition discussed next.

4.2.3 Arnoldi Decomposition

The starting point of Arnoldi decomposition is the Krylov basis of the form (4.13). Unfortunately, using this basis directly is not a good idea. It is evident that as k increases, the columns of K_k become increasing dependent due to large correlations present in them. The column space is dominated by the space spanned by the dominant eigenvectors of $\hat{A}$. Therefore, replacing the Krylov basis with another basis with low condition number would be ideal. The procedure for achieving this is outlined below. Requiring that the columns

```
1.  for k = 1,2,... (until convergence)
2.    $|q_{k+1}\rangle = \hat{A}|q_k\rangle$
3.    $|h_k\rangle = \hat{Q}_k^{-1}|q_{k+1}\rangle$
4.    $|v\rangle = |q_{k+1}\rangle - \hat{Q}_k|h_k\rangle$
5.    $h_{k+1,k} = \sqrt{\langle v|v\rangle}$
6.    $|q_{k+1}\rangle = |v\rangle / h_{k+1,k}$
7.    $\hat{H}_k = \begin{pmatrix} \hat{H}_{k-1} & |h_k\rangle \\ 0 & h_{k+1,k} \end{pmatrix} = \begin{pmatrix} \tilde{H}_k \\ h_{k+1,k}\langle \mathbf{e_k}| \end{pmatrix}$
8.    $\tilde{H}_k \hat{V}_k = \hat{V}_k \hat{L}_k$
9.    $\hat{\Phi}_k = \hat{Q}_k \hat{V}_k$
10.   $\hat{R}_k = \hat{A}\hat{\Phi}_k - \hat{\Phi}_k \hat{L}_k = (|r_1\rangle \ldots |r_k\rangle)$
11.   Check Convergence using $\hat{R}_k$
12. end
```

Figure 4.2: Simple Arnoldi Iteration. In steps (9)-(11) we compute the *residual* $(|r_1\rangle \ldots |r_k\rangle)$ for each Ritz pair $(\lambda_i, |\phi_i\rangle) \in \{\hat{L}_k = diag(\lambda_1 \ldots \lambda_k), \hat{\Phi}_k = (|\phi_1\rangle \ldots |\phi_k\rangle)\}$ and then use it to check for convergence. Note that by construction $\hat{Q}_k^{-1} = \hat{Q}_k^H$, the conjugate transpose of the matrix.

of K_{k+1} is linearly independent the iterative procedure is setup with a QR factorization of $\hat{K}_{k+1}$:

$$\hat{K}_{k+1} = \hat{Q}_{k+1}\hat{R}_{k+1}.$$

In order that definitions and derivations are consistent, let $\hat{A} \in \mathbb{C}^{n\times n}$ and $\hat{K}_k \in \mathbb{C}^{n\times k}$ so that $\hat{Q}_k \in \mathbb{C}^{n\times k}$ and $\hat{R}_k \in \mathbb{C}^{k\times k}$. $\hat{K}_{k+1}$ can be decomposed as,

$$(\hat{K}_k \;\; A^k|q\rangle) = (\hat{Q}_k \;\; |q_{k+1}\rangle) \begin{pmatrix} \hat{R}_k & r_{k+1} \\ 0 & \rho_{k+1,k+1} \end{pmatrix},$$

Let $\hat{S}_k = \hat{R}_k^{-1}$, then

$$\begin{aligned}
\hat{A}\hat{Q}_k &= \hat{A}\hat{K}_k\hat{S}_k \\
&= \left(|q_1\rangle \;\; \hat{A}\hat{K}_k\right)\begin{pmatrix} 0 \\ \hat{S}_k \end{pmatrix} \\
&= \hat{K}_{k+1}\begin{pmatrix} 0 \\ \hat{S}_k \end{pmatrix} \\
&= \hat{Q}_{k+1}\hat{R}_{k+1}\begin{pmatrix} 0 \\ \hat{S}_k \end{pmatrix} \\
&= \hat{Q}_{k+1}\hat{H}_k, \qquad (4.17)
\end{aligned}$$

where,

$$\hat{H}_k \equiv \hat{R}_{k+1}\begin{pmatrix} 0 \\ \hat{S}_k \end{pmatrix}. \qquad (4.18)$$

$\hat{H}_k \in \mathbb{C}^{(k+1)\times k}$ is a Hessenberg matrix with sub diagonal elements $h_{i+1,i} = r_{i+1,i+1}/r_{ii}$. By induction:

$$\hat{H}_k = \begin{pmatrix} \hat{H}_{k-1} & |h_k\rangle \\ 0 & h_{k+1,k} \end{pmatrix} = \begin{pmatrix} \tilde{H}_k \\ h_{k+1,k}\langle \mathbf{e_k}| \end{pmatrix},$$

where $\tilde{H}_k \in \mathbb{C}^{k\times k}$ and $\langle \mathbf{e_k}| = \langle \mathbf{0}\;\mathbf{0}\;...\;\mathbf{1}| \in \mathbb{C}^{1\times k}$ is the standard basis vector. Finally the *Arnoldi decomposition* is given by:

$$\begin{aligned}
\hat{A}\hat{Q}_k &= \hat{Q}_{k+1}\hat{H}_k \\
&= \hat{Q}_k\tilde{H}_k + h_{k+1,k}|q_{k+1}\rangle\langle \mathbf{e_k}|. \qquad (4.19)
\end{aligned}$$

Note that by construction $\hat{Q}_k$ is an orthonormal set of vectors so that $\hat{Q}_k^{-1}|q_{k+1}\rangle = 0$. This means that $\tilde{H}_k = \hat{Q}_k^{-1}\hat{A}\hat{Q}_k$ – precisely what was defined to be the Rayleigh quotient. Therefore, the Arnoldi decomposition allows the calculation of the required Ritz pairs. The general algorithm for the Arnoldi procedure is shown in 4.2. The idea is to construct the orthonormal Krylov subspace together with the required Ritz pairs. Once the Ritz pairs are constructed, convergence can be checked using the residual for each pair. Depending on the number of approximate eigenpairs needed the subspace might become too large. As such alternate strategies are needed. It it possible, for example, to focus on certain eigenvalues by using the *shift-and-invert enhancement* [47]. Additionally, there are extensions of the Arnoldi It-

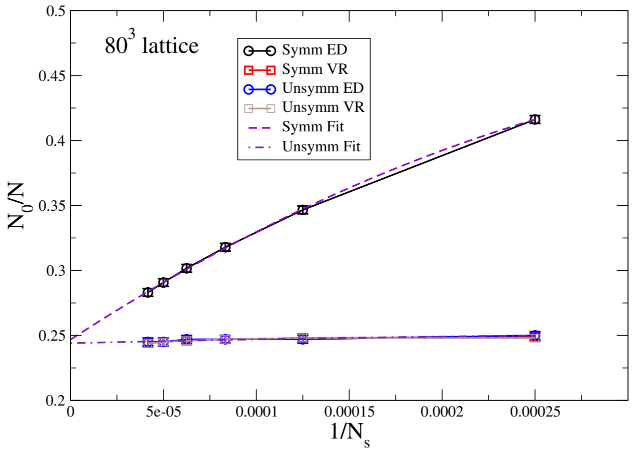

Figure 4.3: (Color online.) Convergence of condensate fraction N_0/N as a function of number of samples N_s for VR and ED calculations of symmetrized and unsymmetrized $\hat{\rho}_1$. The system is a trapped 80^3 optical lattice with strength $s = 12$, temperature $k_BT/t = 8.13$. Dashed or dot dashed lines are fits to Hermitian and non-Hermitian n_0 data as discussed in the text.

eration method that take advantage of restarting strategies, called the *Implicitly Restarted Arnoldi Method (IRAM)* that can be used to compute many approximate eigenvectors without growing the subspace beyond storage capacity [48]. For the purposes of the systems studied here, fortunately further sophistications are not generally needed. Extensive tests over a wide range of matrices confirm that the ED calculations agree extremely well with this procedure for all extractable eigenpairs. As such in future discussions ED will be used synonymously with calculations via Arnoldi iteration.

Using the Arnoldi procedure discussed so far, it is finally possible to attempt to diagonalize and extract the condensate fraction for large systems. Two examples are presented for realistic system sizes that provide an overview of the different factors discussed so far.

Example 4.2.1. Results of n_0 for a realistic optical lattice of size 80^3 is presented in Fig. 4.3 [46]. The lattice depth is $s = 12\ E_R$ and contains $\sim 4.0 \times 10^5$ particles. Here the total number of samples is $N_s^{\max} = 24000$, which measures about 6×10^7 off-diagonal matrix elements. Although the total number of off-diagonal matrix elements visited seems significant ($\sim 1.5 \times 10^{10}$), $\hat{\rho}_1$ is still $\sim 95\%$ sparse. The importance of the study of the symmetrization procedure, discussed earlier, is revealed as the problems discussed for small systems clearly are applicable for larger calculations. It is evident that ED on symmetrized ρ_1 converges slowly as N_s increases. In contrast, ED on unsymmetrized ρ_1 converges quickly to the final result, and its curve coincides with the VR calculations on both symmetrized and unsymmetrized ρ_1. In order to extrapolate to $N_s \to \infty$, both symmetrized and unsymmetrized ED data is fit to

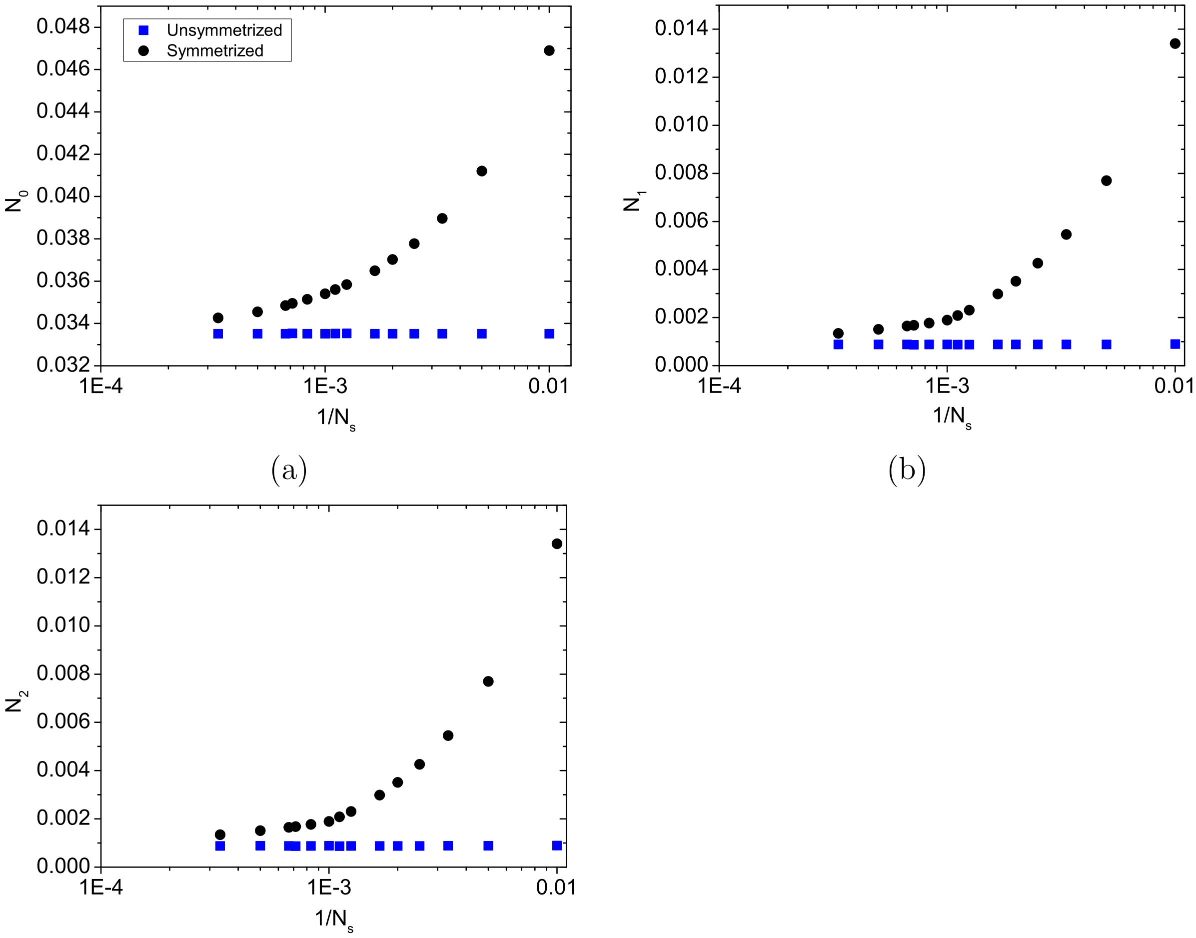

(a)

(b)

(c)

Figure 4.4: Convergence of occupation numbers of the largest mode N_0 and the next two largest modes N_1, N_2 as a function of number of samples N_s for ED calculations of symmetrized (black circles) and unsymmetrized (blue squares) $\hat{\rho}_1$. The system is a trapped 54^3 optical lattice of depth $s = 12\ E_R$ and disorder strength $\Delta = 1\ E_R$, at temperature $k_BT/t = 1.0$.

a quadratic function $a(1/N_s)^2 + b(1/N_s) + c$, which yields n_0 values of 0.247(3) (Hermitian) and 0.244(3) (non-Hermitian), respectively. These symmetry techniques will be used later in Part III for full scale simulations that are compared with experiments.

Example 4.2.2. For the second example, results are presented from ED of a disordered system that will be discussed in detail later in part III. The system is composed of $N = 27000$ particles for a $s = 12\ E_R$ system in the presence of a disorder field of strength $\Delta = 1.0\ E_R$ at ultra low temperatures of $k_BT/t = 1.0$. In fig. (4.4a-c) the convergence of the largest eigenmode N_0 as well as the next two largest eigenmodes are presented. The general effects of the symmetrization bias that leads to a slow convergence of the eigenvalues is clearly visible. Given the discrepancy in the eigenvalues between the Hermitian and non-Hermitian ρ_1

constructed from blocks of different sample sizes (N_s), the quality of the eigenvectors come into question.

The first point of interest is the dominant eigenvector ($|\psi_0\rangle$). In order to understand its change with increasing sample size, the overlap between the eigenvector generated from the smallest sample of $N_s = 100$ and those generated from larger samples is computed. Fig. (4.5a) shows these results for symmetrized and unsymmetrized ρ_1. It is clear that the non-Hermitian ρ_1 dominant vector is stable. On the other hand the Hermitian ρ_1 eigenvectors change so that the initial and final vectors are quite different. The overlap between consecutive dominant eigenvectors generated from i^{th} and the $(i+1)^{th}$ block (corresponding to different sample sizes) is shown in fig. (4.5b). It illustrates the rotation of the dominant eigenvector as the sample size is increased. As a consequence of this rotation, $|\psi_0\rangle$ from the symmetrized matrix converges to the stable eigenvector of the non-symmetrized matrix, as shown in fig. (4.5c).

An important consequence of the non-Hermitian matrix is illustrated in fig. (4.6a): despite the convergence in the value of the second and third largest occupation numbers the eigenvectors are not orthogonal, but the property is slowly restored as N_s increases. This behavior can be understood by checking the overlap between the symmetrized and unsymmetrized eigenvectors as a function of increasing sampled sizes. Fig. (4.6b-c) shows that the higher order eigenvectors (corresponding to smaller eigenvalues) also rotate so that eventually in the large sample limit they are coincidental, as expected. For intermediate sample sizes, the higher order eigenvectors may not be well behaved. Thus, identifying the minimum number of samples needed before the convergent behavior sets in is generally a good idea before the information is used to access any physical properties. Note that the discrepancies are not a result of the Arnoldi iteration process since the Ritz pairs converge with residual $< 1.0 \times 10^{-8}$.

In conclusion, this chapter discussed two important aspects to computing eigenmodes for large systems. The first concerned aspects of the noise eigenvalue problem for reduced density matrices. On general grounds we can surmise that symmetrization can lead to introduction of noise that can bias the results and lead to slow convergence of QMC results. The non-symmetric problem that converges rapidly exhibits no problems for the the dominant eigenvector; however, the other smaller modes are not as straightforward. The non-Hermitian nature does not guarantee orthogonal vectors and may produce unphysical vectors. On the other hand the eigenvectors from the symmetrized matrices that are guaranteed to be orthogonal can still be significantly biased away from the true vectors of the system. Fortunately, as

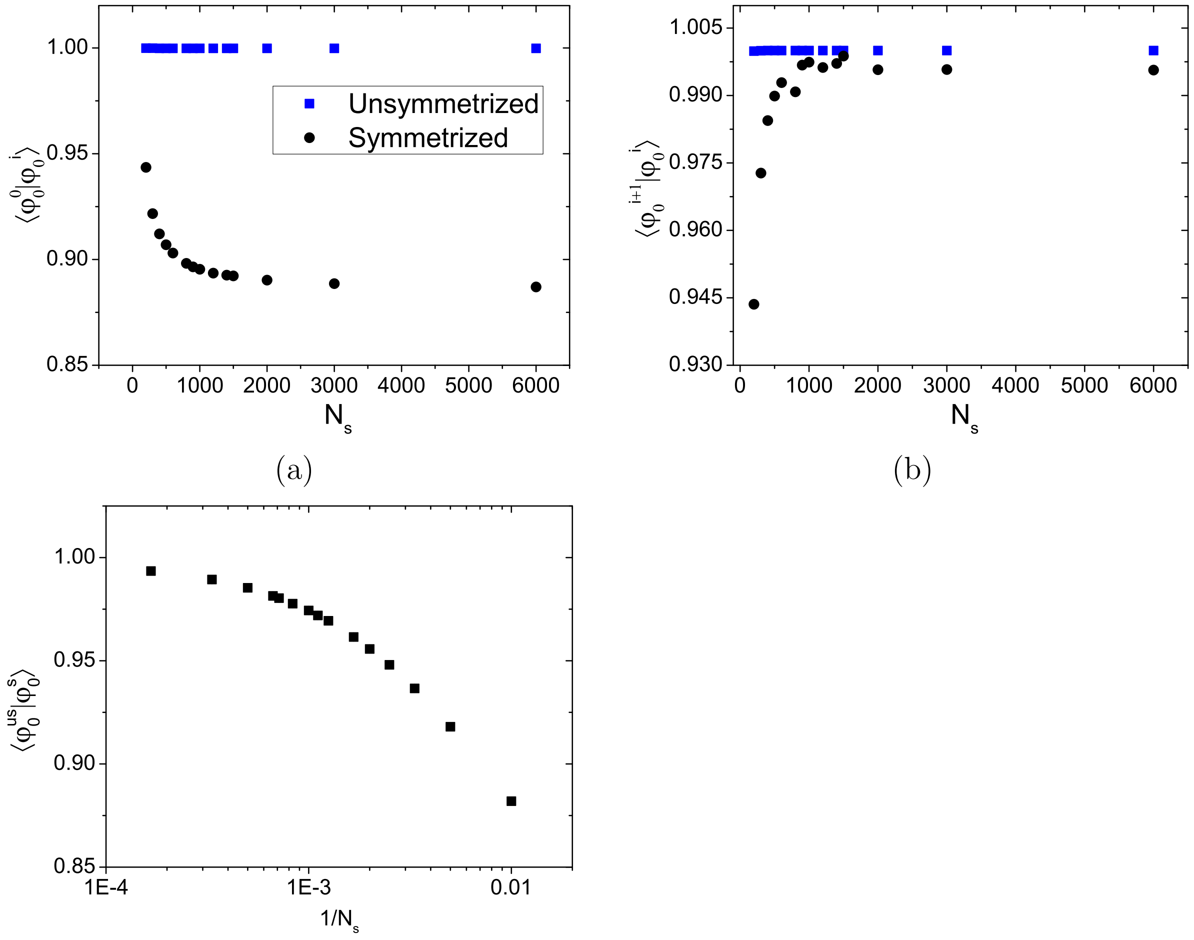

(a)

(b)

(c)

Figure 4.5: (a) Overlaps for the largest eigenmode ($|\psi_0\rangle$) from block generated with 100 samples and subsequent i blocks generated with increasing sample sizes N_s. (b) Overlap between consequtive blocks (i and $i+1$) generated from larger samples. For example, ($i=0$,$i=1$) pair overlap corresponds to ($N_s=100$,$N_s=200$) samples. The x-axis is labelled according to the number of samples used to generate block i. (c) Overlap of largest eigenmode generated from the symmetrized ($|\phi_0^s\rangle$) and unsymmetrized ($|\phi_0^{us}\rangle$) ρ_1. It shows how the Hermitian results converge to the true value in the limit of large N_s (See text for discussion).

the sample size is increased, the results from the symmetrized matrices and unsymmetrized matrices converge. The long run converged behavior can be obtained quickly for the largest mode but might require significant computation time for higher order modes. Ultimately the diagonalization of large systems cannot rely on standard exact diagonalization techniques and alternate strategies are required. Such a strategy involves the Arnoldi Iteration method that builds on the idea of Krylov subspaces and Ritz eigenpairs. This method works remarkably well for sparse systems provided only a small number of eigenpairs are needed. Combining observations made for the noise eigenvalue problem together with iterative tech-

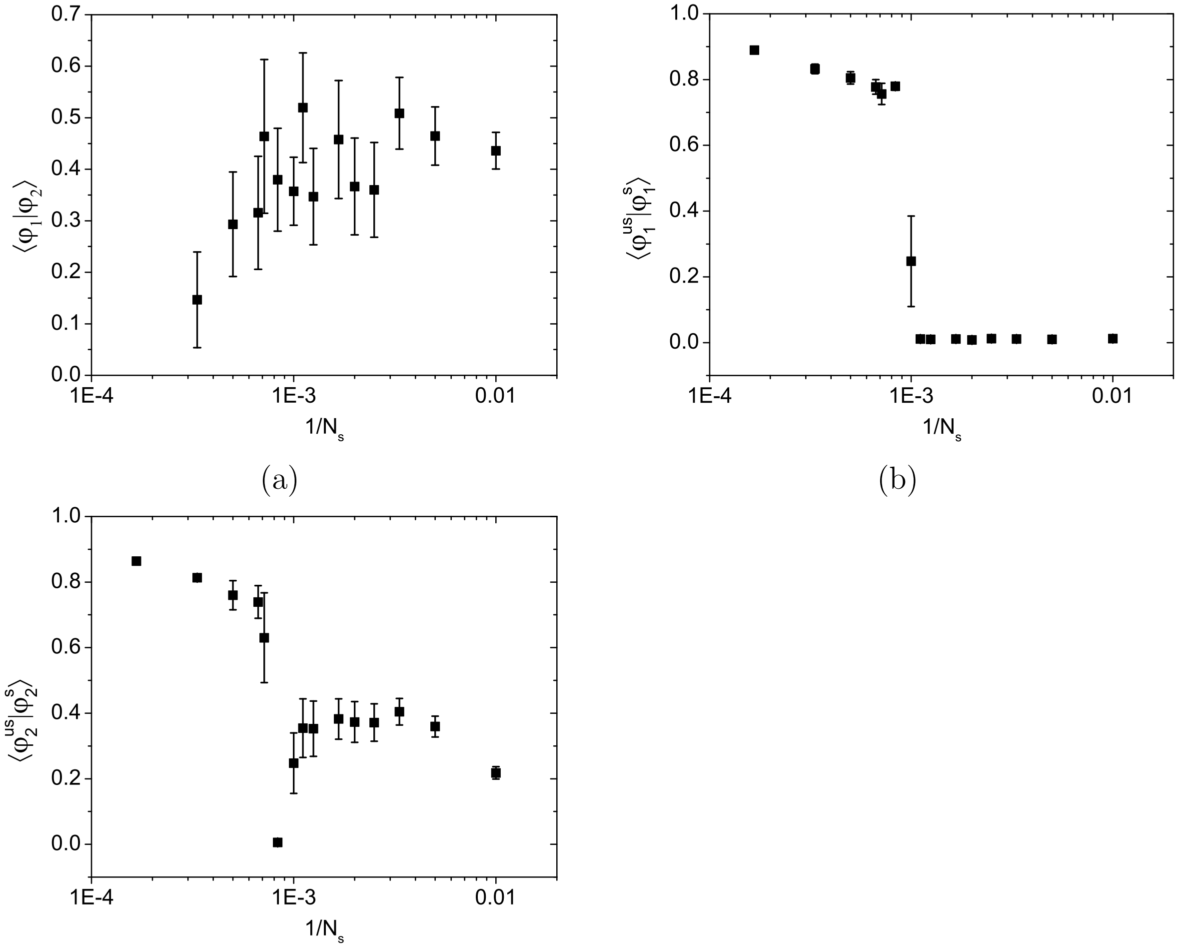

(a)

(b)

(c)

Figure 4.6: (a) Overlap between the first ($|\phi_1\rangle$) and the second largest ($|\phi_2\rangle$) eigenvectors obtained from diagonalizing non-Hermitian matrix. The Hermitian matrix is guaranteed to produce orthonormal eigenvectors. (b) and (c) show the calculated overlap between the nth symmetrized ($|\phi_n^s\rangle$) and unsymmetrized ($|\phi_n^{us}\rangle$) eigenmodes for $n = 1, 2$ (respectively). For the 1st and 2nd eigenpair, the eigenvectors are not aligned correctly for small sample sizes. As the sample size increases the eigenvectors for both sets begin to rotate towards the correct direction. This leads to the restoration of the orthogonality of the non-Hermitian matrix as shown in fig. (4.5) and the reduction of errors due to the stochastic noise in the Hermitian matrix. The discontinuity in (b) and (c) and the behavior at low N_s sizes show the need for care in using smaller eigenvectors. Over the range of systems studied, the largest eigenpair consistently showed remarkably robust behavior for non-symmetrized ρ_1.

niques, it is possible to access large systems comparable to size of experiments. These results will be used extensively in part III to study important aspects of both clean and disordered systems.

Chapter 5

Coarse-Graining Single-Particle Hamiltonians

The full many-body Hamiltonian of a system ($\hat{\mathscr{H}}$) captures all the ingredients that contributes to the behavior of the system (this itself is obtained by making – to start with – some reasonable assumptions about what contributes). However, in many cases, this is too complicated of a problem to solve and carries information that may not be pertinent to the regime of inquiry. It might therefore be useful to narrow the regime of interest and to devise methods to understand the behavior of the system within that regime.

The main objective of Condensed Matter physics is to understand the low energy behavior of systems. Towards this end, a possible strategy is to try to reduce $\hat{\mathscr{H}}$ to some effective coarse-grained Hamiltonian $\hat{H}$ that retains certain properties of the original Hamiltonian. The criteria could be that $\hat{H}$ retains the low energy properties of the reduced density matrices (RDM) that capture the 1-body, 2-body (etc.) behavior of the physical system. This is motivated by the fact that the linear response of a system to external perturbation (such as a field, particle insertion or removal, coupling to another subsystem etc.) is determined by its single-particle density matrix [49, 50, 51]. Additionally, two-body correlations are responsible for a wide class of behavior such as superconductivity in Fermions [19]. Indeed, it is possible to directly construct $\hat{H}$ on the basis of this criteria and it is an active area of research. However, this form of direct mapping is very hard for large systems. Thus, exploring alternative indirect formulations could be extremely useful.

The basic idea is to coarse grain the continuum Hamiltonian in a way that removes the high energy contribution due to small length scales and only keep the effective Hamiltonian up to some relevant length scale set by the natural setup of the system. For instance, in the case of atoms in a periodic potential, the physics below the length scale of a single unit cell may play little or no role in the collective behavior occurring at much larger length scales. Therefore, it would make sense to integrate out dynamics of such small scales. Indeed, this is the reason behind the transformation of continuum systems to some effective lattice model, that could in principle be more tractable while retaining enough details that are physically useful. As will be shown in part III, such an approach is indeed very powerful to gain insight into a range of exotic phenomena that is possible in condensed matter systems. The purpose of this chapter is to outline one method of constructing such effective lattice models that is very useful when analytical solutions do not exist – for instance in the case of disordered systems.

5.1 Indirect Coarse-Graining

The starting point is a very general second quantized Hamiltonian for a D dimensional system:

$$\hat{\mathscr{H}} = \int d^D\vec{r}\hat{\psi}^\dagger(\vec{r})\left[-\frac{\hbar^2}{2m}\nabla^2 + V(\vec{r})\right]\hat{\psi}(\vec{r}) + \frac{1}{2}\int\int d^D\vec{r}_2 d^D\vec{r}_1\hat{\psi}^\dagger(\vec{r}_2)\hat{\psi}^\dagger(\vec{r}_1)U(\vec{r}_2-\vec{r}_1)\hat{\psi}(\vec{r}_2)\hat{\psi}(\vec{r}_1) \tag{5.1}$$

defined in the chosen position basis. $V(\vec{r})$ characterizes the single-particle potential that individual particles experience independent of all other particles. In condensed matter systems this potential typically results from ions (e.g. protons, assumed to be fixed under the Born-Oppenheimer approximation) interacting with the fundamental particle of interest (e.g. electrons). $U(\vec{r}_2-\vec{r}_1)$, on the other hand encapsulates all the inter-particle interactions (e.g., between electrons) assumed to be of the two-body type, i.e., particles interact in a pairwise fashion.[1]. Notice that the first term in the sum ($\equiv \hat{\mathscr{H}}_1$) encapsulates all single-particle phenomena and essentially constitutes a non-interacting problem. The interaction term given by the second term ($\equiv \hat{\mathscr{U}}$) lives in the 2-body sector and complicates affairs considerably. As it stands the Hamiltonian is not in a diagonal form and very little physical insight into the system can be obtained. If the basis could be manipulated to bring it ($\hat{\mathscr{H}}$) to a diagonal form then we would be done. This is, however, rarely possible in the case of real interaction systems and we must resort to approximations. The entire problem of condensed matter system is about handling this term. While a completely general solution is unknown, there are several approximate schemes that are applicable to wide class of systems. Further discussions of such methods leads into the familiar canon of condensed matter that is too extensive to be

---

[1] Exceptions do exist, e.g., 3-body forces in nuclei between protons and neutrons

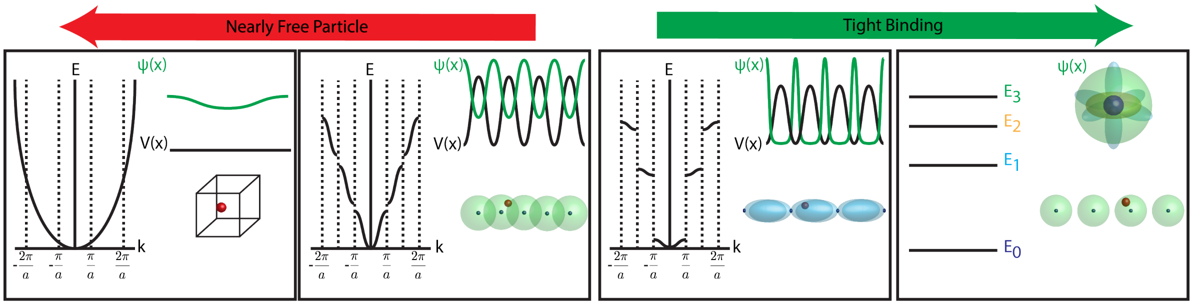

Free Particle Shallow Lattice Deep Lattice Atomic Limit

Figure 5.1: Basis for different physical situations. For shallow lattices, the appropriate basis leads to nearly free particle models. On the other hand, for deep lattices tight binding models are better suited. For the atomic limit the eigenpairs $\{\psi_i, E_i\}$ do not require the energy band and crystal momentum indexing. For free particles the full parabolic spectrum could be broken up into Brillouin zones, but the energies do not have any gaps. For the intermediate regime there are gaps in the spectrum and the bands acquire (loose) atomic (free-particle) character as the potential becomes stronger (weaker).

discussed here, but can be found in [52, 53, 54, 55] (among other excellent references). Below we only discuss aspects that directly inform the systems to be studied in this dissertation.

The indirect coarse graining approach transfers the direct RDM matching problem for the exact 5.1 to an approximate form. The idea is to match the low energy RDM of the continuum single-particle Hamiltonian ($\hat{\mathscr{H}}_1$) with an effective discrete or *lattice* Hamiltonian $\hat{H}_1$ via some procedure. The resulting basis transformations are then used to reduce the continuum interaction term ($\hat{\mathscr{U}}$) to an effective lattice interaction term ($\hat{U}$). The resulting coarse-grained Hamiltonian $\hat{H} \equiv \hat{H}_1 + \hat{U}$ can then by expected to capture all the essential low energy physics. Ultimately its validity is tested in nature via experiments. The procedure that can be used to discretize $\hat{\mathscr{H}}_1$ relies on the properties of the system being considered. For a wide class of condensed matter systems, a standard feature is the presence of a periodic (or quasi-periodic) single-particle confining potential $V(\vec{r}) = V(\vec{r} + \vec{R})$, where $\vec{R}$ characterizes the periodicity of the potential usually called a *lattice vector*. Given this "simple" additional information, many inferences can be drawn about the solutions of the system. These will be discussed next as it will lend insight to more general circumstances.

5.2 Bloch's Theorem and Periodic Potentials

According to Bloch, the eigenstate of the Hamiltonian must also possess the same periodic structure as the underlying *lattice potential* so that $\psi^\dagger(\vec{r}) = \psi^\dagger(\vec{r} + \vec{R})$. So although the continuous translational symmetry is removed a different kind of discrete symmetry is still present due to the periodicity of the potential. Additionally the periodic property also results in a *Band structure* where the eigenstates together with the energy of the Hamiltonian $\{\psi_i(\vec{r}), E_i\}$ can be grouped into *Bands*. There are many texts on this subject, below is an outline of a formulation that appeals to the mathematical structure of subspaces [52].

Consider the Schrödinger equation for a single-particle with a periodic potential $V(x) = V(x + ma)$ with $m \in \mathbb{Z}$ in 1D:

$$-\frac{\hbar^2}{2m}\frac{d^2\psi(x)}{dx^2} + V(x)\psi(x) = E\psi(x).$$

Using the fact that V(x) can be written in the equivalent Fourier space:

$$V(x) = \sum_{n=-\infty}^{\infty} \tilde{V}(q_n)e^{iq_nx} = \sum_{n=-\infty}^{\infty} \tilde{V}(q_n)e^{i(\frac{n\pi}{a})x}.$$

Consider the application of Schrödinger's equation to the plane wave state $f_k(x) = \frac{1}{\sqrt{L}}e^{ikx}$ with $k \in \mathbb{R}$:

$$\begin{aligned} H(x)\left[\frac{1}{\sqrt{L}}e^{ikx}\right] &= \frac{1}{\sqrt{L}}\left[\frac{\hbar^2k^2}{2m}e^{ikx} + \sum_{n=-\infty}^{\infty} \tilde{V}(q_n)e^{i(q_n+k)x}\right] \\ &= \left[\frac{\hbar^2k^2}{2m}f_k(x) + \sum_{n=-\infty}^{\infty} \tilde{V}(q_n)f_{k+q_n}(x)\right] \qquad (5.2) \end{aligned}$$

That is, the resulting vector belongs to the subspace $\mathcal{S}_k \equiv \{f_k(x), f_{k+q_1}(x), f_{k-q_1}(x), f_{k+q_2}(x), f_{k-q_2}(x), ...\}$. Note of-course that the action of $H(x)$ on any member of the space is a closed operation. This means that these vectors span the sub-space and so a general solution can be written in terms of the subspace vectors:

$$\psi_k(x) = \sum_n \tilde{u}_n(k)\frac{1}{\sqrt{L}}e^{i(k+q_n)x} \equiv e^{ikx}u_k(x), \qquad (5.3)$$

with

$$u_k(x) = \frac{1}{\sqrt{L}}\sum_n \tilde{u}_n(k)e^{ikx}. \qquad (5.4)$$

Given the nature of the plane wave basis, it is clear that two subspaces $\mathcal{S}_k$ and $\mathcal{S}_{k'}$ are are equal iff $k' = k + n\frac{2\pi}{a}$ for $n \in \mathbb{Z}$. Therefore the set of k values with $-\frac{\pi}{a} < k < \frac{k}{a}$ are unique labels to the corresponding set of subspaces $\{\mathcal{S}_k\}$. This set is referred to as the *first Brillouin*

Zone. Using 5.10 in the Schrd̈inger equation:

$$H(x)\psi_k(x) = E_k\psi_k(x)$$

$$\sum_n \frac{\hbar(k+q_n)^2}{2m}\tilde{u}_n(k)\frac{1}{\sqrt{L}}e^{i(k+q_n)x} + \sum_n V(x)\tilde{u}_n(k)\frac{1}{\sqrt{L}}e^{i(k+q_n)x} = E_k\frac{1}{\sqrt{L}}\sum_n \tilde{u}_n(k)e^{i(k+q_n)x} \tag{5.5}$$

Taking inner product with $\frac{1}{\sqrt{L}}e^{i(k+q_m)x}$:

$$\begin{aligned} E_k\tilde{u}_n(k)\delta_{mn} &= \frac{\hbar^2(k+q_n)^2}{2m}\tilde{u}_n(k)\delta_{mn} + \tilde{u}_n(k)\frac{1}{L}\int_0^L e^{-i(q_m-q_n)x}V(x)dx \\ E_k\tilde{u}_n(k)\delta_{mn} &= \frac{\hbar^2(k+q_n)^2}{2m}\tilde{u}_n(k)\delta_{mn} + \tilde{u}_n(k)\tilde{V}(q_m-q_n) \end{aligned} \tag{5.6}$$

So that we get a matrix system:

$$\begin{bmatrix} \ddots & & & & & & \\ \cdots & \left[\frac{\hbar^2(k+q_{-2})^2}{2m}\right] & \tilde{V}(q_{-1}-q_{-2}) & \tilde{V}(q_0-q_{-2}) & \cdots & \cdots & \cdots \\ \cdots & \tilde{V}(q_{-2}-q_{-1}) & \left[\frac{\hbar^2(k+q_{-1})^2}{2m}\right] & \tilde{V}(q_0-q_{-1}) & \cdots & \cdots & \cdots \\ \cdots & \tilde{V}(q_{-2}-q_0) & \tilde{V}(q_{-1}-q_0) & \left[\frac{\hbar^2(k+q_0)^2}{2m}\right] & \tilde{V}(q_1-q_0) & \tilde{V}(q_2-q_0) & \cdots \\ \cdots & \tilde{V}(q_{-2}-q_1) & \tilde{V}(q_{-1}-q_1) & \tilde{V}(q_0-q_1) & \left[\frac{\hbar^2(k+q_1)^2}{2m}\right] & \tilde{V}(q_2-q_1) & \cdots \\ \cdots & \tilde{V}(q_{-2}-q_2) & \tilde{V}(q_{-1}-q_2) & \tilde{V}(q_0-q_2) & \tilde{V}(q_1-q_2) & \left[\frac{\hbar^2(k+q_2)^2}{2m}\right] & \cdots \\ & & & & & & \ddots \end{bmatrix} \begin{bmatrix} \vdots \\ \tilde{u}_{-2}(k) \\ \tilde{u}_{-1}(k) \\ \tilde{u}_0(k) \\ \tilde{u}_1(k) \\ \tilde{u}_2(k) \\ \vdots \end{bmatrix}$$

$$= (E_k - \tilde{V}(0)) \begin{bmatrix} \vdots \\ \tilde{u}_{-2}(k) \\ \tilde{u}_{-1}(k) \\ \tilde{u}_0(k) \\ \tilde{u}_1(k) \\ \tilde{u}_2(k) \\ \vdots \end{bmatrix} \tag{5.7}$$

which can be diagonalized to get the necessary solutions $\{E_k^n, \psi_k^n(x)\}$ of the system, where now n indexes a band. So as stated before, remarkably the Hamiltonian with a periodic potential admits a certain structure to the eigenpairs $\{\psi_i(\vec{r}), E_i\}$ characterizing the solutions of the system, *viz.* that the indices (i) can be grouped into bands (n) and crystal momentum

(k) or more succinctly, $i = i(n, k)$. The grouping is not that surprising and it captures the intervening picture between free particles and collection of isolated systems. For the purposes of coarse graining, the choice of the basis is important as it allows easier manipulations and analysis of the structure of the continuum Hamiltonian. Typically for weak potentials the one-body problem can be treated perturbatively in the so called *Nearly Free Particle* picture, where the natural choice of the basis is Plane waves from free particles. Alternatively, for deeper potentials the expectation is that the eigenstates will be localized, thus a natural choice for the basis is localized orbitals obtained from the atomic limit [53]. These ideas have been summarized in fig. (5.1). Using these basis functions it is possible to write the single-particle operator as $\hat{\psi}(\vec{r}) = \sum_n \sum_{\vec{k}} \psi_k^n(\vec{r})\hat{b}_{n,k}$ and using that to rewrite 5.1 as:

$$\mathscr{H} = \sum_{n,\vec{k}} E_k^n \hat{b}^\dagger(\vec{k}, n)\hat{b}(\vec{k}, n) + \sum_{\substack{n_1,n_2,n_3,n_4,\\ \vec{k}_1,\vec{k}_2,\vec{k}_3,\vec{k}_4}} U_{n_1,n_2,n_3,n_4}^{k_1,k_2,k_3,k_4} \hat{b}^\dagger(\vec{k}_1, n_1)\hat{b}^\dagger(\vec{k}_2, n_2)\hat{b}(\vec{k}_3, n_3)\hat{b}(\vec{k}_4, n_4) \quad (5.8)$$

So the first term corresponding to the single-particle Hamiltonian is already diagonal, but the second term corresponding to the interactions between particles is not. The natural question to ask now, is how to eliminate terms in 5.8 so that the effective lattice Hamiltonian is obtained. One approach is to consider the resulting single-particle energy spectrum $\{E_k^n\}$ and eliminate all terms for which E_k^n is too large – for instance, by restricting only a single band to feature. Additionally, by looking at the relative weights of the the interaction matrix elements given by $U_{n_1,n_2,n_3,n_4}^{k_1,k_2,k_3,k_4}$ all terms corresponding to small parameters could be eliminated. However, this procedure is not easy to generalize to large systems as the single-particle problem is also not particularly easy to solve analytically for arbitrary potentials and must rely on numerical schemes. In general exact diagonalization is the only way to access multiple excited states that will be needed to capture all the modes of the bands being retained. Fortunately an alternate basis exists that can be handled more easily. This basis utilizes the localized wave functions called Wannier states. Below a coarse graining method is discussed for such states.

5.3 Coarse-Graining with Wannier Functions

Wannier functions can analytical be constructed from Bloch wave functions $\psi_k^n(x)$ via the prescription:

$$w_j^n(\vec{r}) = \sum_{\vec{k}} e^{-ik\vec{r}_j} \psi_k^n(\vec{r}) \quad (5.9)$$

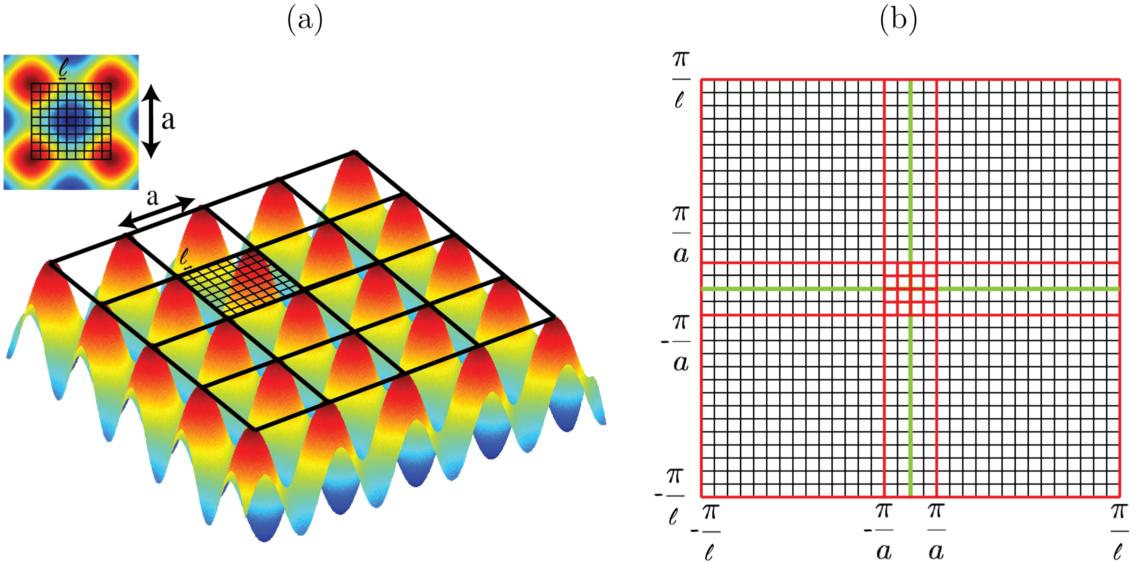

Figure 5.2: Basic idea of coarse graining: Physics occurring at different spatial length scales showed in (a) correspond to momentum length scales showed in (b). Since position and momentum are conjugates, dynamics occurring at small length scales (l) correspond to large momentum ($\frac{\pi}{l}$) behavior. Conversely, dynamics at larger length scales a correspond to small momentum $\frac{\pi}{a}$ behavior. Notice that the essential long wavelength or low momentum properties of the system occurs in the smaller grid (shown in red in (b) that coincides with the first Brillouin zone) and the remaining momentum space accounts for dynamics at larger momenta. By choosing the correct basis, we can essentially integrate out such high momentum phenomenon, while retaining the correct low energy physics.

Here j labels some point in space that can be chosen appropriately. For instance, a very useful choice, is the location of maximal weight of the Wannier function, which should coincide with the minima in the potential within a unit cell. Wannier functions have the extremely useful property of being orthonormal. They are also localized (around a particular point in space) provided the energy bands do not overlap [53]. Using $\{w_j^n(\vec{r})\}$ as a basis it is possible to do a basis transformation of the form $\hat{\psi}(\vec{r}) = \sum_{j,n} w_j^n(\vec{r})\hat{b}_{n,j}$. The second quantized Hamiltonian then becomes:

$$\begin{aligned}\hat{\mathscr{H}} = &- \sum_{n,m,i\neq j} t_{ij}^{nm}\hat{b}^\dagger(n,i)\hat{b}(n,j) + \sum_{n,m,i} \epsilon_i^{nm}\hat{b}^\dagger(n,i)\hat{b}(n,i) \\ &+ \frac{1}{2}\sum_{\substack{n_1,n_2,n_3,n_4,\\ i,j,k,l}} U_{i,j,k,l}^{n_1,n_2,n_3,n_4}\hat{b}^\dagger(n_1,i)\hat{b}^\dagger(n_2,j)\hat{b}(n_3,k)\hat{b}(n_4,l),\end{aligned}$$

which is of the same form as 5.10 but now since the Wannier functions are not eigenstates of the single-particle Hamiltonian we get off-diagonal and diagonal terms characterized by the parameters given by:

$$t_{ij}^{nm} \equiv -\int \bar{w}_i^n(\vec{r})H(\vec{r})w_j^m d^D\vec{r} \tag{5.10}$$

$$\epsilon_i^{nm} \equiv \int \bar{w}_i^n(\vec{r})H(\vec{r})w_i^m d^D\vec{r} \tag{5.11}$$

$$U_{i,j,k,l}^{n_1,n_2,n_3,n_4} \equiv \int\int \bar{w}_i^{n_1}(\vec{r}_1)\bar{w}_j^{n_2}(\vec{r}_1)U(\vec{r}_1-\vec{r}_2)w_k^{n_3}(\vec{r}_1)w_l^{n_4}(\vec{r}_2)d^D\vec{r}_1 d^D\vec{r}_2 \tag{5.12}$$

This result can be further simplified using additional information of the system to be studied. In particular it is possible to eliminate the contribution of a large number of bands. In the case of Fermions, for instance, all bands apart from the conduction and valence band could be eliminated. (More generally for metallic type of behavior, multiple bands could be involved in creating the Fermi surface and as such all such terms would be included. Even more generally, given the specified temperature of interest it is possible to define a window of bands that could potentially contribute to the system being considered.) For Hard-core Bosons, a similar analysis holds since the hard-core nature is similar to the Pauli Exclusion principle.

For Soft-core Bosons, which are of key importance in this dissertation, a single band can accommodate all particles participating in the dynamics of the system. In such cases, the temperature also sets the number of bands involved since large temperatures would permit transitions to higher energy bands. A working approximation is obtainable using the confining property of the lattice potential. Using Taylor expansion, $V(\vec{r}) = V(\vec{r_i}) + \frac{1}{2}\frac{\partial^2 V(\vec{r_i})}{\partial r^2}(\vec{r}-\vec{r_j})^2 + O(r^4)$, where $\vec{r_i}$ is the location of any minima in the system which can be set to zero. This is in the form of a Harmonic oscillator potential so that the energy separation between different energy levels is given by $\sqrt{\frac{\hbar^2}{m}\frac{\partial^2 V(\vec{r_i})}{\partial r^2}}$, which should be a usable for the separation between the lowest ($n = 0$) and the second lowest ($n = 1$) band. Thus, provided $k_B T \ll \sqrt{\frac{\hbar^2}{m}\frac{\partial^2 V(\vec{r_i})}{\partial r^2}}$ it is possible to eliminate all bands $n > 0$. These approximations lead to a single band Hamiltonian that can be written in a hierarchy of terms corresponding to on-site, nearest neighbor $\langle ... \rangle$, next-to-nearest neighbor terms $\langle\langle ... \rangle\rangle$ and so forth:

$$\begin{aligned}\hat{H} = &\left[-\sum_{\langle ij\rangle} t_{ij}\hat{b}_i^\dagger\hat{b}_j + \sum_i \epsilon_i\hat{b}_i^\dagger\hat{b}_i - \sum_{\langle\langle ij\rangle\rangle} t_{ij}\hat{b}_i^\dagger\hat{b}_j + \dots\right] \\ &\left[+\frac{1}{2}\sum_i U_i\hat{n}_i(\hat{n}_i - 1) + \frac{1}{2}\sum_{\langle ij\rangle} U_{ij}\hat{n}_i\hat{n}_j + \dots\right]\end{aligned} \tag{5.13}$$

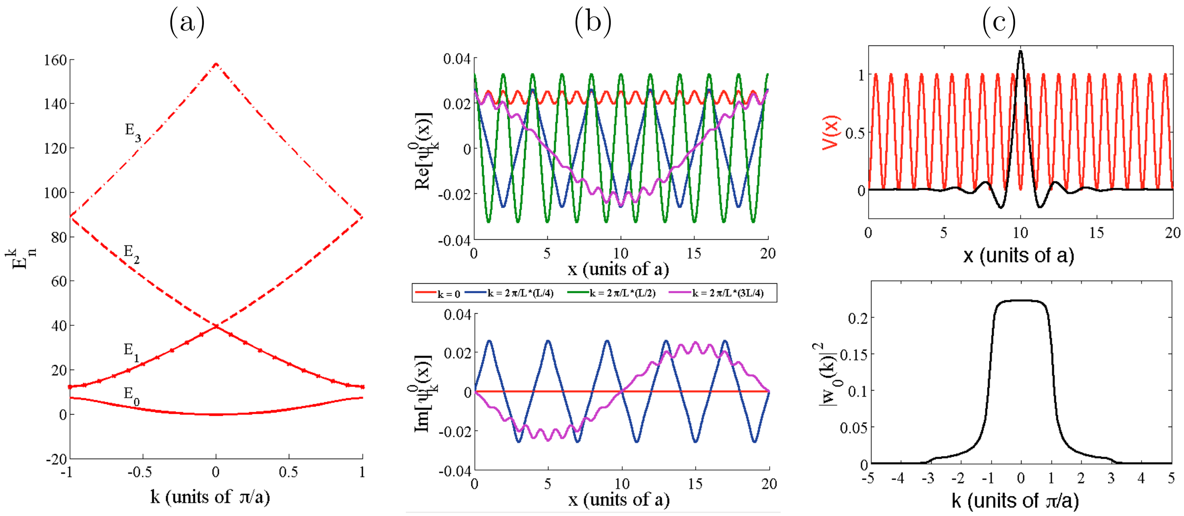

Figure 5.3: (a) Band energies in the reduced scheme where higher order Brillouin zones are mapped back into the first Brillouin Zone. (b) Shows Real (top) and Imaginary (bottom) components of typical Bloch wavefunctions for the lowest energy band (c) Wannier wavefunction constructed from the Bloch wavefunctions centered at site $x = 10$. These images were constructed for a system of 20 sites with L = 20a. The sinusoidal potential strength ($V_0 = 1\ E_R$) in optical lattice experiments is specfied in units of recoil energy $E_R = \frac{\hbar^2\pi^2}{2ma^2}$, where m is the mass of the atom being used and a is the lattice constant set by the wavelength of the of the laser used to create the artificial lattice (See text).

Using the estimated parameters it is possible to quantify the relative strengths of different terms and therefore obtain the coarse-grained Hamiltonian $\hat{H} = \hat{H}_1 + \hat{U}$, as was the intention of this exercise. Note that ignoring higher order bands is the same as coarse graining over all dynamics taking place at length scales smaller than the lattice constant. This means that the coarse grained Hamiltonian is accessing only the first Brillouin zone and dynamics at larger quasi-momentum do not contribute (see fig. 5.2). In the next section, the lattice Hamiltonian for a physical system that will be considered in part III is constructed. It will serve as a concrete example and can be used to benchmark the more general numerical procedure that is needed for disordered systems.

5.4 Low Energy Hamiltonian for Optical Lattice Experiments

Optical lattice experiments construct artificial tunable lattices by loading atoms into a periodic potential created from lasers. Such lattices afford unprecedented control of the parameters of the Hamiltonian. These aspects will be discussed in detail later in part III. For the

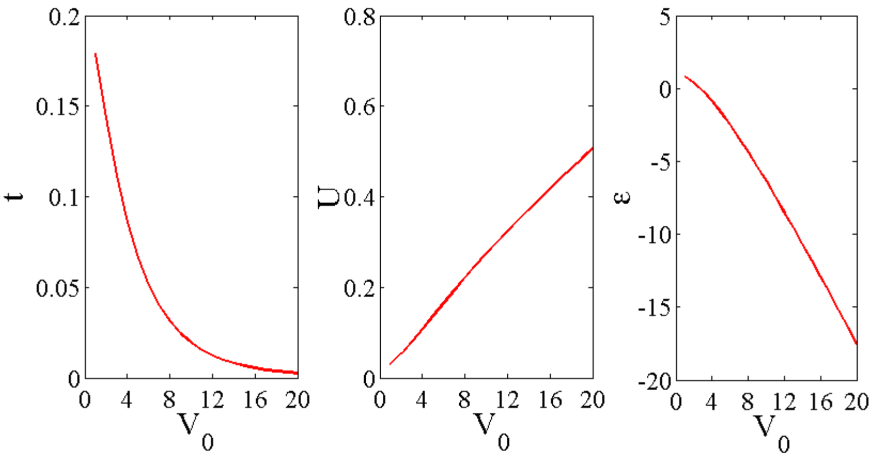

Figure 5.4: Dependence of the nearest neighbor hopping term ($t_{\langle ij\rangle}$), onsite interaction term (U_i) and onsite occupation energy ϵ_i on the strength of the lattice potential (V_0). All units are in atomic recoil energies E_R.

purposes of this discussion the only detail needed from the experiments is the form of the single-particle potential $V(\vec{r}) = V_0 \sum_{\alpha=1}^{D} sin^2(k \cdot x_\alpha)$ with $k = 2\pi/\lambda$. λ is the wavelength of the laser used to setup the optical lattice, with the lattice constant $a \equiv \lambda/2$. The potential is clearly separable so the solution for a $1D$ system can be generalized in a straightforward way to higher dimensions.

Consider then the $1D$ problem only with $V(x) = V_0 sin^2(\pi x/a)$. The Fourier transform of $V(x)$ is given by:

$$\begin{aligned}
\tilde{V}(q_n) &= \frac{1}{L}\int_0^L V_0 sin^2(\pi x/a) e^{-iq_n x} dx \\
&= \frac{1}{L}\int_0^L e^{-iq_n x}\frac{V_0}{2}\left(1 - \frac{e^{i\frac{2\pi x}{a}} - e^{-i\frac{2\pi x}{a}}}{2}\right) dx \\
&= \frac{1}{L}\int_0^L e^{-iq_n x}\frac{V_0}{2}\left(1 - \frac{e^{i\frac{2\pi x}{a}} - e^{-i\frac{2\pi x}{a}}}{2}\right) dx \\
&= \frac{V_0}{2L}\int_0^L e^{-iq_n x} dx - \frac{V_0}{4L}\int_0^L e^{-i(q_n - \frac{2\pi}{a})x} dx - \frac{V_0}{4L}\int_0^L e^{-i(q_n + \frac{2\pi}{a})x} dx \qquad (5.14)
\end{aligned}$$

Since $q_n = \frac{2\pi n}{a}$, we get:

$$\tilde{V}(q_n) = \frac{V_0}{2}\delta_{n0} - \frac{V_0}{4}\delta_{n1} - \frac{V_0}{4}\delta_{n2} \qquad (5.15)$$

Thus the eigenvalue problem 5.7 reduces to a simple tridiagonal matrix:

$$\begin{bmatrix} \ddots & & & & \\ -\frac{V_0}{4} & \left[\frac{\hbar^2(k+q_{-1})^2}{2m}+\frac{V_0}{2}\right] & -\frac{V_0}{4} & & \\ & -\frac{V_0}{4} & \left[\frac{\hbar^2(k+q_0)^2}{2m}+\frac{V_0}{2}\right] & -\frac{V_0}{4} & \\ & & -\frac{V_0}{4} & \left[\frac{\hbar^2(k+q_1)^2}{2m}+\frac{V_0}{2}\right] & -\frac{V_0}{4} \\ & & & & \ddots \end{bmatrix} \begin{bmatrix} \vdots \\ \tilde{u}_{-2}(k) \\ \tilde{u}_{-1}(k) \\ \tilde{u}_0(k) \\ \tilde{u}_1(k) \\ \tilde{u}_2(k) \\ \vdots \end{bmatrix}$$

$$= E_k \begin{bmatrix} \vdots \\ \tilde{u}_{-2}(k) \\ \tilde{u}_{-1}(k) \\ \tilde{u}_0(k) \\ \tilde{u}_1(k) \\ \tilde{u}_2(k) \\ \vdots \end{bmatrix}, \quad (5.16)$$

which can be solved easily on the computer using a truncated series for q_n, i,e, $q_n \in [-M\pi/a, M\pi/a]$ for some large M. Additionally invoking periodic boundary conditions for the lattice of size L, since $\psi^k(L) = \psi^k(0)$ we get quantized values for $k = \frac{2\pi m}{L}$, with $m \in \mathbb{Z}$ restricted to the first Brillouin Zone; as noted earlier higher quasi-momenta are redundant in the single band model. Examples of typical Bloch wavefunctions, energy bands and resulting Wannier functions are shown in fig. (5.3). The parameter values for onsite and nearest neighbor terms of the effective Hamiltonian is shown in fig. (5.4). The onsite energy term U is calculated using a contact form of interaction,

$$U(\vec{r} - \vec{r'}) = \frac{4\pi\hbar^2 a_s}{m}\delta(\vec{r} - \vec{r'}), \quad (5.17)$$

where m is the mass of the species of atoms involved and a_s is the scattering length. The physical justification for this form of interaction potential will be given in part III.

As noted earlier, using the Wannier construction it is straightforward to test the limits of coarse-graining approximations and to ascertain regimes of validity. For instance, by computing the minimum difference between the first and second band energies it is possible to ascertain the validity of the single band approximation and temperature ranges for which such approximations are valid. Additionally, using the spatial overlap between wannier

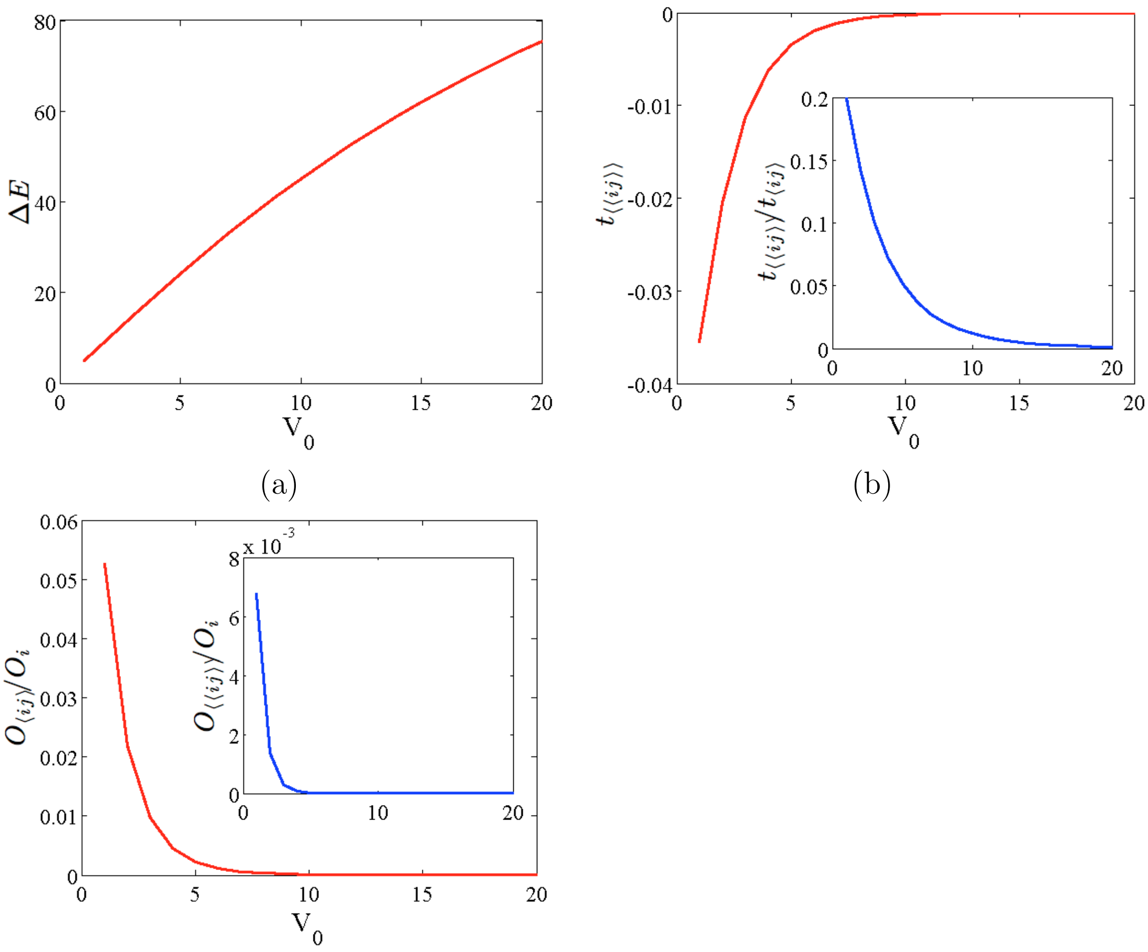

(a)

(b)

(c)

Figure 5.5: a) The energy gap between the first and second bands as a function of the lattice potential depth. b) Dependence of next-to-nearest neighbor off-diagonal hopping term on the strength of the lattice potential. The inset shows the weight of the next-to-nearest neighbor term relative to the nearest neighbor term $t_{\langle\langle ij\rangle\rangle}/t_{\langle ij\rangle}$. It is clear that in general the nearest neighbor term is much larger than the next-to-nearest term and safely ignorable for large values of V_0. Typically for studies done in the tight binding limit $V_0 \geq 4$. c) Spatial overlap of the probability densities of the Wannier states between nearest neighbors and next-to-nearest neighbors (inset) relative to the onsite overlap. It is clear that diagonal terms in the coarse grained Hamiltonian are not influenced by nearest neighbor terms.

functions on sites i and j given by $O_{ij} \equiv \int dx|\psi_i(x)|^2|\psi_j(x)|^2$ it is possible to ascertain how many diagonal terms must be included in the hierarchy of terms describing the coarse-grained Hamiltonian. For off-diagonal terms, t_{ij} itself is a good indicator and comparing the relative weights it is possible to ascertain the validity of the nearest neighbor approximation. Fig. (5.5) shows the dependence of these measures for the sinusoidal potential. Therefore, using information about the nature of the underlying single-particle potential it was possible to use an indirect coarse-graining procedure that allowed the continuum many-body Hamiltonian to be transformed into an effective low energy lattice Hamiltonian.

5.5 Generalized Coarse-Graining Procedure

In earlier sections, the coarse graining procedure has been defined as a way to transform the continuum Hamiltonian to a discrete Hamiltonian using a new basis indexed by discrete numbers (obtained from the quantum numbers of the single-particle Hamiltonian) and then eliminating terms that have small relative parameters. This was crucially made possible by the fact that there were bands in the system separated by energy gaps. This property allows the generalization of the coarse-graining procedure to systems where Bloch's theorem may not hold. Below, following the method outlined in [51], a general prescription for constructing generalized Wannier functions even in non-periodic systems is shown. This method fundamentally uses the criteria that the one-body RDM of the continuum Hamiltonian must be equal to the corresponding coarse grained lattice Hamiltonian so that all low energy physics of the continuum is retained.

The one-body RDM in the continuum, $\hat{\rho}_1$ is given by,

$$\hat{\rho}_1(\tau) = \hat{\psi}^\dagger(\vec{r})\langle\vec{r}|e^{-\tau\mathscr{H}_1}|\vec{r'}\rangle\hat{\psi}(\vec{r'}), \tag{5.18}$$

where τ is some temperature or imaginary time. Consider an initial set of vectors $\{w_i(\vec{r};\tau = 0)\}$ that are orthonormal and localized around the minima of the underlying potential indexed by i. This vector can be used to construct the basis $\psi(\vec{r}) = \sum_i w_i(\vec{r};0)\hat{b}_i$, which can be used to transform 5.19 as:

$$\hat{\rho}_1(\tau) = \sum_{ij} \hat{b}_i^\dagger \left[w_i^*(\vec{r};0)\langle\vec{r}|e^{-\tau\mathscr{H}_1}|\vec{r'}\rangle w_j(\vec{r'};0)\right]\hat{b}_j \tag{5.19}$$

Assuming that the single-particle properties of interest is only over the localization length scales set by an unit cell, it is possible to integrate over all smaller length scales in $\hat{\rho}_1$ to get $\hat{S}$ given by:

$$\hat{S}(\tau) = \sum_{ij} \hat{b}_i^\dagger \left[\int\int d^D\vec{r}d^D\vec{r'}w_i^*(\vec{r};0)\langle\vec{r}|e^{-\tau\hat{\mathscr{H}}_1}|\vec{r'}\rangle w_j(\vec{r'};0)\right]\hat{b}_j \equiv \sum_{ij}\hat{b}_i^\dagger S_{ij}(\tau)\hat{b}_j, \tag{5.20}$$

where

$$S_{ij}(\tau) = \int \int d^D\vec{r} d^D\vec{r'} w_i^*(\vec{r};0)\langle\vec{r}|e^{-\tau\hat{\mathscr{H}}_1}|\vec{r'}\rangle w_j(\vec{r'};0) \equiv \langle w_i(0)|e^{-\tau\hat{\mathscr{H}}_1}|w_j(0)\rangle. \tag{5.21}$$

The objective is to find the low temperature or large τ coarse-grained Hamiltonian $\hat{h}$ that produces this 1-RDM, i.e., find the $\hat{h}$ that satisfies:

$$\hat{S}(\tau) = e^{-\tau\hat{h}}. \tag{5.22}$$

The formal solution $\hat{h} = -\tau^{-1} ln[\hat{S}(\tau)]$ is not guaranteed to preserve the convenient localized basis structure. Instead, an alternative method exists that follows the idea of Löwdin orthonormalization to produce a maximally localized single-particle basis. Taking a derivative of $\hat{S}(\tau)$ with respect to τ:

$$\begin{aligned} \frac{d\hat{S}(\tau)}{d\tau} &= lt_{M\to\infty} \sum_{i=1}^{M} e^{-\frac{\tau i}{M}\hat{h}} \frac{d}{d\tau}\left(e^{-\frac{\tau\hat{h}}{M}}\right) e^{-\frac{\tau}{M}(M-i-1)\hat{h}} \Delta i \\ &= lt_{M\to\infty} \sum_{i=1}^{M} e^{-\frac{\tau i}{M}\hat{h}} \frac{\Delta i}{M} \left(-\hat{h} - \tau\frac{d\hat{h}}{d\tau}\right) e^{-\frac{\tau}{M}(M-i)\hat{h}}. \end{aligned} \tag{5.23}$$

Let $\lambda = \frac{\tau i}{M}$ so that $\Delta\lambda = \frac{\tau\Delta i}{M}$. Using the $lt_{M\to\infty}\frac{\tau\Delta i}{M} = d\lambda$, the transformation becomes:

$$\begin{aligned} \frac{d\hat{S}(\tau)}{d\tau} &= -\int_0^\tau \frac{d\lambda}{\tau} e^{-\lambda\hat{h}} \hat{h} e^{-(\tau-\lambda)\hat{h}} - \int_0^\tau d\lambda e^{-\lambda\hat{h}} \frac{d\hat{h}}{d\lambda} e^{-(\tau-\lambda)\hat{h}} \\ &= -\hat{h}e^{-\tau\hat{h}} - \int_0^\tau d\lambda e^{-\lambda\hat{h}} \frac{d\hat{h}}{d\lambda} e^{-(\tau-\lambda)\hat{h}}. \end{aligned} \tag{5.24}$$

Applying $S^{-\frac{1}{2}}(\tau)$ on both sides, the final form is

$$\hat{S}^{-\frac{1}{2}} \frac{d\hat{S}(\tau)}{d\tau} \hat{S}^{-\frac{1}{2}} = -\hat{h} - \int_0^\tau d\lambda e^{(\frac{\tau}{2}-\lambda)\hat{h}} \frac{d\hat{h}}{d\lambda} e^{(\lambda-\frac{\tau}{2})\hat{h}}. \tag{5.25}$$

If in the limit of large $\tau \to \infty$, $\hat{h}$ is independent of imaginary time then the second term in the relation above can be ignored so that:

$$\hat{h} = -\hat{S}^{-\frac{1}{2}} \frac{d\hat{S}(\tau)}{d\tau} \hat{S}^{-\frac{1}{2}} \tag{5.26}$$

Utilizing 5.21

$$\begin{aligned}\frac{dS_{ij}(\tau)}{d\tau} &= -\langle w_i(0)|\hat{\mathscr{H}}_1 e^{-\tau\hat{\mathscr{H}}_1}|w_j(0)\rangle = -\langle w_i(0)|e^{-\frac{\tau}{2}\hat{\mathscr{H}}_1}\hat{\mathscr{H}}_1 e^{-\frac{\tau}{2}\hat{\mathscr{H}}_1}|w_j(0)\rangle \\ &= -\langle w_i(\tau/2)|\hat{\mathscr{H}}_1|w_j(\tau/2)\rangle \end{aligned} \tag{5.27}$$

and the element of the coarse-grained 1-body Hamiltonian is given by:

$$\begin{aligned} h_{ij} &= \sum_{kl}(\hat{S}^{-\frac{1}{2}})_{ik}\langle w_k(\tau/2)|\hat{\mathscr{H}}_1|w_l(\tau/2)\rangle(\hat{S}^{-\frac{1}{2}})_{lj} \\ &= \langle \tilde{w}_i(\tau/2)|\hat{\mathscr{H}}_1|\tilde{w}_j(\tau/2)\rangle \end{aligned} \tag{5.28}$$

using $|\tilde{w}(\tau/2)\rangle = \hat{S}^{-\frac{1}{2}}|w(\tau/2)\rangle$. Note that since $\hat{S}_{ij} = \langle w_i(\tau/2)|w_j(\tau/2)\rangle$, it guarantees via the Löwdin orthonormalization that $|\tilde{w}(\tau/2)\rangle$ are orthonormalized basis functions.

The physical essence of this procedure is best understood by considering the imaginary time evolution of the initial Wannier state. Essentially, due to the projection by the density matrix, the initial state aligns towards the direction of the contributing eigenvalues of the Hamiltonian (much like the discussion of Krylov subspaces in the earlier chapter). The point is to project long enough that contribution from all higher order bands gets removed, but not so long that the state becomes completely delocalized. In a system where a gap is present for large enough τ, all states above the gap are eliminated and only states below it survive [51]. Further propagation will project the state along the lowest energy of the band and the diffusion will proceed very slowly. By all accounts the state is virtually temperature independent at this stage. For the purposes of the coarse-graining construction this is an ideal local to stop further projection and proceed with the localization scheme via construction of the overlap matrix $\hat{S}$ followed by the orthonormalization. From an implementation point of view the projection scheme is straightforward:

$$\begin{aligned} |w_i(\beta)\rangle &= e^{\beta\hat{\mathscr{H}}_1}|w_i(0)\rangle \\ &= \left[e^{-\frac{\beta}{n}\hat{\mathscr{H}}_1}\right]^n |w_i(0)\rangle \\ &= \left[e^{-t\hat{\mathscr{H}}_1}\right]^{n-1}\left[e^{-t\hat{\mathscr{H}}_1}\right]|w_i(0)\rangle, \end{aligned}$$

where $t \equiv \frac{\beta}{n}$ so that the projection can be done by successively applying the projector one step at a time. So each step is given by:

$$\begin{aligned}|w_i(\tau+t)\rangle &= e^{-t\hat{\mathscr{H}}_1}|w_i(\tau)\rangle = e^{-t(\hat{\mathscr{T}}_1+\hat{\mathscr{V}}_1)}|w_i(\tau)\rangle \\ &\sim e^{-t\hat{\mathscr{T}}_1}e^{-t\hat{\mathscr{V}}_1}e^{-\frac{t^2}{2}[\hat{\mathscr{T}}_1,\hat{\mathscr{V}}_1]}|w_i(\tau)\rangle \\ &\sim e^{-t\hat{\mathscr{T}}_1}e^{-t\hat{\mathscr{V}}_1}|w_i(\tau)\rangle.\end{aligned}$$

Here $\hat{\mathscr{T}}_1$ is the single-particle kinetic energy and $\hat{\mathscr{V}}_1$ is the single-particle potential due to the underlying lattice. Also the splitting of the exponential operator is done by utilizing the Baker-Campbell-Hausdorff formula. For small enough t, terms of the order $O(t^2)$ can be ignored. Projecting to a specific basis $|\vec{r}\rangle$, the Wannier function is given by:

$$\begin{aligned}\langle\vec{r}|w_i(\tau+t)\rangle &= \langle\vec{r}|e^{-t\hat{\mathscr{T}}_1}e^{-t\hat{\mathscr{V}}_1}|w_i(\tau)\rangle \\ &= \int d^D\vec{k}\langle\vec{r}|e^{-t\hat{\mathscr{T}}_1}|\vec{k}\rangle\langle\vec{k}|\int d^D\vec{r'}e^{-t\hat{\mathscr{V}}_1}|\vec{r'}\rangle\langle\vec{r'}|w_i(\tau)\rangle \\ &= \int d^D\vec{k}\langle\vec{r}|\vec{k}\rangle e^{-t\frac{\hbar^2\vec{k}^2}{2m}}\int d^D\vec{r'}\langle\vec{k}|\vec{r'}\rangle e^{-t\mathscr{V}_1(\vec{r'})}\langle\vec{r'}|w_i(\tau)\rangle \\ w_i(\vec{r},\tau+t) &= \int d^D\vec{k}e^{-i\vec{k}\cdot\vec{r}}e^{-t\frac{\hbar^2\vec{k}^2}{2m}}\int d^D\vec{r'}e^{i\vec{k}\cdot\vec{r'}}e^{-t\mathscr{V}_1(\vec{r'})}w_i(\vec{r'},\tau) \\ &= \mathcal{F}\left[e^{-t\frac{\hbar^2\vec{k}^2}{2m}}\mathcal{F}^{-1}\left[e^{-t\mathscr{V}_1(\vec{r'})}w_i(\vec{r'},\tau)\right](\vec{k})\right](\vec{r}), \qquad (5.29)\end{aligned}$$

where $\mathcal{F}[\ldots](\vec{r})$ indicates the Fourier transformation operator and $\mathcal{F}^{-1}[\ldots](\vec{k})$ indicates the Inverse-Fourier transformation operator. Note that the Fourier transforms can be accomplished using the FFT algorithm that is very fast (∼O(NlogN)). Following the necessary convergence, the overlap matrix $\hat{S}$ can be easily constructed. The most computationally intensive step is the calculation of $\hat{S}^{-\frac{1}{2}}$ that would normally require some form of diagonalization routine (Householder Transformations, Singular Value Decompositon etc.). After this the orthonormal basis can be readily calculated via:

$$|\tilde{w}_i\rangle = \sum_j(\hat{S}^{-\frac{1}{2}})_{ij}|w_j\rangle \qquad (5.30)$$

Following the calculations of the Wannier functions, 5.12 can be used to calculate all the necessary parameters. Additionally overlap parameters can be used, as discussed earlier, to analyze how many terms are needed to be included to construct the coarse-grained Hamiltonian.

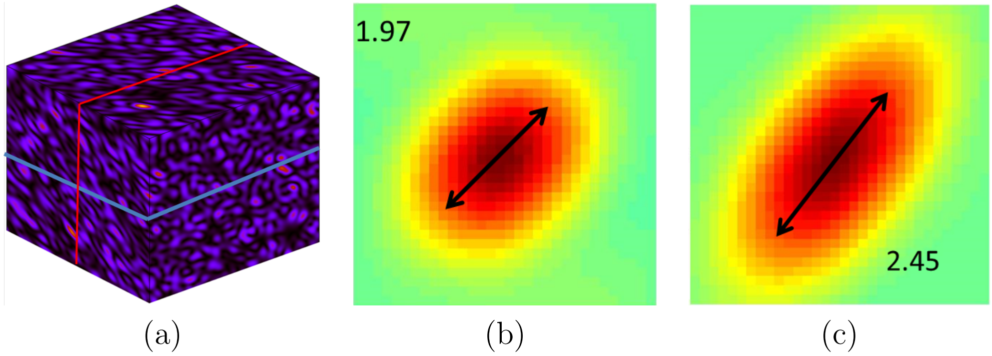

(a) (b) (c)

Figure 5.6: (a) Typical speckle field for generating Hubbard parameters of size 460^3 $(18.4\mu m)^3$ (b) Speckle auto-correlation width for the slice in blue on the x-y plane (c) Slice in red on the y-z plane.

5.6 Coarse-Graining Disordered Potentials from Speckle Fields

This section discusses the specific implementation of the algorithm used to coarse-grain the disordered optical lattice used in experiments. The underlying potential is well approximated by the sinusoidal potential considered earlier in section 5.4:

$$V(\vec{r}) = V_0 \left[sin^2\left(\frac{\pi}{a}x\right) + sin^2\left(\frac{\pi}{a}y\right) + sin^2\left(\frac{\pi}{a}z\right) \right] \tag{5.31}$$

where a sets the lattice constant, and V_0 is the depth of the potential. Additionally, the disorder potential due to the speckle potential is given by:

$$V_d(r) = \Delta \times \left| \mathcal{F}\left[\Theta(d^2 - q_x^2 - q_y^2) \times exp\left\{ -\frac{q_x^2 + q_y^2}{w^2} + i(\gamma z(q_x^2 + q_y^2) + \phi(q_x, q_y) \right\} \right] \right|^2$$

where Δ is the strength of the disorder potential, $\mathcal{F}$ is the Fourier transform in 2d space (q_x, q_y), d is the radius of the aperture, w is the width of the Gaussian beam used to generate the field, γ is its radius of curvature and $\phi(q_x, q_y)$ is an uncorrelated random phase uniformly distributed in $[0, 2\pi)$ [51, 56]. In experiments, the speckle field is rotated such that the z axis above is pointed along $\frac{1}{2}n_1 + \frac{1}{2}n_2 + \frac{1}{\sqrt{2}}n_3$ of the optical lattice. This introduces an anisotropy in the disorder-field such that the disorder grain size is larger along the z direction compared to the x or y directions (see fig. 5.6 where $d = 0.66\pi/a$, $w = 2.16\pi/a$ and $\gamma = 0.1a$ with a being the lattice spacing). Typically, the disorder grain size is slightly more than a single site, i.e., the speckle field introduces a finely grained disorder. Once the potential is setup the algorithm discussed earlier can be used to generate the Hamiltonian parameters. An example of the Wannier functions after propagation in imaginary time followed by orthonormalization is showed in fig. (5.7).

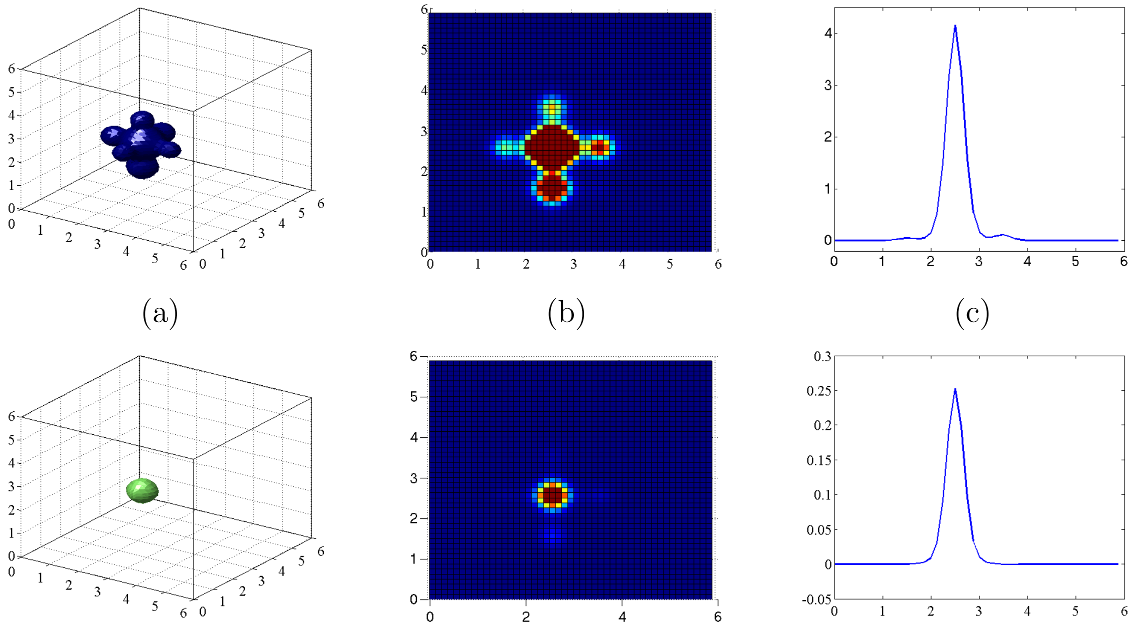

(a) (b) (c)

(d) (e) (f)

Figure 5.7: Illustration of Coarse-Graining Procedure. (a)-(c) are 3d, 2d, 1d images for unorthonormalized Wannier functions generated for site (2,2,2) using the algorithm discussed in the text. Following the imaginary time propagation, Löwdin orthonormalization is performed to restore the localization properties. The resulting functions are shown in (d)-(f). A basis is constructed using these orthonormalized functions. These images correspond to a system of 6^3 lattice points constructed from the continuum meshed using 8^3 points. The lattice depth is set to $V_0 = 14\ E_R$, with disorder strength of $\Delta = 1\ E_R$.

Results for small systems are straightforward to calculate and can be found in [51]. It turns out that the coarse-grained Hamiltonian resulting from the optical speckle potential together with speckle disorder can be written adequately in terms of nearest-neighbor hopping terms and on-site terms. Further terms such as next-to-nearest neighbor hopping or nearest-neighbor inter-particle (diagonal) interaction terms are not needed. So the Hamiltonian preserves the basic structure of the underlying clean Hamiltonian. The new model has disorder in tunneling terms, onsite occupation energy terms and the interaction term. The standard deviation of the these distributions is related to Δ. Extensive tests have shown that the $\sigma(\epsilon) \sim 0.95\Delta$, $\sigma(t_{\langle ij\rangle}) \sim (-0.00095V_0 + 0.02204)\Delta$ and $\sigma(U_i) \sim 0$ valid for $\Delta <\sim 1.2$ E_R.

If disorder strength increases too much (experience has shown the following discussion to apply when $\Delta \geq 1.5\ E_R$) then it is easy to imagine a situation when the occupation energy of the second lowest level or band on a site becomes comparable to the lowest energy level of an adjacent site. In such cases higher order bands must be included in the Hamiltonian. Consequently, the projection method discussed above that projects out all but the lowest band from the Wannier function will not be adequate. In such cases sites will need more than one basis function. Physically this happens when the energy bands start overlapping and the gap between the bands shrink. Computationally, one finds that in such situations the orthonormalization process becomes unstable and produces unphysical answers. Experience has shown that the overlap matrix becomes singular and the inverse-square root needed to perform orthonormalization becomes unusable. In any event such multi-band models will not be considered in this dissertation, since it signals the break down of the lattice picture itself. The intermediate region $1.2 < \Delta < 1.5\ E_R$ exhibits anomalies locally – some Wannier functions may not be completely orthonormal and the nearest-neighbor hopping term (t) can becomes negative. Usually there are only a small fraction of such sites $< 1 - 6\%$ (depending on V_0 and Δ). It is possible to absorb them by ignoring the sign, since the t values are not actually physical. This procedure regularizes the terms of the lattice, but in an ad hoc way.[2]

5.6.1 Coarse-Graining Strategies for Large Systems

The main motivation to extend the parameter generation to large system is to be able to reproduce the low energy Hamiltonian corresponding to experiments as closely as possible. This is important, because it is useful to know what aspects of the disorder potential play a role in the properties of the system. Most theoretical studies to date, consider only disorder in the on-site energy term (ϵ_i) that is uniformly distributed in the interval $[-\Delta, \Delta]$ (called Box disorder) [57, 58, 59]. However, there is no *a priori* reason to expect this to correspond to real potentials. In fact, in the case of real systems, disorder in the underlying potential will distort the wave function that should affect all parameters in the coarse grained Hamiltonian, i.e., there should be disorder in both the hopping terms as well as the on-site interaction energy terms. The elimination of such terms can proceed only after it has been established that the disorder in them is indeed small – otherwise the assumptions are ad hoc. Additionally, to what extent a single band lattice Hamiltonian is valid (in the sense that it faithfully represents a coarse-grained continuum Hamiltonian) in the presence of strong disorder is questionable. The region of validity of such models in so far as they capture real physical systems should be checked. In any event, for the speckle field used in experiments, the properties of the phase diagram do not correspond to the Box type of dis-

---

[2] Whenever such a process is used for actual data, it will be explicitly stated.

order and systematic comparisons become difficult. The only way around this problem is to generate the parameters on the large scale so that all distribution properties are maintained. In this way no *ad hoc* assumptions need to be made.

For comparisons with experiments, however, generally the required lattice size is between 40^3 to 60^3. Using a modest meshing size of 8^3 around each lattice point, the full continuum Hamiltonian is encoded in 320^3 to 480^3 system. This is not a huge problem, but if each wave function has to be stored over this entire space then total size is as large as $60^3 \times 480^3$. Additionally the calculation of the overlap matrix is itself problematic. Naively if all elements need to be computed then the size of the system quickly becomes intractable (60^6 elements in the matrix). These problems can be circumvented using physical insights into the problem at hand together with parallelization strategies that exploit the shared and distributed framework of modern computing. The parallel algorithm is executed in stages since the distribution and threading strategies are not uniform throughout the calculations. The stages are summarized below:

- **Wannier Function Calculations:** An important feature of the imaginary time evolution procedure is that if the starting wavefunction centered around a particular lattice site ($|w_i(0)\rangle$) is localized then the projection with finite times (such that all high order contributions are removed but not the lowest band) will not lead to a delocalized state that extends over the entire system. An example is shown in fig. (5.7a-c). Since the projected wavefunction does not extend beyond a few sites all calculations can be done using smaller cells. The wavefunction is safely assumed to be zero outside such cells. In-fact, the size of the cell can be dynamically controlled - expanded or contracted as needed based on how much the of the wavefunction grows. This variable sized mashing strategy for the cells greatly reduces the memory requirements. (For example, if only 6^3 sites are used for every cell then for a 60^3 system, the memory requirement is reduced by 1000 times.) Additionally, the time evolution of each wavefunction centered around a site proceeds independently of all other sites. Therefore, the entire process can be parallelized (via a distributed memory scheme or a shared memory scheme). After the expansion the wave functions do not need to be kept in primary memory so they can stored in secondary memory with appropriate indexing so that they can be recalled on demand.

- **Overlap Matrix Computation:** The next step is the calculation of the overlap matrix given by the elements S_{ij}. Once again not all elements need to be calculated since the projected wavefunction is not extended throughout the system. Only a limited

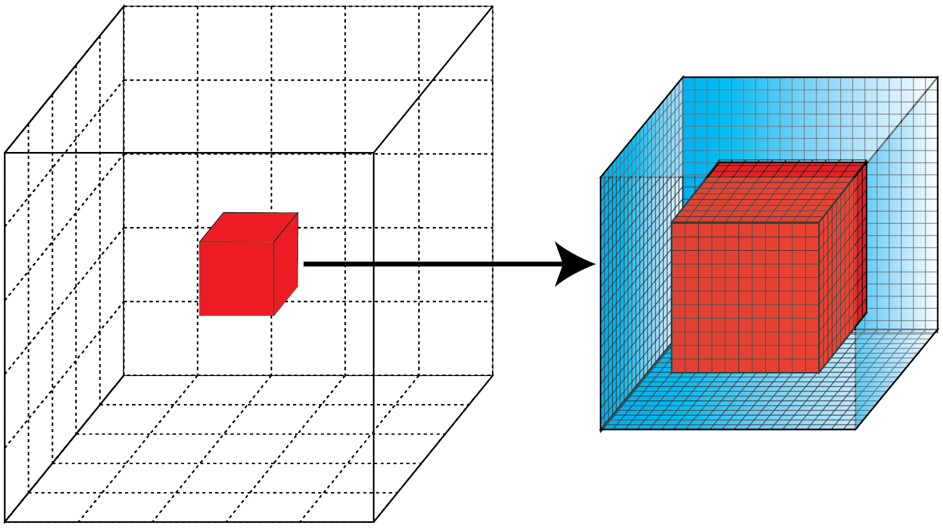

Figure 5.8: Distributed Overlap Calculation: The full system is broken up into cells, an example of which is shown in red. Each cell is assigned to a node (left image). Each node then calculates elements of S_{ij} by computing the overlap between wannier functions located on sites i (in the red cell) with other sites and j. Since all sites are not needed, only a cube of sites (shown in blue) are loaded.

number of elements need to be calculated and stored. This calculation can also be parallelized. The distributed strategy is to divide the system into cells and distribute them over the different nodes. Each node then loads all sites within the cell and all other sites needed to compute the local elements of the overlap matrix. The last requirement is based on the fact that sites on the surface of the cell and some inner sites (constituting a shell of finite thickness) requires sites outside of the cell. The box of sites that needs to be loaded is larger than the cell of sites for which computations need to done. These ideas are illustrated in fig. (5.8). At the end of the computation, the nodes synchronize so that the full matrix is written to secondary memory.

- **Inverse Square Root of Overlap Matrix:** This is the most computationally intensive step and requires a new approach other than standard Singular Value Decomposition (SVD) or ED method of calculating eigenvalues. Large-scale diagonalization techniques (such as Arnoldi Iteration etc.) are impossible in this case also since all eigenvalues are needed to perform the necessary calculation. Fortunately, an alternative strategy exists using iterative schemes. However, simple strategies like the one outlined in [51] does not work because of stability issues. A more sophisticated stable iteration is given by Ianazzo iteration based on the Newton Iteration method [60].

Given the requirement $\hat{X}^2 = \hat{A}$, let $\hat{Y}$ be an approximate solution with $\hat{Y} + \hat{\epsilon} = \hat{X}$, $\hat{\epsilon}$

will be determined, then $\hat{A} = (\hat{Y} + \hat{\epsilon})^2 = \hat{Y}^2 + \hat{Y}\hat{\epsilon} + \hat{\epsilon}\hat{Y} + \hat{\epsilon}^2$. Dropping higher order error terms $\hat{\epsilon}^2$, the Newton iteration leads to:

$$\begin{aligned} \hat{X}_k\hat{\epsilon}_k + \hat{\epsilon}_k\hat{X}_k &= A - \hat{X}_k^2 \\ \hat{X}_{k+1} &= \hat{X}_k + \hat{\epsilon}_k \end{aligned} \tag{5.32}$$

A theorem guaranteeing $[\hat{X}_k, \hat{A}] = 0$ provided $[\hat{X}_0, \hat{A}] = 0$, allows a simplification of this equation to the form below with $\hat{X}_0 = \hat{A}$ [60]:

$$\hat{X}_{k+1} = \frac{1}{2}(\hat{X}_k + \hat{X}_k^{-1}\hat{A}) \tag{5.33}$$

Another theorem states that provided $\hat{A}^{\frac{1}{2}}$ does not have pure imaginary eigenvalues, X_k converges quadratically to $\hat{A}^{\frac{1}{2}}$ [60]. There are many theoretical aspects to this computation, but is beyond the scope of this work. However, [60] has an exhaustive and excellent discussion. Using 5.32 and 5.33:

$$\begin{aligned} \hat{\epsilon}_{k+1} &= \frac{1}{2}(\hat{X}_{k+1}^{-1}\hat{A} - \hat{X}_{k+1}) \\ &= \frac{1}{2}\hat{X}_{k+1}^{-1}(\hat{A} - \hat{X}_{k+1}^2) \\ &= \frac{1}{2}\hat{X}_{k+1}^{-1}(\hat{A} - \frac{1}{4}(\hat{X}_k + \hat{X}_k^{-}1\hat{A})^2) \\ &= \frac{1}{2}\hat{X}_{k+1}^{-1}(\frac{2\hat{A} - \hat{X}_k^2 - \hat{X}_k^{-2}\hat{A}^2}{4}) \\ &= -\frac{1}{2}\frac{(\hat{X}_k - \hat{X}_k^{-1}\hat{A})^2}{4} \\ &= -\frac{1}{2}\hat{X}_{k+1}^{-1}\hat{\epsilon}_k^2 = -\frac{1}{2}\hat{\epsilon}_k\hat{X}_{k+1}^{-1}\hat{\epsilon}_k \end{aligned} \tag{5.34}$$

Finally Ianazzo iteration is obtained using $\hat{X}_0 = \hat{A}$ and $\hat{\epsilon}_0 = \frac{1}{2}(\hat{I} - \hat{A})$, with successive iterations given by:

$$\begin{aligned} \hat{X}_{k+1} &= \hat{X}_k + \hat{\epsilon}_k \\ \hat{\epsilon}_{k+1} &= -\frac{1}{2}\hat{\epsilon}_k\hat{X}_{k+1}^{-1}\hat{\epsilon}_k \end{aligned} \tag{5.35}$$

This of-course requires a large scale matrix inversion algorithm. A fast algorithm to compute $\hat{A}^{-1}$ is outlined below using for initial conditions $\hat{X}_0 = \frac{1}{||\hat{A}||_1^2}\hat{A}^T$:

$$\hat{X}_{k+1} = \hat{X}_k(2\hat{I} - \hat{X}_k\hat{A}) \tag{5.36}$$

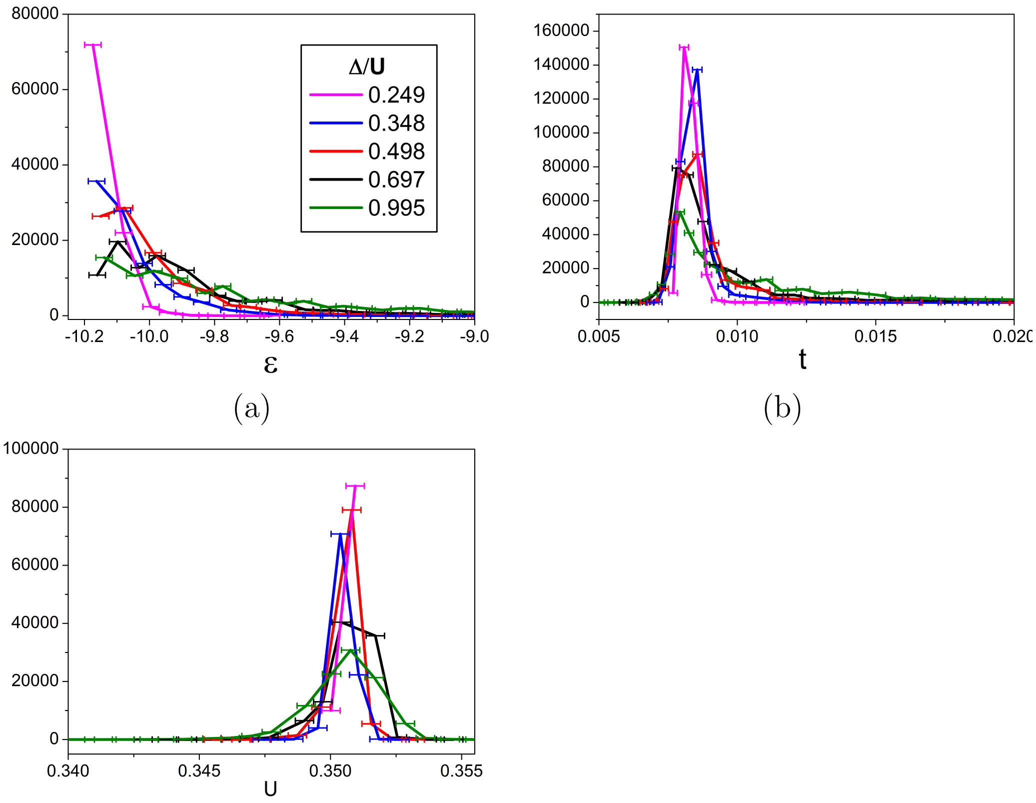

(a) (b)

(c)

Figure 5.9: Distributions of the on-site energy (ε), hopping (t) and interaction (U) terms for a 46^3 lattice at various disorder strengths (Δ). The standard deviation of the distributions are given by $\sigma(\varepsilon) = 0.95\Delta$, $\sigma(t) = 0.0088\Delta$ and $\sigma(U) = 0.0047\Delta$.

The iteration procedure that is composed of basic matrix operations is particularly amenable to parallelization strategies. Also while $\hat{S}$ starts out as a clustered somewhat sparse matrix, experience has shown that over the course of the iterations discussed above that intermediate matrices can become very dense. This is especially true when disorder is large. The distributed procedure breaks up all the matrices row-wise among nodes. All subsequent matrix operations can be performed following appropriate distributions of elements over the nodes – needed only for multiplication, since additions or subtractions happen independent of other and can happen locally. Norm estimates needed to check convergence can perform calculations locally and sent to the master node to accumulate and compute the full norm of the matrix. The convergence criteria for the square root is given by $||\hat{\epsilon}_k||_F$.

- **Orthonormalization of Wannier Functions:** Once the inverse square root is calculated, the orthonormalization is straightforward using $|\tilde{w}_i\rangle \equiv \sum_j (\hat{S}^{-\frac{1}{2}})_{ij} |w_i\rangle$. For a collection of sites $\{i\}$ defined within a cell all sites $\{j\}$ in the extended space can be loaded just as was done for calculating the overlap matrix.

- **Coarse Grainined Parameters:** The final coarse grained parameters requires the computation of the kinetic energy term that requires second order derivatives. These can be done using finite size central differencing schemes. Once again all terms are calculated by distributing across nodes as was done in the computation of the Wannier functions, overlap matrix and orthonormalization.

At the end of this method, coarse grained parameters for large systems can be calculated. An example of the distributions of the different terms in the lattice Hamiltonian is shown in fig. (5.9). One major advantage of this method is that it doesn't fail outright even when the disorder is too large and the gap between bands is closed. In such cases, ED methods cannot compute the inverse square root of the overlap matrix. On the other hand the iterative procedure can compute most terms accurately while failing locally where bands get crossed. This translates to a failure of orthonormality and negative hopping terms that need to be fixed by hand.

Part III

Applications

The focus of this part is on the disordered Bose-Hubbard Model as it is realized in experiments. Towards this end, the first enterprise is to study the properties of the clean system. Chapter 6 is concerned with obtaining a quantitative comparison between theory and experiment. Calibration aspects of experiments and observables such as the peak fraction and how it relates to theory are discussed. In addition, a novel collaborative enterprise between analytics and simulation results is used in the framework of Landau damping to explain experiments. Chapter 7 starts with the preliminary aspects of the dirty Boson problem. The general effects of disorder and how it applies to lattice Bosons are presented. The general qualitative aspects of the phases and phase transitions are discussed before turning to quantitative quantum Monte-carlo (QMC) results. The latter is used to illustrate the equilibrium properties of the novel Bose-glass state. Finite temperature aspects are also discussed. Chapter 8 covers the physics of strongly correlated trapped disordered Bose gases. Experimental results measuring the transport properties of these gases are presented. Next, the discussion turns to QMC to illustrate the rich domain structure of these disordered gases using observables at different length scales. The method to identify the domains is discussed and used to identify the re-entrant superfluid phase that has remained elusive to experiments. Finally, the general phase diagram due to speckle disorder is presented together with an analysis of the effects of tunneling disorder. Chapter 9 deals with a novel collaborative enterprise between experiments and theory to identify the superfluid-Bose-glass boundary as it arises in these systems. The quenching technique used in experiments explores the quantum Kibble-Zurek mechanism as it may apply to disordered systems. QMC calculations are used to obtain the phase boundary that is found to be in excellent agreement with experiment. The chapter concludes with glassy dynamics seen in experiments and future prospects.

Chapter 6

Bose-Hubbard Model

The Bose-Hubbard model is given by,

$$\hat{\mathscr{H}} = -t \sum_{\langle ij \rangle} \hat{b}_i^\dagger \hat{b}_j + \frac{U}{2} \sum_i \hat{n}_i (\hat{n}_i - 1) - \mu \sum_i \hat{n}_i, \tag{6.1}$$

where t is the hopping parameter, characterizing the kinetic energy lost by particles diffusing to neighboring sites, U is the on-site interaction parameter that characterizes the energy cost associated with particles occupying the same site, μ is the chemical potential term that controls the particle number, $\hat{b}^\dagger$ ($\hat{b}$) are Boson creation (annihilation) operators, $\hat{n} \equiv \hat{b}^\dagger \hat{b}$ is the particle number operator that counts the number of particles, and $\langle ij \rangle$ indicates that the sum is over nearest neighbors only. This model is a very general description of the simple, but extremely fundamental phenomena of *interacting* particles in a lattice. It exhibits a variety of general phenomena such as lattice superfluidity, Bose-Einstein condensation [61, 19], Superfluid-Mott Insulator phase transitions [10], critical phenomena [62], etc. Indeed, studying the host of phenomena accommodated in this simple microscopic model offers important insight into related phenomena in material realizations such as Helium-4, Josephson Junction arrays, and even long-wavelength behavior of Cooper pairs in superconductors. Despite it's simplicity, the full range of behavior afforded by this model has still not been completely explored; in particular dynamic properties have recently become a subject of great interest due to the advent of synthetic materials made from ultra cold atoms and laser fields.

Despite great progress in optical lattice experiments, there are still many open questions and challenges. Most theoretical techniques, whether approximate (e.g. at the mean field level) or exact QMC, address the equilibrium properties of this model; however, cold atomic experiments are closed systems and their equilibration is not well understood. Indeed, whether the Eigenstate Thermalization Hypothesis (ETH) applies at all to such mesoscopic closed systems is unknown [63, 64, 65]. Even if the ETH holds, understanding relaxation and equilibration dynamics in strongly correlated systems is challenging. Exact dynamics can only be calculated reliably for one-dimensional systems and for short times. In two and three dimensions, often the only resort available is to rely on approximate time-dependent mean-field theories, which ignore correlation effects, or exact simulations of small numbers of particles, which may not reproduce experiments.

Aside from such fundamental theoretical issues, there are also technical problems in experiments. Measuring temperature in closed quantum systems is challenging. In systems connected to a reservoir, such as electronic solids, thermal contact is maintained with a carefully calibrated thermometer. In contrast, in closed systems, temperature must be measured via its relation to an observable derived from the system itself. Such a procedure can be problematic when the physics and energy spectrum of the system of interest are not fully understood. Generally, in optical lattice experiments low temperatures are attained by cooling the gas confined in a parabolic trap and then slowly turning on an optical lattice potential. Reaching lower temperatures in the lattice requires achieving lower entropy per particle in the trap. At best, turning on the lattice preserves entropy per particle. Generally, imperfections in the experiment, such as spontaneous scattering of the lattice light, and nonadiabaticity will lead to heating, and the entropy per particle of the gas in the lattice will be higher than the initial state. There are also proposals to cool the relevant degrees of freedom for atoms in the lattice, which have not been realized in experiments. In either approach, understanding and verifying equilibration and measuring temperature are critical to exploring low entropy states.

In this chapter, a combination of experiment, quantum Monte Carlo (QMC) simulations, and semi-analytic theory is used to explore equilibration and temperature in a prototypical strongly correlated system realized via the Bose-Hubbard Hamiltonian. An important feature of this model is that the equilibrium properties can be computed using a variety of theoretical tools, and thus the experiments and theory can be benchmarked against one another. The primary observables of interest are the condensate fraction (n_0) and entropy per particle (S/N), both of which can be estimated. However, it is worth noting that experiments can access condensate fraction only through a proxy-measurement of the peak fraction (f_0). The exact relationship between n_0 and f_0 will be explored using exact QMC and experimental procedures, as a way of calibration that is extremely important in order to understand the limitations and scope of the observable. It will also reveal a puzzling phenomena of metastability of the condensate – indicative of lack of thermalization. It is worth adding that in the absence of such issues, however, f_0 measured from Time-of-flight (TOF) could be used for thermometry.

The chapter is organized as follows. In the next section, details are presented of mean field approximations that are applicable to weak and strong coupling regimes of this model for homogenous systems. Following this in Section 6.2 a simple protocol known as the local density approximation is used to extend the results to the trapped system. In Section 6.3, the experimental procedure along with the measurement protocols used to obtain f_0 as well as the entropy per particle S/N is discussed. In Section 6.4, the details of QMC results is presented. The discussion starts with the measurement of the momentum distribution as well as the condensate momentum distribution for finite TOF as in experiments and the resulting effects. These effects play an important role in explaining the discrepancies between f_0 and n_0. Next, the procedure used to calculate S/N from QMC measurement of the energy per particle is discussed. This allows for direct comparisons with experiments. Section 6.5 discusses comparisons of mean-field theory results against QMC. Generally the agreement is poor, and caution is needed in using such theories in an ad-hoc way. In Section 6.6, the important features of experimental measurements *vis-á-vis* QMC predictions is discussed. The discrepancy with experimental measures of f_0 inevitably points to a lack of adiabaticity during loading and the need for a better understanding of the time scales of dynamics in this system. Subsequently in Section 6.7, an attempt is made to obtain a rough estimate of the time scales for relaxation of the peak fraction by calculating the Landau damping time in the lattice for the experimentally measured entropies. Calculations suggest that the time scale for equilibration is comparable to the time scale for heating, implying that the lack of agreement between the theoretical and experimental results may be due to a nonequilibrium effect.

6.1 Mean Field Approximations

In order to gain some insight into the physics of the problem, it is useful to consider mean field solutions to the Bose-Hubbard Hamiltonian (6.1). These theories have been extensively used in literature as a way to gain insight into experiments or otherwise, but there has been no way to test their validity in different regimes [21, 66, 67, 68, 61, 56, 69, 70, 71, 72]. This was one of the tasks that was undertaken in this dissertation work as a precursor to tackling the much more challenging disordered problem discussed in later chapters. In a limited qualitative way, it will be shown that these approximations can account for basic thermodynamic observables and correlation functions in the weakly interacting (small U/t) and strongly interacting (large U/t) limits. In regimes where the parameters in Hamiltonian are comparable ($U/zt \sim 1$, where z is the coordination number, equal to 6 for $D = 3$) – the strongly correlated regime, that bridges the Superfluid to Mott-Insulating (SF-MI) phase transition, none of the MF theories are applicable and there is no known analytical prescription that satisfactorily connects the limits mentioned above [70]. Nonetheless, these theories might be useful in other contexts where exact QMC techniques cannot be applied directly, for instance in non-equilibrium situations. In the sections below, first solutions for the weakly interacting limit are presented within the framework of finite temperature Hartree-Fock (HF) theory [61]. Following this the theory is extended by allowing for mixing of particle-like and hole-like excitations via the Bogoliubov and Popov approximations [61, 73, 74]. Finally the strong coupling regime is explored via site-decoupled MFT or the Gutzwiller ansatz [75].

An intuitive way to think about the prescriptions discussed next, is to consider the main difficulty in handling 6.1 that stems from the interaction term since it eliminates the possibility of factoring the many-body Hamiltonian into just a sum over single-particle Hamiltonians. Failing the possibility of straightforward basis transformations (practically true of any non-integrable system), the only alternative left is to choose an appropriate basis that allows the transformation of the full Hamiltonian into a more manageable form with systematic reduction of the complexities (e.g., using a perturbative framework).

Generally, the choice of a basis should be such that there is maximal overlap between the low energy eigenmodes of the Hamiltonian (assuming the interest is in low energy properties) and a small number of the basis functions. Putting it more quantitatively, if $\{|\psi_i\rangle\}$ are the eigenmodes of the Hamiltonian so that $\hat{\mathscr{H}}|\psi_i\rangle = E_i|\psi_i\rangle$, then these eigenmodes can be represented by any basis $\{|\phi_i\rangle\}$ via $|\psi_i\rangle = \sum_{j=0}^{M} |\phi_j\rangle\langle\phi_j|\psi_i\rangle$. M is the largest number of functions that are needed to capture the eigenmodes (i) of interest. Between two basis the better basis is one where the M is smaller. A corollary of this observation, is that if it suspected that only a small number of terms in the eigenbasis expansion is needed, then the Hamiltonian itself can be transformed by retaining only the small number of terms of interest (this will become clear below). A possible way to identify a basis set is to consider the parameters in the Hamiltonian and transform it to a perturbative framework in terms of small parameters (i.e. say $\hat{\mathscr{H}} = \hat{H}_0 + \lambda \hat{H}_1$ where λ is "small"). Then the basis could be the eigenstates of the base Hamiltonian ($\hat{H}_0$).[1] Additionally, it is also possible to introduce a mean-field description, where many-particle interactions are replaced by particles interacting only with some fluctuation-less mean-field resulting from inter-particle interactions. This mean-field is determined self-consistently, in the sense that resulting solutions must satisfy the thermodynamic constraints imposed on it (more below).

When the perturbative parameter is no longer small, the transformations used on the full Hamiltonian becomes too prohibitive. Physically this means that the chosen basis would require a large number of terms to account for actual states (i.e., M becomes large). This inevitably means that results corresponding to this form of mean field treatment fail to capture the real physics and deviate from actual results. In the most grevious cases, they may fail to even qualitatively capture the physical situation. Thus, it is of paramount importance to understand the regimes of validity of such techniques.

6.1.1 Weak-Coupling Approximation

The weak-coupling MF approximations apply when $\frac{U}{t} < 1$, so that the expectation is that the ground state and low lying excitations can be adequately captured by plane-waves (in lattice space, i.e. indexed by quasi-momentum of the crystal) corresponding to solutions of the non-interacting spectrum. Therefore, for both HF and HFBP, the momentum basis is a natural choice, so that:

$$\hat{b}_j = \frac{1}{\sqrt{V}} \sum_{\vec{p} \in 1^{st} BZ} e^{i\vec{p}\cdot\vec{j}} \hat{b}_p. \tag{6.2}$$

The sum is a discrete sum for the BH Hamiltonian, since it is on a lattice and the $\vec{p}$ values are restricted to the 1st Brillouin Zone as indicated. Using this basis, 6.1 can be transformed

---

[1] The perturbative framework is different for Bosons and Fermions, this is because the non-interacting Bosonic ground state in homogenous systems has all particles in the ground state. Refer to [76] for the corresponding Field theory formulations.

as follows:

$$
\begin{aligned}
\hat{\mathscr{H}} &= -t\sum_{\langle ij\rangle}\hat{b}_i^\dagger\hat{b}_j + \frac{U}{2}\sum_i \hat{n}_i(\hat{n}_i-1) - \mu\sum_i \hat{b}_i^\dagger\hat{b}_i \\
&= -t\sum_{\langle ij\rangle}\hat{b}_i^\dagger\hat{b}_j + \frac{U}{2}\sum_i \hat{b}_i^\dagger\hat{b}_i^\dagger\hat{b}_i\hat{b}_i - \mu\sum_i \hat{b}_i^\dagger\hat{b}_i \\
&= -t\sum_i\sum_{\hat{r}\in\{\hat{x},\hat{y},\hat{z}\}}\frac{1}{V}\left[\sum_{\vec{p},\vec{q}}\hat{b}_p^\dagger\hat{b}_q e^{-i(\vec{p}-\vec{q})\cdot\vec{i}}e^{i\vec{q}\cdot\hat{r}} + \hat{b}_p\hat{b}_q^\dagger e^{i(\vec{p}-\vec{q})\cdot\vec{i}}e^{-i\vec{q}\cdot\hat{r}}\right] \\
&\qquad + \frac{U}{2V^2}\sum_i\sum_{\vec{p},\vec{q},\vec{r},\vec{s}} e^{i(\vec{p}+\vec{q}-\vec{r}-\vec{s})\cdot\vec{i}}\hat{b}_p^\dagger\hat{b}_q^\dagger\hat{b}_r\hat{b}_s - \frac{\mu}{V}\sum_i\sum_{\vec{p},\vec{q}}\hat{b}_p^\dagger\hat{b}_q e^{-i(\vec{p}-\vec{q})\cdot\vec{i}} \\
&= -t\sum_{\hat{r}\in\{\hat{x},\hat{y},\hat{z}\}}\left[\sum_{\vec{p},\vec{q}}\hat{b}_p^\dagger\hat{b}_q\delta(\vec{p}-\vec{q})e^{i\vec{q}\cdot\hat{r}} + \hat{b}_p\hat{b}_q^\dagger\delta(\vec{p}-\vec{q})e^{-i\vec{q}\cdot\hat{r}}\right] \\
&\qquad + \frac{U}{2V}\sum_{\vec{p},\vec{q},\vec{r},\vec{s}}\delta(\vec{p}+\vec{q}-\vec{r}-\vec{s})\hat{b}_p^\dagger\hat{b}_q^\dagger\hat{b}_r\hat{b}_s - \mu\sum_{\vec{p},\vec{q}}\delta(\vec{p}-\vec{q})\hat{b}_p^\dagger\hat{b}_q \\
&= \sum_{\vec{p}}\hat{b}_p^\dagger\hat{b}_p\left[-2t\sum_{\hat{r}\in\{\hat{x},\hat{y},\hat{z}\}} cos(\vec{p}\cdot\hat{r})\right] + \frac{U}{2V}\sum_{\vec{p},\vec{q},\vec{r},\vec{s}}\delta(\vec{p}+\vec{q}-\vec{r}-\vec{s})\hat{b}_p^\dagger\hat{b}_q^\dagger\hat{b}_r\hat{b}_s \\
&\qquad - \frac{\mu}{V}\sum_{\vec{p}}\hat{b}_p^\dagger\hat{b}_p \\
&= \sum_{\vec{p}}\hat{b}_p^\dagger\hat{b}_p\left[\varepsilon(\vec{p})-\mu\right] + \frac{U}{2V}\sum_{\vec{p},\vec{q},\vec{r},\vec{s}}\delta(\vec{p}+\vec{q}-\vec{r}-\vec{s})\hat{b}_p^\dagger\hat{b}_q^\dagger\hat{b}_r\hat{b}_s \qquad (6.3)
\end{aligned}
$$

Where $\varepsilon(\vec{p}) \equiv 2Dt - 2t\sum_{\hat{r}} cos(\vec{p}\cdot\hat{r})$ and the transformation $\mu = \mu + 2Dt$ was made so that at the bottom of the band $\varepsilon(\vec{p}=0) = 0$. So far no approximations have been made, and the transformation is exact. The issues is once again the interaction term, involving the scattering of two particles with momentum $\vec{r}$ and $\vec{s}$ into states with momentum $\vec{p}$ and $\vec{q}$, so that the total momentum is conserved (ensured via the δ function). In order to progress forward, approximations need to be made.

- **Hartree Fock Approximation** In the HF approximation, the interaction term is truncated by allowing only scattering into the same states either directly (called Hartree process) where $\vec{p} \leftrightarrow \vec{r}$, $\vec{q} \leftrightarrow \vec{s}$ or via an exchange (called Fock process) $\vec{p} \leftrightarrow \vec{s}$, $\vec{q} \leftrightarrow \vec{r}$, so that:

$$\sum_{\vec{p},\vec{q},\vec{r},\vec{s}}\delta(\vec{p}+\vec{q}-\vec{r}-\vec{s})\hat{b}_p^\dagger\hat{b}_q^\dagger\hat{b}_r\hat{b}_s \sim \sum_{\vec{p},\vec{q}}\hat{b}_p^\dagger\hat{b}_q^\dagger\hat{b}_p\hat{b}_q + \hat{b}_p^\dagger\hat{b}_q^\dagger\hat{b}_q\hat{b}_p \qquad (6.4)$$

Now further expansions are possible centered around the macroscopic zero momentum mode which is assumed to be devoid of fluctuations, i.e. $\hat{b}_0^\dagger \hat{b}_0 = \langle \hat{n}_0 \rangle + O(\delta \hat{n}_0) \sim N_0$, which is the same as saying $\langle \hat{b}_0 \rangle = \langle \hat{b}_0^\dagger \rangle = \sqrt{N_0}$. So the interaction term becomes:

$$\begin{aligned}\sum_{\vec{p},\vec{q}} \hat{b}_p^\dagger \hat{b}_q^\dagger \hat{b}_p \hat{b}_q + \hat{b}_p^\dagger \hat{b}_q^\dagger \hat{b}_q \hat{b}_p &\sim \hat{b}_0^\dagger \hat{b}_0^\dagger \hat{b}_0 \hat{b}_0 + \left\{ \hat{b}_0^\dagger \hat{b}_q^\dagger \hat{b}_0 \hat{b}_q + \hat{b}_0^\dagger \hat{b}_q^\dagger \hat{b}_q \hat{b}_0 + \hat{b}_p^\dagger \hat{b}_0^\dagger \hat{b}_p \hat{b}_0 + \hat{b}_p^\dagger \hat{b}_0^\dagger \hat{b}_0 \hat{b}_p \right\} \\ &\quad + \sum_{\vec{p}\neq 0,\vec{q}\neq 0} \hat{b}_p^\dagger \hat{b}_q^\dagger \hat{b}_p \hat{b}_q + \hat{b}_p^\dagger \hat{b}_q^\dagger \hat{b}_q \hat{b}_p \\ &\sim N_0(N_0 - 1) + 4N_0 \hat{b}_p^\dagger \hat{b}_p + 2 \sum_{\vec{p}\neq 0,\vec{q}\neq 0} \hat{b}_p^\dagger \hat{b}_p \hat{b}_q^\dagger \hat{b}_q - \hat{b}_p^\dagger \hat{b}_p \delta_{\vec{p}\vec{q}}\end{aligned} \tag{6.5}$$

Note that there is no sign change due to exchange since the particles are Bosons. Also, for contact interaction, both Hartree and Fock terms are identical. The resulting Hamiltonian is obtained by additionally ignoring terms that are O($\frac{N}{V}$):

$$\hat{H} = \frac{N_0^2 U}{2V} + \sum_{\vec{p}\neq 0} \left[\varepsilon(\vec{p}) + 2n_0 U\right] \hat{b}_p^\dagger \hat{b}_p + \frac{U}{V} \sum_{\vec{p}\neq 0,\vec{q}\neq 0} \hat{b}_p^\dagger \hat{b}_p \hat{b}_q^\dagger \hat{b}_q - \mu \sum_{\vec{p}} \hat{b}_p^\dagger \hat{b}_p \tag{6.6}$$

Now although the assumption that the macroscopic condensate is fluctuation free has been used, it is still important to address the HF non-zero momentum interactions. Towards this end, allowing for small fluctuations about a *thermally averaged* occupation it is possible to write,

$$\hat{b}_p^\dagger \hat{b}_p = \langle \hat{n}_p \rangle + \delta \hat{n}_p. \tag{6.7}$$

Using this the interaction term may be transformed in terms of only first order fluctuations:

$$\begin{aligned}\hat{b}_p^\dagger \hat{b}_p \hat{b}_q^\dagger \hat{b}_q &= (\langle \hat{n}_p \rangle + \delta \hat{n}_p)(\langle \hat{n}_q \rangle + \delta \hat{n}_q) \\ &= \langle \hat{n}_p \rangle \langle \hat{n}_q \rangle + \langle \hat{n}_p \rangle \delta \hat{n}_q + \langle \hat{n}_q \rangle \delta \hat{n}_p + O(\delta \hat{n}_p^2) \\ &\sim \langle \hat{n}_p \rangle \langle \hat{n}_q \rangle + \langle \hat{n}_p \rangle [\hat{b}_q^\dagger \hat{b}_q - \langle \hat{n}_q \rangle] + \langle \hat{n}_q \rangle [\hat{b}_p^\dagger \hat{b}_p - \langle \hat{n}_p \rangle] \\ &= \langle \hat{n}_p \rangle \hat{b}_q^\dagger \hat{b}_q + \langle \hat{n}_q \rangle \hat{b}_p^\dagger \hat{b}_p - \langle \hat{n}_p \rangle \langle \hat{n}_q \rangle\end{aligned} \tag{6.8}$$

So that

$$\frac{U}{V}\sum_{\vec{p}\neq 0,\vec{q}\neq 0}\hat{b}_p^\dagger\hat{b}_p\hat{b}_q^\dagger\hat{b}_q = \frac{2U}{V}\sum_{\vec{q}\neq 0}\left[\sum_{\vec{p}\neq 0}\langle\hat{n}_p\rangle\right]\hat{b}_q^\dagger\hat{b}_q - \frac{U}{V}\sum_{\vec{p}\neq 0,\vec{q}\neq 0}\langle\hat{n}_p\rangle\langle\hat{n}_q\rangle$$

$$= 2Un_{th}\sum_{\vec{p}\neq 0}\hat{b}_p^\dagger\hat{b}_p - \frac{U}{V}\sum_{\vec{p}\neq 0,\vec{q}\neq 0}\langle\hat{n}_p\rangle\langle\hat{n}_q.\rangle \tag{6.9}$$

Using these approximations, the final HF Hamiltonian is:

$$\hat{H}_{HF} = \frac{N_0^2 U}{2V} + \sum_{\vec{p}\neq 0}\left[\varepsilon(\vec{p}) + 2nU\right]\hat{b}_p^\dagger\hat{b}_p - \frac{U}{V}\sum_{\vec{p}\neq 0,\vec{q}\neq 0}\langle\hat{n}_p\rangle\langle\hat{n}_q\rangle - \mu\sum_{\vec{p}}\hat{b}_p^\dagger\hat{b}_p \tag{6.10}$$

where $n = n_0 + n_{th}$. In order to calculate the chemical potential for some fixed condensate number N_0, note that since the condensate carries no entropy,

$$\mu = \left.\frac{\partial\langle\hat{H}\rangle}{\partial N}\right|_S = \left.\frac{\partial\langle\hat{H}\rangle}{\partial N_0}\right|_{\langle n_p\rangle,\vec{p}\neq 0}$$

$$= U(n_0 + 2\sum_{\vec{p}\neq 0}\hat{b}_p^\dagger\hat{b}_p) = (n_0 + 2n_{th})U, \tag{6.11}$$

which is equivalent to using the saddle-point criteria in the Grand Canonical Hamiltonian. The total number of non-condensate atoms is given by:

$$N_{th} = \sum_{\vec{p}\neq 0}\frac{1}{e^{\beta(\varepsilon(\vec{p})+2nU-\mu)} - 1}$$

$$= \frac{1}{2}\left[\sum_{\vec{p}\neq 0}\coth\left(\frac{\beta E_{HF}(\vec{p})}{2}\right) - 1\right] \tag{6.12}$$

where $E_{HF}(\vec{p}) \equiv \varepsilon(\vec{p}) + 2nU - \mu$. Note that effectively, this problem requires the correct n_0 given n, and so equations 6.11 and 6.12 constitute self-consistent equations that need to be solved numerically via iterative schemes starting with some initial guess for n_0. It is perhaps easier to see the self-consistent equation by utilizing $\mu = U(2n - n_0)$ so that 6.12 is re-written as:

$$n_0 = n - \frac{1}{2V}\left[\sum_{\vec{p}\neq 0}\coth\left(\frac{\beta(\varepsilon(\vec{p}) + Un_0)}{2}\right) - 1\right] \tag{6.13}$$

Once n_0 is found, all thermodynamic observables can be readily calculated. For instance, an observable that is important with regards to experiments is the entropy, given by:

$$S = \sum_{\vec{p}\neq 0}\left[\frac{\beta\varepsilon(\vec{p})}{e^{\beta\varepsilon(\vec{p})}-1} - ln\left(1-e^{-\beta\varepsilon(\vec{p})}\right)\right], \tag{6.14}$$

where $\varepsilon(\vec{p}) = E_{HF}(\vec{p})$ for the HF Hamiltonian.

- **Hartree-Fock-Bogoliubov-Popov Theory**

  The basic idea of HFBP theory is the same as HF, except more terms are retained in the interaction term, which now allows the mixing of particle- and hole-like excitations. The formulation requires the use of Bogoliubov transformation and is worth deriving in its own right. Although it is possible to use the same expansion procedure as before, i.e. via the transformation of the basis states to arrive at the key elements of the HFBP approximation, an alternate route following [73] is used below. This is done to reveal a key connection between fluctuations in real space with k-space operators, that helps in understanding the nature of the approximations.

  The MF approximation involves the expansion the local field operator in terms of a static classical field corresponding to the macroscopic condensate and fluctuations about that field:

$$\begin{aligned}\hat{b}_i &= \sqrt{\frac{N_0}{V}} + \delta\hat{b}_i \\ &= \frac{\langle\hat{b}_0\rangle}{\sqrt{V}} + \frac{1}{\sqrt{V}}\sum_{\vec{p}\neq 0} e^{i\vec{p}\cdot\vec{r}/\hbar}\hat{b}_p\end{aligned} \tag{6.15}$$

  with $\langle\hat{b}_0\rangle = \sqrt{N_0}$ and we ignore all fluctuations for the zero-momentum macroscopic mode. The kinetic component of the Hamiltonian transforms as before, so the focus is on the interaction term:

$$\begin{aligned}\sum_i \hat{b}_i^\dagger\hat{b}_i^\dagger\hat{b}_i\hat{b}_i &= \sum_i\left(\sqrt{\frac{N_0}{V}}+\delta\hat{b}_i^\dagger\right)\left(\sqrt{\frac{N_0}{V}}+\delta\hat{b}_i^\dagger\right)\left(\sqrt{\frac{N_0}{V}}+\delta\hat{b}_i\right)\left(\sqrt{\frac{N_0}{V}}+\delta\hat{b}_i\right) \\ &= \sum_i\Bigg[\left(\frac{N_0}{V}\right)^2 + 2\left(\frac{N_0}{V}\right)^{\frac{3}{2}}\delta\hat{b}_i^\dagger + 2\left(\frac{N_0}{V}\right)^{\frac{3}{2}}\delta\hat{b}_i + \frac{N_0}{V}\delta\hat{b}_i^\dagger\delta\hat{b}_i^\dagger \\ &\qquad + \frac{N_0}{V}\delta\hat{b}_i\delta\hat{b}_i + 4\frac{N_0}{V}\delta\hat{b}_i^\dagger\delta\hat{b}_i + 2\sqrt{\frac{N_0}{V}}\delta\hat{b}_i^\dagger\delta\hat{b}_i\delta\hat{b}_i + 2\sqrt{\frac{N_0}{V}}\delta\hat{b}_i^\dagger\delta\hat{b}_i^\dagger\delta\hat{b}_i \\ &\qquad + \delta\hat{b}_i^\dagger\delta\hat{b}_i^\dagger\delta\hat{b}_i\delta\hat{b}_i\Bigg]\end{aligned} \tag{6.16}$$

Consider the terms:

$$\sum_i \delta\hat{b}_i = \sum_{\vec{p}\neq 0}\sum_i e^{i\vec{p}\cdot\vec{i}}\hat{b}_p = \sum_{\vec{p}\neq 0}\delta(\vec{p})\hat{b}_p = 0 \tag{6.17}$$

$$\sum_i \delta\hat{b}_i\delta\hat{b}_i = \sum_{\vec{p}\neq 0,\vec{q}\neq 0}\sum_i e^{i(\vec{p}+\vec{q})\cdot\vec{i}}\hat{b}_p\hat{b}_q = \sum_{\vec{p}\neq 0,\vec{q}\neq 0}\delta(\vec{p}+\vec{q})\hat{b}_p\hat{b}_q = \sum_{\vec{p}\neq 0}\hat{b}_p\hat{b}_{-p} \tag{6.18}$$

$$\sum_i \delta\hat{b}_i^\dagger\delta\hat{b}_i = \sum_{\vec{p}\neq 0,\vec{q}\neq 0}\sum_i e^{i(-\vec{p}+\vec{q})\cdot\vec{i}}\hat{b}_p^\dagger\hat{b}_q = \sum_{\vec{p}\neq 0,\vec{q}\neq 0}\delta(\vec{q}-\vec{p})\hat{b}_p^\dagger\hat{b}_q = \sum_{\vec{p}\neq 0}\hat{b}_p^\dagger\hat{b}_p \tag{6.19}$$

$$\begin{aligned}\sum_i \delta\hat{b}_i^\dagger\delta\hat{b}_i^\dagger\delta\hat{b}_i &= \sum_{\vec{p}\neq 0,\vec{q}\neq 0,\vec{r}\neq 0}\sum_i e^{i(-\vec{p}-\vec{q}+\vec{r})\cdot\vec{i}}\hat{b}_p^\dagger\hat{b}_q^\dagger\hat{b}_r = \sum_{\vec{p}\neq 0,\vec{q}\neq 0,\vec{r}\neq 0}\delta(\vec{p}+\vec{q}-\vec{r})\hat{b}_p^\dagger\hat{b}_q^\dagger\hat{b}_r \\ &= \sum_{\vec{p}\neq 0,\vec{q}\neq 0}\hat{b}_p^\dagger\hat{b}_q^\dagger\hat{b}_{p+q} \end{aligned}\tag{6.20}$$

$$\begin{aligned}\sum_i \delta\hat{b}_i^\dagger\delta\hat{b}_i^\dagger\delta\hat{b}_i\delta\hat{b}_i &= \sum_{\vec{p}\neq 0,\vec{q}\neq 0,\vec{r}\neq 0,\vec{s}\neq 0}\sum_i e^{i(-\vec{p}-\vec{q}+\vec{r}+\vec{s})\cdot\vec{i}}\hat{b}_p^\dagger\hat{b}_q^\dagger\hat{b}_r\hat{b}_s \\ &= \sum_{\vec{p}\neq 0,\vec{q}\neq 0,\vec{r}\neq 0,\vec{s}\neq 0}\delta(\vec{p}+\vec{q}-\vec{r}-\vec{s})\hat{b}_p^\dagger\hat{b}_q^\dagger\hat{b}_r\hat{b}_s \end{aligned}\tag{6.21}$$

If the HF approximation is used then processes of the form (6.20), where two particles of different momentum scatter such that there is complete transference of momentum to one particle, while the other is transferred into the condensate with zero momentum or vice-versa, are ignored since the probability is extremely low. However, these will play an important role in the dynamics of the condensate and equilibration, to be discussed later 6.7. Processes of the form (6.21) is transformed as in (6.4) so that the interaction term becomes:

$$\begin{aligned}\frac{U}{2}\sum_i \hat{b}_i^\dagger\hat{b}_i^\dagger\hat{b}_i\hat{b}_i = \frac{UN_0^2}{V} + \frac{n_0U}{2}\sum_{\vec{p}\neq 0}\left[\hat{b}_p\hat{b}_{-p} + \hat{b}_p^\dagger\hat{b}_{-p}^\dagger\right] + 2(n_0+n_{th})U\sum_{\vec{p}\neq 0}\hat{b}_p^\dagger\hat{b}_p \\ - \frac{U}{V}\sum_{\vec{p}\neq 0,\vec{q}\neq 0}\langle\hat{n}_p\rangle\langle\hat{n}_q\rangle \end{aligned}\tag{6.22}$$

So that the Hamiltonian is:

$$\begin{aligned}\hat{H} &= \frac{N_0^2U}{V} + \sum_{\vec{p}\neq 0}(\varepsilon(\vec{p}) + 2nU - \mu)\hat{b}_p^\dagger\hat{b}_p + \frac{n_0U}{2}\sum_{\vec{p}\neq 0}\left[\hat{b}_p\hat{b}_{-p} + \hat{b}_p^\dagger\hat{b}_{-p}^\dagger\right] - \frac{U}{V}\sum_{\vec{p}\neq 0,\vec{q}\neq 0}\langle\hat{n}_p\rangle\langle\hat{n}_q\rangle \\ &= \frac{N_0^2U}{V} + \sum_{\vec{p}\neq 0,\vec{p}\in\Omega/2}\left\{(\varepsilon(\vec{p}) + 2nU - \mu)\left[\hat{b}_p^\dagger\hat{b}_p + \hat{b}_{-p}^\dagger\hat{b}_{-p}\right] + n_0U\left[\hat{b}_p\hat{b}_{-p} + \hat{b}_p^\dagger\hat{b}_{-p}^\dagger\right]\right\} \\ &\quad - \frac{U}{V}\sum_{\vec{p}\neq 0,\vec{q}\neq 0}\langle\hat{n}_p\rangle\langle\hat{n}_q\rangle \end{aligned}\tag{6.23}$$

As before the chemical potential can be obtained by differentiating with respect to n_0, so that $mu = 2Un - Un_0$. In this current form it is possible to use the Bogoliubov transformation to bring (6.23) into a diagonal form (see Appendix C), so that the transformed HFBP Hamiltonian is:

$$\begin{aligned}
\hat{H}_{HFBP} &= \frac{N_0^2 U}{V} + \sum_{\vec{p}\neq 0, \vec{p}\in\Omega/2} \Big\{ \sqrt{(\varepsilon(\vec{p}) + n_0 U)^2 - (n_0 U)^2} (\hat{\alpha}_p^\dagger \hat{\alpha}_p + \hat{\alpha}_{-p}^\dagger \hat{\alpha}_{-p}) \\
&\qquad + \Big[\sqrt{(\varepsilon(\vec{p}) + n_0 U)^2 - (n_0 U)^2} - (\varepsilon(\vec{p}) + n_0 U) \Big] \Big\} \\
&= \frac{N_0^2 U}{V} + \sum_{\vec{p}\neq 0, \vec{p}\in\Omega/2} \Big[\sqrt{(\varepsilon(\vec{p}) + n_0 U)^2 - (n_0 U)^2} - (\varepsilon(\vec{p}) + n_0 U) \Big] \\
&\quad + \sum_{\vec{p}\neq 0} \sqrt{(\varepsilon(\vec{p}) + n_0 U)^2 - (n_0 U)^2} \hat{\alpha}_p{}^\dagger \hat{\alpha}_p
\end{aligned} \tag{6.24}$$

where,

$$\begin{aligned}
\hat{\alpha}_p = &\left\{ \frac{1}{2} \left[\frac{(\varepsilon(\vec{p}) + n_0 U)}{\sqrt{(\varepsilon(\vec{p}) + n_0 U)^2 - (n_0 U)^2}} + 1 \right] \right\}^{\frac{1}{2}} \hat{b}_p \\
&+ \left\{ \frac{1}{2} \left[\frac{(\varepsilon(\vec{p}) + n_0 U)}{\sqrt{(\varepsilon(\vec{p}) + n_0 U)^2 - (n_0 U)^2}} - 1 \right] \right\}^{\frac{1}{2}} \hat{b}_{-p}^\dagger
\end{aligned} \tag{6.25}$$

The transformation that brings the HFBP Hamiltonian into its diagonal form, reveals that the eigenstates of the Hamiltonian have a remarkably simple form. The eigenstates are called Bogoliubov quasi-particles and are made up of a superposition states created by removing a particle from the condensate and causing an excitation with momentum $-\vec{p}$ or removing a hole from the condensate and causing an excitation with momentum $\vec{p}$. So these quasi-particles are a mixture of particles and holes.

Since the particle number is constrained, the total number of non-condensate particles can be obtained using (C.11). First it is convenient to define the HFBP spectrum by,

$$E_{HFBP} \equiv \sqrt{(\varepsilon(\vec{p}) + n_0 U)^2 - (n_0 U)^2} \tag{6.26}$$

and recall that the HF spectrum is given by,

$$E_{HF} \equiv \varepsilon(\vec{p}) + n_0 U \tag{6.27}$$

So that,

$$
\begin{aligned}
N_{ex} &= \sum_{\vec{p}\neq 0} \frac{E_{HF}(\vec{p})}{E_{HFBP}(\vec{p})} \frac{1}{e^{\beta E_{HFBP}(\vec{p})}-1} + \frac{1}{2}\left(\frac{E_{HF}(\vec{p})}{E_{HFBP}(\vec{p})} - 1\right) \\
&= \sum_{\vec{p}\neq 0} \frac{E_{HF}(\vec{p})}{E_{HFBP}(\vec{p})} \left[\frac{1}{e^{\beta E_{HFBP}(\vec{p})}-1} + \frac{1}{2}\right] - \frac{1}{2} \\
&= \frac{1}{2}\sum_{\vec{p}\neq 0} \left[\frac{E_{HF}(\vec{p})}{E_{HFBP}} \coth\left(\frac{\beta E_{HFBP}(\vec{p})}{2}\right) - 1\right] \qquad (6.28)
\end{aligned}
$$

As before, just like the HF calculations, the HFBP approximation requires a self-consistent solution. Once n_0 is computed all thermodynamic observables can be calculated.

6.1.2 Strong Coupling Approximation

The idea of strong coupling approximation, is to perturb not in U/t but rather in t/U, since for strong interactions the latter is small. The approach here is the so-called site-decoupled MF theory (SDMFT) following which the kinetic component of the Hamiltonian is treated perturbatively whereas the interaction term is kept exact [75]. Using,

$$
\begin{aligned}
\hat{b}_i^\dagger \hat{b}_j &\sim (\langle \hat{b}_i^\dagger\rangle + \delta\hat{b}_i^\dagger)(\langle \hat{b}_j\rangle + \delta\hat{b}_j) \\
&\sim \langle \hat{b}_i^\dagger\rangle\langle \hat{b}_j\rangle + \langle \hat{b}_i^\dagger\rangle\delta\hat{b}_j + \delta\hat{b}_i^\dagger\langle \hat{b}_j\rangle + O(\delta\hat{b}^2) \\
&\sim \langle \hat{b}_i^\dagger\rangle\langle \hat{b}_j\rangle + \langle \hat{b}_i^\dagger\rangle(\hat{b}_j - \langle \hat{b}_j\rangle) + (\hat{b}_i^\dagger - \langle \hat{b}_i^\dagger\rangle)\langle \hat{b}_j\rangle \\
&\sim \langle \hat{b}_i^\dagger\rangle \hat{b}_j + \hat{b}_i^\dagger\langle \hat{b}_j\rangle - \langle \hat{b}_i^\dagger\rangle\langle \hat{b}_j\rangle, \qquad (6.29)
\end{aligned}
$$

it is possible to decouple the Hamiltonian. Let $\langle \hat{b}_i\rangle = \alpha$ so that

$$
\begin{aligned}
\hat{H} &= -t\sum_{\langle ij\rangle} \hat{b}_i^\dagger \hat{b}_j + \frac{U}{2}\sum_i \hat{n}_i(\hat{n}_i - 1) - \mu\sum_i \hat{n}_i \\
&\sim -t\sum_{\langle ij\rangle}(\langle \hat{b}_i^\dagger\rangle \hat{b}_j + \hat{b}_i^\dagger\langle \hat{b}_j\rangle - \langle \hat{b}_i^\dagger\rangle\langle \hat{b}_j\rangle) + \frac{U}{2}\sum_i \hat{n}_i(\hat{n}_i - 1) - \mu\sum_i \hat{n}_i \\
&= \sum_i -zt(\alpha^*\hat{b}_i + \hat{b}_i^\dagger\alpha - |\alpha|^2) + \frac{U}{2}\hat{n}_i(\hat{n}_i - 1) - \mu\hat{n}_i. \qquad (6.30)
\end{aligned}
$$

The site independent Hamiltonian is, then, given by,

$$
\hat{h} = -zt(\alpha^*\hat{b}_i + \hat{b}_i^\dagger\alpha - |\alpha|^2) + \frac{U}{2}\hat{n}_i(\hat{n}_i - 1) - \mu\hat{n}_i. \qquad (6.31)
$$

The appropriate basis for this equation is obtained simply by using a truncated occupation number basis $|n\rangle$. The algorithm is straightforward:

1. Initialize $\alpha = \alpha_0$
2. (6.31) can be diagonalized so that $\hat{h}|\phi_i\rangle = E_i|\phi_i\rangle$
3. The new α can be obtained using:

$$\begin{aligned}\alpha &= \frac{1}{Z}\sum_i \langle\phi_i|\hat{b}e^{-\beta E_i}|\phi_i\rangle \\ &= \frac{1}{Z}\sum_i \langle\phi_i|\hat{b}e^{-\beta E_i}\sum_n |n\rangle\langle n|\phi_i\rangle \\ &= \frac{1}{Z}\sum_i\sum_n \sqrt{n}e^{-\beta E_i}\langle\phi_i|n-1\rangle\langle n|\phi_i\rangle \qquad (6.32)\end{aligned}$$

4. Repeat steps 2-3 until α is converged.
5. All observables can be computed using the converged solution.

It is worth pointing out that the SDMFT computation is the same as using a Gutzwiller variational ansatz,

$$|\psi\rangle = \prod_{i\in sites}\sum_{n=0}\frac{c_n}{\sqrt{n!}}(\hat{b}_i)^n|0\rangle, \qquad (6.33)$$

to compute the ground state energy $\langle\psi|\hat{H}|\psi\rangle$ and minimizing it with respect to the coefficients $\{c_n\}$. Standard results from these approximations are readily available, so they will not be presented here. Instead these approximations will be used to compute observables that can be compared with experiments. However, the theories discussed above are only applicable to homogeneous systems, and will need to be extended in order allow for inhomogeneities due to the confining harmonic trap used in experiments (see Section 6.3).

6.2 Inhomogeneous Systems

The presence of the confining potential in experiments renders the Bose-Hubbard model inhomogeneous and needs an additional term $\sum_i[\frac{1}{2}m\omega^2a^2]i^2\hat{n}_i$ in the Hamiltonian 6.1 to account for it, where ω is the trapping frequency and a is the lattice constant used to

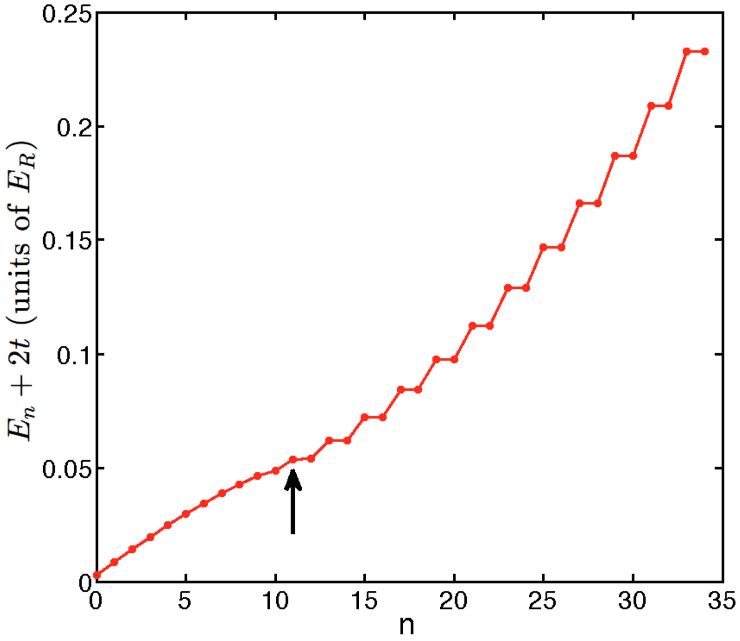

Figure 6.1: single-particle energy spectrum for a single-particle in a Bose-Hubbard model with a trap in 1D. The black arrow indicates the critical value $n_c \sim \left\lfloor 2\sqrt{\frac{2t}{\Omega}} \right\rfloor = 11$, above which the harmonic oscillator states are localized states at the edge of the trap. The degenerate energies corresponds to localized state in the left and right edges of the trap. This plot corresponds to values of $t = 2.05$ nK with $\Omega = 0.12$ nK (60 Hz trap for parameters discussed in text).

coarse-grain the continuum system. The inhomogeneous Hamiltonian is then:

$$\mathscr{H} = -t \sum_{\langle ij \rangle} \hat{b}_i^\dagger \hat{b}_j + \frac{U}{2} \sum_i \hat{n}_i(\hat{n}_i - 1) - \mu \sum_i \hat{n}_i + \sum_i \frac{1}{2}[m\omega^2 a^2] i^2 \hat{n}_i \tag{6.34}$$

In this situation, the lattice-translational invariance is lost, and quasi-momentum is no longer a good quantum number. To gain insight into what the trap does, it is worth considering the single-particle problem since it might reveal properties that are important. The corresponding Hamiltonian is:

$$\mathscr{H}_1 = -t \sum_{\langle ij \rangle} \hat{b}_i^\dagger \hat{b}_j + \Omega \sum_i i^2 \hat{n}_i, \tag{6.35}$$

where $\Omega \equiv \frac{1}{2} m\omega^2 a^2$ characterizes the trapping energy. For ^{87}Rb atoms and a lattice constant $a \sim 400$ nm (used in many experiments), $\Omega/4 \sim 0.02$ to 0.04 nK for $\omega = 50$ Hz to 70 Hz. The general solution of this system involves Matheiu functions, but asymptotic solutions are possible in two limits $t \geq \Omega/4$ and $t < \Omega/4$ [66, 77]. For most experimental realizations the former limit generally holds – for lattice depths of $6 - 20$ E_R ($= 167$ nK for parameters discussed here), $t = 8.53$ - 0.42 nK. An example of the spectrum corresponding to this regime is shown in Fig. (6.1). As is evident, the spectrum E_n (with n labelling the states) is separated to two regions, with the critical value $n_c \sim \left\lfloor 2\sqrt{\frac{2t}{\Omega}} \right\rfloor$, above which the harmonic oscillator states are localized states at the edge of the trap. The degenerate energies corresponds to the left and right edges of the trap. Below this value the states are extended and much like the trap-free Bose-Hubbard model the bandwidth of this region $\sim 4t$. If $t < \Omega/4$, then all states are localized and the particle does not have sufficient kinetic energy to tunnel to adjacent sites. Therefore, the case $t \geq \Omega/4$ is the only way to access properties that may correspond the Bose-Hubbard model, and the primary interest is in weak traps that satisfies $t >> \Omega/4$.

In the presence of the trap, it is possible to reformulate the MF theories discussed above so that the amplitude of the classical field becomes site dependent. This leads to the Bogoliubov transformation to become considerably more complicated and the spectrum no longer has a simple analytical form. The solution involves much more elaborate numerical computations and as the self-consistency condition needs to be carefully handled, since solutions may not be stable [78]. In the case of SDMFT, the site can be decoupled using an alternate formulation that introduces site dependence to the complex field α (discussed above). The problem then involves diagonalizing L^D, $(n+1)^2$ matrices (where n is the largest occupation number allowed in the truncated basis) and iterate multiple times until convergence as before [79]. These approaches are computationally not as easy as the standard techniques, and at the time of writing they have not been used to study realistic system sizes and used only for small systems. However, they do allow for correlations to be present across sites. If this requirement is removed, it is possible to use a computationally less expensive approach, which should be particularly amenable for weak traps.

6.2.1 Local Density Approximation

The idea of the local density approximation, is that the trap can be incorporated as a local chemical potential shift, i.e,

$$\mu(r) \equiv \mu - \Omega i^2, \tag{6.36}$$

and then solve the system assuming every site is completely decoupled from other sites. The results for different sites are then integrated or summed to compute the total observable of interest. Only minor modifications are needed to the techniques discussed earlier:

- **HF and HFBP**: In this case, starting with some initial guess for the density at the center of the trap, the local chemical potential and condensate density can be calculated self-consistently. After this step, the new chemical potential for a site is simply calculated using 6.36. Using estimates of $n(i-1)$ and $n_0(i-1)$, new guesses can be made for values in the current site i. These guesses are used for a new set of self-consistent $n(i)$ and $n_0(i)$. For each site, the corresponding observables of interest can be computed $O(i)$ and this process is repeated for all sites. Finally at the end of the calculation the final global observable is just $O \equiv \sum_i O(i)$.

- **SDMFT**: This is calculation proceeds, much like the HF/HFBP case. 6.36 is used to compute the observable of interest for each site, and the global observable is computed as discussed above.

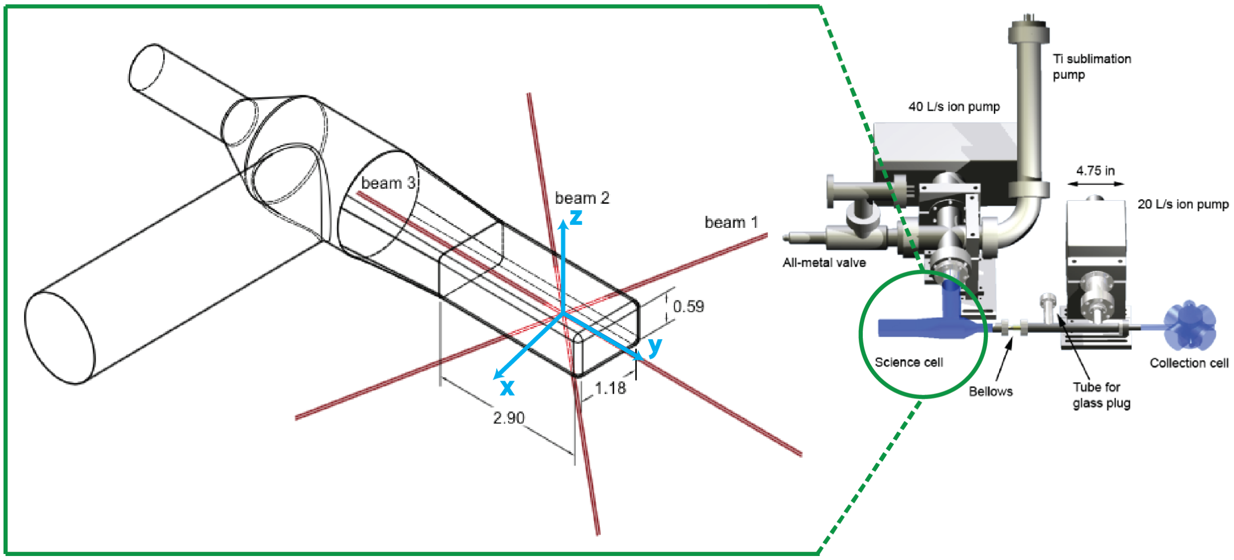

Figure 6.2: Experimental setup used to create optical lattices (images courtesy of DeMarco Lab, refer to [80] for more details). In this type of a setup the there are *Rb* dispensers in the collection cell that releases atoms into the cell. Atoms are then trapped using a Magnet-Optical Trap (MOT) made of magnetic fields and lasers. These atoms are then transferred to a spherical quadrupole magnetic trap that is mounted on a translation stage (not shown here). It moves that atoms from the collection cell to the science cell. The last stage in preparation occurs in the science cell, where atoms are loaded into another type of trap such as the Ioffe-Pritchard magnetic trap (IP). In this trap, atoms are further cooled via Evaporative cooling to produce a Bose-Einstein Condensate (BEC). At this stage, the system is ready for further modifications such as the loading of a clean optical lattice to realize the Bose-Hubbard model. (See text for further discussion.) Notice that the lattice laser beams are not oriented along conventional coordinates of the lab reference frame (shown in blue with gravity pointing along $-z$).

6.3 Experiments

6.3.1 Setup

The experiments are performed using laser and vacuum systems shown in Fig. (6.2). The captions detail the first part of the procedure used to trap and cool the gas in a MOT, eventually transferring it to the science cell where it is further confined and cooled to degeneracy. The system considered in this Section is prepared using 200,000 ^{87}Rb $|F=1, m_F=-1\rangle$ atoms confined in a harmonic trap that is formed from a single-beam optical dipole trap at 1064 nm traveling perpendicular to gravity and a magnetic quadrupole trap balancing gravity and providing additional harmonic confinement in the two horizontal directions. The entropy per particle is controlled by evaporating to different depths of the dipole trap, after which the depth is ramped to a constant value with a mean harmonic trap frequency of $\omega_0 = 2\pi\,(35.78 \pm 6)$ Hz. To keep the atom number roughly fixed for the different temperatures, the efficiency of the evaporation is selectively adjusted.

A cubic optical lattice is formed by exponentially ramping on three sets of retro-reflected lattice beams at $\lambda = 812$ nm over 100 ms using a 200 ms time constant (for most of the data in this chapter) as shown in Fig. (6.2). The lattice potential depth is characterized as sE_R, where $E_R = (h/\lambda)^2/2m = 2.31\times10^{-30}$ J is the recoil energy. Kaptiza-Dirac diffraction is used to calibrate s to within 7%. The potential is given by (5.31) which is of the sinusoidal form. Thus all the parameters can be obtained as discussed in (5.4). However, there is another component in experiments that renders the system inhomogeneous – a harmonic confining potential is needed to keep that atoms from flying away or dropping due to gravity. On top of this, the lattice beams add additional harmonic confinement, and the overall confinement is well-described by $\omega = \sqrt{\omega_0^2 + \frac{8sE_R}{m(2\pi)^2(120\mu m)^2}}$.

6.3.2 Measurements

There are two main observables of interest that can be used for a variety of different purposes, these are the peak fraction (f_0) and entropy-per-particle (S/N). For instance it will be shown that once correctly calibrated, $f_0(S/N)$ can be used to obtain information about the temperature of the strongly interacting system – a long standing problem in OLEs. However, before direct comparisons can be made it is important to understand the exactly what is being measured. Towards this end, the details of measurement procedures are discussed below. For the system considered in this section, after turning on the lattice and waiting for 10 ms, all potentials are turned off and the atoms are allowed to expand for 20 ms time-of-flight. Atoms are optically pumped into the $F = 2$ state, and absorption imaging is performed on the $F = 2$ to $F' = 3$ cycling transition.

The optical depth (OD) in absorption images saturates for $OD > 3$ (i.e., high column density) because of non-absorbable light in the imaging laser beam. This is a complication for imaging condensed gases at non-zero temperature, which possess high-density peaks and a low-density thermal component. To increase the dynamic range of imaging and obtain high signal-to-noise ratio data for the condensate and non-condensate atoms, a series of two images is taken in separate measurements. High OD images are produced by transferring all the atoms into $F = 2$, and low OD images are acquired by pumping a fraction of the atoms so that the $OD < 2$. High OD images are used to measure the atoms outside of the condensate peaks, and low OD images are employed to measure the atoms in the peaks (which are saturated in the high OD images). The relative number between high and low OD images is

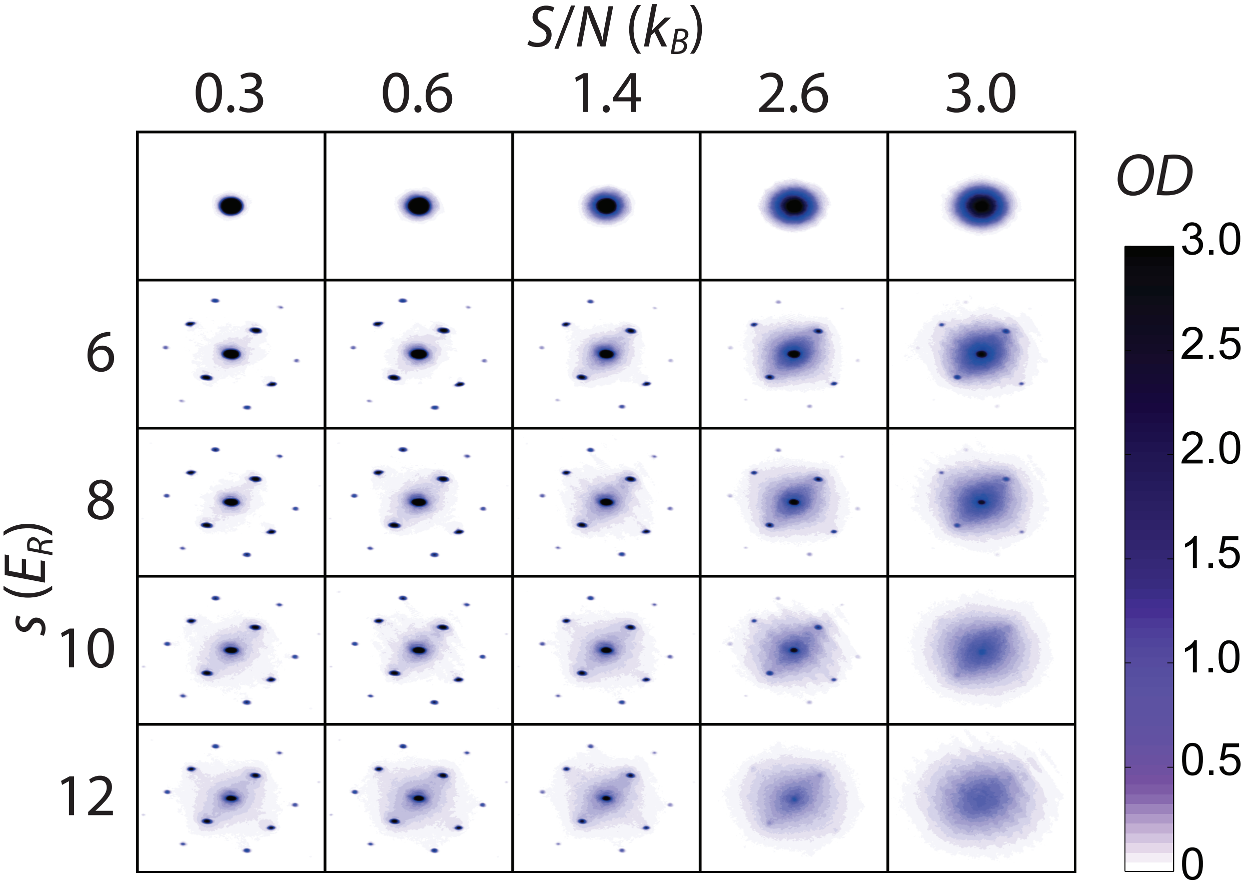

Figure 6.3: High OD TOF images for a variety of lattice depths (in units of E_{R}) and initial entropies averaged over 7 iterations. The top line shows the gas released from the harmonic trap; the starting conditions were almost identical for all lattice depths. The OD saturates at approximately 3 because of non-absorbable light in the laser beam used for imaging.

calibrated and quantities such as condensate fraction are verified to agree between the two modalities using a gas released from the trap.

A typical experimental sequence at a given lattice depth and entropy per particle involved 7 sets of 4 images: a high OD and low OD image in the harmonic trap, and a high OD and low OD image in the lattice. All quantities presented in this discussion are averages over these 7 sets of images. Fig.Fig. 6.3 illustrates the resulting averaged high OD images.

To determine S/N for the gas before turning on the lattice, images for gases released from the harmonic trap were fit using a multi-step scheme similar to that employed in Ref. [81] to determine the condensate fraction. The high OD image was fit to a Thomas-Fermi (TF) profile combined with an independent Gaussian function, taking into account the line-of-sight integration. The pixels within a radius 10% greater then TF radius were masked, and the

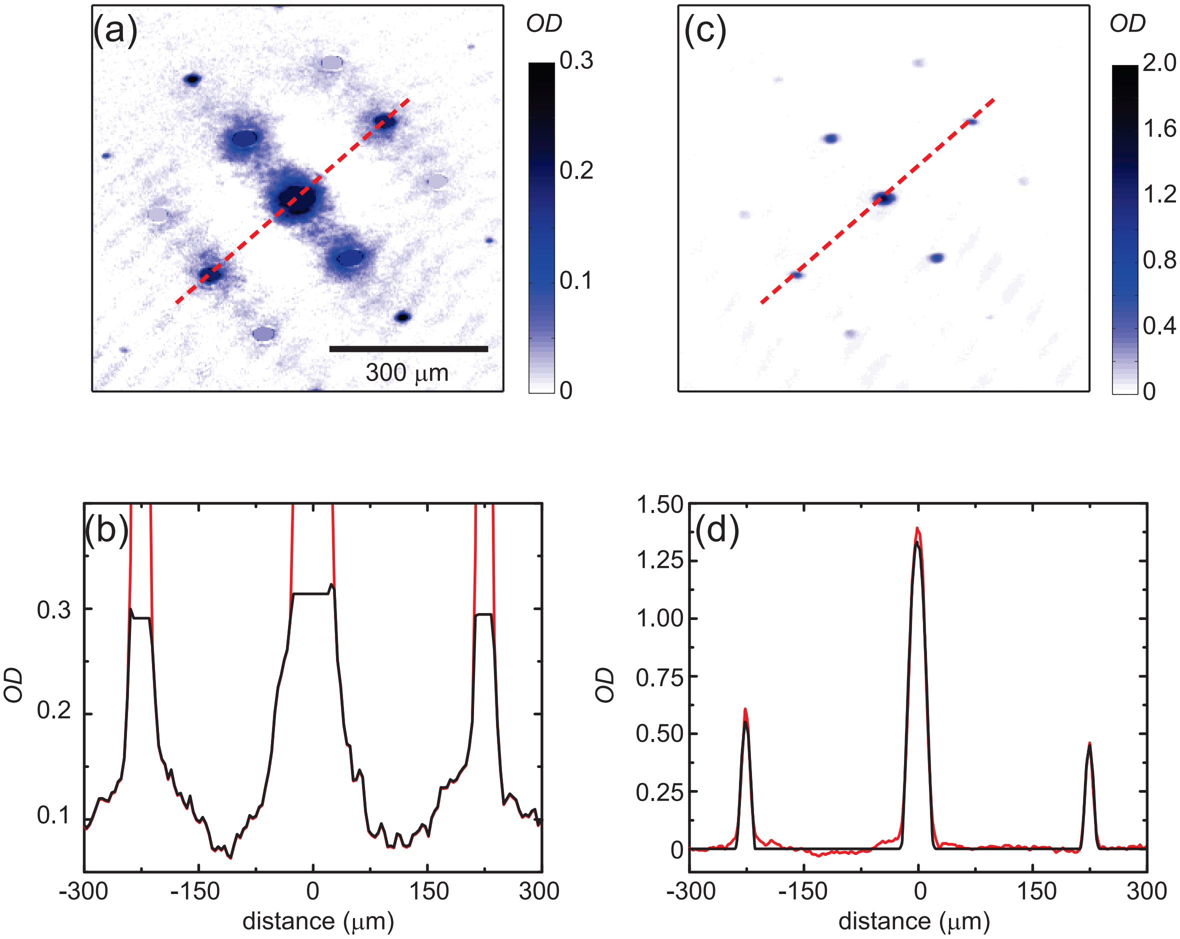

Figure 6.4: (Color Online) Illustration of the fitting procedure used to determine peak fraction from a high *OD* image (a and b) and from a low *OD* image (c and d). Here an averaged image for $s = 10$ and $S/Nk_B \approx 1.35$ (middle image in Figure 6.3) is used. For all these images, first a Gaussian fit is subtracted off as described in the main text. In (a), the high OD image with the peaks masked and the non-peak distribution coincident with the peak assumed to be a uniform distribution is shown. Note that the nine peaks that correspond to zero momentum and the first- and second-order diffraction peaks have been masked. The higher-order peaks, which contain a negligible number of atoms have been ignored. A slice along the red dashed line is displayed in (b). The black line is the non-peak distribution, and the red line is the complete image including the peaks. In (c), the low *OD* image used to determined the peak number is shown. A slice along the red dashed line is displayed in (d). The black line is the TF fit to the peaks and the red line is the data from the image. Note that there is a scale factor between the high and low OD images of approximately 5.75.

remaining image was fit to a Bose-Einstein distribution to determine the number of thermal atoms N_{th}. In images with sufficient signal, the low *OD* image was fit to a combined TF–thermal profile, and the condensate number N_{BEC} was determined from the TF component. The condensate fraction was determined as $N_{\mathrm{BEC}}/(N_{\mathrm{th}} + N_{\mathrm{BEC}})$ in this case. If the signal-to-noise ratio was too small to resolve the thermal component in the low *OD* image, a fit to a simple TF profile was used determine the number of atoms N_{TF} within the TF radius. The total number of atoms N was determined in this case by adding the number of atoms outside the TF radius in the high OD image. The condensate fraction was then $1 - N_{\mathrm{th}}/N$. Entropy per particle was determined from the condensate fraction and total number using the semi-ideal model [82].

Peak fraction f_0 was determined from images of the gas released from the lattice using the procedure from Ref. [83]. Several complications make interpreting fits to TOF images for lattice gases difficult. Unlike the trapped case, the functional form of the density distribution after TOF is unknown. Furthermore, atoms that appear outside of the condensate peaks are a combination of superfluid atoms (expelled from single-particle low-momentum states by strong interactions) and thermal atoms. A final challenge is specific to this apparatus—there is no spherical symmetry in a lattice momentum distribution, and the imaging direction is not along a lattice direction. This makes even the non-interacting distribution difficult to fit (see Eq. 23 in Ref. [84]).

In the face of these difficulties, a heuristic approach is adopted that is fast and independent of experiment details. In the high OD image, the peaks are masked and the distribution is fit to a single Gaussian. The number of atoms from this fit is N_{Gauss}. Next, the Gaussian fit is subtracted from the image and we fit each peak to a TF profile. These fits are used to mask the peaks, and remaining signal is summed to determine the number of atoms $N_{\sum}$ outside of the peaks and not included in the Gaussian fit. These steps capture all the non-peak atoms, except those that are part of the broader distribution and coincident with (or "under") the peaks in the image. Counting these atoms accurately would require knowledge of the density distribution after TOF, including the effects of interactions [85, 86, 87, 88]. Since analytical expressions for the TOF distribution are unknown, the simple assumption that the non-peak distribution that overlaps with the peak is uniform, is made; see (a) and (b) of Fig. 6.4. The average non-peak OD coincident with the peak is determined by averaging the OD around the perimeter of the peak. The number of non-peak atoms N_{unpk} coincident with the peak is estimated using a uniform distribution with this average OD. The total non-peak number of atoms is $N_{\mathrm{nonpk}} = N_{\mathrm{Gauss}} + N_{\sum} + N_{\mathrm{unpk}}$.

Only the peaks of the low OD image is fit to determine the peak number N_{pk} using a series of TF profiles (subtracting off a Gaussian if there is sufficient signal); see (c) and (d) of Figure 6.4. The total number is then $N = N_{\mathrm{pk}} + N_{\mathrm{nonpk}}$, and the peak fraction is $f_0 = 1 - N_{\mathrm{nonpk}}/N$. In the next Section the relationship between f_0 and the true condensate fraction n_0 of the system is explored by applying this fitting procedure to simulated TOF images produced using exact QMC calculations. This will also allow the assessment of equilibration in the lattice.

6.4 Quantum Monte Carlo Measurements

QMC simulations are carried out using the stochastic series expansion method (SSE) [36]. SSE is an exact method suffering from no biases or approximations. The condensate fraction n_0 is obtained directly from the single-particle density matrix in adherence to its rigorous definition as the ratio of the occupation number of the macroscopically occupied single-particle mode to the total particle number. These have been discussed in detail in part 2. For the purposes of comparisons with experiment there are details pertaining to the momentum distribution and S/N calculations that will be discussed next.

6.4.1 Finite Time-of-Flight Effects

Recall that the momentum distribution calculated from the single-particle density matrix for clean systems (3.38) can be decomposed into single-particle eigenmodes:

$$n(\vec{k}) = |w(\vec{k})|^2 \sum_{jl} e^{i\vec{k}\cdot(\vec{j}-\vec{l})} \rho(\vec{i},\vec{j}) = n_0(\vec{k}) + \sum_{p=1} n_p(\vec{k}). \tag{6.37}$$

However, in order to match with experiments it is important to include finite TOF effects [89], by adding an additional site dependent phase term to (3.38) so that each component is modified via

$$n_p^\tau(\vec{k}) = |w(\vec{k})|^2 N_p \sum_{\vec{j}\vec{l}} e^{i\vec{k}\cdot(\vec{j}-\vec{l}) - i(m/2\hbar\tau)(\vec{j}^2-\vec{l}^2)} \langle\vec{j}|\psi_p\rangle\langle\psi_p|\vec{l}\rangle, \tag{6.38}$$

where τ is the TOF time, m is the particle mass. $n_0^\tau(\vec{k})$ is used to denote the finite TOF condensate and $n_{nc}^\tau(\vec{k}) \equiv \sum_{p\neq 0} n_p(\vec{k})$ for the finite TOF non-condensate distributions. At sufficiently low temperature, $n_{nc}(\vec{k})$ shows the quantum depleted (QD) atoms excited from $n_0(\vec{k})$ by the interactions. At intermediate temperatures, both thermal and interaction effects will cause depletion of the condensate, however, there is no simple criteria for separating them into thermal and quantum depleted portions. From an experimental standpoint, extracting n_0 requires no knowledge of the details of the different non-condensate modes. However, the finite TOF can affect the shape of the momentum distributions and so the experimental

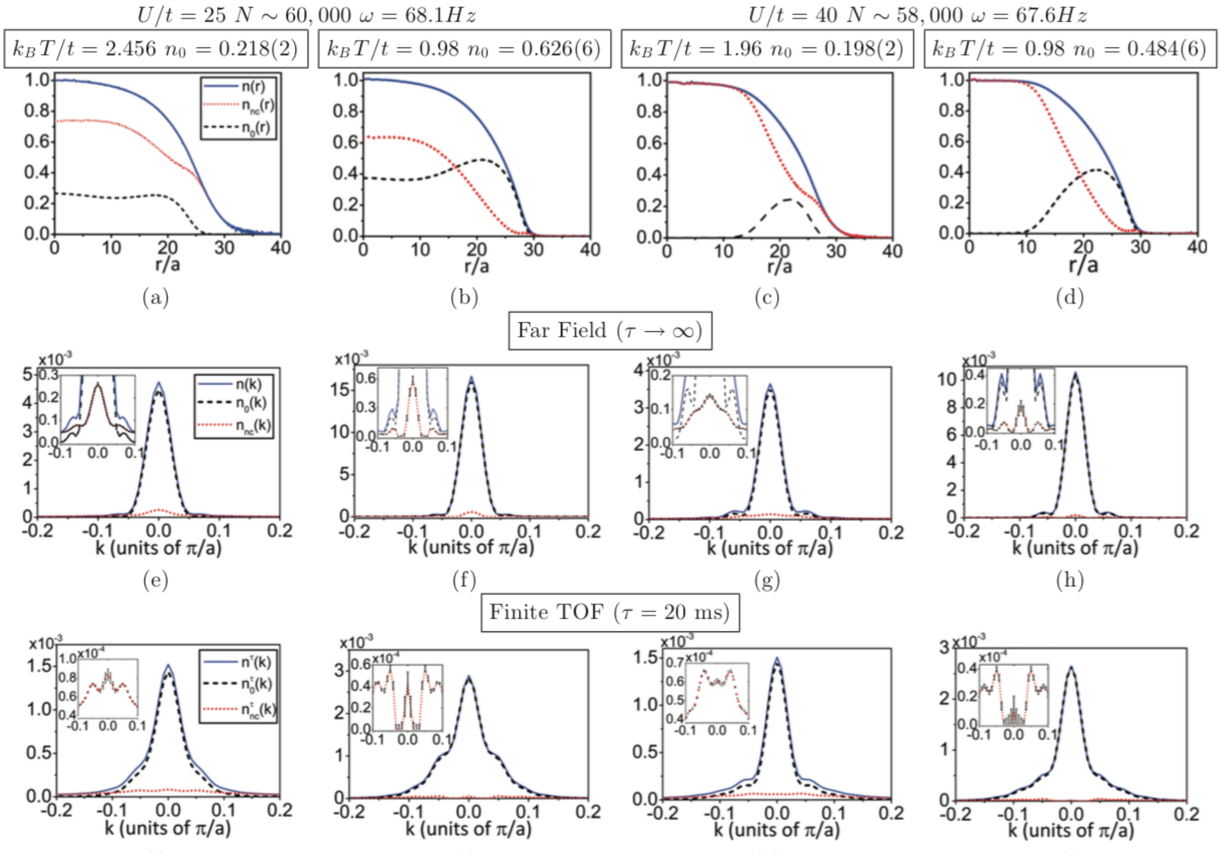

(a) (b) (c) (d)

(e) (f) (g) (h)

(i) (j) (k) (l)

Figure 6.5: (Color online.) Top row (a-d) are the spatial particle densities, middle row (e-h) and bottom row (i-l) are the far field column integrated and finite TOF momentum distributions. Insets of (e-h) show fine features for all distributions and of (i-l) show zoomed versions of the finite TOF non-condensate distribution ($n^{\tau}_{nc}(k)$). For the momentum distributions in the middle and last line the y-axis is in arbitrary units, but the scale is the same for all images.

procedure to obtain estimates of the n_0 must account for these effects.

In order to ascertain the behavior of these, effects QMC simulations were undertaken for two types of trapped systems [90]: one set of parameters correspond to the superfluid regime at $U/t = 25$, while the other corresponds to the Mott-Insulating regime ($U/t = 40$). For these simulations, the number of particles, $N \sim 58000$ to 64000. In Fig. (6.5a-d), the exact $n(r)$ corresponding to large U has been presented. (The trap frequency has been adjusted so that $n(r = 0) = 1$; the density is 1 atom/lattice site at the center of the trap.) At $U/t = 40$, the Mott Insulating (MI) domain appears as an integer plateau.

The corresponding column integrated momentum distributions in the far-field, shown in Fig. (6.5e-h), exhibit secondary peaks similar to [91, 92]. Note that these peaks can arise not only due to the finite extent of the condensate but rather all modes (Fig. (6.5e-h) insets).

However, it is only around the MI regime that it forms around $k = 2\pi/\xi_0$, where ξ_0 is the width of the condensate. This is specifically due to the way the condensate forms between domain boundaries (in this case between the MI and the vacuum).

Finite TOF effects, presented in Fig. (6.5i-l), alter the far field distributions by suppressing and blurring the central low k values, as expected [89]. Higher order modes of $\hat{\rho}_1$ with rapid spatial variations are not significantly affected by the site dependent phase shift. Thus, the maximum effect is on the condensate distribution. The time scale for the condensate to reach the far field (τ_{ff}) is $\propto R\xi_0(1 - \xi_0/2R)$, where R is the radial extent of the condensate. This leads to larger τ_{ff} for $U/t = 25$ and so for the fixed $\tau = 20$ms, the central peak sees a greater suppression (and surrounding region greater enhancement) than $U/t = 40$. Although, $n(k)$ and $n^{\tau}(k)$ are both broader due to the secondary peaks, the latter case has relatively more condensate atoms. Standard schemes used by experiments discussed in the previous Section would *not* be able to capture this type of broadening. Note that the broader structure is observable within the experimental resolution. Using $\Delta k = (m\lambda\pi/h\tau)\Delta r/a$, where λ the wavelength of the optical lattice, τ the expansion time, Δr the resolution, we obtain the Δk resolution. Using ${}^{87}Rb$, $\tau = 20$ ms, $\lambda = 800nm$ and typical resolving power of $\Delta r = 3\mu m$ gives $\Delta ka \sim 0.026\pi/a$. Features in Fig. (6.5i-l) are spread over $\Delta k \sim 0.06\pi/a$. The exact nature of the error that results from this form of finite TOF broadening depends on the specific fitting procedure used. Therefore it is vitally important that experimental protocol is calibrated against exact distributions. This idea is used later for full scale comparisons between theory and experiment. Before continuing in that direction, it is useful to consider what kind of qualitative discrepancies might result due to ad-hoc fitting procedures.

Although the error in estimating n_0 will be specific to the fitting procedure used, we can systematically try to analyze its bounds. f_0 can be estimated by calculating the ratio of atoms under the central peak (up to a limit k_l) to the total number of atoms. (The numbers are calculated from column integrated images without the wannier envelope to circumvent the need to de-convolve it.) The range is chosen large enough to accommodate finite optical resolvability in experiments. It should also allow for related fitting procedures. Comparisons with exact results is presented in Fig. (6.6a and b) approximated by:

$$n_0(T) = n_0^*(1 - exp(g(1 - \frac{T_i}{T})), \tag{6.39}$$

away from the critical regime.[2] At low T, the depletion is severely overestimated whereas

---

[2] The function (6.39) is a good fit for our QMC data provided $k_bT/t \leq 2.183$ (2.807) where $n_0 \geq 0.0891(4)$ (0.0726(3)) for $U/t = 25$ (40)

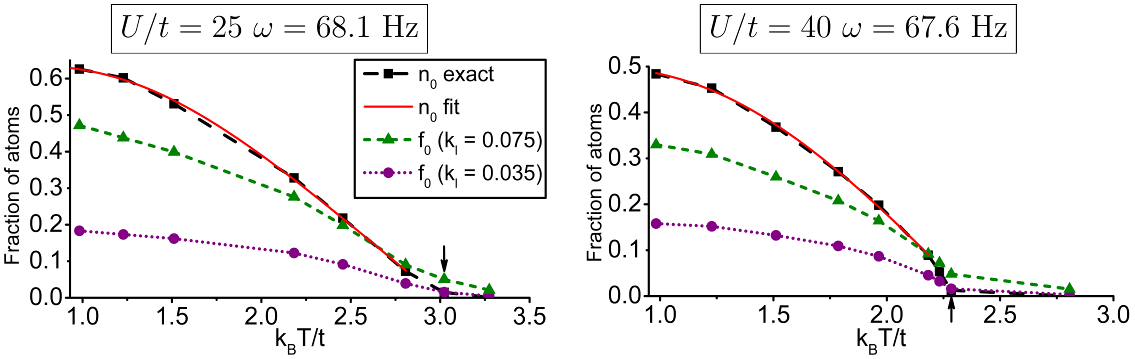

(a) (b)

Figure 6.6: (Color online.) Condensate fraction (n_0) as a function of temperature (T) compared with coherence fraction ($f_0(T)$) measurements for different cutoff k_l. ($f_0 \equiv \sum_{|k|<k_l} n_0(k)/N$.) We have fit n_0 to (6.39) where $n_0^* = 0.638(7)$ $(0.502(6))$, $k_B T_i/t = 2.99(2)$ $(2.36(1))$ and $g = 1.91(9)$ $(2.4(1))$ for $U/t = 25$ (40). The short arrows indicate $k_B T_c/t = 3.023$ (2.285) for $U/t = 25$ (40) where $n_0 \sim 0.01$. The error bars are smaller than point size used in plots.

around the transition it is underestimated. Care is needed in the estimation of T_c using f_0. The specific nature of the error in measuring T_c from $f_0(T)$ will depend on the exact form of the latter. For instance, from the fitting procedure use here, for $k_l \geq 0.035$, $f_0(k_l) > n_0$. If T_c is to be estimated correctly, $|\partial^2 f_0/\partial T^2| > |\partial^2 n_0/\partial T^2|$ is required for rapid convergence to the same $n_0(T) \to 0$. The most rigourous way to estimate T_c would be to study the trap-size scaling behavior analogous to finite size scaling studies done for homogeneous systems that would also identify critical exponents for trapped systems [93]. Here a simple working definition of $n_0(T_c) \sim 0.01$ suffices to show that estimates of T_c using f_0 directly would be incorrect: in Fig. (6.6a and b), $k_B T_c/t = 3.022$ (2.284), but using f_0, $3.023(2.29) < k_B T_c/t < 3.3(2.81)$ for $U/t = 25$ (40). Furthermore, a smooth decrease in $f_0(T)$ across the transition may prevent the presence of a clear inflection point thereby making accurate estimates of T_c difficult.

Having discussed the general effects of finite TOF and the errors that result, the next discussion focusses on direct comparisons of experiment with theory. For such purposes, QMC simulations are undertaken that match all the parameters of the experiments – so that calculations are of the *ab initio* type. The particle number is kept constant to within 5% of $N = 200,000$ for optical lattice depths of s = 6,8,10 and 12. Furthermore, the confining potential is accounted for exactly in the QMC simulations, unlike MFTs which use the LDA. The momentum distribution $n(\vec{k})$ from QMC simulations is used to generate line-of-sight integrated images. Finite TOF effects—which lead to additional overlap between the condensate and non-condensate distributions—are fully accounted for as discussed above, following Ref. [90], and the integration direction is matched to the experiment. These images are then used to extract the peak fraction using the fitting procedure applied to the

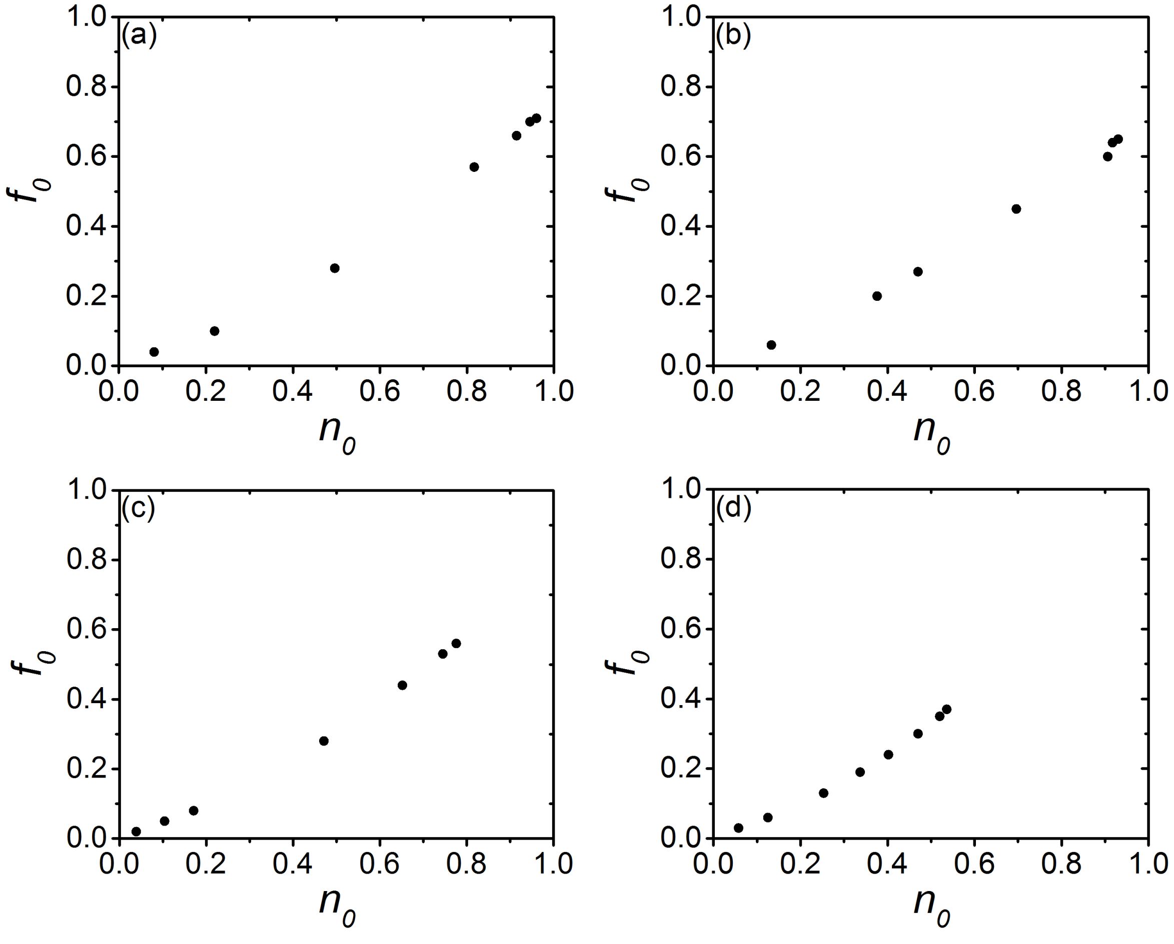

Figure 6.7: Comparison of condensate n_0 and peak f_0 fraction obtained from QMC simulations for $s = 6, 8, 10, 12$ (a-d, respectively). n_0 was obtained directly by diagonalizing the single-particle density matrix. f_0 was calculated by fitting QMC momentum distributions for a finite TOF of 20 ms using experimental fitting procedures. The monotonic dependence is clear, but it is to be noted that the procedure cannot be used when $n_0 < 0.05$. The uncertainty in these values is smaller than 1%. The maximum n_0 and f_0 is smaller at higher s because of quantum depletion.

experiment modified to work with a single image. Fig. 6.7 shows n_0 and f_0 computed at the same temperature for the s sampled in the experiment. It is evident that n_0 and f_0 are monotonically related, and that peak fraction can be used to determine temperature in the experiment (assuming that equilibrium is achieved). The relationship between f_0 and n_0 also does not depend strongly on lattice potential depth. When $n_0 < 0.05$, the fitting procedure cannot identify the presence of condensate even with virtually noiseless QMC data.

Generally, f_0 is less than n_0. This discrepancy between f_0 and n_0 arises from inaccurate accounting of the condensate and non-condensate distributions. In part, this is due to the high-momentum tails of the condensate that extend into the broad Gaussian-like part of

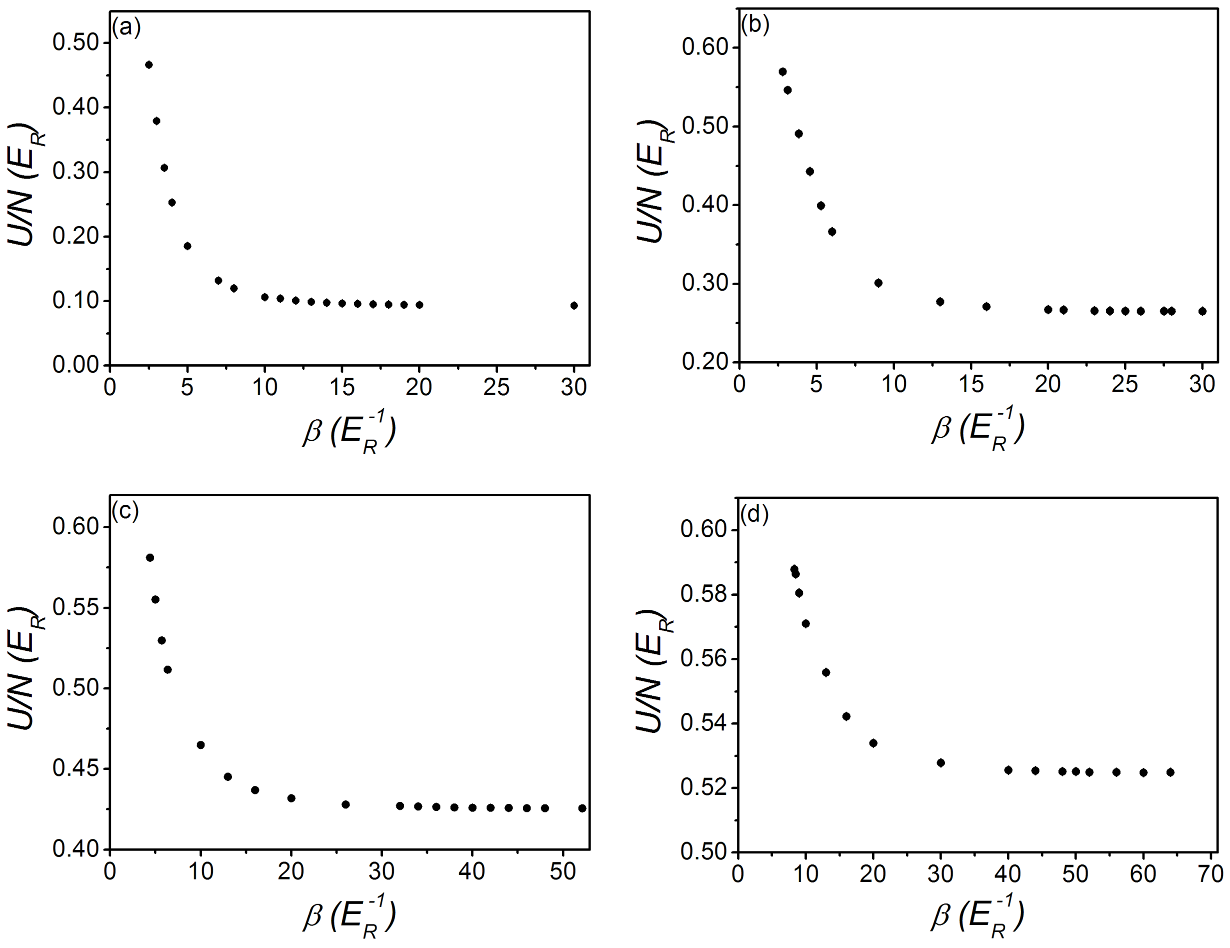

Figure 6.8: The energy per particle for varying lattice depths $s = \{6, 8, 10, 12\}$ (a-d, respectively) for a system of $N \sim 200,000$ particles in a trap. These point were fitted using a procedure outlined in the text to obtain the entropy per particle that can be compared with experiment. Temperatures only below the critical temperature for superfluidity are sampled.

the momentum distribution, and that are mistakenly accounted for as non-condensate by the fitting procedure discussed above [90]. Apart from these systematic errors in the fitting protocol, there may also be additional interaction effects that arise during TOF that cannot be accounted for in the QMC simulations.

6.4.2 Entropy Estimation

The QMC simulations are carried out at temperatures that span the range explored by the experiment, but that are chosen independently of the measurements. In order to compare with experiments that have access to the entropy per particle but not temperature, QMC simulations are used to compute the temperature dependence of S/N. This is done by integrating the internal energy per particle ($u(\beta) \equiv U/N(\beta)$) shown in Fig. 6.8, obtained from

QMC simulations, where $\beta = 1/k_B T$.

Using the definition $u(\beta) = u_0 + f(\beta)$, where $u_0 \equiv lim_{\beta\to\infty} u(\beta)$ is the ground state energy and $f(\beta)$ is a monotonically decreasing function that characterizes the temperature dependence with $lim_{\beta\to\infty} f(\beta) \to 0$,

$$S/N(\beta) = \beta f(\beta)|_{\infty}^{\beta} + \int_{\beta}^{\infty} f(\beta) d\beta = \beta f(\beta) + \int_{\beta}^{\infty} f(\beta) d\beta, \tag{6.40}$$

is obtained. Here the limit $lim_{\beta\to\infty} \beta f(\beta)$ can be taken provided $f(\beta)$ decays faster than linearly—a condition that is easily met since the data fit well to an exponential function with a reduced $\chi^2 \sim 1$. The strategy used here is to integrate u using a fit to all sampled points. The high β tail is fit to an exponential decay, since finite temperature methods cannot be directly used to access the true ground-state energy at $\beta \to \infty$. The high temperature points are fit using a cubic spline. Error bars for S/N are computed using a resampling procedure [94]. For each $u(\beta)$ that has been computed, a gaussian of mean $u(\beta)$ and standard deviation $\sigma(u)$ is sampled to generate a sample $u_i(\beta)$. A collection of u_i describe the vector $U_i \equiv \{u(\beta)\}$ that is fitted to obtain an estimate of $(S/N)_i$. This procedure is repeated multiple times to obtain an estimate of $\langle S/N(\beta) \rangle$ and $\sigma(S/N)$.

6.5 Comparisons between MFT and QMC

Predictions for condensate fraction n_0 at different entropies per particle and lattice potential depths are shown in Fig. (6.9) for QMC simulations and MFTs. In each case, T and μ are varied to match S/N and N as computed by the method of interest. While all approaches show the same qualitative trend, it is clear that HF theory is, in general, not in good agreement with the QMC approach. This disagreement is expected because HF theory does not account for the mixing of particle and hole-like excitations that result from interactions. The comparisons of QMC against Gutzwiller and HFBP results suggest that for moderate interaction strengths (at $s = 6$ to 8) these MFTs work generally well. For stronger interactions (at $s = 10$), HFBP calculations fail to capture finite temperature effects, whereas the Gutzwiller approximation is able to capture qualitative features. At the highest lattice potential depths we sample ($s = 12$), the Gutzwiller method can capture the high temperature regime, but cannot accurately compute the correlations at low temperature, as is evidenced by the 15-25% error in n_0 for $S/N < 0.5\ k_B$.

As an additional comparison, Fig. (6.10) shows the same data as in Fig. (6.9) but with

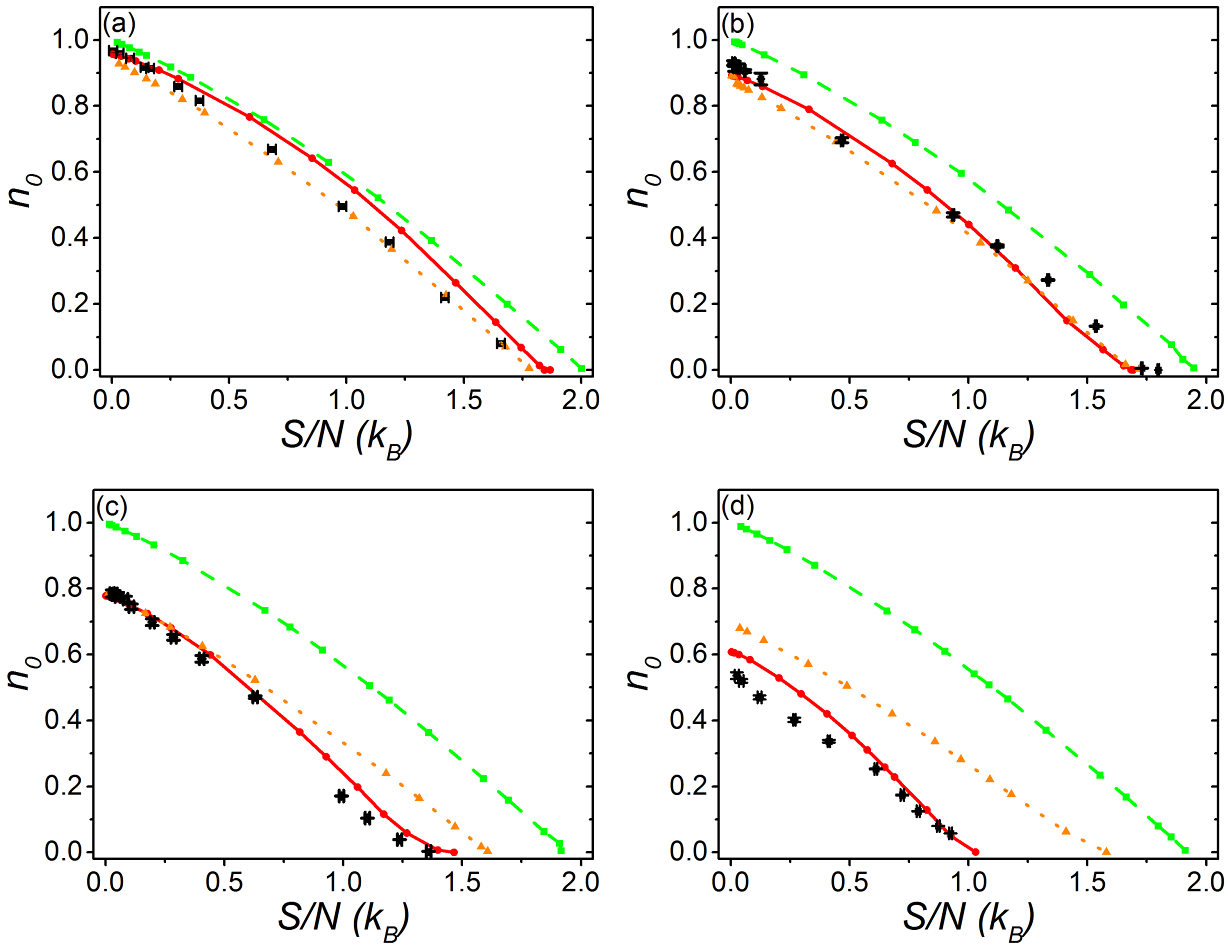

Figure 6.9: (Color online) Comparison between different types of mean field theories against QMC results. Panels (a)-(d) correspond to s = 6,8,10,12, respectively. The particle number was kept constant at $N \sim 200,000$. All other parameters were matched to experimental specifications presented in Fig. (6.12). Green squares (dashed line) correspond to HF, orange triangles (dotted line) to HFBP, red circles (solid line) to Gutzwiller, and black diamonds (with error bars) to QMC. The error bars show the statistical uncertainty in the QMC results.

inverse temperatures instead of S/N. The advantage of this comparison is that it subverts the need to estimate S/N from the fitting procedure discussed earlier. Via this comparison it is also clear that the thermodynamic observables can deviate significantly for approximate theories.

While the validity of the Gutzwiller approximation over a wide range of interaction strengths and temperatures is suggestive, this is only likely true for the high filling limit (a central density of approximately 3 particles per site) considered in this work. QMC simulations for low filling systems show that the differences with the Gutzwiller approximation can be quite large, as evident for the results for a central density of one particle per site

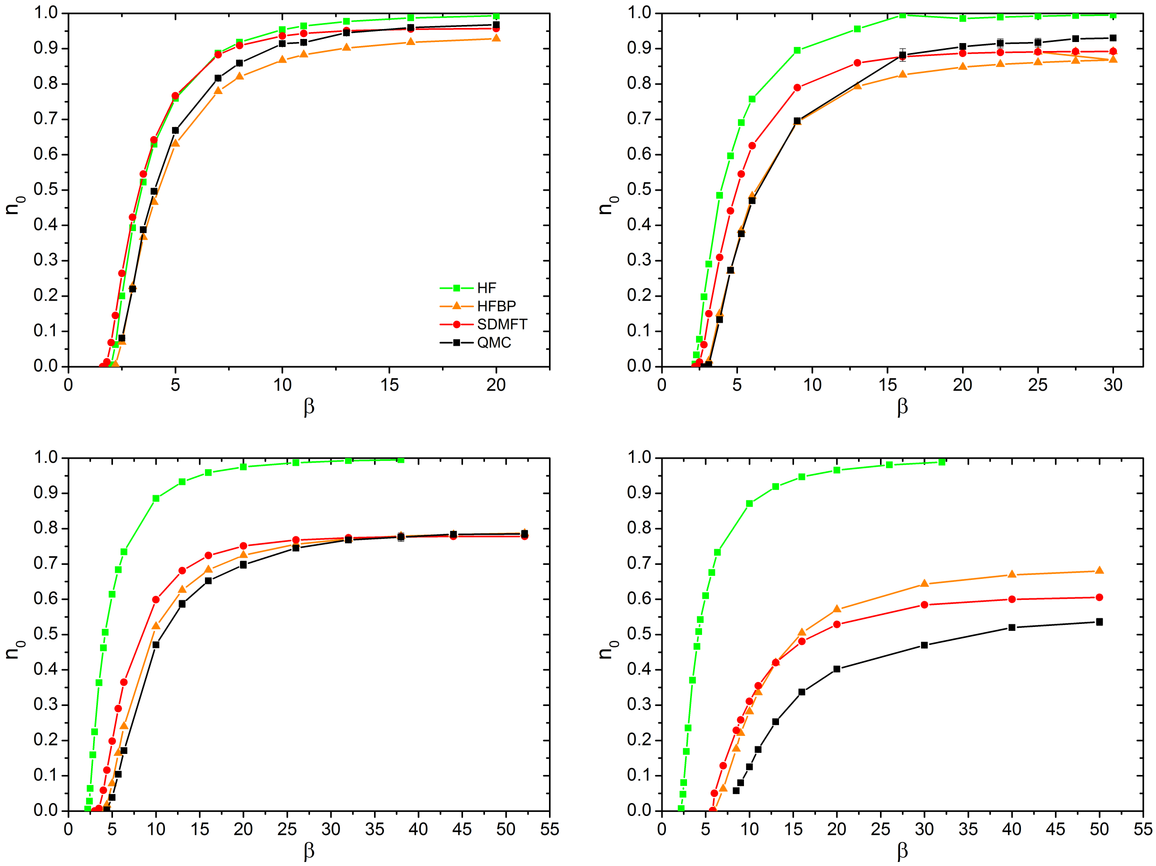

Figure 6.10: Shows the same data as in reffig:datatheorycomp but temperature dependence instead of S/N. It is evident that as the system becomes strongly correlated there are strong discrepancies with exact results.

shown in Fig. (6.11). The discrepancy apparent in Fig. (6.11) may also arise from quantum critical behavior, as the lattice potential depth is set close to the MI–SF phase transition.

In conclusion HF and HFBP approximations should not be used to compute observables such as n_0 and thermodynamic variables like S/N. While the Gutzwiller approximation can provide quantitatively accurate results at high filling and for moderate lattice potential depths, it fails at low S/N and for strong interactions and for low densities. Therefore all further comparisons are made using only QMC simulation results to compute S/N and f_0 for comparisons with the experimental data.

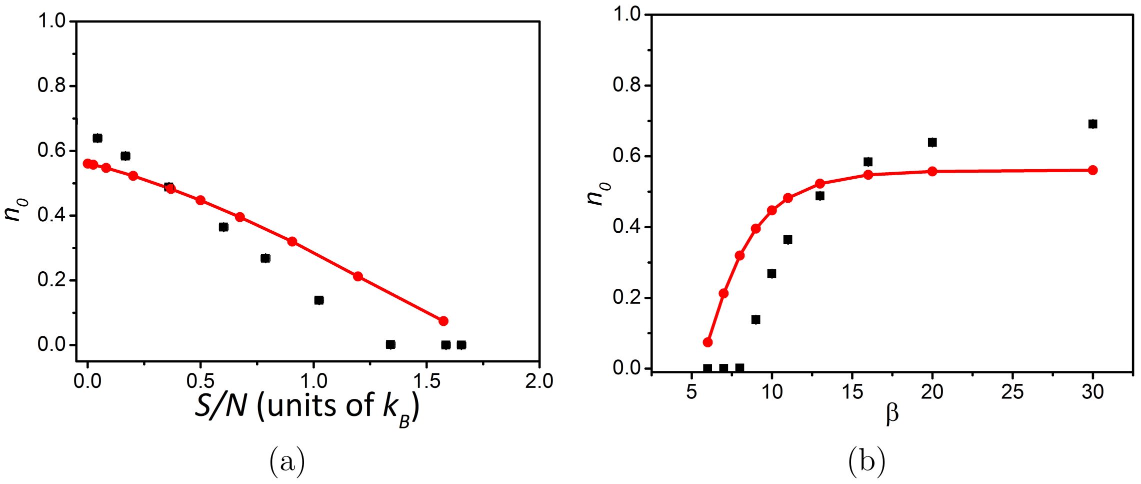

(a) (b)

Figure 6.11: (a) Comparison between Gutzwiller (red circles) and QMC (black squares) results for a strongly interacting system ($s = 13.6$) at low filling. The central density for these results is approximately one particle per site with $\omega = 2\pi \times 55.6\ Hz$ and $N \sim 60,000$. The line is a guide to the eye. (b) Shows the corresponding results for n_0 vs β

6.6 Metastability of the Condensate

To assess thermal equilibrium in the experiment, a comparison between the experimentally measured f_0 (determined from images shown in 6.3 and the fitting procedure described in 6.3 and the equilibrium QMC prediction at the same S/N is shown in Fig. 6.12. A strong discrepancy is evident: there is alarming degree of disagreement between the QMC results and the experiment at high temperatures (i.e., high S/N). The experimentally observed peak fraction (and therefore condensate fraction) are systematically high compared with the QMC prediction. What is more troubling is that the condensate survives beyond the transition temperature, which is marked by f_0 (and n_0) vanishing in the QMC predictions.

This discrepancy can be explained by systematic errors in the analysis of the experimental data. One source of error might be that binary collisions between atoms in different peaks eject condensate atoms during TOF [95, 96]. While this effect may play a role in suppressing peak fraction for the lowest entropies at $s = 6$, its impact should be reduced at higher lattice potential depths and temperatures as the condensate density decreases. Furthermore, this effect would lead to lower, not higher, peak fractions than the equilibrium QMC prediction.

Another possibility is the erroneous identification of peaks in the TOF image. It has been previously discussed that sharp peaks in momentum distributions may not be uniquely associated with a condensate [97, 98]. However, calculations focusing on trapped systems for realistic experimental conditions and experiments have demonstrated that the visibility,

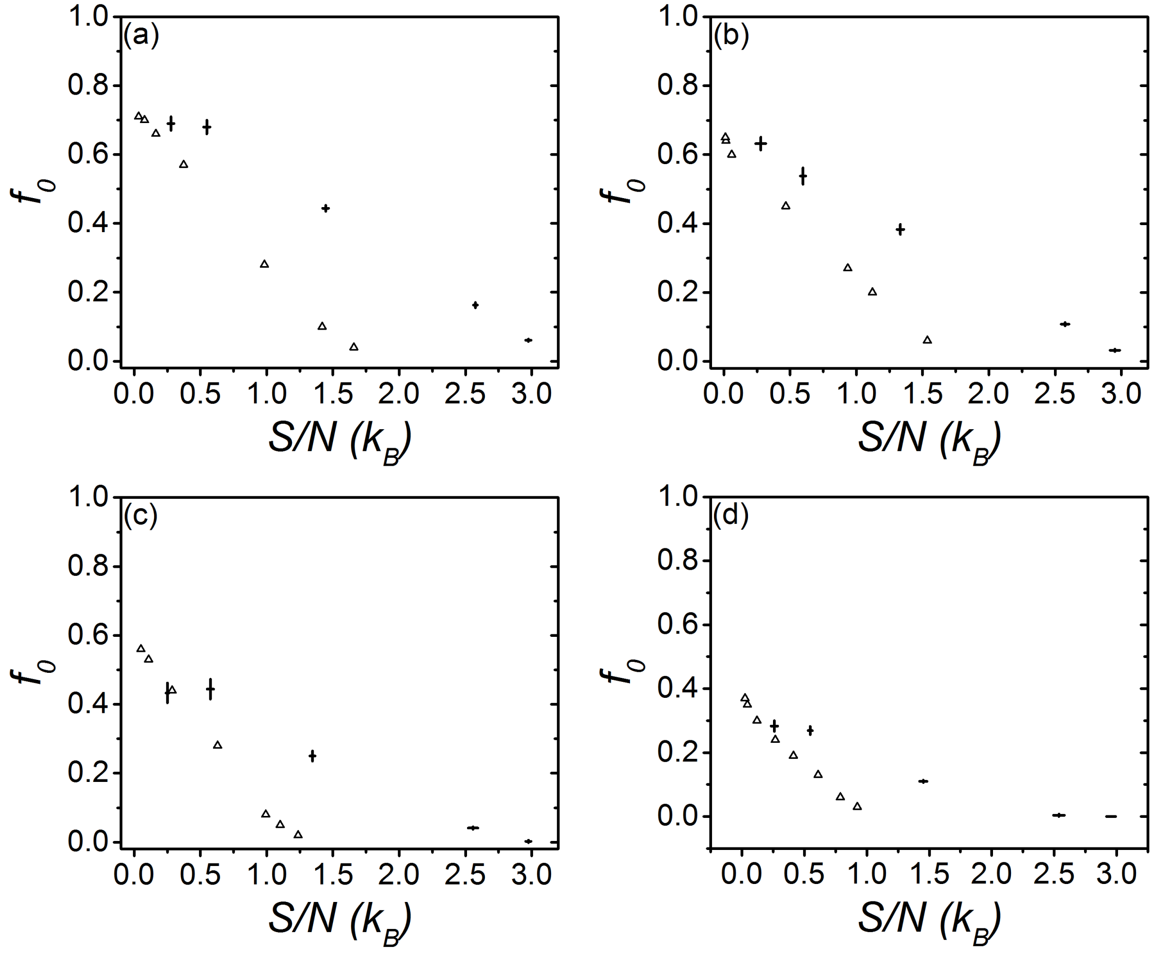

Figure 6.12: Experimentally determined peak fraction at each lattice depth as a function of the initial entropy per particle in the harmonic trap (circles). Corresponding peak fraction from QMC simulations determined by fitting the momentum distribution using the same procedure used in experiments in the lattice are also shown (triangles). The number of atoms at each experimental point (from lowest to highest entropy) is (a) $s = 6$, $N = \{2.38 \pm 0.03, 2.08 \pm 0.06, 1.64 \pm 0.03, 2.04 \pm 0.07, 2.06 \pm 0.09\} \times 10^5$, (b) $s = 8$, $N = \{2.36 \pm 0.06, 2.05 \pm 0.11, 1.66 \pm 0.07, 2.02 \pm 0.09, 1.73 \pm 0.05\} \times 10^5$, (c) $s = 10$, $N = \{2.41 \pm 0.08, 2.15 \pm 0.11, 1.68 \pm 0.09, 2.03 \pm 0.16, 1.85 \pm 0.09\} \times 10^5$ and, for (d) $s = 12$, $N = \{2.55 \pm 0.12, 1.98 \pm 0.10, 1.65 \pm 0.04, 2.06 \pm 0.11, 1.74 \pm 0.11\} \times 10^5$. QMC curves are constrained to a constant number, which is the mean of the number at each lattice depth ($N \sim 200,000$). The tunneling, interaction energies and trap frequencies for $s = \{6, 8, 10, 12\}$ respectively are $t = \{1.17, 0.711, 0.443, 0.283\} \times 10^{-31}$J, $U = \{3.92, 5.23, 6.48, 7.67\} \times 10^{-31}$J and $\omega = 2\pi \times \{51.27, 55.48, 59.4, 63.07\}$Hz. The error bars in the experimental data show the standard error of the mean for the average across 7 measurements. The horizontal error bars for the measurements also include the influence of the uncertainty in the trap frequency and number of atoms and do not impact the QMC results. The uncertainty in the QMC results are too small to be visible.

which is a quantitative measure of peak sharpness, can distinguish between condensed and non-condensed states [99, 100, 21]. The features we observe at high S/N are narrow and quantitatively similar in extent to the peaks observed at low temperatures. The sharpness of the peaks we measure at high S/N is most apparent in the $s = 6$ and $s = 8$ images shown in Fig. (6.3). This bimodal nature of the TOF images is associated with the existence of a condensate [101], and thus it is highly unlikely that we are systematically finding a non-zero peak fraction in images where a condensate is absent. Furthermore, peaks are not observed in the TOF distribution determined from QMC above T_c.

A further potential source of systematic error is heating by the lattice light [102], which would have the largest impact at low entropy. However, the QMC equilibrium predictions and the experimental data agree well in this regime. For higher entropies, heating should reduce peak fraction below the QMC prediction, which is opposite to the observed behavior.

In conclusion the measured peak fraction is systematically higher than that allowed in equilibrium by the second law of thermodynamics—the measured f_0 implies that the gas is at lower S/N after the lattice is turned on. Furthermore, a condensate appears present at temperatures exceeding the critical temperature for superfluidity in the lattice. Condensate and peak fraction should always decrease in equilibrium as the lattice is turned on to higher s because of quantum depletion resulting from strong inter-particle interactions.

The experimental observations imply that equilibrium is not established and the condensate is metastable during the lattice turn on. A natural question is whether the lattice is turned on too quickly for thermalization to take place. One limitation is non-adabaticity associated with changes in the size of the gas and mass flow [103]. This problem is primarily associated with the Mott-insulator regime, which we do not sample here. Furthermore, estimates of the overall rms radius of the gas changes by less than 20% at $s = 6$ and $S/N \approx 1.5\ k_B$ when the lattice is turned on, which is not likely to cause the large discrepancy evident in Fig. (6.12) for these parameters.

Another issue is how the lattice turn-on time compares with natural timescales in the Hamiltonian. The 100 ms lattice turn-on time is slow compared with the Hubbard timescales h/t and h/U, which vary from 6–24 ms and 2–1 ms for $s = 6$–12. The many-particle timescale for thermalization may be longer than these single- and two-particle times, however. This possibility is examined at $s = 6$ by turning on the lattice over times up to 1 s for different S/N in the trap. According to Fig. (6.13), data for low S/N shows where the agreement with QMC predictions is good, and high S/N where the experimental peak fraction is non-zero above the critical temperature.

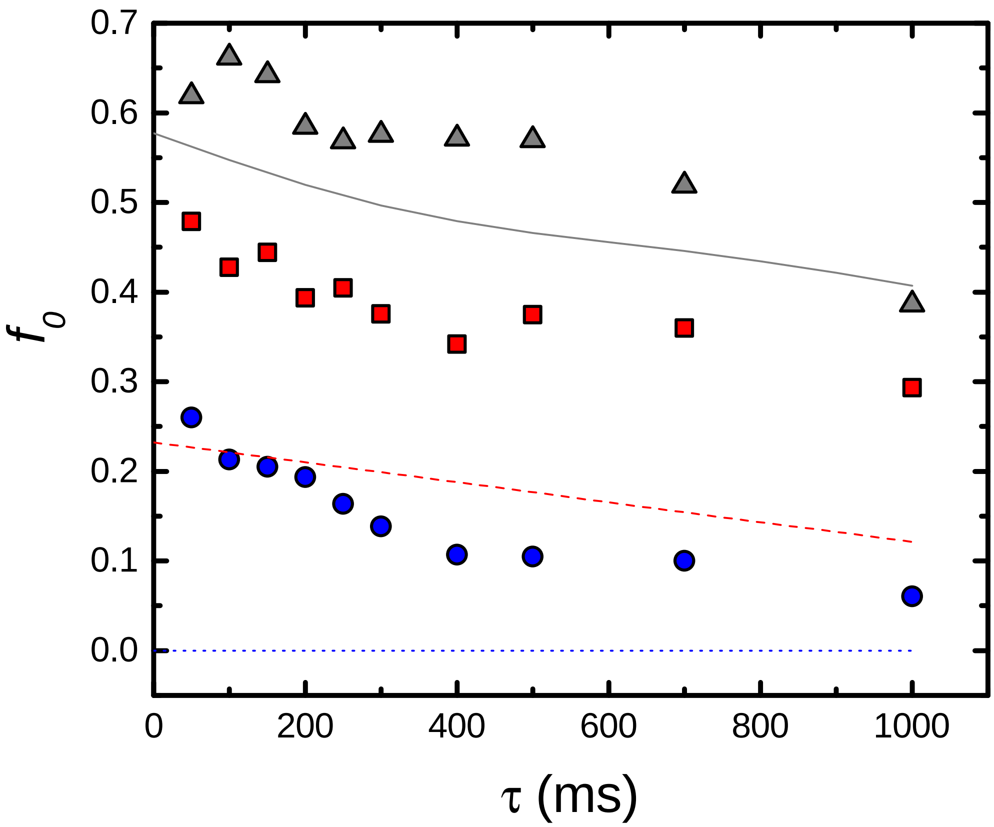

Figure 6.13: (Color online) Peak fraction for different lattice turn-on times τ at $s = 6$. The exponential time constant used for ramping on the lattice light is set to 2τ. Data and theoretical predictions are shown for S/N=0.44 (triangles, solid), 1.2 (squares, dashed), and 2.2 (circles, dotted) k_B. The lines are the equilibrium f_0 predicted by QMC simulations taking into account heating from the lattice light. At the highest S/N, QMC predicts that a condensate should be absent in the lattice.

In all cases, no adiabatic timescale is apparent—the peak fraction continuously decreases with the lattice turn-on time. This behavior is characteristic for all the s sampled in this work. At low and intermediate S/N, the decrease in peak fraction is consistent with the heating from the lattice light. The predicted equilibrium peak fraction including heating for different lattice turn on times τ is computed using QMC results for u. The rate of increase in u from the lattice light and the corresponding increase in S/N and decrease in f_0 are determined using the results from Ref. [102]. It is evident that the adiabatic timescale is comparable to or longer than the timescale for heating, and thus discriminating between the two processes is not possible.

Ultimately, inter-particle interactions via binary collisions are the dominant mechanism by which equilibrium is established and condensate fraction decreases as the lattice potential is turned on. Despite extraordinary advances in methods such as QMC, computing exact dynamics in higher than one dimension for more than a few tens of particles and short times remains infeasible for strongly interacting systems such as the BH model. In the next section, a hybrid of equilibrium QMC simulations and approximate theory is used to compute the timescale associated with the simplest mechanism—Landau damping—for relaxation of n_0.

6.7 Theory for Metastability of Condensate: Landau Damping

In this section, a model for relaxation of the condensate atom number via Landau damping is outlined. In a closed system, the condensate number can change by collisions with quasi-particles, whose number is not conserved. The dominant collision processes involve two-body scattering, where a condensate atom collides with a quasi-particle to produce two new quasi-particles. In equilibrium, the rates for this process and its reverse (whereby two quasi-particles collide to produce a condensate atom and a quasi-particle) are identical but opposite in sign, and the condensate number is conserved. However out of equilibrium, these processes do not cancel, and induce changes in the condensate atom number.

In general, the theoretical problem of how the condensate interacts with the thermal gas is an extremely challenging one, but an understanding of the precise mechanisms for equilibration is paramount to current experiments in optical lattices. Briefly, a condensate can relax by colliding with thermal atoms in two ways: at the mean-field level, the condensate introduces fluctuations in the thermal cloud which in turn lead to a damping of the condensate. This process is termed Landau damping, which is what is calculated. There is a second process where the condensate atoms exchange energy with the thermal atoms via collisions [104, 105]. Although this process is not calculated here, it is roughly of the same order as the Landau damping mechanism [105]. A third process is called Belieav damping, whereby a non-condensed atom collides with a condensate atom and decays into two non-condensed atoms with lower energy. This mechanism is dominant at very low temperatures and its rate decreases rapidly with temperature. Calculating the Landau damping rate thus suffices to estimate the timescales for equilibration in lattices.

The treatment of Landau damping here directly follows that of Tsuchiya and Griffin [106], who computed the damping rate for a homogeneous lattice Bose gas. Physically, this rate corresponds to the annihilation of a Bogoliubov quasi-particle and a condensate atom to produce two Bogoliubov quasi-particles (Fig. 6.14). By conservation of total particle number, integrating the damping rate over all momenta yields the rate at which the condensate fraction changes via Landau damping. For a homogeneous gas, the Landau damping rate for a quasi-particle at momentum $\vec{q}$ is given by [106]:

$$\Gamma(\vec{q}) = \pi n_0 \sum_{\vec{p},\vec{k}} |M_{\vec{q},\vec{k};\vec{p}}|^2 \delta(\varepsilon(\vec{q}) - (\varepsilon(\vec{p}) - \varepsilon(\vec{k})))[f^0(\varepsilon(\vec{k})) - f^0(\varepsilon(\vec{p}))], \tag{6.41}$$

$$M_{\vec{q},\vec{k};\vec{p}} = \frac{2U}{\sqrt{L^D}} \sum_{\vec{G}} \Big[(u_{\vec{q}}u_{\vec{p}} + v_{\vec{q}}v_{\vec{p}} - v_{\vec{q}}u_{\vec{p}})u_{\vec{k}} - (u_{\vec{q}}u_{\vec{p}} + v_{\vec{q}}v_{\vec{p}} - u_{\vec{q}}v_{\vec{p}})v_{\vec{k}}\Big]\delta(\vec{q} + \vec{k} - \vec{p} - \vec{G}), \tag{6.42}$$

where D is the dimension, L is the length of one side of the system, n_0 is the condensate density, the $\vec{G}$ are reciprocal lattice vectors (which incorporate Umklapp scattering), $f^0(x) = (\exp(\beta x) - 1)^{-1}$ is the Bose distribution at temperature $k_B T = 1/\beta$, and $\varepsilon(\vec{k})$ are the usual Bogoliubov quasi-particle dispersions in a lattice of the form in (6.26). The Bogoliubov coefficients $u_{\vec{k}}$ an $v_{\vec{k}}$ are given by $u_{\vec{k}} = \sqrt{\frac{1}{2}(\frac{\varepsilon_{\vec{k}} + Un_0}{\varepsilon(\vec{k})} + 1)}$ and $v_{\vec{k}} = \sqrt{\frac{1}{2}(\frac{\varepsilon_{\vec{k}} + Un_0}{\varepsilon(\vec{k})} - 1)}$. The delta functions enforce energy and momentum conservation.

The detailed derivation of this result can be found in Ref. [106] and is not repeated here. Note that a key assumption in this theory is that thermal (i.e., non-condensed) gas is in local equilibrium, which is enforced on short timescales by collisions between thermal atoms. It is worth emphasizing here that the full far-from-equilibrium problem of relaxation of condensed and non-condensed atoms following a lattice ramp is not being modelled. Rather, the timescales for relaxation when the condensate density departs slightly from its equilibrium value at a given lattice depth is computed. This near-equilibrium computation is the first step in gaining a systematic understanding of relaxation times in generic non-equilibrium situations.

The damping rate for all momenta $\vec{q}$ ranging from $-\pi/d \leq q_i \leq \pi/d$ is numerically computed, where $i = \{x, y, z\}$, and d is the lattice constant. Momenta is discretized in steps of π/L, where L is the system size, defined as where the total density vanishes. The finite system size also sets an infrared cutoff, $q_{\min} = \pi/L$, which renders the one-dimensional integrals convergent. Numerical checks ensure that this cutoff is small enough that changing $q_{\min}$ does not introduce significant errors. The total damping rate is given by $\Gamma_L = \sum_{\vec{q}} \Gamma(\vec{q})/\Omega$, where Ω is the system size. Using a simple rate equation $d\delta n_0/dt = -\Gamma_L \delta n_0$, where $\delta n_0(t) = n_0(t) - n_0^{\text{eq}}$, an estimate for the relaxation time $\tau_{LD} = 1/\Gamma_L$ of the condensate is obtained.

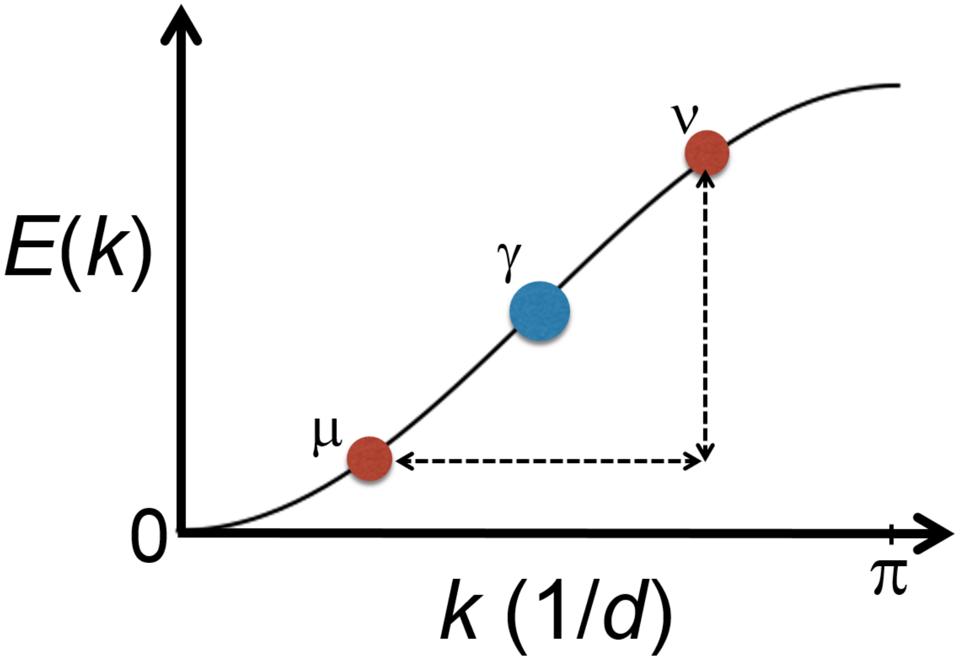

Figure 6.14: (Color online) Schematic representation of Landau damping in one dimension. The dispersion $E(k)$ is shown using a solid line. We consider the process whereby a quasiparticle (γ) can decay by coupling to a resonant transition between two quasiparticles (ν and μ) mediated by the underlying condensate. By conservation of total particle number, this reduces the overall condensate density.

To compute the damping rate, three quantities are required: the condensate density ρ_0, lattice depth s, and the temperature T. For a given lattice depth s and temperature T, ρ_0 from exact QMC simulations discussed above is used to compute the different Landau damping rate. Using the relation between temperature and entropy per particle, the damping rate as a function of entropy per particle for different lattice depths is obtained.

Derivation of the damping rate assumes that all of the condensate atoms are at $\vec{q} = 0$. While this is true in a weakly interacting homogeneous system at low temperature, the presence of a trap and strong correlations modifies this picture significantly, as momentum is no longer a good quantum number. The condensate therefore develops a spread in momentum, which were computed numerically using QMC for a given temperature and lattice depth. To incorporate trap and interaction effects into damping calculations, the Landau damping rate is calculated for two cases: 1) Using the assumption that all the condensate atoms are at $\vec{q} = 0$. This yields an *upper bound* on the damping rate. 2) A *lower bound* on the damping rate is obtained by assuming that the total condensate number is equal to only the contribution to the momentum distribution at $\vec{q} = 0$. The experimentally observed damping rate must be between these two bounds.

The results of these calculations presented in Fig. 6.15 paint a fascinating picture. At low entropy, the lower bound on the Landau damping time ranges from 200 ms to 10 ms from the lowest to highest lattice depth $s = 6E_R$ to $s = 12$, while the upper bound varies roughly from 1 s to 100 ms. At the highest S/N, the Landau damping time is at least 20 times larger than the Hubbard tunneling time h/t. The decrease in the damping time for higher lattice potential depth is consistent with the increase in interaction strength. For $s = 6$, where the system can be treated as weakly interacting, the two bounds coincide at low entropy because the condensate largely resides at zero momentum. Interactions induce a significant broadening of the condensate momentum distribution, which leads to a large difference between the upper and lower bounds at higher s. This is particularly stark at high entropies per particle, because the condensate is almost entirely absent. Note that for $n_0 = 0$, $\Gamma_L \to \infty$. Strictly speaking, this theory is not accurate when the condensate number is small, either because of non-zero temperature or strong interactions. At high temperatures, interactions between non-condensate atoms play an important role that is not captured by the approach discussed here. For the strongly interacting case, quantum depletion reduces n_0 and the Bogoliubov spectrum, which is the underlying assumption in this theory, is not valid. Therefore the upper bounds in the damping time at $S/Nk_B = 1$ for $s = 10$ and 12 may not be correct.

Comparing the predicted Landau damping times to the 100 ms lattice turn-on used for the data in Fig. 6.13 is complicated by the lack of equilibrium in the lattice. Generally, the damping time exceeds 100 ms at the highest S/N, where the discrepancy between the QMC and experimental f_0 is greatest. This implies that the lattice turn-on time used for Fig. 6.12 was non-adiabatic, since times much longer than τ_{LD} are required to achieve equilibrium in the lattice. The predicted Landau damping time is also long at low S/N, but n_0 changes less in this regime as the lattice is turned on, and thus the impact of non-adiabatic behavior is less apparent. Diabaticity with respect to Landau damping at high S/N explains the experimental observation that the peak and condensate fraction in the lattice is higher than the equilibrium prediction, since the condensate does not have sufficient time to decay as the lattice is turned on.

The upper bound on the damping time in combination with the heating rate from the lattice light implies that adiabaticity may be impossible to achieve under certain conditions. At $s = 6$, for example, the upper bound on the Landau damping time at $S/N > 1$ is close to

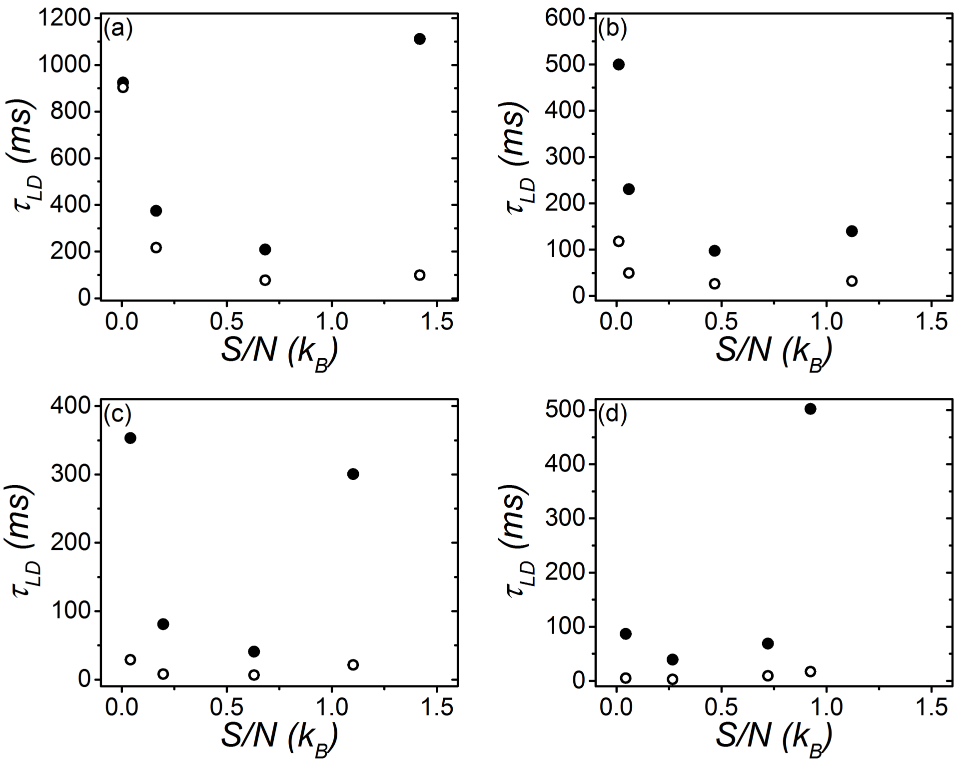

Figure 6.15: Estimates of the lower (empty circles) and upper bound (filled circles) of the decay time associate with Landau damping vs. entropy per particle for $s = 6, 8, 10, 12$ (a-d).

1 s. This time is longer than the heating timescale observed for the data shown in Fig. 6.13. Differentiating between heating and thermalization becomes more challenging at higher s, since the characteristic energy scale t drops rapidly, but the heating rate from the lattice light grows linearly with s.

6.8 Conclusions and Outlook

In conclusion, this chapter detailed theoretical methods, both at the mean field level as well as exact Quantum Monte-Carlo, that is used to compare with the experimental realization of the clean Bose-Hubbard model in a trap. In particular, the peak fraction measured in experiments were calculated and compared with theoretical results in the superfluid regime of a cubic lattice for varied entropy per particle and lattice potential depth.

Qualitatively, the experimentally observed peak fraction behaved as theoretically expected: lower initial entropies led to higher peak fractions, and higher lattice depths (lower t/U) resulted in lower peak fractions. However, quantitative agreement with exact QMC simulations at high entropy per particle was not obtained. Instead the condensate is observed to be metastable, and non-zero peak fraction is seen to persist above the critical temperature for superfluidity for times much longer than general Hubbard timescales (set by microscopic parameters t and U). The timescales for relaxation of the condensate were investigated by calculating the Landau damping time in the lattice. Calculations indicate that the relaxation time is comparable or greater than typical lattice turn-on times. The Landau relaxation time is also longer than the timescale associated with heating from the lattice light, which may make adiabaticity impossible to achieve.

Going forward, these theory-experiment comparison points to the urgent need to carefully understand timescales for dynamics in strongly correlated optical lattice experiments. Furthermore, using this model as a starting point, one can envision branching out to situations where competing theories disagree, break down or do not even exist. A canonical example is that of strongly correlated systems far-from-equilibrium, where the very paradigms for how to think about these systems are only now being developed. In addition to being of fundamental importance, questions of non-equilibrium dynamics serve a practical purpose in cold atom experiments, which are largely isolated from the environment. Understanding the mechanisms for driving these systems to equilibrium is thus essential in order to understand timescales for maintaining adiabaticity.

Chapter 7

The Disordered Bose-Hubbard Model: Preliminaries

The historical roots of the Dirty-Boson problem arguably origins in the seminal paper due to Fisher et. al. [26] that considered the effects of on-site disorder on the standard Bose-Hubbard Hamiltonian:

$$\hat{\mathscr{H}} = -t \sum_{\langle ij \rangle} \hat{b}_i^\dagger \hat{b}_j + \frac{U}{2} \sum_i \hat{n}_i(\hat{n}_i - 1) - \sum_i (\mu + \delta\mu_i)\, \hat{n}_i. \tag{7.1}$$

Here $\hat{b}^\dagger$ ($\hat{b}$) are Bose creation (annihilation) operators, $\hat{n} \equiv \hat{b}^\dagger \hat{b}$ is the occupation number operator, t is hopping parameter, U is the on-site interaction term, μ is the chemical potential and $\delta\mu_i$ is the onsite potential shift due to a static disorder, commonly called *quenched disorder*. Most theoretical studies consider $\delta\mu_i \in [-\Delta/2, \Delta/2]$, that is the disorder induced chemical potential shift is assumed to be drawn from a uniform distribution – often called a *Box disorder* [26, 59, 57, 58, 79]. The physical justification of such an assumption is possible only under certain circumstances. To see why this is, consider a real system with impurities present that distorts the regular periodic structure of the crystal potential. Then the localized single-particle wave functions on a particular site will get distorted leading to disorder present in all terms of the Hamiltonian. If some of these terms are small, for instance the disorder in the interaction energy or kinetic energy term, then it could be ignored and the resulting Hamiltonian is just 7.1 with disorder appearing as local potential shifts. Additionally, there is also no obvious reason why the disorder should be uniform, it could very well be non-uniform and skewed. These details should be accounted for, while addressing *universal* behavior and they become particularly important in the case of experiments, as will be shown later. However, for qualitative purposes useful observations are possible using

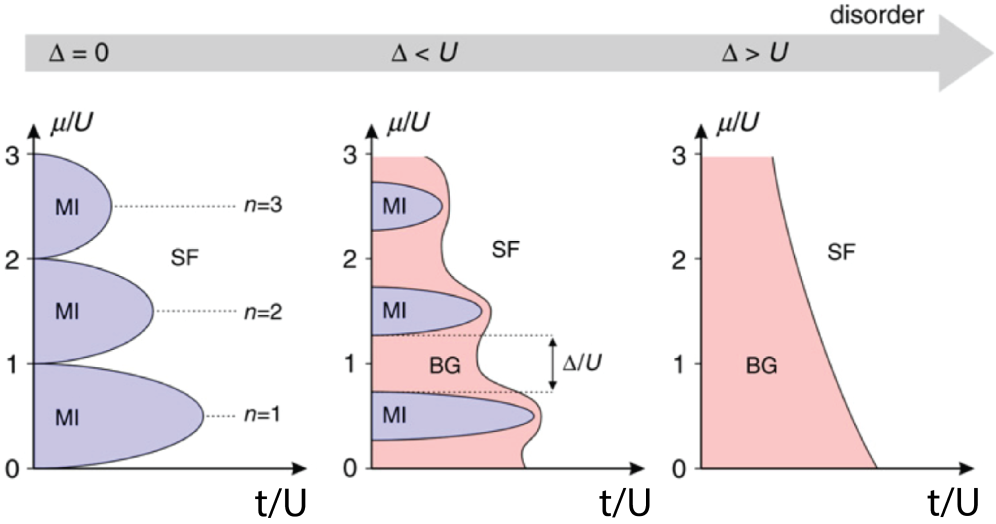

Figure 7.1: Sketch of the phase diagram of the Disordered Bose-Hubbard Model as disorder is tuned from $\Delta = 0$ to intermediate cases ($\Delta < U$) and then finally, more large disorder with ($\Delta > U$). Taken from [27]. (See text for discussion.)

the simplified picture due to 7.1.

A qualitative sketch of the phase diagram according to Fisher et. al [26] is shown in Fig. (7.1). At $\Delta = 0$, i.e., disorder is absent, the phase diagram exhibits the well known Superfluid and Mott-Insulating phases. The latter appear as domes of constant density. The dashed lines correspond to constant density contours that would be followed in the Canonical ensemble with fixed particle number. As disorder is turned on (but still $\Delta < U$) a new phase arises, called the Bose-Glass phase (discussed in detail below). As the Bose-Glass forms the Mott-Insulating dome shrinks, since patches or clusters of sites in the system can have sufficiently large disorder that locally destroys the Mott-Insulating gap, and local puddles of superfluid-like compressible regions can develop – hallmark of the glassy phase. Finally, when the disorder is larger than the gap at any U the Mott-insulating state vanishes completely.

Although this basic picture is qualitatively useful, there are still a host of questions. The central of these pertain to the nature of the new glassy phase and the mechanisms by which phase transitions occur. Associated questions are universal features such as critical exponents of the different kinds of transitions, finite temperature behavior, sensitivity to disorder distribution and so forth. The strategy in this chapter will be to discuss equilibrium properties of the Disordered Bose-Hubbard model generally in 3D without traps.[1] Explicit

---

[1] The results generally apply to other dimensions, but whenever there are exceptions of note it will be

comparisons will be made, when possible, between simple box types of disorder and the speckle type of disorder used in experiments (note that the latter is topic of this dissertation, since it is the most pertinent with regards to experiments). The coarse-grained Hamiltonian corresponding to the speckle type of disorder is given by:

$$\hat{\mathscr{H}} = -\sum_{\langle ij \rangle} t_{ij} \hat{b}_i^\dagger \hat{b}_j + \frac{1}{2} \sum_i U_i \hat{n}_i (\hat{n}_i - 1) - \sum_i (\mu + \delta\mu_i)\, \hat{n}_i, \tag{7.2}$$

where t_{ij}, U_i, $\delta\mu_i$, now correspond to disorder distributions discussed in Section 5.6. While there have been a lot of studies dealing with the simple case of box disorder, there has been only one other theoretical study to date that attempts to include the off-diagonal disorder (in addition to the diagonal disorder) present in speckle type of disorder, but this was at the mean field level using Stochastic Mean Field Theory (SMFT) [58, 107]. Also, the disorder type used in this study does not account for the correlation present in the off-diagonal and on-site energy terms. It is thus an uncontrolled approximation. Additionally, SMFT cannot account for the trap, where it is even more unclear (compared to the clean case) to what extent the LDA is applicable. In this dissertation all of these approximations are avoided, and a clear picture is developed incrementally while addressing approximations that have been made in other studies. The study of the trap free system will lend insights into the development of tools that will ultimately help to understand the far more complicated and rich case of the trapped system where multiple domains are bound to develop.

7.1 General Effects of Disorder on Continuous Phase Transitions

Before entering into the specifics of the DBHM, it is useful to consider the general effects of disorder on systems. This topic is an old one and there is a lot of literature on the topic, for a recent review see [25] (and references therein). A basic question to ask is: given a clean continuous phase transition in a system, how does weak amounts of disorder affect the phase transition? For instance, it would seem reasonable to expect the system to be divided into independent regions due to defects, each of which separately undergoes a phase transition. Consequently, it would seem that a clean phase transition is destroyed and replaced by a smeared out transition. However, it turns out that things are not so simple. One of the first attempts to understand the stability of classical phase transitions in clean systems when perturbed by weak disorder was made by Harris [108]. Following this, the analysis was

---

explicitly stated.

extended and proved by Chayse et. al [109] for the much more general case of disordered systems and disorder induced phase transitions. Essentially their argument showed, that provided such a transition can be characterized by a change in the scaling behavior of a finite volume system, it would be possible to define a correlation length, which behaved the same way as in clean systems. Therefore, Harris' argument would be applicable to this case as well.

The Harris criteria of the stability of the critical point is easy to demonstrate and is outlined below for quantum phase transitions following [110]; it generalizes from Harris' argument for classical phase transitions. Let g be a general parameter of the Hamiltonian describing a system and suppose at $g = g_c$ the system undergoes a quantum phase transition from the disordered to the ordered state. Now focussing on a particular region in the system of size L_r, it is possible to define a local critical value of the parameter not necessarily equal to g_c, where the local region crosses over to the ordered state. According to the central limit theorem, the standard deviation of N independent random numbers is of order $\sqrt{N}$. This means that the deviation of the local parameters ($\Delta g_c \equiv g - g_c$) must scale according to $L_r^{-d/2}$, so that $L_r \sim (g - g_c)^{-2/d}$. This follows the intuitive notion that the larger the deviation from the expectation value of the critical parameter, the smaller is the possible size of the region. On another front, from ideas of scaling theory [30], the correlation length ξ which denotes the size of domains in the system, must scale according to $\xi \sim (g - g_c)^{-\nu}$ near the critical point. Here ν is the correlation length *critical exponent*.[2] Then in order for such local regions not to disturb the critical point, or in other words for the disorder to be renormalized out at long length scales, $L_r << \xi$, which immediately implies:

$$(g - g_c)^{-2/d} << (g - g_c)^{-\nu}, \tag{7.3}$$

which gives the stability criteria,

$$\nu d \geq 2 \tag{7.4}$$

So provided this condition is met, the critical point remains unaffected by disorder since it get renormalized out at larger and larger length scales, becoming irrelevant at the thermodynamic limit. A corollary of this is that all thermodynamic observables are self-averaging, i.e., it doesn't change from one sample to another. One important caveat to note is that this argument requires disorder to be uncorrelated or (correlated over very short ranges). For long range correlations, the dimensionality d will need to be modified [25].

---

[2] For a discussion on Critical Exponents and the Renormalization Group refer to [30, 111] for an excellent introduction.

The next obvious question to ask is what happens when the Harris criteria is not satisfied. There is no answer to this question using simple scaling arguments, but research has shown that there are several possibilities [25]. The simplest possibility is that the transition remains sharp and continuous, but the critical behavior changes to another Universality class with new exponents such that $\nu d \geq 2$. The disorder gets renormalized out at large length scales to non-zero but finite value. In such cases observables are no longer self-averaging at the critical point [112, 113, 114]. These definitions can be put on a firmer footing.

Self-averaging is defined as the property of an observable X, such that it satisfies $R(X) \equiv (\overline{X^2} - \overline{X}^2)/\overline{X^2} \to 0$ as the system size is increased to thermodynamic limit. The overbar indicates disorder averaging over different instances of the disorder distribution. Thus, in addition to the statistical averaging, there is an additional averaging that is needed. It is possible to define two limits for self averaging: strong self-averaging (SA) implies $R(X) \sim L^{-d}$, and weak self-averaging (WA) implies that $R(X) \sim L^{-\upsilon}$, where L is the linear size of the system in one dimension and υ is a small positive number. According to [113], SA is satisfied whenever $L >> \xi$, i.e., away from the critical point *whether or not* Harris criteria is satisfied. On the other hand when $L << \xi$ such as near or at the critical point, if Harris criteria is satisfied by the clean system, then in the corresponding disordered system observables obey WA. On the other hand, if Harris criteria is not satisfied then observables do not self-average, and the distribution of the values approaches a non-Gaussian with size-independent relative cumulants. In basic terms, SA simply means that doing a disorder averaging over different instances of the disorder distribution is the same as taking a very large sample of one disorder instance.

There is another possibility for systems that violate the Harris criteria. Instead of the disorder getting renormalized to a finite value, the inhomogeneities increases without limit under coarse graining. The corresponding fixed points are called infinite-randomness critical points. The probability distributions of observables in such cases are very broad where the width diverges with system size. The averages are dominated by rare events such as spatial regions with rare configurations. An example of such phases are Griffiths phases (for details refer to [112] and the references therein).

It turns out that the critical behavior at the general SF-MI transition critical point of the d-dimensional Bose-Hubbard model is governed by the (d+1) dimensional classical XY model at $T = 0$ [26], that has a lower critical dimension of 1 and an upper critical dimension of 3. This means that the 3D BHM falls under the 4D XY model, so that all the critical exponents are MF like, with $\nu = 1/2$ (the dynamical critical exponent, $z = 2$). This implies that the Harris criteria is violated and so the SF-MI transition must be replaced by another type of transition. This is precisely the SF-BG transition, for which the critical exponents are given by $\nu = 0.88(5)$ ($z = 3$) [115], which again satisfies the Harris criteria as discussed earlier. As per the discussion earlier, then the expectation is that the critical point does not self average. On the other hand the details of the MI-BG transition is unknown since it is conjectured to be a Griffiths type of transition. There are strong reasons to believe this to be the case and will be discussed under the Theorem of Inclusions discussed next. This theorem also addresses the question of the possibility of a direct SF-MI transition in the presence of disorder, which cannot be ruled out since the fate of transitions that violate the Harris criteria is still an open question – there are only specific examples, but no general theory that suggests what happens.

7.2 Theorem of Inclusions

A major debate with regards to the DBHM was the possibility of a direct transition from the MI to the SF state in the presence of disorder. This question is actually a very general one and is applicable to a variety of other types of continuous phase transitions with diagonal disorder. For instance it is pertinent to the paramagenetic-ferromagnetic transition in magnetic systems and metal-insulator transitions with spin-1/2 Fermions. The basic idea of the Theorem of Inclusions is to consider how diagonal disorder affects the phases of the system in the vicinity of a phase transition point [57]. In this argument a basic requirement is that the phase boundary is dependent both on the disorder bound and the properties of the disorder distribution (collectively called Υ) that include all microscopic parameters apart from the disorder bound. Additionally, the phase boundary is expected to be continuous on physical grounds and the transition is considered only at a non-extremal point. These conditions allow the phase boundary to be represented as in Fig. 7.2, without any loss of generality. Now for a particular realization of the disorder represented by (Υ^*) it is always possible to find arbitrarily large regions that are representable by another disorder distribution (Υ') such that $\Delta_c(\Upsilon') < \Delta_c(\Upsilon^*)$. Therefore such regions appear as local domains of the phase possible at larger disorder strengths (SF, in the DBHM). In other words, even at a point $\Delta < \Delta_c$ at a given Υ^*, it is possible to have domains in the system that corresponds to disorder values thought to be unattainable for the distribution Υ^* at the current disorder strength Δ (Note that the converse is trivially possible). For DBHM, this immediately forbids a direct transition between the MI and the SF, and implies that there must be an intervening state

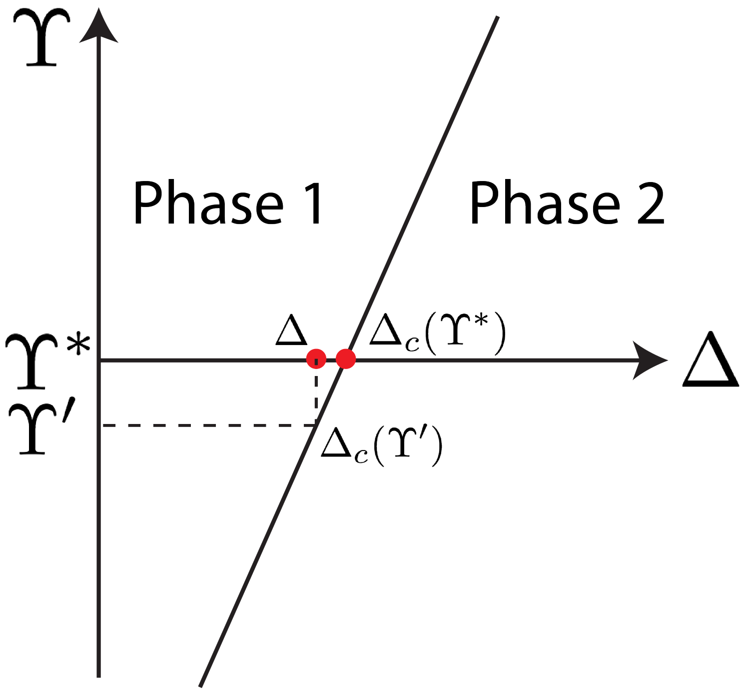

Figure 7.2: Illustration of the Theorem of Inclusions. The phase boundary between two phases depends continuously on the disorder distribution parameterized by Υ. For a disorder distribution characterized by Υ^* with critical disorder strength $\Delta_c(\Upsilon^*)$, it is always possible to find a point Δ arbitrarily close to the critical point such that there are local regions corresponding to the large disorder phase (here Phase 2). This is because such a region can be parametrized by another distribution Υ' such that $\Delta_c(\Upsilon') < \Delta_c(\Upsilon^*)$. This argument assumes the system to be in the thermodynamic limit.

– the BG.

This argument seems to preclude any transition between the MI and the BG. However, the loophole is the exceptional case where the phase boundary in fact has no dependence on any other property other than the disorder bound, i.e., it corresponds to a vertical line in Fig. 7.2 through a critical point. Since the MI can be destroyed only if the gap is removed, this means that $\Delta_c = E_{gap}$ is the only possible value for this phase boundary. The physics of such a non-generic type of transition is precisely the mechanism of a Griffith's type of transition [57, 25]. In a bounded disorder system, such a transition is possible only at the precise value where the gap is destroyed and the transition proceeds by the manifestation of extremely rare regions which mimic a regular pure system in an external field. More specifically for the DBHM, there must be appear a region with an uniform potential shift such that it locally drives the system into a SF state. Close to the critical point such regions will be extremely rare, and will be almost impossible to observe in numerically accessible system sizes. In fact they may not be observable in finite system sizes at all! Thus it is reasonable to expect that even very large simulation cells will have massive finite size errors. This is precisely the root cause behind mistaken identification of BG states as MI states; it is very possible for the compressibility to be extremely small while being non-zero, making the BG state hard to identify near the critical point.

Having discussed the general structure of the phase diagram, viz., that the BG phase must always intervene between the MI and SF, and the Griffiths mechanism of transition between the MI-BG, the next section discusses the SF-BG transition mechanism. This transition type is applicable for a much larger part of the phase diagram as it involves all densities and temperatures. Note that the MI-BG transition is restricted to commensurate filling, and at finite temperatures both the insulating states must give way to cross-over type of transitions to the normal state. More details of finite temperature behavior will be covered later in section 7.5.3.

7.3 The Percolation Picture

The standard idea of the SF-BG type of transition that is universally accepted is in the form of percolation clusters [59, 57, 116, 58, 79]. Essentially, at $\Delta = 0$ there is a macroscopically connected region over which the Many-body wavefunction remains phase coherent resulting in a global superfluid. In the path integral picture, this is synonymous with a macroscopic number of particles forming long loops (or permutation cycles) *wound* over the sample. As disorder is turned on, regions in space become unfavorable to maintain connections over leading to a thinning out of the superfluid flow. However, at these intermediate disorder strengths, it is still favorable for there to be a globally connected superfluid. At some critical disorder strength, the superfluid flow gets reduced to zero, in a way that the global connections break up throughout the system. This picture follows the phenomenology of percolation. The system now has patches of coherent superfluid puddles that not correlated with each other. So the expectation is that the BG consists of puddles embedded in an incoherent background. Given this general phenomenology, it is further possible to obtain estimates of the percolation threshold in terms of the parameters of the DBHM. There are two different routes to consider here corresponding to slightly different types of percolation pictures.

7.3.1 Local Hamiltonian Approach

The first method is simple and analytically tractable. It pertains to the picture of highly localized superfluid puddles with localization lengths of the order of a lattice site [116]. It is possible to decouple the DBHM Hamiltonian (7.1) by ignoring the kinetic part to obtain a more local form:

$$\hat{H} = (\epsilon - \mu)\hat{n} + \frac{U}{2}\hat{n}(\hat{n} - 1), \tag{7.5}$$

where ϵ is the local potential shift due to disorder drawn from the disorder distribution $\mathscr{P}(\epsilon)$. It can be minimized to obtain the particle number at a particular potential shift:

$$n(\delta\mu) = \frac{\mu - \delta\mu + U/2}{U} \tag{7.6}$$

Then the average occupation is given by

$$\langle n \rangle = \int d\epsilon \mathscr{P}(\epsilon) \left[\frac{\mu - \epsilon + U/2}{U} \right]. \tag{7.7}$$

This equation can be solved using the additional fact that since there can't be any negative occupation $\epsilon \leq \mu + U/2$. For a particular filling $\langle n \rangle = \bar{n}$, the equation may be inverted to find the corresponding $\bar{\mu} = \mu(\bar{n})$. Now using $\bar{\mu}$, the smallest possible ϵ_c at which $n = 0$ is

$$\epsilon_c = \mu(\bar{n}) + U/2. \tag{7.8}$$

The probability that given the filling density $\bar{n}$, and $\mathscr{P}(\epsilon)$, all disorder values are less than ϵ_c is precisely the percolation threshold given by:

$$p_c = \int_{-\infty}^{\epsilon_c} \mathscr{P}(\epsilon) d\epsilon, \tag{7.9}$$

which can be obtained form the classical percolation problem on a lattice with site disorder. In 3D, $p_c = 0.31$ [117]. Using this general idea it is possible to obtain specific results for the Box disorder and the exponential form of diagonal disorder that the speckle disorder reduces to if disorder in the onsite interaction term and the tunneling term can be ignored. These have been derived below.

- *Box Disorder* [118]: where $\mathscr{P}(\epsilon) = \frac{1}{\Delta}$ for $\epsilon \in [-\Delta/2, \Delta/2]$. So that,

$$\begin{aligned} \langle n \rangle &= \int_{-\Delta/2}^{\mu+U/2} d\epsilon \frac{1}{\Delta} \left[\frac{\mu - \epsilon + U/2}{U} \right] \\ &= \frac{(\mu + U/2 + \Delta/2)^2}{2\Delta U}. \end{aligned} \tag{7.10}$$

Given some filling $\bar{n}$,

$$\bar{\mu} = \sqrt{2\Delta U \bar{n}} - (U/2 + \Delta/2). \tag{7.11}$$

The corresponding ϵ_c so that the occupation of a site reduce to 0 is given by $\epsilon_c = \sqrt{2\Delta U \bar{n}} - \Delta/2$. The percolation threshold then satisfies

$$\begin{aligned} p_c &= \int_{-\Delta/2}^{\epsilon_c} \frac{1}{\Delta} d\epsilon \\ &= \sqrt{\frac{2U}{\Delta}\bar{n}}. \end{aligned} \tag{7.12}$$

Using $p_c = 0.31$, the estimate of the boundary is therefore at

$$\Delta/2U = 10.41\bar{n}. \tag{7.13}$$

- *Exponential Disorder:* with $\mathscr{P}(\epsilon) = \frac{1}{\Delta} exp(-\epsilon/\Delta)$. For this distribution $\sigma[\mathscr{P}(\epsilon)] = \Delta$ just like speckle disorder. Then the average occupation is given by

$$\begin{aligned} \langle n \rangle &= \int_{0}^{\mu+U/2} d\epsilon \frac{exp(-\epsilon/\Delta)}{\Delta} \left[\frac{\mu - \epsilon + U/2}{U} \right] \\ &= \frac{a}{U} + \frac{\Delta}{U} \left\{ exp\left(-\frac{a}{\Delta}\right) - 1 \right\} \\ \frac{U\bar{n}}{\Delta} &= \frac{a}{\Delta} + exp\left(-\frac{a}{\Delta}\right) - 1, \end{aligned} \tag{7.14}$$

where $a \equiv \bar{\mu} + U/2$. Now the ϵ_c at which the occupation of a site reduce to 0 is given by $\epsilon_c = \bar{\mu} + U/2 = a$. The percolation threshold then satisfies:

$$\begin{aligned} p_c &= \int_{0}^{\epsilon_c} \frac{1}{\Delta} exp(-\epsilon/\Delta) d\epsilon \\ &= 1 - exp(-a/\Delta). \end{aligned} \tag{7.15}$$

The guiding equations (7.14) and (7.15) can be combined to obtain the relationship

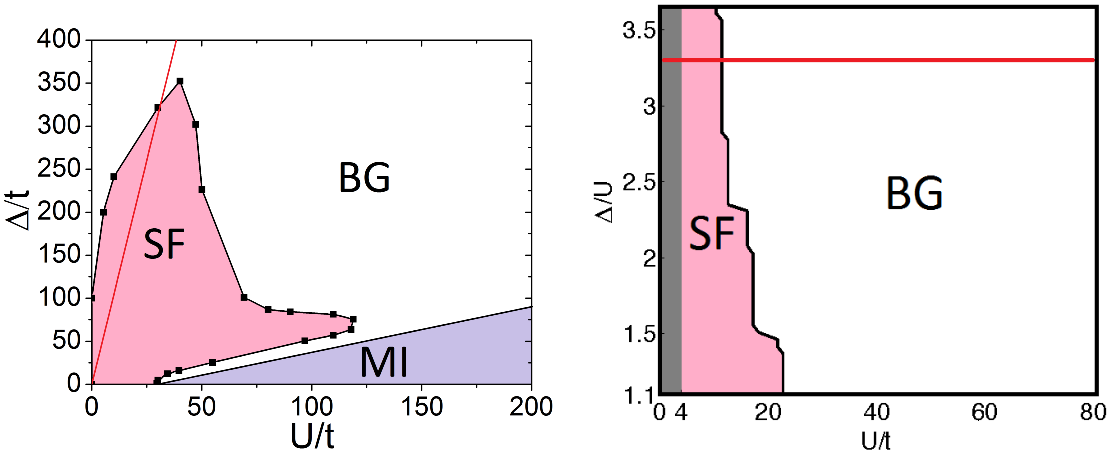

(a) (b)

Figure 7.3: (a) Percolation threshold is shown in red using the simple local form of the Hamiltonian 7.5 for the unit filling box disorder system. The phase diagram has been obtained from [116]. (See text for discussion.) (b) Percolation threshold shown in red at $\Delta/U = 3.27$ for the speckle disorder (approximated as exponential form of disorder) for a filling $\bar{n} = 0.2$. The region in gray has no data. (Additionally this image was not generated using scaling type of calculations so the SF-BG boundary is estimated using a superfluid fraction threshold of 0.001, and is to be used for qualitative purposes only.)

between the percolation threshold and other parameters of the Hamiltonian:

$$\begin{aligned} \frac{U\bar{n}}{\Delta} &= -ln(1-p_c) - p_c = 0.0611 \\ \frac{\Delta}{U} &= 16.367\bar{n}. \end{aligned} \tag{7.16}$$

The percolation threshold values for the box disorder and speckle disorder are both very large and scale linearly with the filling. For box disorder at unit filling ($\bar{n} = 1$) the percolation threshold derived here agrees approximately with QMC data in the regime $0 \leq U/t \leq 30$ shown in Fig. (7.3a). Clearly as expected the kinetic energy term stabilizes the superfluid phase so that generally larger disorder strength is needed for the system to undergo a percolation transition. The corresponding phase diagram for the speckle disorder (approximated by the exponential form of disorder) cannot be obtain using QMC, since the disorder value of $\Delta/U = 16.367$ is too large and the single band DBHM is not appropriate at these values. Using the density dependence of the threshold it is possible to try to check the percolation threshold at low filling shown in Fig. (7.3b) for $\bar{n} = 0.2$. The threshold in this case is $\Delta/U = 3.27$. Note that the phase diagram here is only to be used for qualitative purposes, the right edge of the boundary has not been computed using a scaling procedure but rather a threshold for the superfluid fraction $\rho_s \sim 0.001$ for a system of size 14^3. However the within the SF phase, the values are accurate and this picture suggests that the SF is stable well beyond the percolation threshold for $U/t \leq 10$. On the other hand for larger U/t, the SF is replaced by the BG well before the threshold values. It is not known how well threshold would agree for lower filling values for the box disorder. Clearly, for both cases, this type of calculation cannot account for the phase boundary and more sophisticated techniques are needed.

7.3.2 Mean Field approach and Scaling based on Classical Percolation

The second method is much more intensive, requiring a combination of mean field theories as well as a classical percolation type of approach [119]. The calculations were done only for the 2D DBHM using box disorder at a commensurate filling of $\bar{n} = 1$. A similar calculation of the 3D phase diagram for speckle disorder is beyond the scope of this work since they are almost as intensive as QMC scaling calculations, while it is remains unclear whether it is as accurate. However, the method is outlined below and will be pursued elsewhere. The discussion below is motivated using existing results from [119]. The primary MF method that has received a lot of attention is the Gutzwiller approach discussed earlier, but now extended to disordered systems [79, 119]. The method starts as before by decoupling (7.1) as:

$$
\begin{aligned}
\hat{H} &= \sum_i \hat{H}_i \\
\hat{H}_i &= (\epsilon_i - \mu)\hat{n}_i + \frac{U}{2}\hat{n}_i(\hat{n}_i - 1) - t\gamma_i(\hat{a}_i + \hat{a}_i^\dagger - \alpha_i)
\end{aligned}
\tag{7.17}
$$

where $\gamma_i \equiv \sum_{ij} A_{ij}\alpha_j$, such that $A_{ij} = 1$ for nearest neighbors and 0 otherwise in the DBHM. In this decoupling, a standard SDMFT approximation $\hat{a}_i\hat{a}_j^\dagger \sim \alpha_j\hat{a}_i + \alpha_i\hat{a}_j^\dagger - \alpha_i\alpha_j$ is used where, due to the U(1) symmetry, the expectation value of the annihilation operator can be chosen to real, i.e., $\alpha_i \equiv \langle\hat{a}_i\rangle \in \mathbb{R}$. This a ground state method (called local mean-field theory, LMF) so that all expectation values are taken using the ground state value of $\hat{H}_i$ only.[3] The local superfluid order parameter $\psi_i \equiv \sum_{n=0}^{\Lambda} c_n^{i*} c_n^i \sqrt{n_i}$, where Λ is the upper bound of the

---

[3] Note that for a system of L^3 sites and truncation of occupation numbers to Λ (this is the basis in which the local Hamiltonian is formulated), the problem is solved by computing an exact diagonalization (ED) for each $\hat{H}_i$. So each iteration step involves solving L^3 $(\Lambda+1)\times(\Lambda+1)$ ED problems, which has to be repeated several times ($\sim$ 1000 times or more) for convergence

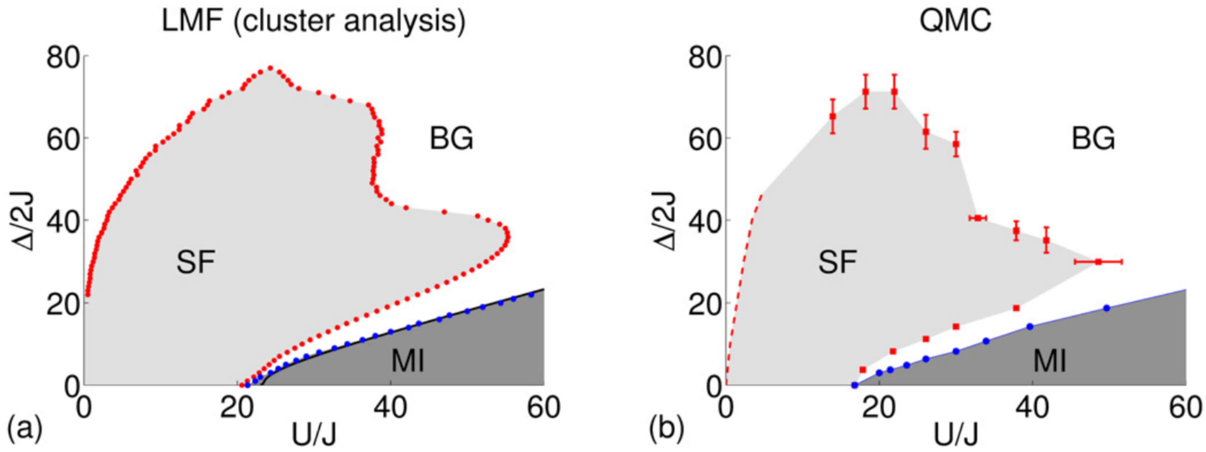

Figure 7.4: (a) Phase diagram calculated from LMF cluster analysis for commensurate filling of $\bar{n} = 1$ taken from [119]. (b) Corresponding QMC calculations taken from [120]. (See text for discussion.)

occupation number basis used for practical purposes. From this, the global superfluid order parameter is $\psi \equiv \frac{1}{N} \sum_i \psi_i$, where N is the total number of sites. It is possible to extend this formulation to finite temperatures [79]. In this section, an alternative aspect will be discussed in order to study the percolation picture.

According to [119] the phase boundary for the SF-BG transition can be obtained by using using the local density $\langle n_i \rangle$. The idea is to use $\langle n_i \rangle$ to characterize the local state of the system. Accordingly, the system is partitioned into two regions, SF clusters for which $\langle n_i \rangle \notin \mathbb{Z}$ and insulator regions for which $\langle n_i \rangle \in \mathbb{Z}$. Once the SF clusters are identified, it can be checked to see if the clusters connect globally. If it does then the full system is in a SF state; otherwise it is a BG. By performing similar calculations over many disorder realizations, the probability of percolation can be calculated. Subsequently scaling calculations can be performed for different system sizes in order to identify the critical exponents. These calculations were performed for commensurate filling in 2D systems and the coherence length critical exponent $\nu = 1.33$ was obtained that falls into to conventional 2D percolation universality class [119, 117]. The phase diagram from QMC and percolation analysis has been shown in Fig. (7.4). The general features are in qualitative agreement and it seems likely that the percolation picture holds. However, discussion from the earlier chapter make it clear that while the phase boundary may be close, actual observables may not be in good agreement at all. Indeed, with this LMF calculation the actual SF observable, ψ is unable to capture the SF-BG transition and severely underestimates the phase boundary. To what extent ψ captures a real observable is in itself a question, since in the broken U(1) symmetry picture the ground state does not conserve particle number [19]. Additionally, this approach of using non-integer values of density as an indicator for participation in a SF cluster is not very general. For instance the BG exists also at non-commensurate densities and non-integer regions may not be part of the SF. Also, at finite temperatures density modulations may be present while still not being a part of the SF phase.

The general expectations discussed thus far can be used to guide further inquiries into the phase diagram. For instance, it is clear that away from the critical points, the observables should self-average, so simulations of large cells should correspond well to disorder averaged samples. Additionally, near the critical point, the BG states could appear to be MI states. From the discussion above, actually it is evident that the BG-MI transition may not be accessible numerically at all. In fact most theoretical studies to date simply include it in the phase diagram by locating it at $\Delta = E_{gap}$. For speckle disorder the situation changes dramatically, as will be seen.

7.4 Features of the Phase Diagram

To date a complete QMC calculation of the phase diagram in terms of the effective chemical potential (μ/U), effective interactions (t/U) and effective disorder (Δ/U) has not been done for the box type of disorder. Perhaps, the main reason for this is that these calculations are expensive and since the phase boundary is sensitive to the disorder distribution, unless a physical system can be shown to explicitly posses such properties these calculations would not be very practical. However, mean-field type of results are available [58, 79], together with the phase diagram for a constant (commensurate) filling of $\langle n \rangle = 1.0$ calculated by exact QMC [116]. The latter was particularly beneficial in answering a long standing question about the possibility of a direct transition from the superfluid to the Mott-insulating state, and resulted in the theorem of Inclusions [57], discussed earlier. Using the techniques developed in part 2, this dissertation will discuss several aspects of the full phase diagram (over a range of relevant parameters) for the speckle disorder that is accessible to experiments. In fact later it will be shown that this approach produces remarkable agreement with experiments and will be able to explain many discrepancies and puzzles that have not yet been answered.

The phase diagram for this model is obtained using observables that fall within the framework of the order parameter and spontaneously broken symmetries due to Landau [30]. The idea is to measure local observables that can be averaged over the entire system to obtain

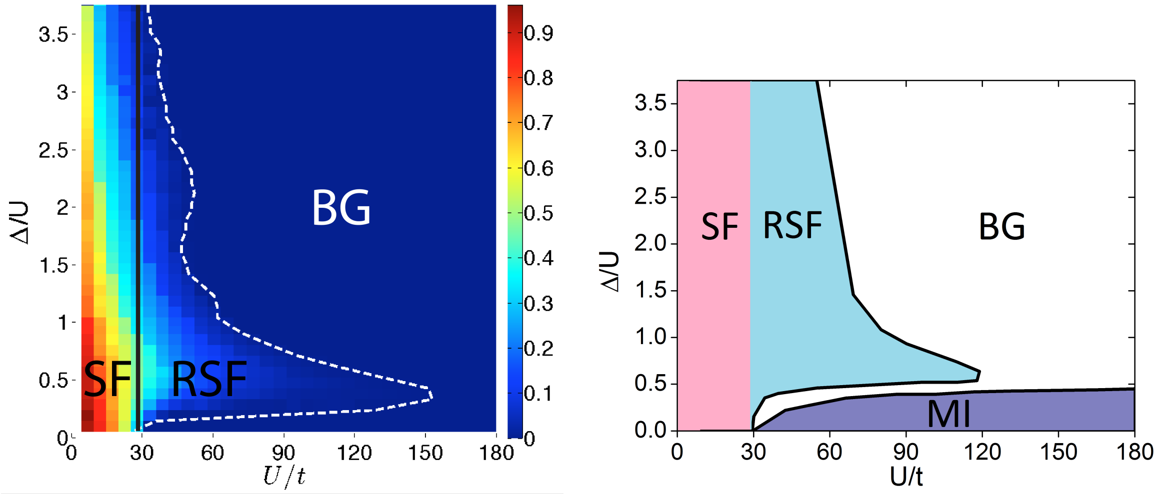

(a) Speckle Disorder (b) Box Disorder

Figure 7.5: The unit filling phase diagram for (a) speckle disorder where the superfluid fraction and the corresponding phases have been shown. BG stands for the Bose-glass, SF is the regular Superfluid phase, RSF is the Re-entrant Superfluid and MI is the Mott-Insulator phase. The border between the SF and BG is shown via the dashed white line. Qualitatively there is no difference between the SF and RSF, but the resurgence of the superfluid in the region that corresponds to an insulating phase in the clean system is a spectacular example of disorder induced order possible in quantum systems. The location of the MI phase can be defined only for the clean system. In the thermodynamic limit, there can be no MI phase possible for arbitrarily small amounts of disorder since the disorder distribution is an unbounded exponential. (See text for discussion.) (a) Shows box disorder (data from [116]).

a global estimate of order in it. Within this framework, the SF phase is identifiable via the superfluid fraction order parameter discussed earlier. The absence of superfluidity makes a system insulating, and therefore is a good way to distinguish between conductors and insulators. The MI and BG both have no global superfluidity, so the superfluid fraction for such systems is identically equal to zero in the thermodynamic limit. In order to distinguish between the two insulating states another observable is required. The compressibility of the system is a useful observable to detect between gapped and gapless systems. Thus it can be used to distinguish between the gapped MI, for which compressibility is zero (strictly only true at T = 0) and the gapless BG that has finite compressibility.

7.4.1 Commensurate Filling

Fig. (7.5a) shows the commensurate filling density ($\langle n \rangle = 1$) phase diagram generated via QMC calculations for speckle disorder. These calculations were done using 20 disorder averages for system sizes of 16^3 sites. At these sizes, the superfluid order parameter is practically free of finite size errors. Generally, the determination of the exact SF-BG boundary (at the thermodynamic limit) requires a finite size scaling calculation so that the zero of the order parameter can be rigorously determined together with critical exponents. However, this route has not been pursued here since the exact boundary is not particularly useful for comparisons against experiments due to the presence of the trap (discussed later). Instead a threshold value of the superfluid fraction order parameter $\rho_s = 1.0 \times 10^{-3}$ has been used to approximate the location of the phase boundary.

For the speckled system values of $\Delta/U > 3.75$ cannot be accessed using a single band model. In fact for smaller U/t (corresponding to weaker substrate potentials, i.e., lower values of s, the depth of the potential created in optical lattices) there are significant regions of the lattice that locally does not subscribe well to the single band model whenever the speckle disorder strength $\Delta > 1.5$ (E_R). In such cases there are a finite fraction of sites that locally do not have completely orthonormal Wannier functions and the corresponding lattice parameters are not converged properly. For instance this leads to negative values of the hopping term t_{ij}. It should be noted that the box disorder model is not constructed from the coarse-graining of a real continuum Hamiltonian. Therefore, although the disorder strength can be set arbitrarily, it may not correspond to a real physical system. Thus, care should be taken when using results from the box disorder case at large Δ/U.

The speckle disorder phase diagram can be compared against the box disorder case shown in Fig. (7.5b). It is evident that the general features of the phases are present in both cases. It is important to note that the standard deviation of the box disorder $\sigma(\delta\mu) = \frac{\Delta}{2\sqrt{3}}$, where $\delta\mu \in [-\Delta/2, \Delta/2]$, whereas for speckle disorder $\sigma(\delta\mu) \sim \Delta$. So relatively speaking, for the same parameter Δ, the disorder is stronger for the case of speckle disorder. Remarkably, the features of the phases are very robust including the finger-like projection of the re-entrant superfluid (RSF) that is generally expected to be fragile [57, 58]. Note that stochastic mean field theory which has been applied to 3D systems, is unable to capture this feature; it severely underestimates the extent of the finger that terminates at $U/t \sim 70$ [58]. This indicates that the RSF is stabilized by a large quantum fluctuations, and the general expectation – confirmed in Fig. (7.6a) – is that the compressibility of the RSF should be large. Interestingly, there is a crossover regime in the BG phase. The glass undergoes a massive change in compressibility (over 2 orders of magnitude) for a relatively small change in disorder strength (see Fig. 7.6b). This is indicative of qualitative changes in the nature of the BG and will be taken up later, since there is the question of a possible transition between two different types of glasses. Aside from differences in the relative strength of the disorder (for

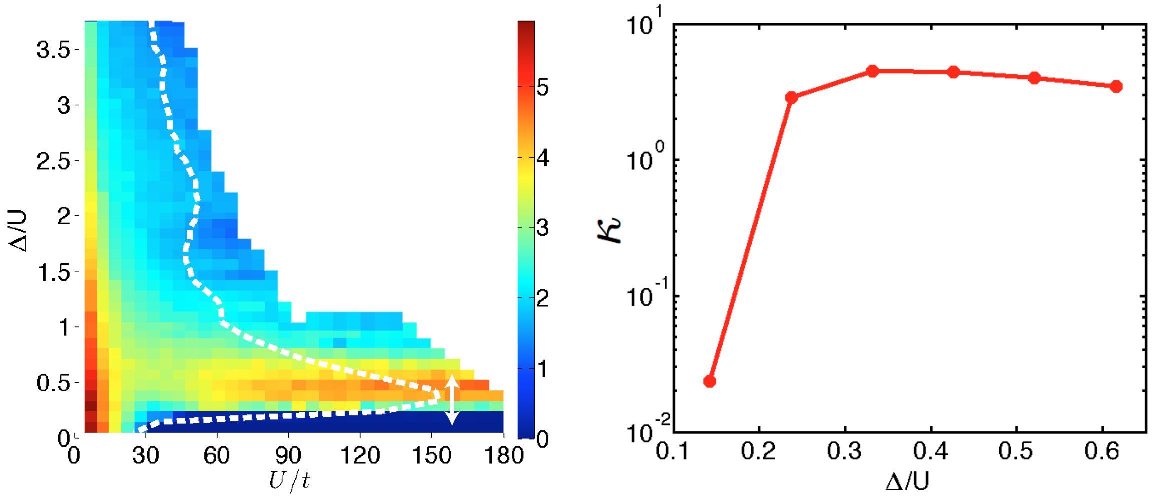

(a) (b)

Figure 7.6: (a) The compressibility per particle ($\kappa \equiv \frac{\beta}{N}\left[\langle N^2\rangle - \langle N\rangle^2\right]$) of the unit filling DBHM for speckle disorder. For the detection of the phase boundary the compressibility of the entire region is generally not needed and so data for some regions is unavailable. Complete phase diagrams are shown later in Chapter 8 for particular U/t. There are two important features to note: First, the RSF in the finger like projected state has large compressibility due to large density (and hence amplitude) fluctuations). Second, there is a crossover regime (shown by the black arrow) in the BG phase where the glass goes from ultra low compressibility to large compressibility. (b) Shows a typical way κ changes over the crossover regime. Data here is for $U/t = 155.085$. Note that it changes by over 2 orders of magnitude. Also at $\Delta = 0.0$, $\kappa = 0.0$ in the MI phase.

the same Δ value), speckle disorder also leads to a a skewness in the local potential values, with large weight towards lower disorder values. It also has no upper bound.[4]

The absence of any upper bound on the diagonal term has strong implications for the MI-BG phase boundary. In the thermodynamic limit the exponential (and unbounded) form of the onsite disorder implies that an arbitrary shift in the potential is possible even for arbitrarily small disorder strengths – following the idea of Lifshitz regions [121]. Therefore, the MI state is not possible for arbitrary disorder values in the thermodynamic limit since, there can always be regions with chemical potential shifts that locally destroy the gap (E_{gap}). However, in real (finite) physical systems there would be a cutoff (for instance in optical lattice experiments, the cutoff is set by the laser power) and the maximum disorder strength possible – the disorder bound – will vary depending on the particular instance of the disorder distribution. If the bound is larger than E_{gap}, then the true (thermodynamic limit) phase diagram will be accessible with no MI present at finite disorder values. For large values of

---

[4] Typically for experiments the upper value is cutoff by the power of the laser, but it is possible for the local potential to be shifted by very large values, albeit the chance being exponentially small.

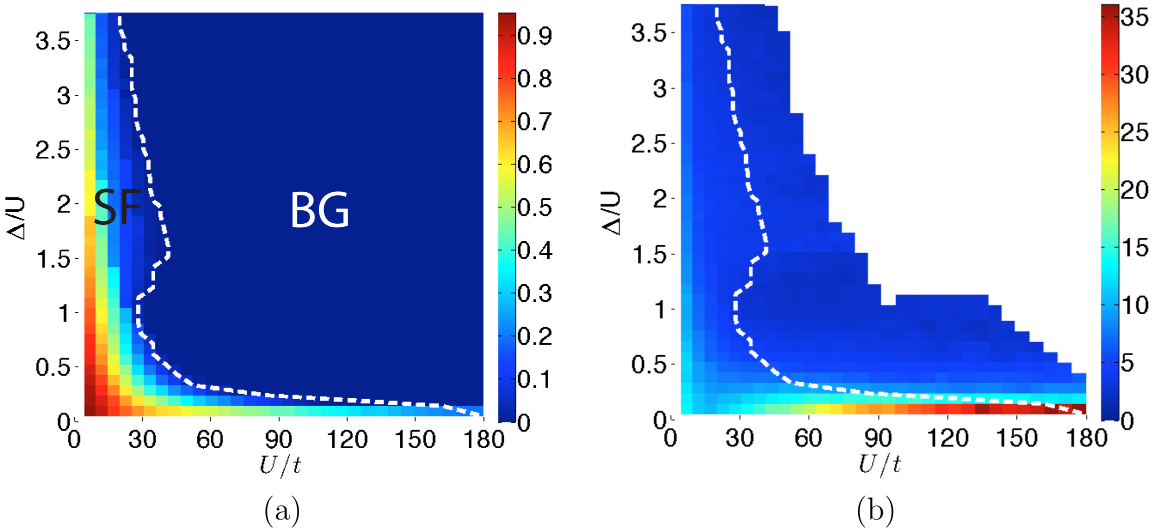

Figure 7.7: (a) The superfluid fraction values and the corresponding phases for a system at half-filling ($\langle n \rangle = 0.5$ (b) The compressibility per particle (κ) defined earlier.

E_{gap}, large system sizes are needed to be able to see the formation of the BG. As far as experiments in optical lattices are concerned, the finite size implies that the MI state may be present even if the phase diagram shows such a state is not possible.

7.4.2 Incommensurate Filling

Aside from the commensurate filling case, it is also worth investigating the system at lower filling. This is important because experiments with the trap access low density systems. The phase diagram at half filling is shown in Fig. (7.7) together with the superfluid fraction and the compressibility per particle. Comparing with the commensurate filling shown above it is apparent that at these densities the BG is highly compressible. Additionally, the SF remains remarkably stable at low interaction strengths, whereas at larger U/t it is rapidly destroyed. At low disorder strengths, the SF is stabilized as in the RSF with large amplitude fluctuations that leads to large compressibility. At large disorder strengths despite the low density, the glassy state rapidly exhibits very low compressibilities, but it saturates for large Δ/U. In order to compare with optical lattice experiments a more useful phase diagram than the fixed density type of diagrams shown in this section (or Canonical ensemble phase diagram), is the constant chemical potential or Grand-Canonical phase diagram. These will be discussed in the next chapter in the context of experiments.

7.5 Equilibrium Properties of the Bose-Glass

At this juncture it might be most useful to consider the properties of the BG as it truly arises in the DBHM. The QMC framework developed in the dissertation makes it possible to study to the true properties of BG exactly, without the need for any approximations. Thus far the BG has been described only in terms of global properties whether it by via QMC calculations or MFTs. The puddle like picture has been evoked to explain the interesting global properties of the BG, but these have not been observed directly in 3D (at T = 0 or finite T, whether it be via QMC, Experiments or MFTs). In 1D, only one MF type of calculation has attempted to probe this phase in terms of standard observables such as the single-particle density matrix and the superfluid fraction [79]. The picture that emerges is a fascinating one, evoking the concept of *quasi-condensates* [122]. This work, extends these ideas into 3D, but it doesn't suffer from the systematic problems introduced by approximations made in MFT.

7.5.1 Commensurate Filling

The prototypical system analyzed here is a large (46^3) system at $U/t = 40$ for unit filling $\langle n \rangle = 1$ at $t/k_B T = 2$ (which is near the T = 0 limit, as will be evident shortly). This location in the phase diagram is ideal because it contains all features observable in the DBHM phase diagram. Consider Fig. (7.5) at $U/t = 40$ all three phases are accessible: the MI at $\Delta/U = 0.0$, the BG for $0.0 < \Delta/U <\sim 0.15$ and the SF for $\Delta/U > 0.15$. The latter is of the re-entrant type which is of great interest since it has not yet been observed experimentally (more on this in the next chapter). Shown in Fig. (7.8) are column integrated values of three observables taken for three disorder values ($\Delta/U = 0.0$, 0.124 and 0.248) that exemplify the three phases. The top row shows the integrated densities, the middle column corresponds to the compressibility per particle (κ) and the bottom row corresponds to the largest singe particle eigenmode calculated from the single-particle density matrix (ρ_1). The densities reveal clear differences in the three phases. The MI appears to be featureless as expected with a commensurate filling. The SF state appears to have large density fluctuations arranged in a stripe like fashion (owing to the underlying speckle which is anisotropic). The BG fits the paradigm discussed earlier, where it takes flavors of both the MI and SF state. Although it is tempting to conclude that the density modulated regions in the BG correspond to SF puddles, care needs to be taken. In this form of local picture, the highly compressible sectors would be expected to correspond to the SF, whereas the incoherent background would be expected to take on compressibility values much like the MI. However, the compressibility

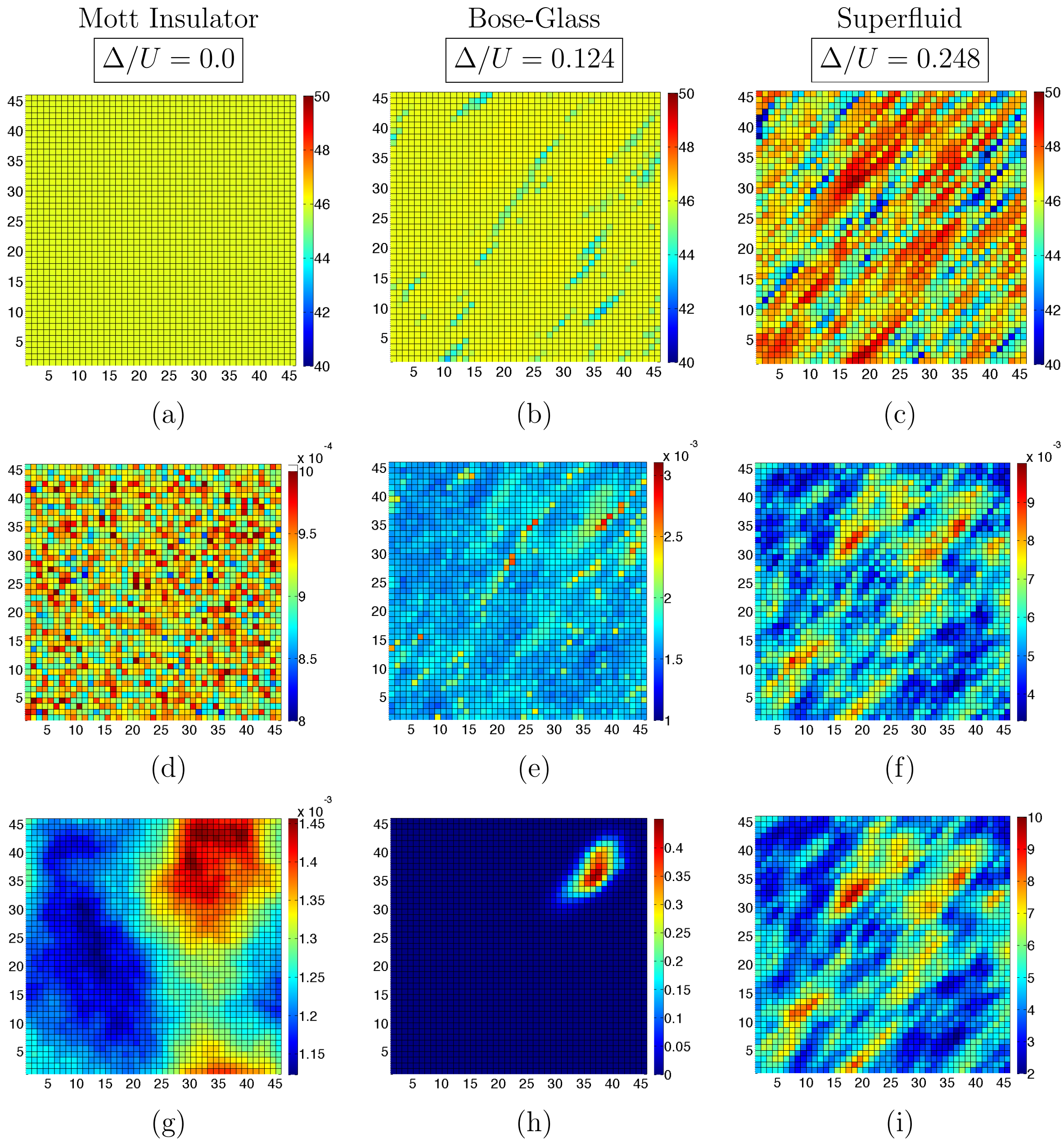

(a) (b) (c)

(d) (e) (f)

(g) (h) (i)

Figure 7.8: Each image was made by summing along one primary axis. The system is of size 46^3 at $U/t = 40$ for unit filling $\langle n \rangle = 1.0$ (a)-(c) Integrated densities (d)-(f) Integrated compressibility per particle (κ) and (g)-(i) Integrated largest single-particle eigenmodes. (See text for discussion.)

figures showed (d)-(f) paints a different picture. Note that the BG is generally at a higher compressibility than the MI, even locally. The SF is the most compressible. The global compressibility per particle of the three phases are 0.0092(4), 0.30(1) and 2.6(1) for the MI (at finite temperature), BG and SF respectively. These textures actually indicate a rich landscape in imaginary time which is particularly illuminating in the SSE or path integral language.

In the worldline picture (see Part II, Chapter 2) the passage of the worm on an equilibrated system is synonymous with the movement of particles (or holes) across space time. The average distance that the worm explores in space is related to the spatial correlation length, whereas the distance explored in time is related to the imaginary time correlation length. For the MI state, the system has short correlation length in both space and time and the correlations decay exponentially. The worm does not wind around in imaginary time which is the mechanism by which the particle number changes. This is why the MI state has zero superfluid susceptibility at $T = 0$ that implies zero compressibility. Additionally, there is no long range order in the system. At finite temperatures these values deviate from zero but remain exponentially suppressed. There are only a small number of kinetic operators corresponding to short range localized hops.

In the SF state the picture changes dramatically. There are comparatively larger number of hopping terms arranged in a way that leads to connected clusters of sites spread throughout the system. When the worm propagates in this phase, it moves through out the system and winds around the periodic cell (in space and time) following the permutation cycles of the superfluid. The system exhibits long range order in both space and time. At T=0 this would lead to infinite superfluid susceptibility leading to a compressible system. The long range order in space, where the spatial correlation decay to a finite value additionally indicates the presence of Bose-Einstein condensate.

The BG state is different qualitatively from both the MI and SF. The kinetic terms are distributed in a way that allows for permutation cycles to spread out over patches locally, but not globally. The worm propagates so that there are only short range correlations - it moves through regions larger than the MI, but not SF. The spatial correlations decay in a way that prohibits the system from having long range order – leading to the formation of quasi-condensation instead of true Bose-Einstein condensation. On the other hand the worm winds around in imaginary time, and the correlation length has finite values at $t = \beta/2$ (where $\beta = 1/T$ in normalized units). This leads to infinite superfluid susceptibilities as well as finite compressibility at $T = 0$. Within this framework it is clear that a large range of behavior is possible for the BG both in terms of the compressibility as well as spatial order parameters. For instance, if the limiting value of the imaginary time correlation function is small (large), then the corresponding compressibility will be small (large). Additionally, depending on how quickly the spatial correlation length decays, the size of the corresponding quasi-condensates will change.

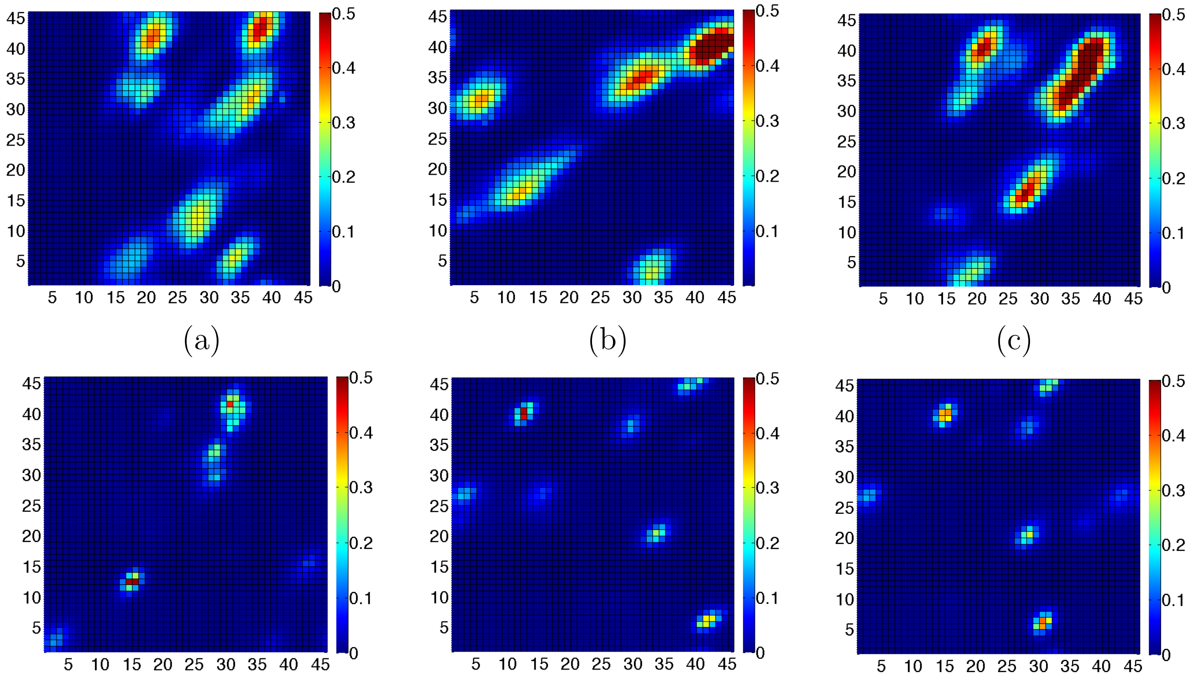

(a) (b) (c)

(d) (e) (f)

Figure 7.9: Collection of the 10 largest single-particle states of the single-particle density matrix that correspond to the superfluid puddles or quasi-condensates. (a)-(c) correspond to images by integrating along the three different axes for $\Delta/U = 0.124$. (d)-(f) correspond to images for $\Delta/U = 0.062$

The discussion above explains the behavior of the single-particle modes extracted from the single-particle density matrix. For the system considered here, the superfluid fraction is identically zero for the BG and MI phases; the SF state has a superfluid fraction of 0.058(3) measured from the winding number formulation discussed earlier [45]. The occupation number (fraction) of the largest single-particle state is 0.000027(5) for the MI, 0.00020(1) for the BG and 0.103(4) for the SF. The corresponding column integrated spatial distributions are shown in Fig. (7.8g-i). These images show the dramatic differences in the three states. The SF state here coincides with the macroscopic BEC. The MI eigenstate is essentially flat with minor variations due to finite temperature effects and the occupation number is $\sim O(1)$. The spectacular localized form of the quasi-condensate is obvious in the BG state. These states have been extracted using the procedure discussed in Part II. Fig. (7.9a-c) shows a collection of the first ten single-particle eigenstates corresponding to quasi-condensates or superfluid puddles with occupation numbers $\sim$ 19.5 to 7.2 particles. As an additional illustration of the way the BG state proceeds, Fig. (7.9d-f) shows the quasi-condensates for a lower disorder strength of $\Delta/U = 0.062$ which is closer to the MI-BG transition. The occupation num-

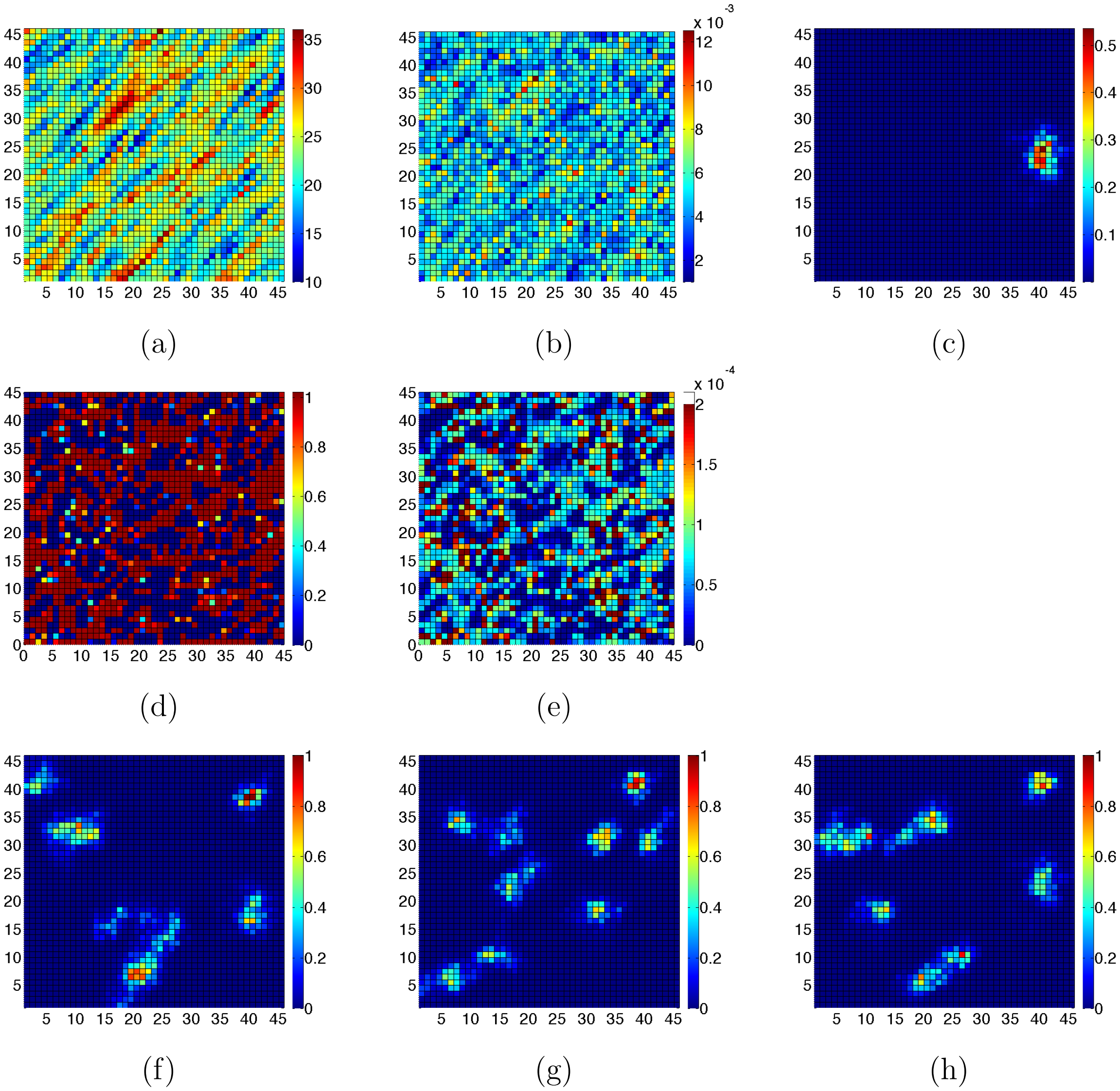

(a) (b) (c)

(d) (e)

(f) (g) (h)

Figure 7.10: These images correspond to a Bose-glass system at $U/t = 40$ and disorder strength $\Delta/U = 0.744$ with a filling of $\langle n \rangle = 0.5$. (a) Integrated density (b) Integrated compressibility per particle (c) Integrated largest quasi-condensate profile (d) Slice of the density (e) Slice of the compressibility per particle. (f)-(h) are integrate profiles along the three different principal axes for the ten largest quasi-condensates. (See text for discussion.)

bers in these modes are much lower ranging from ~ 2.5 to 3.1, close to MI single-particle occupation numbers (but the form of the eigenstates are completely different).

7.5.2 Incommensurate Filling

The density, compressibility and the quasi-condensate states are presented in Fig. (7.10) at $\Delta/U = 0.744$ for $U/t = 40$ and $\beta = 200$ for the incommensurate filling of $\langle n \rangle = 0.5$. Compared to the commensurate filling case, the BG case here is much more compressible with

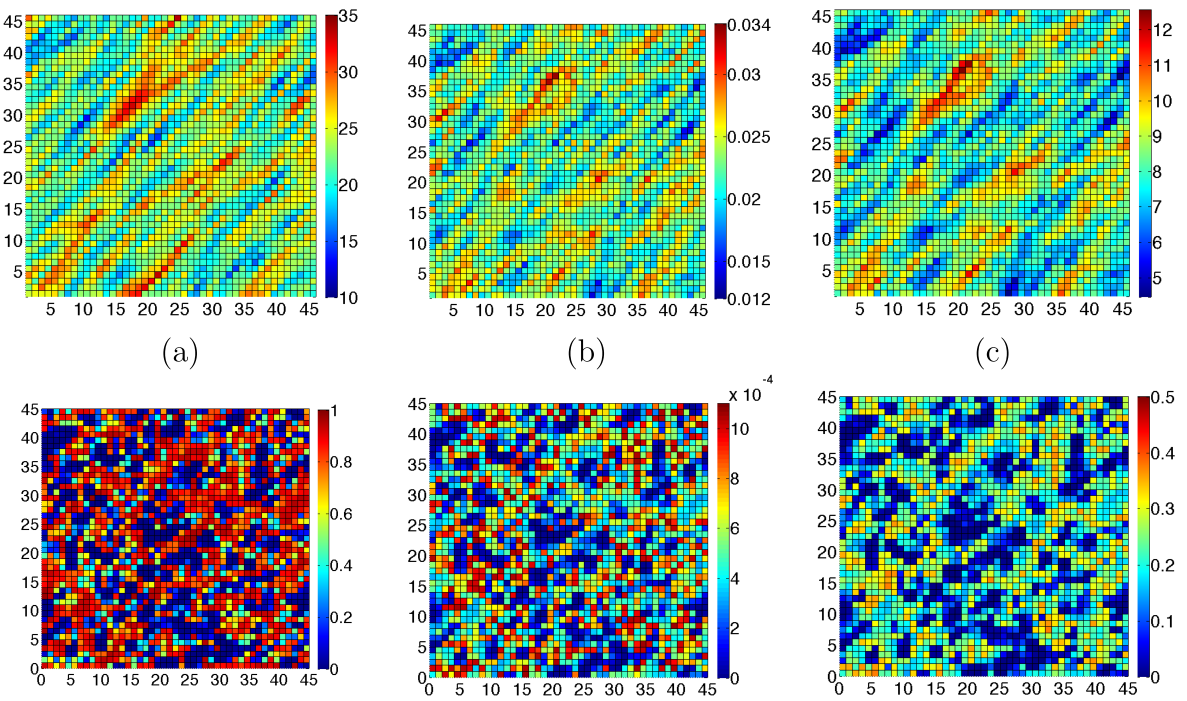

(a) (b) (c)

(d) (e) (f)

Figure 7.11: These images correspond to a Superfluid system at $U/t = 40$ and disorder strength $\Delta/U = 0.248$ with a filling of $\langle n \rangle = 0.5$. (a) Integrated density (b) Integrated compressibility per particle (c) Integrated largest quasi-condensate profile. Slice of (d) Density, (e) Compressibility per particle and (f) Condensate distribution. (See text for discussion.)

$\kappa = 3.9(1)$. A slice through the density distribution in Fig. (7.10d), shows that despite the overall half-filled system, the system is made largely of unit filled clusters interspersed with the vacuum. The clusters are not MI like however, as indicated by their compressibility that is significantly larger. The ten largest localized quasi-condensates are shown in Fig. (7.10f-h) with occupation numbers between 7 to 10 particles. Compared to the commensurate filling case, these puddles appear to be more sharply peaked or localized.

The corresponding SF state at $\Delta/U = 0.248$ is presented in Fig. (7.11). The average density distribution indicated in Fig. (7.11a) is remarkably similar to the BG state (c.f. Fig. 7.10a); however, the system is much more compressible. Slices shown in Fig. (7.11d) and (7.10d), on the other hand, show that the basic structure of the density distributions look similar between the two states, but the SF state has larger density modulations. The global SF state in this strongly interacting system therefore seems to be supported by networks of highly compressible SF threads (compressibility of a slice is shown in Fig. 7.11e).

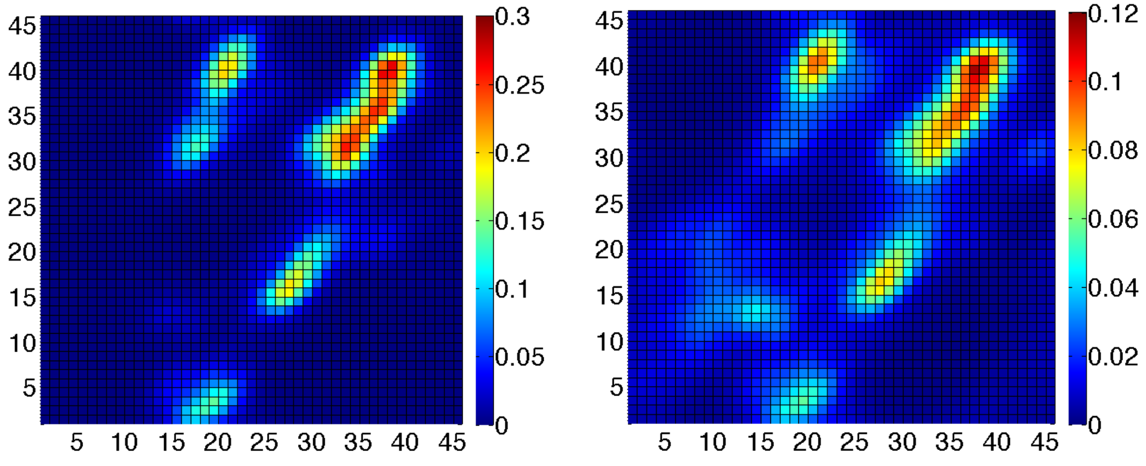

(a) $\beta = 80\ E_R^{-1}$ (b) $\beta = 40\ E_R^{-1}$

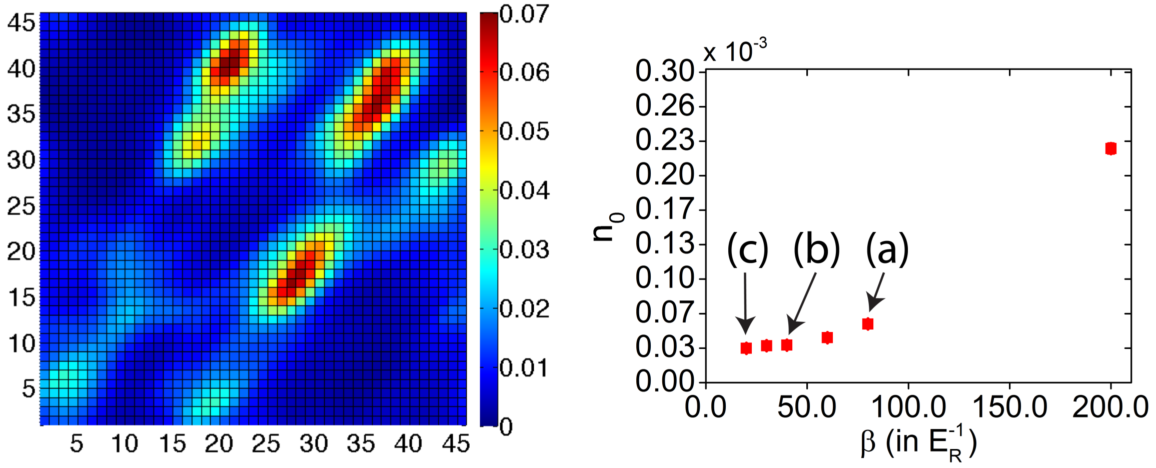

(c) $\beta = 20\ E_R^{-1}$ (d)

Figure 7.12: Behavior of the first 10 largest quasi-condensate puddles with reducing temperature from (a)-(c) for a strongly correlated system at $U/t = 40$ and $\Delta/U = 0.124$. The images have been constructed by integrating along the one of the principal axis. (d) Shows the quasi-condensate population of the largest single-particle mode as a function of inverse temperature. The quasi-condensate density distribution point corresponding to $\beta = 200$ is shown in Fig. (7.8h).

7.5.3 Stability of the Bose-Glass State to Finite Temperature Effects

The stability of the BG to finite temperature effects is an essential feature worth exploring. The crossover process by which the BG changes to a normal state is not well understood and there are no studies to date on this topic. This is also an important question with regards to experiments because such inquiries require a comprehensive understanding of the finite temperature crossover regime. The stability of the BG localized modes can be studied by exploring their structure and how the occupation numbers change as the system's temperature is increased. A typical example has been shown in Fig. (7.12a-d) corresponding to $U/t = 40$, $\Delta/U = 0.124$. It is evident that the structure of the localized puddle states are remarkably stable for a large range of temperatures: $T = 0.005$ to 0.05 ($E_R = 167\ nK$).

7.6 Finite Temperature Effects

In order to gain insight into the finite temperature of the different phases simulations were undertaken for $U/t = 40$ with large systems of size 46^3. The behavior of the key observables of superfluid fraction (ρ_s) and compressibility per particle (κ) have been shown for three different filling densities $\langle n \rangle = 1$, $\langle n \rangle = 0.8$ and $\langle n \rangle = 0.5$ in Fig. (7.13). At unit filling, notice that the SF has a lower critical temperature for the Normal-SF transition at higher disorder strengths - the disorder stabilizes the superfluid state. The is a phenomenal example of disorder induced order possible in quantum systems. The BG in the low disorder regime has ultra low κ that appears to follow the form $\kappa \sim exp(-b/T^{\alpha}) + c$ that corresponds to the so called Mott-Glass (MG) state [123]. Note that the superfluid state that manifests at unit filling corresponds to the re-entrant type of SF that is an exotic disorder induced phenomena. At these interaction strengths the clean system would be an insulator.

At lower densities of $\langle n \rangle = 0.8$, the system transitions from a SF state at $\Delta/U = 0$ to a BG for small Δ/U. At larger disorder the BG transforms to a SF and finally at larger Δ/U it transforms back to a BG (not seen in this figure but see Fig. (8.13) in the next chapter). The transition temperatures are close for all SF types, but it appears that disorder stabilizes the SF much like the unit filling case.

At even lower filling of $\langle n \rangle = 0.5$, disorder no longer stabilizes the SF and a rapid destruction of the SF is seen with increasing disorder. Additionally, the critical temperature of the SF is reduced for larger disorder strengths. Interestingly, it is evident that there are different qualitatively types of behavior for the BG. At higher filling, the BG compressibility changes much like the expected behavior of the MG phase. At intermediate densities, the BG takes on a different qualitative behavior, being much more compressible that does not show much dependence on temperature.

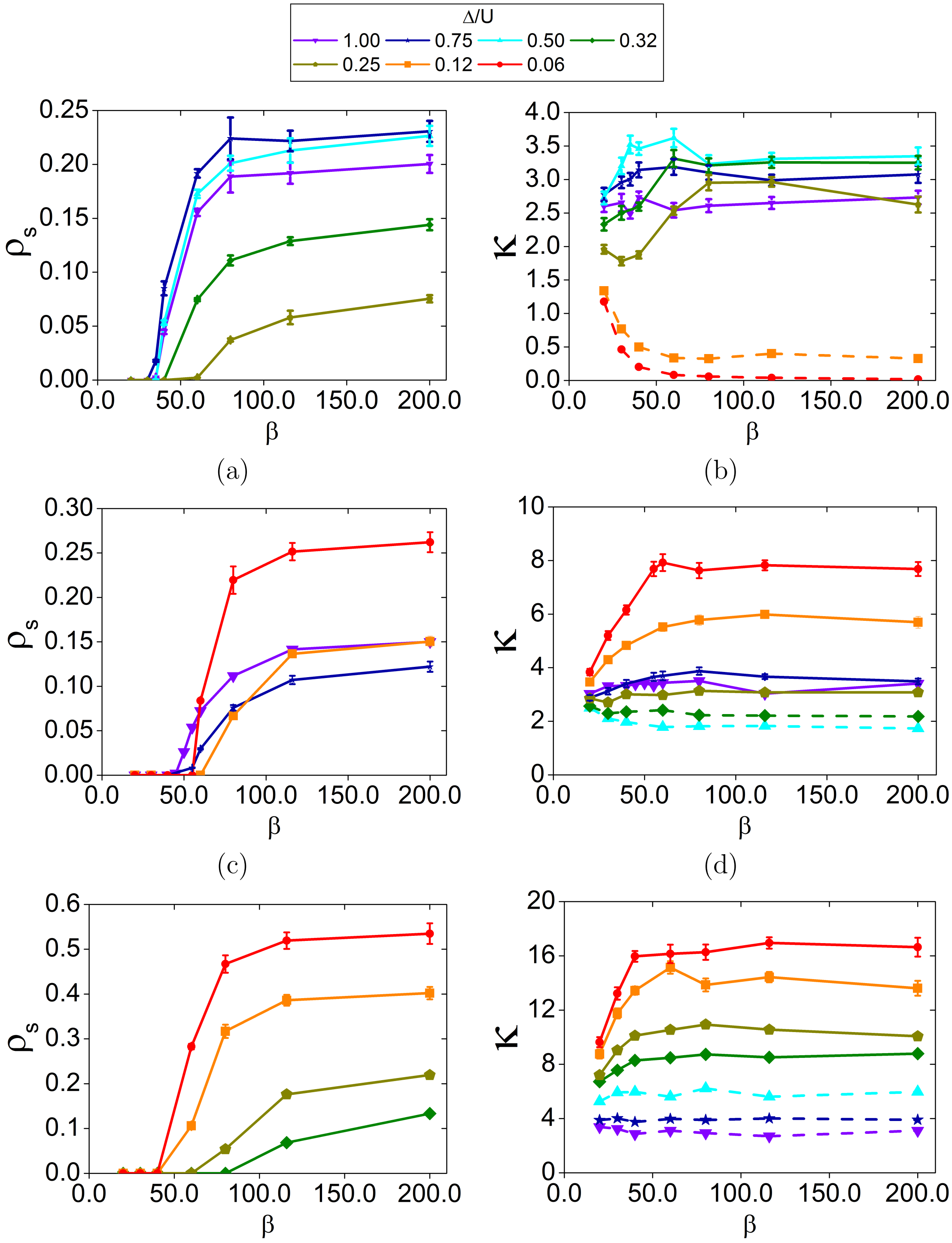

(a) (b)

(c) (d)

(e) (f)

Figure 7.13: These images correspond to simulations for 46^3 system at $U/t = 40$. The top images correspond to unit filling $\langle n \rangle = 1.0$, the middle images are for $\langle n \rangle = 0.8$ and the bottom images are for $\langle n \rangle = 0.5$. The solid lines correspond to the Superfluid state and the dashed lines are for the Bose-glass state. The energy scale is set by $E_R = 167\ nK$.(See text for discussion.)

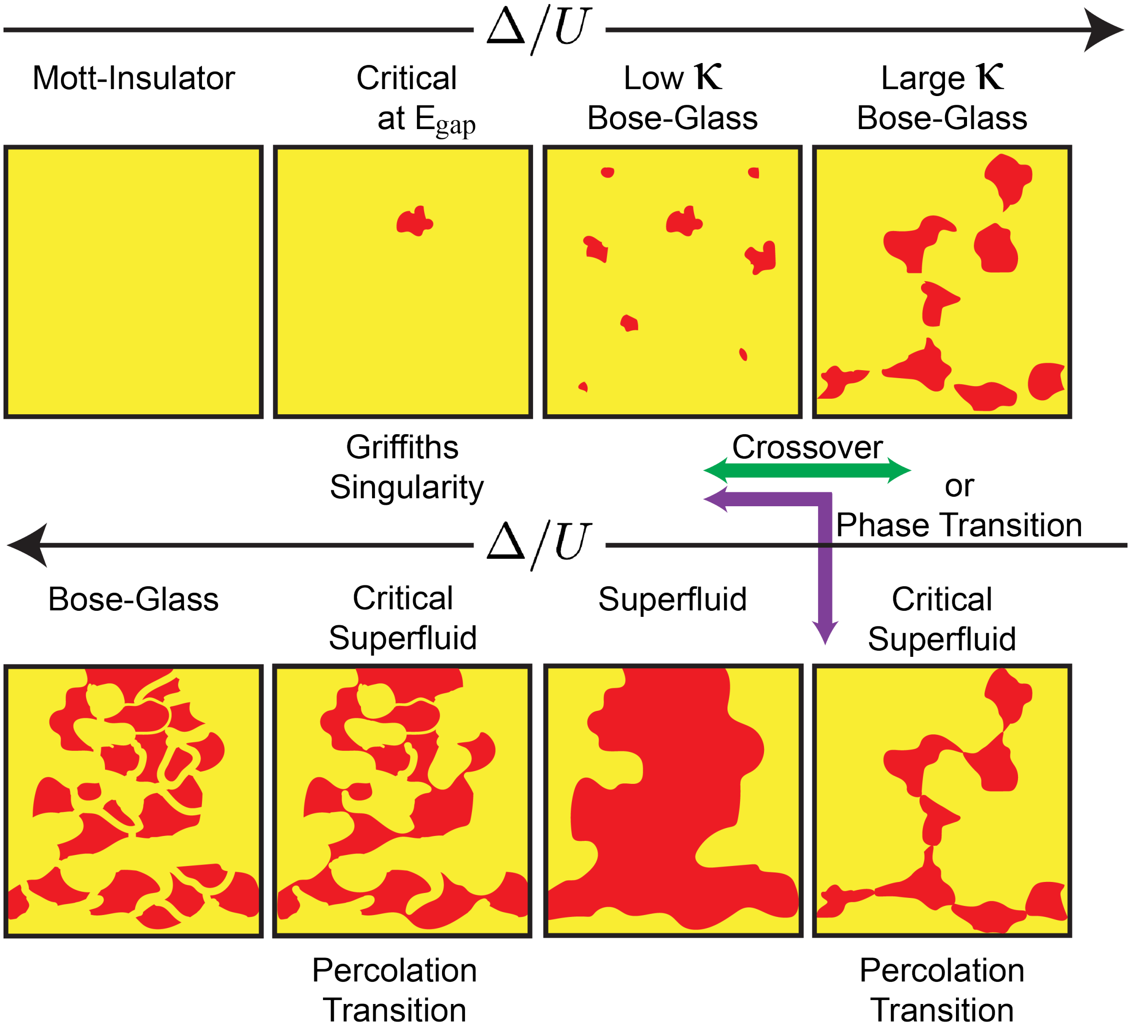

Figure 7.14: Sketch of the states and the corresponding phase transitions as a function of increasing disorder strength Δ/U for commensurate filling and strong interactions. The clean system starts out at as a Mott-Insulating state, and persists until the disorder bound is equal to the Mott-Insulating gap. At this point the system will develop rare regions and under go a phase transition to a BG state possibly via the Griffiths singularity. The low compressibility BG either undergoes a cross over to a highly compressible BG or phase transition to a superfluid via a percolation transition. If the latter route is followed, the coherence is eventually destroyed with sufficient disorder so that it transitions to a BG via another percolation transition.

7.7 Summary of Results

In this chapter, the general picture of the effects of disorder on the Bose-Hubbard model was presented. The phase diagram of the Bose-Hubbard picture gets modified by the appearance of a new exotic quantum phase called the Bose-Glass. Via scaling arguments it was shown that since the MI-SF phase transition violates the Harris criteria, the transition is transformed to a new Universality class: the BG-SF transition, which is expected to be a percolation type of transition. The BG is a Griffiths type of phase, exhibiting Griffiths singularities, that is responsible for the MI-BG type of transition. Using the Theorem of Inclusions, it was further demonstrated that a direct MI-SF transition is forbidden in the presence of disorder. Using large scale QMC simulations, the unit filling phase diagram was computed for the speckle type of disorder and compared against the phase diagram for box disorder. Remarkably the features of the diagrams are very robust despite the fact that the two types of distributions are very different. However, there is a major difference - the MI is absent for arbitrarily small values of disorder strength in the case of speckle disorder in the thermodynamic limit. The Bose-glass phase seems to fall into two different types of qualitative properties corresponding to ultra low compressibility (close to zero) and relatively higher compressibility connected by, what appears to be, a crossover with the compressibility changing over two orders of magnitude despite a relatively small change in disorder strength. The BG corresponding to the incommensurate densities falls into the latter case. Using the single-particle density matrix, it was confirmed that the BG is composed of quasi-condensate superfluid puddles that are remarkably stable to finite temperature effects. A qualitative picture of the different phases and phase transitions have been shown in Fig. (7.14). The finite temperature properties of the different states show that disorder can stabilize the SF state at higher densities, whereas at low densities the opposite is true. The crossover type of phenomena observed at ultra low temperatures that suggest two types of BG states is confirmed via their temperature dependences. The low disorder BG that appears at commensurate densities appears to have a Mott-glass type of compressibility per particle; the incommensurate BG with large compressibility, on the other hand, seems to be robust to temperature effects, undergoing a cross-over to the normal state at large finite temperatures.

Chapter 8

Properties of Trapped Systems with Speckle Disorder

The possibility of experimentally realizing a disordered system in a controlled manner is an exciting proposition. The phenomenology associated with disorder and strongly correlated physics constitute some of the hardest problems in modern physics. The few systems that have been been amenable to theoretical and experimental inquiries, such as superfluid ^4He and ^3He in porous aerogels [124, 125], ultcold atomic gases in quasi-periodic lattices [11] and speckle disorder [56, 69] and disordered quantum magnets [126] have revealed a extraordinarily rich landscape of possible phenomena, very little of which is understood. There are still many unanswered questions with regards to existing results and is an active area of research. For instance, dynamical phenomena associated with disorder can be extremely challenging and theoretically intractable without insight from experiments.

Disordered systems are notoriously difficult to work with. Direct comparison between experiments and theory are made difficult because the observables are sensitive to the disorder distribution itself. It is, thus, not obvious at all whether discrepancies are due to differences in disorder realization or whether there are in fact limitations within the theoretical framework being used or calibration issues with experiments. Additionally, there could be strong non-universal non-equilibrium effects in experiments that do not lend well to systematic descriptions. In light of these difficulties, the advent of optical lattices and controlled speckle disorder that is characterizable by theory is a giant leap forward in this difficult field.

In this chapter and the next, QMC simulations are used to explore the system accessed by experiments with ultra cold atoms in optical lattices with speckle disorder. The idea here is to study the equilibrium properties of such systems as a way of systematically understanding the connections between trapped systems and trap free phases. The results can be used to understand and calibrate experiments. They can also be used check for out-of-equilibrium phenomena and address dynamical aspects when systems are near equilibrium.

In what follows, the general experimental setup is first outlined. Next, in order to motivate the theoretical inquiries undertaken here, results from a fairly recent novel experimental method that probes the transport properties of the disordered Bose-Hubbard model (DBHM) is discussed. Finally the main theme of this chapter, *viz.* the study of the properties of trapped systems is undertaken systematically. Properties of characteristic observables such as the compressibility and density are studied at short on-site length scales as well as global length scales – typically the scale accessible to experimental probes at present. Next it is shown that a more natural length scale is set by the domains that develop in these systems and the procedure to identify such scales is discussed. An interesting inquiry undertaken is to see how the behavior of these systems correspond to the local density approximation (LDA) frequently employed in clean trapped systems. The tools developed along the chapter are then used to answer the long standing question about the possibility of the re-entrant superfluid phase (RSF) arising in trapped systems. Finally, for qualitative purposes, grand-canonical phase diagrams (μ/U vs Δ/U) for different interaction strengths that should be very useful for experiments are presented. Effects of disorder averaging are discussed in this context. The chapter concludes with a short foray into the study of the consequences of tunneling disorder.

8.1 General Experimental Setup

The 3D disordered Bose-Hubbard model has been realized in experimental systems using speckle disorder. This is achieved by introducing a speckle field on top of the optical lattice beams used to setup the cubic lattice discussed in Chapter 6. Just as in the clean case, this setup also requires an additional harmonic confinement of frequency ω to keep atoms confined – rendering the system inhomogeneous (over and above the disorder). The trapped DBHM then is give by:

$$\mathscr{H} = -\sum_{\langle ij\rangle} t_{ij}\hat{b}_i^{\dagger}\hat{b}_j + \frac{1}{2}\sum_i U_i\hat{n}_i(\hat{n}_i - 1) + \sum_i \left(\frac{1}{2}m\omega^2 r_i^2 - \mu + \delta\mu_i\right)\hat{n}_i, \tag{8.1}$$

where, as before, t_{ij}, U_i and $\delta\mu_i$ correspond to disorder distributions generated for the speckle field discussed in Chapter 5 Section 5.6, $\hat{b}^{\dagger}$ ($\hat{b}$) correspond to the creation (annihilation) operators and $\hat{n}$ is the particle number operator. The energy scale is set by atomic recoil energies

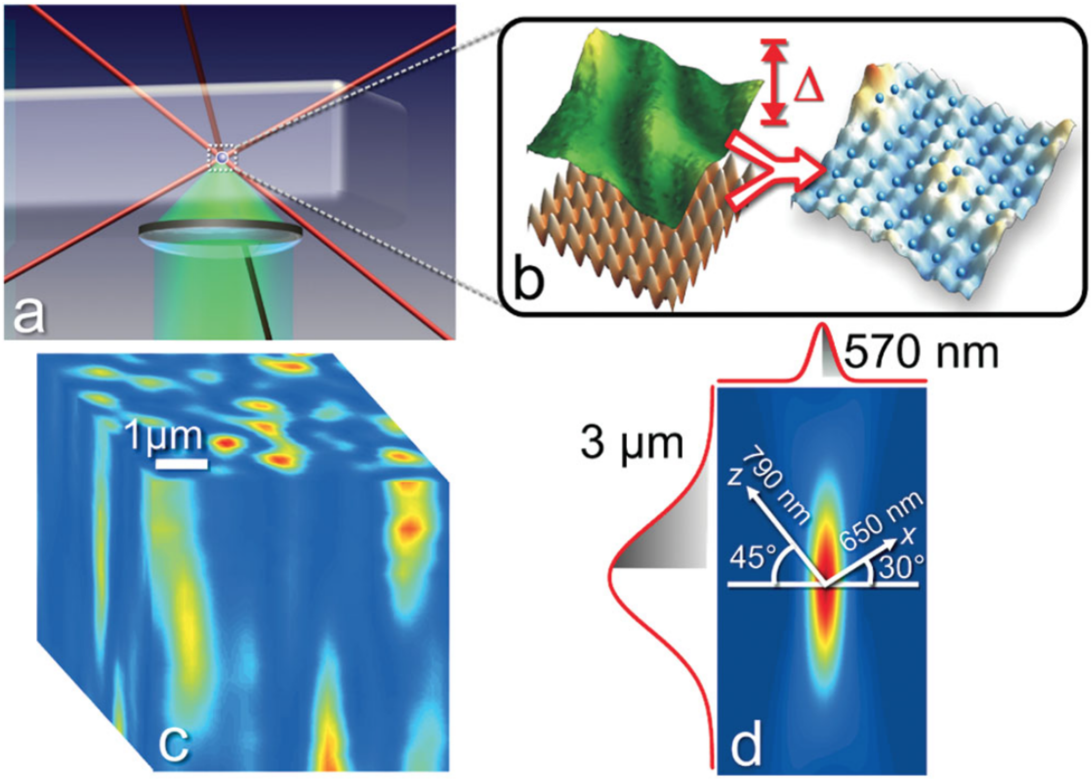

Figure 8.1: Setup of Experimental System (taken from [69]). (a) Shows the retro-reflected laser beams (shown in red) used to setup the optical lattice. The optical diffuser holographic lens together with the diffuser light is shown in green. (b) Shows the effective disorder lattice potential created by combining the speckle field and the regular lattice. The speckle strength is set by Δ. (c) Example of the speckle distribution. (d) The measured speckle intensity used to reconstruct the AC function. The $1/e^2$ radii of the AC distribution are 570 nm and 3 μm along the transverse and speckle propagation directions; the lattice axes project onto the x and z directions in this plane.

($E_R = \hbar^2\pi^2/2ma^2$), where $a = \lambda/2$. λ is the wavelength of the laser used to create the optical lattice. For the experimental system considered in this chapter, $\lambda = 812$ nm and m is the mass of ^{87}Rb atoms, corresponding to which $E_R = 167\ nK$. The speckle field is setup using a 532 nm light projected through a holographic diffuser. The $1/e^2$ autocorrelation length along the transverse (T) and propagation or longitudinal (L) direction is 570 nm and 3 μm, respectively. However, the diffuser light is oriented at different angles relative to the optical lattice beams. This causes the speckle to have different lengths along the lattice beams. The projected lengths are 790 nm and 650 nm so that the ratio of the autocorrelation lengths is ~ 1.22. The setup is shown in Fig. (8.1), using which, different types of experimental measurements are possible. The general tools of TOF imaging and peak fraction measurement are possible as in the clean case discussed in Chapter 6. In addition to these, alternate innovative techniques have been developed to try to assess the properties of the system created in the presence of disorder. The first of these methods, involving the measurement of transport properties is discussed in this chapter. There are many questions left unresolved with regards to these measurements, which will be addressed here using QMC. The next chapter involves a quantum quenching technique that was used to study the superfluid (SF) to Bose-glass (BG) transition in collaboration with QMC techniques developed in this dissertation.

8.2 Measurement of Transport Properties

This experiment, detailed in [56], attempts to distinguish between the insulator and conducting states of the DBHM using transport type of measurements. In the discussion that follows, first the experimental setup is outlined, after which transport measurements are discussed. The specific findings reported by experiments are discussed together with possible interpretations. In the next section, QMC calculations will be discussed to lend further insights into the experimental system.

The general setup is outlined in the earlier section following [69]. The geometric mean of the bare trapping frequency is $\omega' = 40$ Hz created from a hybrid magneto-optical trap consisting a magnetic quadrupole field and a 1064 nm focused laser beam. The optical lattice beams also add additional confinement so that the total confinement created ω is $\sim$ 52 - 69 Hz for $s = 6$ to 16 E_R. The average number of atoms $N = 12 \pm 4 \times 10^3$ that is expected to correspond to $\sim$ 1.4 to 1 atoms at the center of the trap for the clean system for optical lattice depths $s = 6$ and 14 E_R, respectively.

Transport properties are measured by applying an impulse along two speckle directions T and L. The impulse along T is created by translating the 1064 nm laser beam by 7 μm using a 3 ms trapezoidal ramp. The impulse along L is created by applying a magnetic field for 1 ms. The magnitude and durations were adjusted to create approximately equal impulses along the different directions. Systematic uncertainties and determination of zero velocity of the center-of-mass (COM) motion have been discussed in detail in [56]. The general idea of this form of measurement is to study the motion of the COM immediately after application of the impulse. An important aspect to keep under consideration is that extremely rapid impulses can lead to phase slips in the gas. Here the impulse is rapid compared to the harmonic motion but not so fast as to be dominated by phase slips, i.e., $\gamma >> 1/\tau >> \omega$, where τ is time of the impulse, ω is the oscillator frequency for motion in the parabolic confinement and γ corresponds to quantum phase slip rate. The velocity of the COM, is given by $v = (F\tau/m^*)e^{-\gamma\tau}$ where F is the force during the impulse and m^* is the effective

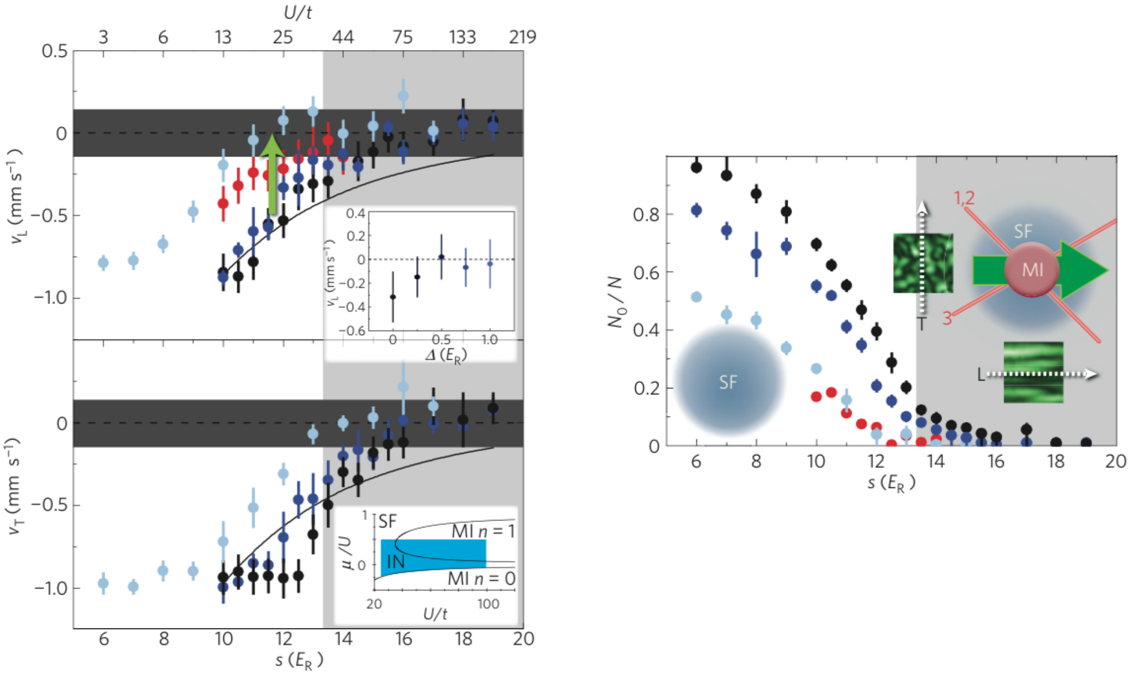

(a)

(b)

Figure 8.2: Taken from [56]. (a) The overall COM velocity v of the gas after an impulse is applied as the lattice depth s is varied for three disorder strengths: $\Delta = 0$ (black), 0.75 (dark blue) and 3.0 E_R (light blue); data are shown for the longitudinal (top) and transverse (middle) directions. The data shown in red corresponds to high-temperature transport in a clean lattice. The solid black line is an estimate of velocity caused purely due to the effective mass induced by the lattice. The dark-grey band indicates the systematic uncertainty in determining zero velocity. The bold green arrow shows how the addition of disorder changes the SF state at $s = 12$ to an insulator for $\Delta = 3$ E_R. The top inset shows how disorder affects v_L for $s = 14$. The bottom inset shows sample slices through the disorder profile. Note, as discussed in Fig. 8.1, the AC speckle sizes are asymmetric in the longitudinal (L) and transverse (T) directions. The illustration also shows the expected shell like structure of the MI surrounded by a SF in a clean system. 1, 2 and 3 mark the three optical laser beams and green is the speckle beam. The error bars represent statistical uncertainty in the (typically) seven measurements averaged for each point. The error bars for v also represent include statical uncertainty in determining zero velocity. (b) The peak fraction (and *not* the condensate fraction) calculated from TOF expansion followed by fits. (See text for discussion.)

mass of the atoms due to the lattice potential. The expectation is that for a fixed s, the insulator does not respond to the impulse so that $\gamma \to \infty$ and $v = 0$.

Fig. (8.2) summarizes the key results for transport measurements undertaken in [56]. In the clean lattice, the velocity approaches zero as expected for an insulator. In this case, as the lattice depth is increased (which implies an increase in the effective interaction strength U/t) the SF gas transforms into a mixture of MI and SF domains arranged in shells. The suppression in COM velocity is attributed to both an increase in the effective mass (shown as a black solid line Fig. 8.2a) and an enhancement in the quantum phase slip rate $\gamma \propto e^{\sqrt{U/t}}$. Note that finite but small velocity is reported even when there is already a MI state in the center of the gas due to the SF shell surrounding it. This is evident from the finite peak fraction.

In the presence of disorder, a strong suppression of the COM velocity is seen at very large $\Delta = 3\ E_R$ for $s = 12\ E_R$. The interpretation here is that at these large values the SF gas is completely transformed to an insulator (IN). This type of measurement cannot distinguish between insulating states, which at finite temperatures may also have undergone a crossover to the normal (N) state. Experiments attempt to answer this problem of a SF-N type of transition by matching the peak fraction values for a clean system at higher temperatures (or entropy per particle). They show that in the corresponding clean system, a SF-N transition has not yet occurred, and suggest that, therefore, the observed disorder induced SF-IN must not be exclusively due to heating, i.e., the IN state is not N. Unfortunately even without any heating, a SF-N transition may have occurred since the critical temperature of the SF-N transition is generally suppressed by large disorder (recall from the previous chapter that enhancement is possible at low disorder values). Additionally at such large values of Δ, the single band model fails and the corresponding phase of the multi-band models are unknown; they may not correspond to a BG type of state at all.

Furthermore this particular value for the transition at $\Delta = 3\ E_R$ (corresponding to $\Delta/U = 9.3$ for $s = 12$) seems to agree well with the phase boundary of the box type of disorder at unit filling. Unfortunately, this is not a good comparison as from the earlier chapter it is clear that the phase boundaries do not agree for the speckle and box disorders. The phase boundary for the unit filling DBHM with speckle disorder is at much larger values (following the percolation type of calculations in the previous section it should be at $\Delta/U \sim 16$ although the precise value cannot be checked via single band calculations). What presumably happens is explained by a key aspect that hasn't been taken into account in studies thus far, and one which will be seen throughout this chapter. In a trap with fixed number of particles, as Δ is increased the gas expands and the central density decreases (shown explicitly and discussed in detail later). This means that the transition actually occurs for a central density ~ 0.58 (although this is a rather crude estimate).

The reduction of the central density with disorder might also explain the reason these experiments cannot see a RSF. But first consider what is actually observed in experiments. According to the first inset of Fig. (8.2) at $s = 14$, increasing values of disorder only leads to reduction in COM velocities, indicating that more of the gas is changing into an IN. The RSF type of behavior is expected to lead to an increase in the COM velocity and then to a decrease as the RSF gets destroyed with additional disorder. All theoretical studies to date explain this apparent disagreement by invoking finite temperature effects [58, 121]. For these experiments, the largest (approximate) entropy per particle $S/N \sim 2 \pm 0.2\ k_B$ which is not very useful since it is rather large. The expectation however, is that the actual S/N is much smaller $\sim 0.5\ k_B$, although there is no rigorous way to ascertain this. All entropies are estimated before the lattice and disorder is turned on as described in Chapter 6 so that an isentropic loading is assumed to hold. Prior to the load, the condensate fraction of the harmonically tapped gas is so large ($> 95\%$) that no thermal component is generally discernible, and the upper bound is an extremely loose estimate.

8.3 QMC Results

The trapped system is an interesting problem because it is a much richer system that the corresponding trap-free system. It is also accessible to experiments and is therefore a good motivation to undertake full scale *ab initio* type of calculations. Trapped systems change the situation considerably owing to the possibility of multiple domains arising in them corresponding to the different phases of the DBHM. The trap effectively samples a continuous line of chemical potential in the fixed chemical potential phase diagram. As such, it is often referred to as a local chemical potential shift. For clean systems the situation is simple because the domains appear as concentric shells respecting the symmetries of the trap. However, with the addition of disorder things can get complicated. Even at low values of disorder and weak trap curvatures, the symmetries of the trap are not enough to define the shape of the domains that develop; it becomes difficult to identify whether local distortions belong to one domain or another. In the limit that the trap curvature $\Omega \equiv \frac{1}{2}m\omega^2$ is extremely weak, the distortions at the interface of the domains is restricted to a narrow region, however, for experimental systems Ω for these systems is $\sim 60Hz$ or more, which is not sufficiently weak to avoid such problems (as will be seen).

In these systems there are two limits that observables can be easily defined, *viz.*, the global system observables and local on-site observables. The global observables follow the definitions outlined in the previous chapter and refer to the entire system. However, the global observable coarse grains over the interesting structures that develop in the trapped system and so sometimes local probes are more appropriate. The other extreme of on-site observables follow the global measures. These are:

- On-site density: $\hat{n}_i$
- On-site compressibility,

  $$\kappa(i) = \beta[\langle n_i^2 \rangle - \langle n_i \rangle^2], \tag{8.2}$$

  where β, is the inverse temperature E_R/k_BT.

- On-site superfluid density,

  $$\rho_s(i) = \frac{2\langle A^2(i) \rangle}{\beta t i_\perp^2}, \tag{8.3}$$

  where $A(i) = \frac{1}{2}\sum_{\alpha=1}^{N}\sum_k i_\alpha(k) \times i_\alpha(k+1)$ is the area subtended by a path in imaginary time and the sums are taken over all the N particles and all time slices indexed by α and k, respectively. Due to the presence of the lattice, the mass of the particles needs to be updated to the effective mass. This introduces the hopping term t into the definition [41]. In the presence of disorder in the hopping term, it becomes unclear what t should be used, but introduces minor changes due to scaling only (of the order of $< 1\%$). For the purposes of this work, the standard is to use the t corresponding to the average tunneling disorder. Alternate values, such as the t corresponding to the equivalent clean system will introduce minor difference in the values.

- On-site condensate density

  $$n_0(i) = n_0|\langle i|\psi_i\rangle|^2, \tag{8.4}$$

  where the largest single-particle eigenstate $|\psi_0\rangle$, is obtained from the single-particle density matrix $\rho_1|\psi_0\rangle = n_0|\psi_0\rangle$. The details of this procedure is given in Part II Chapter 4. It is also possible to obtain the next few eigenstates.

At intermediate local length scales, the observables will need to be modified for some region $\mathcal{R}$. The local compressibility and superfluidity can not just be obtained by summing (8.2) and (8.3). This is because a co-variance term will need to be included. For instance, consider the local compressibility defined for some region $\mathcal{R}$,

$$\kappa_l = \frac{\beta}{N}[\langle N^2 \rangle - \langle N \rangle^2] \tag{8.5}$$

where the local density is $N = \sum_{i \in R} \hat{n}_i$. This can be written as:

$$\kappa_l = \frac{\beta}{N} \sum_{i \in \mathcal{R}} \left[\langle N n_i \rangle - \langle N \rangle \langle n_i \rangle \right] \tag{8.6}$$

$$= \sum_{i \in \mathcal{R}} \left\{ \frac{\kappa(i)}{N} + \frac{\beta}{N} \left[\sum_{j \neq i, j \in \mathcal{R}} \left(\langle n_i n_j \rangle - \langle n_i \rangle \langle n_j \rangle \right) \right] \right\} \tag{8.7}$$

The covariance term will have a minor contribution but is responsible for cancellations and lowering of the compressibility in the MI. So ignoring it generally introduces a finite offset. In this chapter, for the case of compressibility per particle, the local measures are always compared to the values corresponding to the clean system since at finite temperature the MI compressibility is not strictly zero. As such, for identification of domains via these observables it is not so important as to whether the covariance term is included or not. Both approaches have been explored in this work and no qualitative differences have been found due to the finite offset. The upshot of not using the covariance term is that the local measure is free from noise issues. The covariance term generally limits the size of the region over which measurements can be taken – small regions generally have a lot of noise.

Similarly, the local superfluid density is given by:

$$\rho_s^l = \sum_{i \in \mathcal{R}} \frac{2\langle A A(i) \rangle}{\beta t}, \tag{8.8}$$

where $A = \sum_{i \in \mathcal{R}} A(i)$. In the case of the local superfluid order parameter, the argument for the not including the covariance term follows, but generally the domain sizes are large enough that noise in the covariance term is washed out. As such all local observables can be measured to conclusively check that the local superfluid density is indeed $\sim O(0)$. Fortunately, also, the condensate density does not suffer from these noise issues because the diagonalization procedure pushes the noise to the lower modes as discussed in part II Chapter 3.

Unfortunately, at present there are only a few global observables available to experiments that can probe the properties of the system. In terms of these observables it is straightforward to compare with QMC which is done in the next section. It will motivate the need for more local probes needed to see exotic behavior and to gain insight into these systems, which is done afterwards. It is worth mentioning at the very outset that there are still a host of unanswered questions with regards to the closed quantum systems prepared in

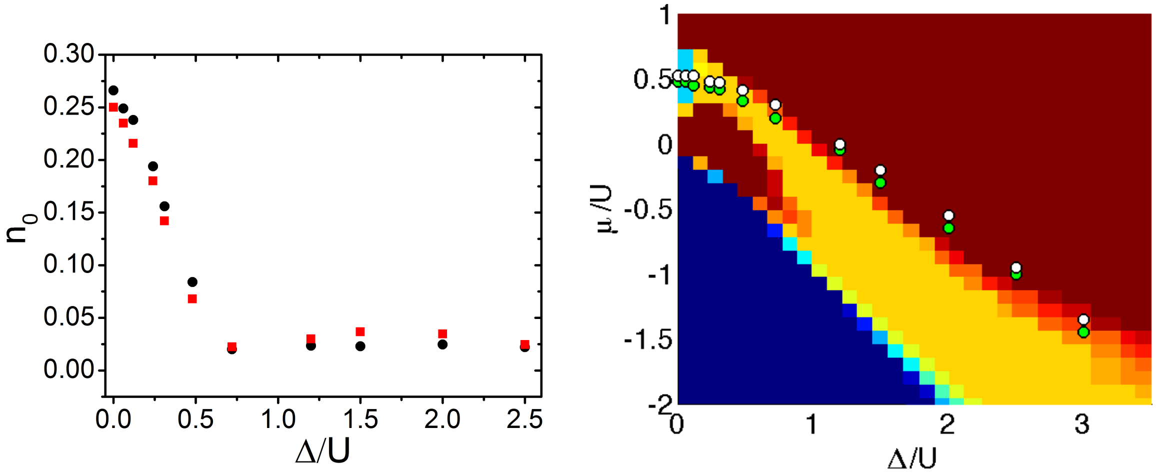

(a) (b)

Figure 8.3: (a) The condensate fraction of the trapped system calculated using the LDA corresponding to experimental parameters $s = 13.6\ E_R$ and trap frequency $\omega = 65.8$ Hz. Number of particles $N \sim 12000$ (black circles) and 14000 (red squares). (b) Shows the phase diagram of $s = 13.6\ E_R$. The dots correspond to the mu/U path needed to create a trapped system of frequency $\omega = 65.8$ Hz with $N = 14000$ particles (white dots) and 12000 particles (green dots) corresponding to possible experimental parameters. The blurry boundary arises due to disorder averaging. (See text for discussion.)

experiments. The finite lifetime of these gases and lack of information on equilibration as well as temperature make direct comparisons extremely difficult. The question of disordered closed quantum systems is also rife with open questions such as Many-Body Localization [23, 24]. These aspects will be apparent in the next chapter where a systematic collaborative effort between theory and experiment was undertaken to gain insights into novel behavior such as dynamical properties.

8.3.1 Comparison with Experiments: A Preview

The main measurable observable in optical lattice experiments that can be compared with QMC is the peak fraction. It is in principle possible to follow the procedure discussed in Chapter 6 for the clean system to map the peak fraction to the condensate fraction in the disordered case. However, such a calculation is a lot more expensive in this case because the momentum distribution in the continuum is given by $\langle n(\vec{k})\rangle = \sum_{jl} w_j^*(\vec{k}) w_l(\vec{k}) e^{i(\vec{j}-\vec{l})\cdot\vec{k}} \rho_1(j,l)$ that requires a convolution with Wannier functions from every site, taken pairwise.[1] A simpler alternative is to use the observation that the peak fraction should got to zero when the condensate fraction goes to zero [12]. As such the condensate fraction may give an indication of the location of the phase transition for a complete SF to insulator (IN) transition.

---

[1] At the present moment this route has not been pursued, but can be implemented if needed.

Experiments also have access to the COM velocity discussed above. In the top inset of Fig. (8.2a) the v_L data suggests that the SF-IN type of transition occurs between $\Delta = 0.5$ to 1.00 E_R ($\Delta/U = 1.35$ to 2.70). However, the peak fraction shown in Fig. (8.2b) suggests that at $s = 14$ E_R, there is a condensate of $\sim 5\%$ present even at $\Delta = 0.75$ E_R. So the transition probably occurs for $\Delta > 0.75$ E_R ($\Delta/U > 2.1$). The large statistical error bars in the experiment make quantitative comparisons difficult. Additionally there is of the order of 6% error in the lattice depth (s) and typically $\sim 40\%$ error in disorder strength (Δ). Also the particle number in experiments ranges between $N \sim 12 \pm 4 \times 10^3$, which will play a role in determining the phase boundary.

In order to get an insight into this system, QMC calculations for $s = 13.6$ E_R were performed to obtain the phase diagram of the trap free system. Additionally an LDA approach was used to ascertain what the path the gas must take in order to create a trapped system of $N = 12000$ to 14000 particles with a trapping frequency of $\omega = 65.8$ Hz corresponding to experimental parameters. This diagram corresponds to simulations at ultra low temperatures of $k_B T/t = 0.25$ corresponding to the $T \to 0$ limit. The LDA based condensate fraction calculation and the phase diagram is shown in Fig. (8.2). The phase diagram has been disorder averaged over 10 uncorrelated disorder samples. As a result there is disorder averaging related effect at the boundary of the different phases. These aspects have been discussed in section 8.5.1. It will be shown later in section 8.4.4 that the LDA picture is remarkably good at obtaining qualitative agreement with in-trap calculations provided the trapped system is not sampling a large part of the critical regime of the phase diagram. Quantitative measurements agree well provided disorder strength is low – LDA tends to overestimate the condensate fraction as it can't account for the inhomogeneities in the condensate induced by the disorder.

Qualitatively speaking, the clean system for both experiments and QMC are in agreement that there is a finite condensate owing to the SF shell around the MI domain in the trap. However, there is a quantitative disagreement between the QMC condensate fraction and the experimental peak fraction measured: 0.25(1) vs ~ 0.11. This disagreement possibly stems from the ideas discussed in Chapter 6 following [90, 12], but there may be additional issues due to disorder (see next chapter). Note that for the particle numbers considered the trajectory in the phase diagram is such that the condensate drops to ultra low values ~ 0.02 at $\Delta/U \sim 0.72$. At this value the low density SF shell at the edge of the trapped gas disappears. However, a small SF domain arises in the center of the trap and persists over a large range of Δ/U, ultimately disappearing for $\Delta/U > 3$. Unfortunately, for these particle numbers the path is very close to the SF-BG boundary throughout the phase diagram, so that for the drift in particle number reported in the experiment, the IN transition can happen over a large range of values. This might in fact explain the large error bars in the experiment. Evidently there seems to be agreement between experiment and theory that the IN transition occurs for $\Delta/U >\sim 2.7$, but conclusive statements can be made only with more measurements.

The QMC calculations presented here will be discussed in due course via incremental inquiries that reveal the equilibrium properties of these trapped systems. However, at the very outset it is worth mentioning that for a different set of parameters an explicit collaborative effort between experiment and theory – work done in the course of this dissertation, revealed excellent agreement. This exciting work, will be discussed in the next chapter since it requires knowledge of the properties of trapped systems. This chapter will lay the foundation to understanding the range of phenomena observed in experiments. Aside from this, the trapped system in general leads to interesting questions about domain formations in disordered systems and the effects of the trap modes.

8.4 Properties of Trapped Systems

To understand the equilibrium behavior of the range of systems accessible to experiments, an useful approach is to try to ascertain the properties of the gas at different length scales. Towards this end, the on-site observables lend some insight, and have been presented in Fig. (8.4) and Fig. (8.5) for a $s = 13.6\ E_R$ trapped system with $N \sim 12000$ particles and a confining trap $\omega \sim 50$ Hz, that closely maps the experimental system discussed above (the relaxed trap frequency will reveal useful information, to be discussed shortly). This strongly correlated system is at a $U/t = 40$, which is larger than the SF-MI critical boundary located at $(U/t)_c \equiv 29.43(2)$ [127]. Thus it approaches the phase boundary from the MI side of the clean phase diagram. As a point of interest a strongly correlated system approaching the phase boundary form the SF side is also considered at $s = 12\ E_R$ $(U/t = 25)$ with $N \sim 27000$ and $\omega \sim 70.5\ Hz$ (closely mapping an experimental system discussed in the next chapter). The onsite observables for this system have been shown in Fig. (8.6) and (8.7).

At a qualitative level, it seems that the on-site observables clearly demarcate obvious domains at low Δ/U. For instance, the on-site density and on-site compressibility appear to integer-like and close to zero for the MI state in the clean system for $s = 13.6$. However, as disorder is introduced, the on-site compressibility and on-site density cannot be used to distinguish between the domains any more, as both SF and BG regions can have density modulations and finite compressibilities. Indeed, at higher disorder strengths, there is considerable scrambling of the domain walls that do not conform to the spherical symmetry of the trap. Additionally the identification of domains on the basis of the behavior of on-site observables is a crude approximation only valid if the correlation length is smaller than a single site – at the atomic limit. Domains have finite correlation lengths, and their properties must be addressed as a whole. It is only in the interior of a domain that conforms to the properties of a phase.

The crux of the problem is, therefore, to be able to identify domains while staying as rigorous as possible. It turns out, that a natural way to think about the regions in these systems is by considering the single-particle eigenstates of ρ_1 that correspond to natural modes for these trapped interacting systems. Note that ρ_1 is *not* an on-site observable, it gives access to on-site information via the eigenstates, but it was constructed from the single-particle density matrix that contains correlation information across *all* sites.

In the presence of a condensate the macroscopically occupied ($\sim O(N)$) eigenmode of the single-particle density matrix (ρ_1) naturally separates the systems into SF and IN domains. For instance in the clean case, Fig. (8.4c) shows how the condensate appears as a shell with the MI at the center. In this simple system the local compressibility ($\kappa(i)$) also confirms the appropriate separations shown in Fig. (8.4b). The occupation number and the spatial extent of the eigenstates of ρ_1 reveal the behavior of the system due to addition of disorder. The type of behavior depends on which part of the phase diagram is being considered, and so the discussion naturally separates for the two cases $U/t > (U/t)_c$ and $U/t < (U/t)_c$.

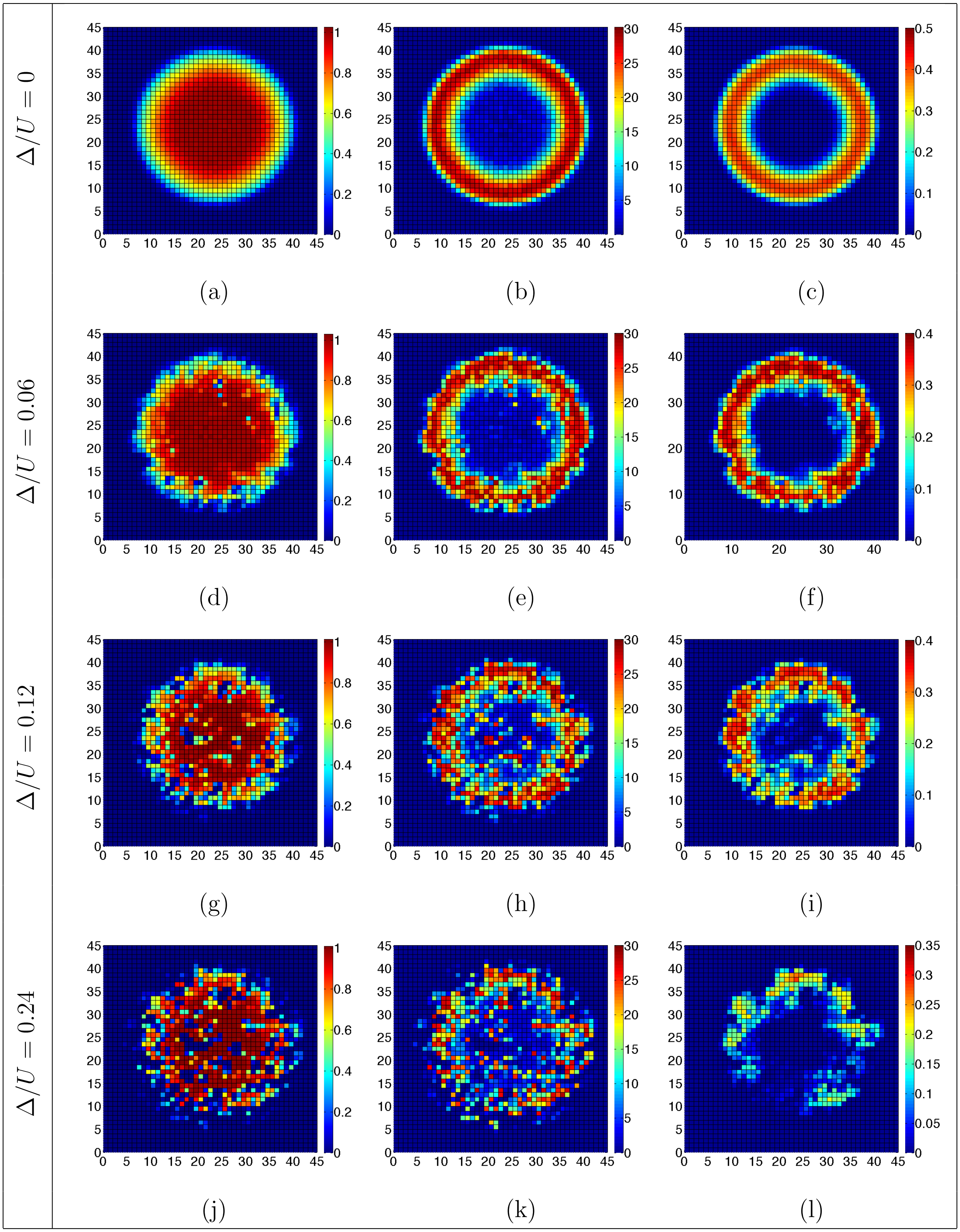

(a) (b) (c)

(d) (e) (f)

(g) (h) (i)

(j) (k) (l)

Figure 8.4: Slices of the density (first column), onsite compressibility (second column) and the largest single-particle eigenstate (third column) for a $s = 13.6\ E_R$ system. (See text for discussion.)

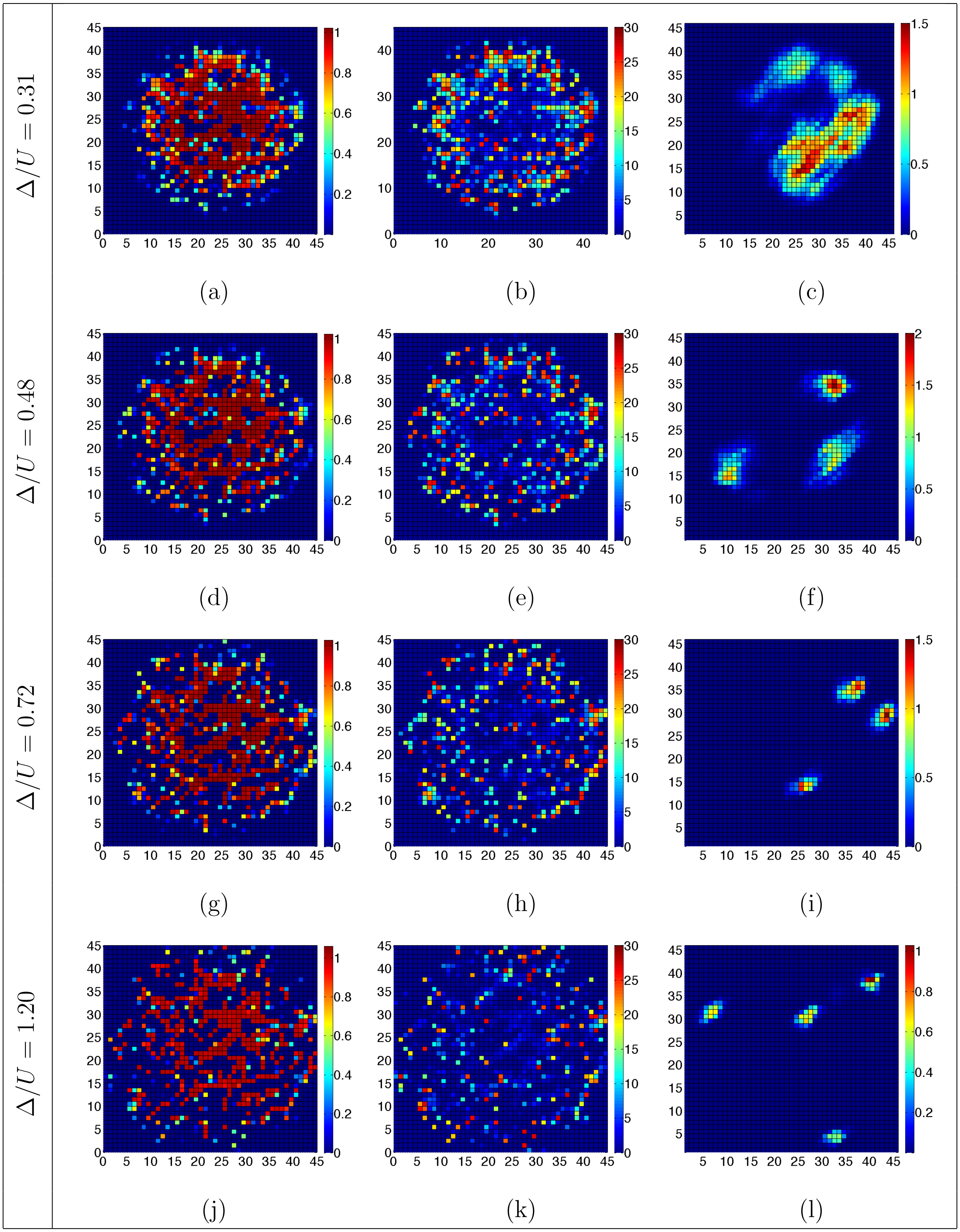

Figure 8.5: Slices of the density (first column) and onsite compressibility (second column). The column integrated profiles of the maximum number of accessible largest single-particle eigenstate is shown in the third column. (See text for discussion.)

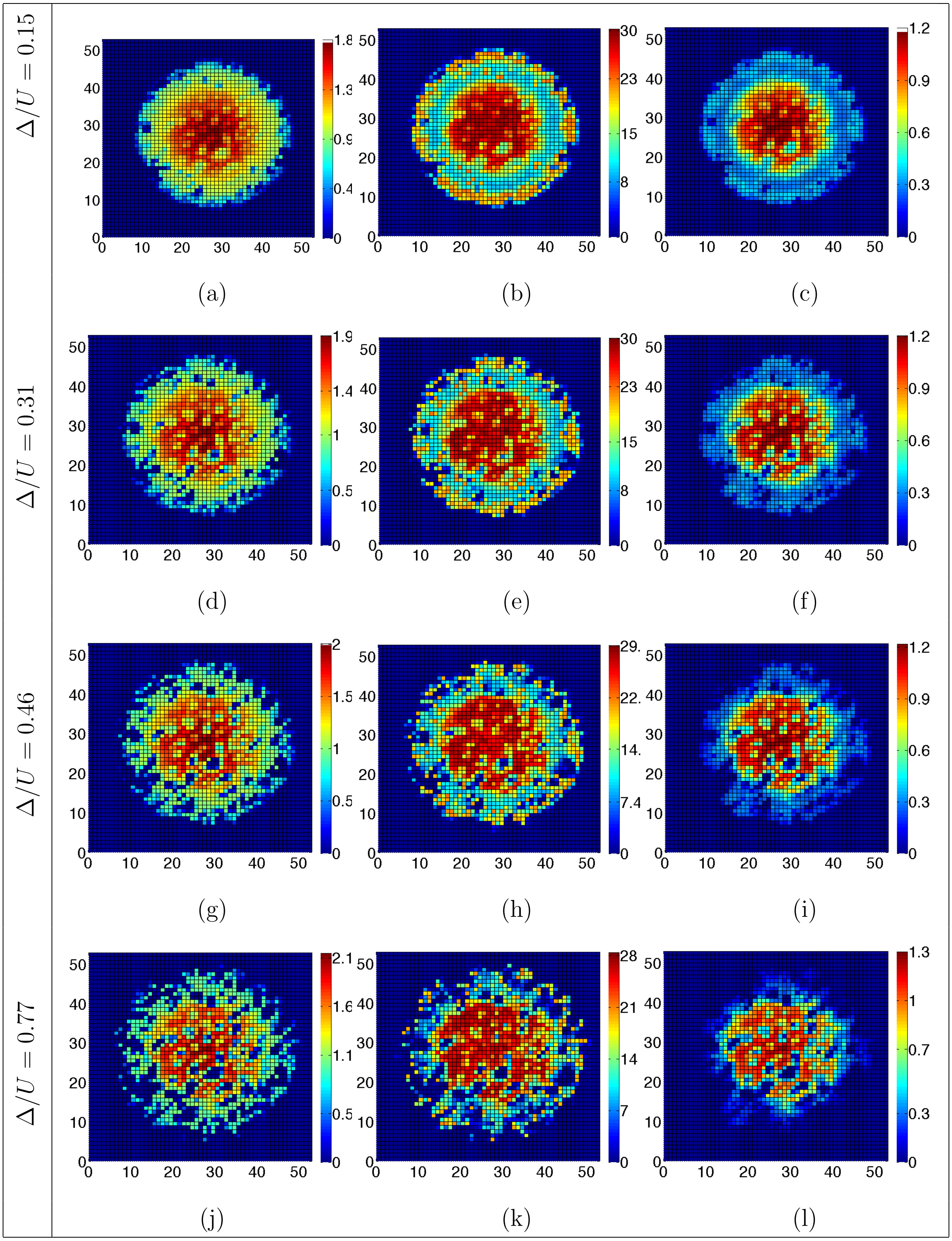

(a) (b) (c)

(d) (e) (f)

(g) (h) (i)

(j) (k) (l)

Figure 8.6: Slices of the density (first column), onsite compressibility (second column) and the largest single-particle eigenstate (third column) for a $s = 12\ E_R$ system. (See text for discussion.)

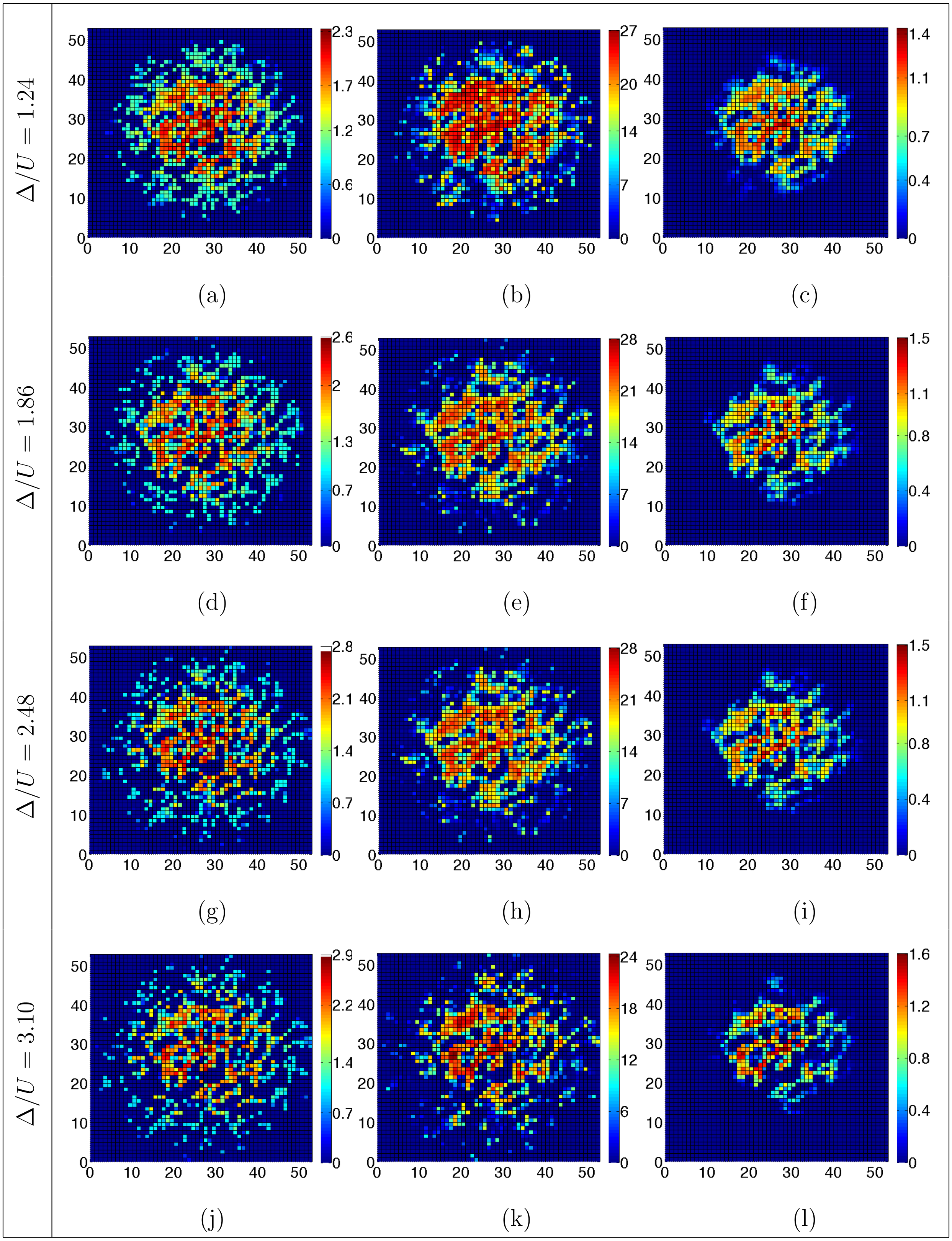

(a) (b) (c)

(d) (e) (f)

(g) (h) (i)

(j) (k) (l)

Figure 8.7: Slices of the density (first column), onsite compressibility (second column) and the largest single-particle eigenstate (third column) for a $s = 12\ E_R$ system. (See text for discussion.)

Consider first the case $U/t > (U/t)_c$, where the MI can arise. For $s = 13.6$ system simulated here, the system divides into two distinct types of behavior: the largest eigenstate of ρ_1 will either be an extended or a localized state. When the largest eigenstate is extended, it delineates the presence of a SF and also defines the region where it is located. The local superfluid density in this region will found to be finite as the condensate and superfluid are synonymous in 3D arising from long range order [19].[2] The excluded region on the other hand will have zero superfluidity and either zero compressibility for the MI (at T = 0) or finite compressibility for the BG (quantitative aspects will be discussed shortly).

For the BG, additionally, the subsequent eigenmodes of ρ_1 will describe localized states with small occupation numbers corresponding to puddles of SF, just as in the case of trap free systems. However, detecting such modes is expensive computationally since the noise is in these modes can be large relative to the macroscopic condensate.[3] The puddles are easier to see whenever the condensate is either strongly depleted or absent. For instance, in the case of $\Delta/U = 0$ to 0.12 shown in Fig. (8.4), the smaller modes are very difficult to extract. However, as the condensate gets depleted, the other modes become more visible.

When the largest eigenstate is localized, the entire system has transformed to a BG. This is precisely what happens for this system when $\Delta/U > 0.31$ shown in Fig. (8.5). In this figure, the images (c),(f),(i) and (l) are not slices but rather column integrated images of the largest number of eigenstates that could be safely extracted. Thus for (f) the three largest quasi-condensates or puddles have been shown with occupation numbers 53.2(8), 41.2(5) and 40.6(5). For (i) there are also three puddles with occupation numbers 20.1(1), 17.6(1) and 12.8(1). For (l) there are four puddles with occupations 8.23(3), 7.15(4), 6.94(7) and 5.38(4). Fig. (8.5a-c) represents a marginal case where the first two eigenstates are of comparable sizes with 300 ± 18 and 175 ± 12 particles. Only the largest state has been shown in the figure. This is actually quite an usual situation, since generally the quasi-condensate do not tend to be this large. Presumable this due to critical phenomena.

The second case corresponds to $U/t < (U/t)_c$, where the MI is not possible. Note that for this regime the SF is remarkable stable and for the unit filling case survives so long as the single band DBHM holds. The general in-trap behavior is strongly affected by this

---

[2] Strictly speaking the definition of long range order applies to homogeneous systems only. For these trapped system a much more general definition due to Penrose and Onsager follows form the single partiale density matrix [44], which is what will be used here.

[3] In a general measurement scheme, the large condensate will be sampled many more times relative to the smaller puddles. More sophisticated measurement schemes are possible but were not pursued in this work.

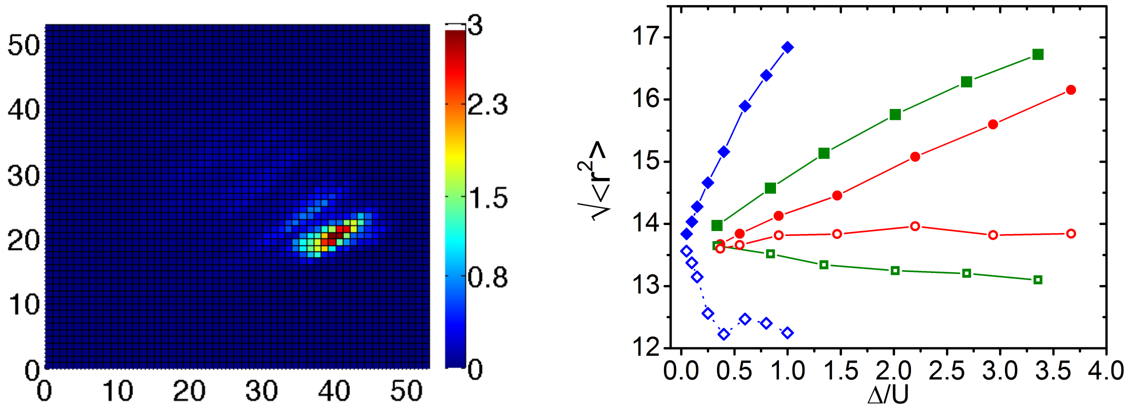

(a) (b)

Figure 8.8: (a) A puddle in the BG domain at the edge of the gas for $\Delta/U = 3.10$. The image has been column integrated to see the localized state. There are $\sim 138(2)$ particles in it. (b) Root mean squared radius of the entire gas (solid symbols) and the condensate (empty symbols). The typical values are shown for a system of $N \sim 27000$ particles for $s = 10\ E_R$ (red circles), $s = 11\ E_R$ (green squares) and $s = 12\ E_R$ (blue diamonds). The trapping frequency ranges from 68 - 71 Hz. (See text for discussion.)

phenomenon. For almost the entire range of disorder accessible, if the density at the center of the trap remains close to unity or more, the SF survives at the trap center. However, the low density gas at the edges of trap undergo a change. Consider the condensate images shown in Fig. (8.6) and (8.7). For these trap parameters the system exhibits two types of distinct phenomena. For Δ/U up to a certain threshold value, the edge of the condensate is overlapped with the gas, and there is no measurable insulating domain present in the system. The quantitative aspects will be discussed shortly, but this is qualitatively evident from Fig. (8.6). However, for Δ/U larger than the threshold, the condensate edge rapidly shrinks leaving behind an insulating regime which at ultra low temperatures considered here corresponds to the BG state. Using large scale simulations, it has been confirmed that there are puddle like states present in the edge of the gas corresponding to the BG state; an example has been shown in Fig. (8.8b). The root mean squared (rms) radius of the gas and the condensate shown in Fig. (8.8b) for this system and other equivalent systems (with same particle number) for weaker interaction strengths reveal mass transport of the gas into the center – a surprising effect, since the interactions are repulsive. This is also evident from the central density where the largest occupied sites increases from ~ 1.8 to ~ 2.9. Notice also that the central condensate density also increases from ~ 1.2 to ~ 1.6.

8.4.1 Measurement of Global Properties

In the previous section, the properties of the two trapped systems corresponding to interaction strengths straddling the SF-MI critical point were discussed using on-site observables of density and compressibility. Additionally, it was shown that the general behavior of the system is discernible in terms of the behavior of the macroscopic condensate or superfluid state. In this section the global properties of several trapped system across the phase diagram will be discussed. These types of observables could in principle be accessed by experiments, although they are quite challenging since there are a host of calibration aspects and so forth. For instance, the condensate fraction shown in Fig. (8.9) could in principle be obtained for experiments by calibrating the peak fraction as was done in Chapter 6. Additionally, the compressibility of the gas could be observed if the fluctuations of the density can be measured. This is perhaps possible by using high precision density images.

Aside from the fact that these observables could be most easily accessed via experimental procedures, they are of fundamental interest since they reveal important information about the physics occurring throughout the system. Fig. (8.9) shows the condensate fraction and compressibility per particle of different systems, ranging from moderate interaction strengths of $U/t = 14$ ($s = 10\ E_R$) to strongly correlated systems at $U/t = 25$ ($s = 12\ E_R$) and $U/t = 40$ ($s = 13.6\ E_R$). A strongly interacting system at $U/t = 100$ ($s = 17.1$) is also considered.

For $U/t < (U/t)_c$, the superfluid behavior persists to large values of disorder and appears to remain robust throughout the regime where the single band model holds, much like the unit filling phase diagram shown in the previous chapter. In general, the weakly interacting gas is more compressible owing to the larger fraction of superfluid present it. Unfortunately not much else can be discerned from these global observables as they coarse grain over the rich underlying structure. Even at or beyond threshold values where the BG develops in these gases, the overall system does not exhibit any noticeable features.

For $U/t > (U/t)_c$, the superfluid is rapidly destroyed by the disorder because the central density in the systems considered here is low (starts out at ~ 1.0 at $\Delta/U = 0$), and from prior discussions this is to be expected. Notice that for $s = 13.6$, the rapid depletion of the condensate is coincidental with the break up of the underlying structure and the emergence of a full BG gas. Concurrently, as the SF is depleted the compressibility also decays rapidly. The $s = 17.1$ system has a SF shell around the MI center for the clean system, as is evident from the finite condensate fraction. Evidently this system is also rapidly depleted of the

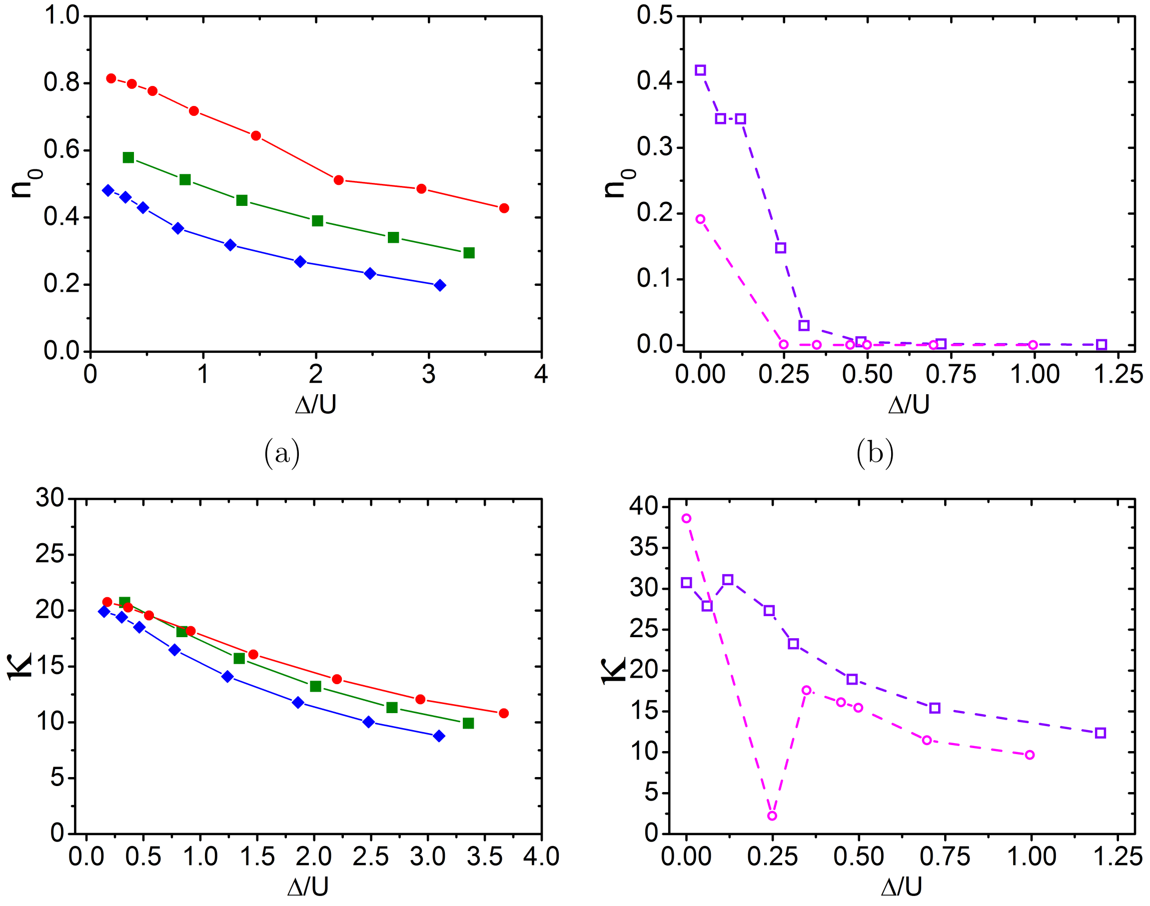

(a) (b)

(c) (d)

Figure 8.9: Images on the left correspond to $U/t < (U/t)_c$ systems with $N \sim 27000$ particles at $\beta t = 1.0$, where β is the inverse temperature and t is the hopping term in the DBHM. Images on the right correspond to $(U/t < (U/t)_c)$ systems with $N \sim 12000$ at the same effective temperature as the other systems. The data is for $s = 10\ E_R$ (red circle), $s = 11\ E_R$ (green squares), $s = 12\ E_R$ (blue diamonds), $s = 13.6\ E_R$ (purple empty squares) and $s = 17.1\ E_R$ (pink empty circles). (a)-(b) are the condensate fraction as a function of effective disorder strength Δ/U. (c)-(d) are the global compressibility per particle.

condensate with increasing Δ/U. A remarkable feature is evident in the compressibility of the gas, which rapidly drops before increasing again. This happens because at low disorder strength values the BG is state is highly incompressible (evident from the unit filling and low density phase diagrams shown earlier but also see later for the grand-canonical or constant chemical potential phase diagram). Since there is no SF present unlike the clean case, the global observable is completely dominated by the incompressible BG state. Finally at larger Δ/U the gas crosses over to a BG state with larger compressibility.

While the global observables are useful to ascertain the overall behavior of the system,

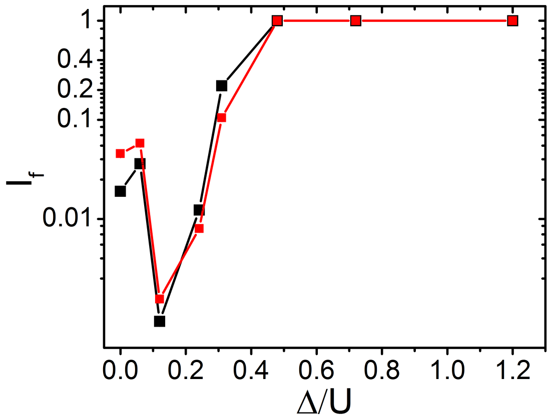

Figure 8.10: The insulator fraction as a function of Δ/U. The two curves correspond to the two different methods A (red) and B (black) used to set the threshold needed to identify regions devoid of any condensate. Number of particles $N \sim 12000(\pm 5\%)$, $s = 13.6\ E_R$ and trap frequency $\omega = 50$ Hz. (See text for discussion.)

it has been seen that it does not reveal much (generally speaking) about the rich layered structure of the system. Thus it seems that both extreme limits of probing the system, viz., the single-site and the global descriptions of the system are somewhat limited. In light of this, it becomes important to try and develop local probes that can handle intermediate length scales corresponding to the sizes of the domain. Such a description is mired by difficulties owing to finite size problems as well as the continuous nature of observables in trapped systems. The main limitations need to be discussed before any further discussions, but it will be seen that reasonable approximations can be made to understand – at-least at the qualitative level the physics involved at local length scales.

8.4.2 Considerations in Domain Identification in Trapped Systems

There is a practical matter with regards to these trapped system when it comes to demarcating domains. While it is straightforward to get a qualitative picture of the behavior of the gas in terms of "large" or "small" observable values, the boundary at which to draw separation lines between domains is difficult. This is because the boundary is not sharp for these trapped systems.

Generally for finite systems, the numerical approach is to use a small threshold value to identify a border and study how observables depend on it. The expectation is that the observable should settle down for some value of the threshold. Unfortunately in these systems, observables do not lend well to this form of analysis as they change smoothly with the threshold value. There are no discernible sharp changes in the respective distributions (density, compressibility or condensate) of the gas which appear to be analytic.

In light of these difficulties some standard has to be adopted. For the purposes of this dissertation, two different standards were tested to discriminate between regions. This allows testing the sensitivity of results to these somewhat arbitrary standards. Both methods involves the determination of an onsite threshold value for exclusion from a region. In the first method (A), the threshold value is determined on the basis of the fact that the chosen observable attains 99.99% of its full value. For instance, in defining the absence of condensate, the threshold is chosen such that only those sites (used to define a region) that would not change the value of the condensate by more than 0.01% are excluded. In the second method (B), the threshold value is set to $1/N$, where N is the number of particles. Results for the Insulator fraction I_f shown in Fig. (8.10a) were calculated by measuring the fraction of particles in regions devoid of any macroscopic extended condensate state. Although the absolute value suffers from a small systematic error due to the difference in tolerances used to identify regions, the qualitative behavior remains the same. For ease of computations, the main procedure to demarcate regions will be method B.

8.4.3 Measurements of Local Observables for Domains

Identifying regions devoid of the macroscopic condensate as an insulating domain uses a fundamental property of phases that result from continuous phase transitions: phase coexistence in such systems is not possible [25]. So regions that have a superfluid cannot also have BG-like properties. An additional check is that the local superfluid density for the *entire* region devoid of the condensate is zero. Locally around a quasi-condensate puddle, the superfluid density is small but non-zero as expected. The different puddles locally look like superfluids, but are uncorrelated with each other leading to cancellations for the entire domain. Note that there is an extremely thin layer of ultra low density gas always present at the edge of the trap ($< 0.01\%$). These do not contribute to local observables measured over the different regions.

These observations makes it possible to demarcate domains in the trapped systems in the presence of disorder. Typical examples of such a procedure is shown in Fig. (8.11), where the densities have been presented for IN and SF domains. The left images correspond to Δ/U less than threshold disorder values at which qualitative changes occur to the domain structures. Notice how for the images on the right for the two strongly correlated systems, show

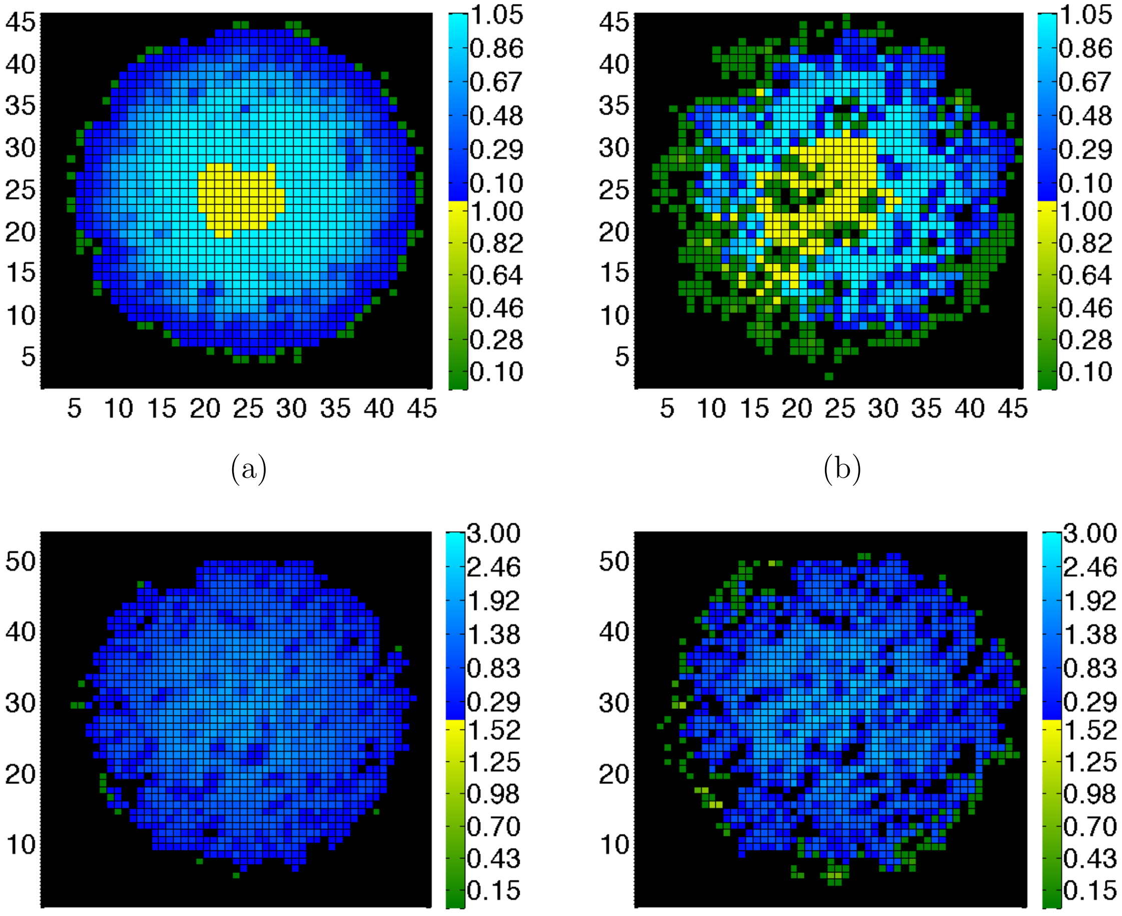

(a) (b)

(c) (d)

Figure 8.11: Examples of superfluid and insulating regions identified using the condensate distribution for $s = 13.6\ E_R$ (top) (a) $\Delta/U = 0.06$ (b) $\Delta/U = 0.31$, and $s = 12\ E_R$ (bottom) (a) $\Delta/U = 0.46$ (b) $\Delta/U = 1.24$

the spectacular behavior where the fundamental properties of regions in the trap changes. The effects are particularly devastating for the SF in the $s = 13.6\ E_R$ system, where the condensate is ripped apart from within as the BG expands.

The IN can be identified by calculating the local compressibility of the region. This method avoids the errors due to using on-site observables because the length scales at which the system is probed is much larger, but it is not so large that it coarse grains over interesting features. Further discrimination of the IN domain into sub-regions of BG and MI would be incorrect. This is because, from discussions in the previous chapter it is clear that even in a trap-free system, there will always be regions (of arbitrary sizes) in a BG that locally looks like a MI state. Actually the definition of a phase only makes sense in the thermodynamic limit and these issues stem from working with finite sized systems. This is further complicated by the Griffiths type of phenomena associated with these states and finite temperature effects. In the author's opinion, the verbiage should strictly be one of IN and SF domains, where additionally observations are possible about the IN compressibility. One way to proceed is to consider how the compressibility of the IN differs from the MI domain in the clean system at the same temperature. If the region has around the same compressibility as the MI (of a clean system) then it could be classified as a MI. If it is more then it could be called a BG. Note however that at finite temperatures the possibility of crossovers to normal state is always possible for either of the two IN states and a finite fraction of the domain will undoubtedly exhibit such properties. At sufficiently low temperatures such components will be minimal.

At the present moment, experiments do not have access to local observables measured over the length scales of domains directly (although indirect routes do exist, and will be discussed in the next chapter). Two examples of such observables have been calculated for this system. The first of these is the insulator fraction I_f that measures the fraction of atoms in the insulating domains be it a MI or a BG. This has been shown in Fig. (8.12a-b).

Consider the case for s = 10 - 12 E_R first. Unlike the global measurements, the insulator fraction (I_f) shows quantitatively, what was seen via the on-site images earlier. These systems exhibit a threshold type of behavior where the SF persists up to a finite disorder strength. Beyond this value, as discussed earlier, the condensate starts shrinking and an insulator regime starts to develop. At these ultra low temperatures, the insulator is clearly a BG state. This is further demonstrated from the the constant density compressibilities shown in Chapter 7 Fig. (7.6-7.7) as well as the phase diagrams presented later in Fig. (8.21-8.22). The low density BG is actually more compressible than the SF; this is why the local compressibility of the insulating state starts out larger than the corresponding global compressibility per particle. With increasing disorder however, the insulating compressibility decreases.

For the strongly interacting cases, the local observables also reveal remarkable information about the underlying structure of the gas. Consider for instance, the insulator fraction for $s = 13.6$ and 17.1. For the $s = 13.6$ system at low Δ/U there is significant amounts of condensate and depleted condensate present in the system. The clean system has a MI at the center that constitutes around 2% of the gas. As disorder is increased the SF shrinks and

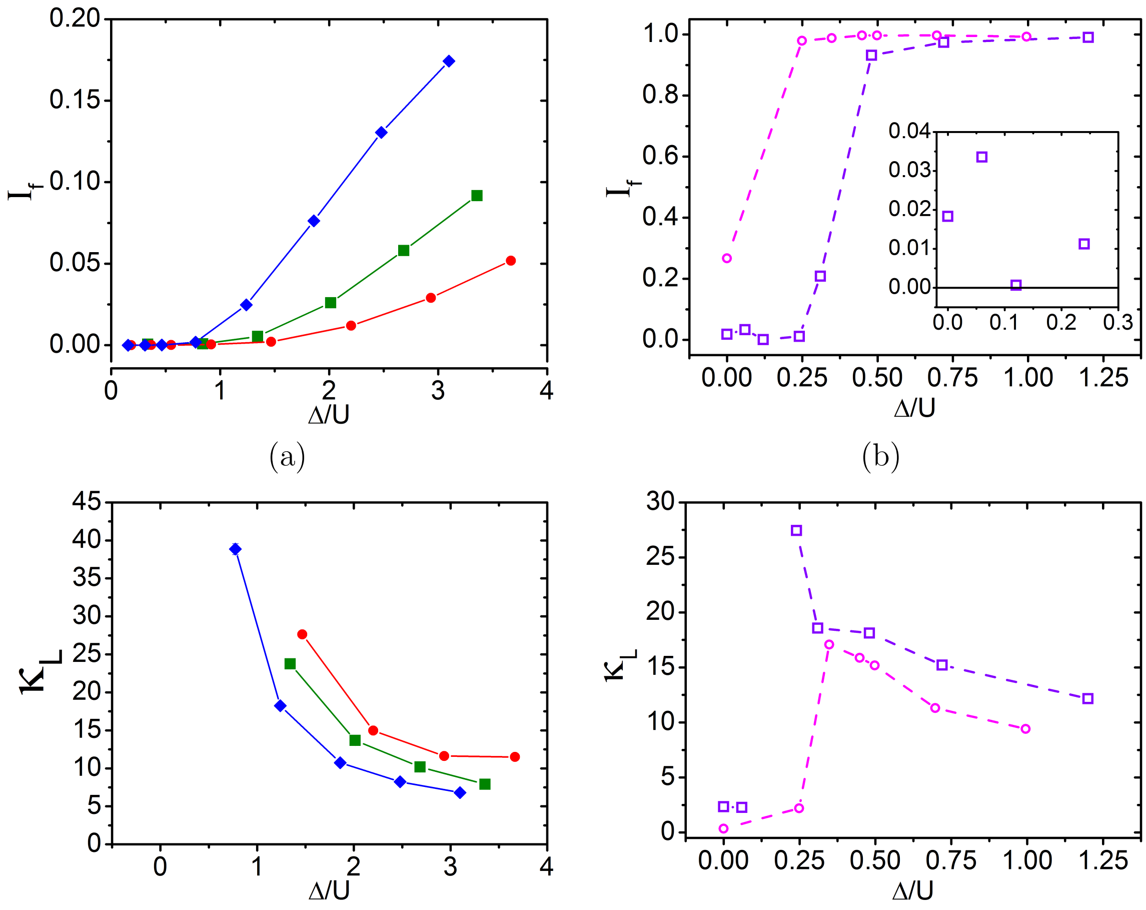

(a) (b)

(c) (d)

Figure 8.12: Images on the left correspond to $U/t < (U/t)_c$ systems with $N \sim 27000$ particles at $\beta t = 1.0$, where β is the inverse temperature and t is the hopping term in the DBHM. Images on the right correspond to ($U/t < (U/t)_c$) systems with $N \sim 12000$ at the same effective temperature as the other systems. The data is for $s = 10\ E_R$ (red circle), $s = 11\ E_R$ (green squares), $s = 12\ E_R$ (blue diamonds), $s = 13.6\ E_R$ (purple empty squares) and $s = 17.1\ E_R$ (pink empty circles). (a)-(b) are the Insulator fraction as a function of effective disorder strength Δ/U. (c)-(d) are the local compressibility per particle (k_L) for the insulator domain. The lines are a guide to the eye. They have not been connected for the point at $\Delta/U = 0.12$ for $s = 13.6\ E_R$, since there is no insulator present for this parameter.

the insulator increases. However, on addition of even more disorder, the expansion of the gas leads to decrease of the density that further leads to the stabilization of the SF. As a result the gas turns completely into a SF state at $\Delta/U = 0.12$. Evidently, this is the reason behind the fact that the global condensate fraction changes only a little when Δ/U is increased from 0.06 to 0.12. Finally with further increasing of disorder, the insulator state arises again and rapidly leads to the destruction of global coherence – corroborated by Fig. (8.4g-l) (more on this peculiar behavior will be discussed in the next section). The $s = 17.1$ system follows the global observables well, showing how the SF for the clean system is rapidly destroyed to give a IN state.

As a point of information, note that there appears to be a discrepancy in the numbers identifying the condensate and insulator regions: they don't add up to the total density. However, recall that condensate in strongly depleted and not all atoms participate in it. Such depleted modes, however are not part of the insulating domain either and are devoid of any superfluid outside of the condensate. The last fact follows from the discussion earlier, that regions outside of the condensate do not have any macroscopic superfluid.

So far no conclusive evidence has been provided to be able to distinguish between the different insulator states that arise in these domains. However, based on the identified regions, it is possible to measure the local compressibility (κ_l) as way to discriminate between the types of insulators. Fig. (8.12d) shows this behavior. Evidently for $s = 13.6$, the domains corresponding to finite size systems remains Mott-Insulating for low disorder values, changing to a BG for larger Δ/U. κ_l for $\Delta/U = 0$ and 0.06 are non-zero and small, but comparable (2.34(4) and 2.27(3), the finite values result from finite temperature effects at $\beta U \sim 40$. Also the covariance term has not been included). On the other hand (κ_l) for $s = 17.1$ shows that the central region of the clean system is definitely a MI state. Note in this case temperature plays a minimal role since $\beta U \sim 100$. As Δ/U is increased, the system rapidly enters a BG state with finite compressibility.

Recall that although there seems to be a disagreement for $s = 13.6$ case at $\Delta/U = 0.06$ with the phase diagram (defined at the thermodynamic limit), it is perfectly allowed whenever the disorder bound in the local region does not exceed the MI gap. Note that while it is clear that a such a behavior is possible at these length scales, it is not clear whether this is typical and representative of the physics of such length scales, i.e., it is not clear that this would happen for all disorder realizations. As discussed in Section 7.1 of Chapter 8, the physics should be qualitatively similar provided the region is not close to the critical regime.[4] Additionally another aspect of trapped systems is the finite size rounding of critical singularities [128] so the system may not show a break down of self averaging at all. The possibility of this happening increases with tighter traps. Unfortunately, at present doing a full disorder averaging on such large trapped systems considered here is too expensive

---

[4] To reiterate, near the critical regime there may be large sample-to-sample deviation of observables that results in the formation of SF or BG or MI. However, this is not really very surprising since the actual value of the superfluid fraction and compressibility is very small and so depending on the disorder instance it may or may not be exactly zero.

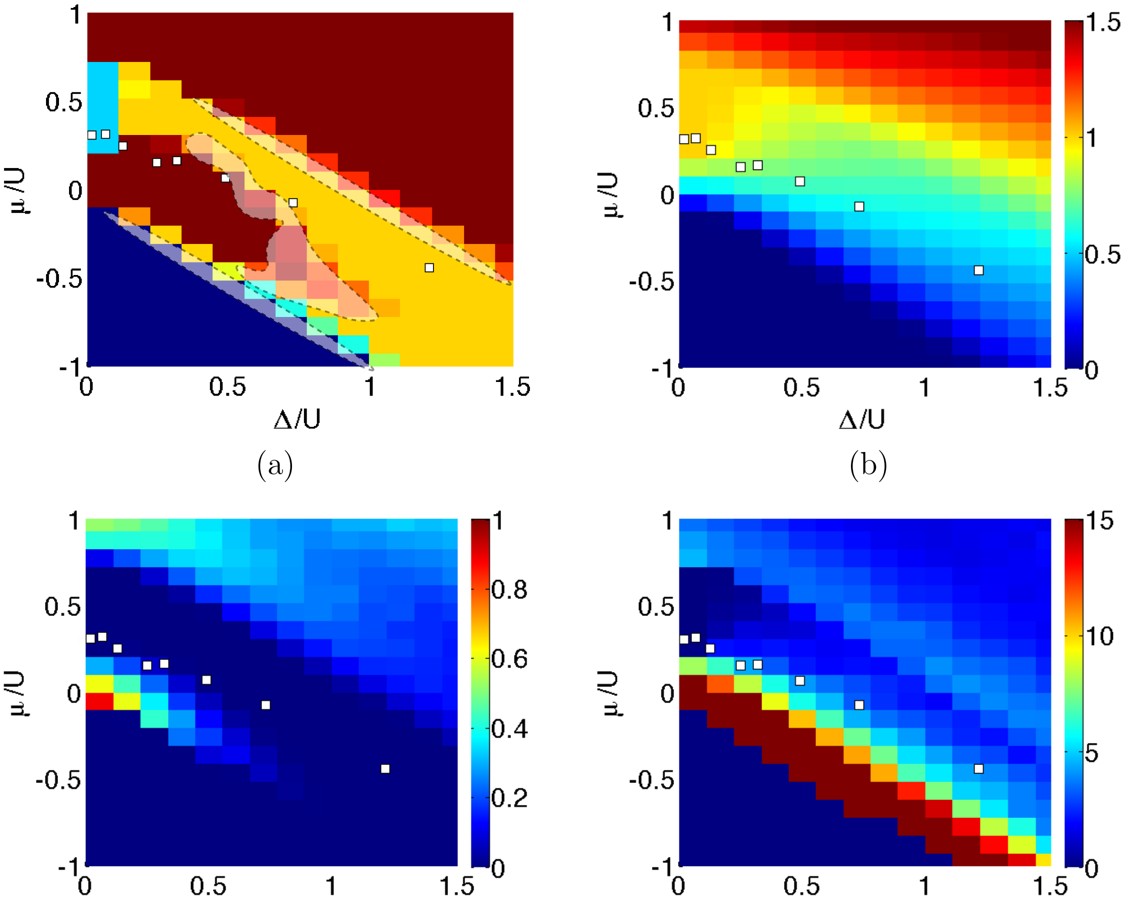

(a) (b)

(c) (d)

Figure 8.13: The phase diagram for $s = 13.6$ constructed using simulation cells of size 14^3 at the $T \to 0$ limit. (a) Shows the different states: SF (red), BG (yellow) and MI (light blue), vacuum (dark blue). The multi-colored regions correspond to shifts due to disorder averaging. The areas masked using the dashed shape corresponds to critical regions that need many more averages for convergence. In these regions SA will break down. The white dots correspond to the μ/U at the center of the trap for which $N \sim 12000$ particles for the different Δ/U =0.0, 0.06, 0.12, 0.24, 0.31, 0.48, 0.72 and 1.20. Corresponding (b) Density (c) Superfluid Fraction, and (d) Compressibility per particle. Notice that for constant number of particles, the central density drops as disorder strength is increased. (See text for discussion.)

(and perhaps not a question that needs to be answered urgently). In light of the fact that some behavior seen in traps may be atypical it might be useful to consider the relationship between the domains and the trap-free phase diagram. These aspects are considered next.

8.4.4 Relationship of Trapped System Domains with the Local Density Approximation

In order to ascertain the effects of disorder averaging and to relate the domains that develop in the trap picture to trap-free phases, QMC calculations were undertaken in the grand canonical ensemble for a $s = 13.6$ system with $L = 14^3$ sites. The phase diagram was obtained by averaging over 10 uncorrelated distributions to see how sensitive the phase boundaries are to disorder. The three main observables: density, compressibility and superfluid fraction were used to compile the phase diagram shown in Fig. (8.13a).[5]

The LDA picture seems to be a satisfactory qualitative description of the domains that develop provided the central chemical potential value is located well away from critical boundaries. The $\Delta/U = 0.0, 0.06$ cases correspond well to the qualitative picture obtained using LDA. The gas is expected to be MI at the center surrounded by a SF shell, which is what happens in the trap. Unfortunately the $\Delta/U = 0.06$ case cannot be resolved here due to the coarseness if the grid. In principal the question could be resolved using a finer grid together with actual disorder averaging types of runs. Intuitively, this question is depended crucially on the system size and the distance between the finite size phase boundary and this point. For the MI-BG phase transition, as discussed earlier, rare regions will be harder to see the closer the system is to the phase boundary, but it is alleviated with system size. For small systems, the IN domain may have properties identical to the MI, despite the fact that the true phase diagram reports a BG. Additionally, for trapped systems the trap curvature leads to changes in density around the interfaces between domains that develop. This can lead to a smoothing out of critical singularities [128], which would mean that the trapped systems would not experience any issues such as the break down of self averaging. There are strong reasons to believe this to be the case for trapping frequencies accessible to experiments ($\omega >\sim 60$ Hz, see next chapter). Unfortunately, there is no *a priori* way of discerning whether critical smoothing will happen without undertaking expensive runs – possibly a wasted effort for just one point (however, a procedure such as this is indeed undertaken in the next chapter to assess such effects in experiments).

The next three points corresponding to $\Delta/U = 0.12$, 0.24 and 0.31 also correspond well to the domains in the trap with the center corresponding to a BG and surrounded by a SF

---

[5] Note that in the coloring scheme for the phase diagram the pixels are shaded according to the value at the bottom left corner, thus sometimes the boundary regions will become harder to identify, owing to the size of the pixels. Precise calculations are possible, but better done on a case-by-case basis since computations are not inexpensive.

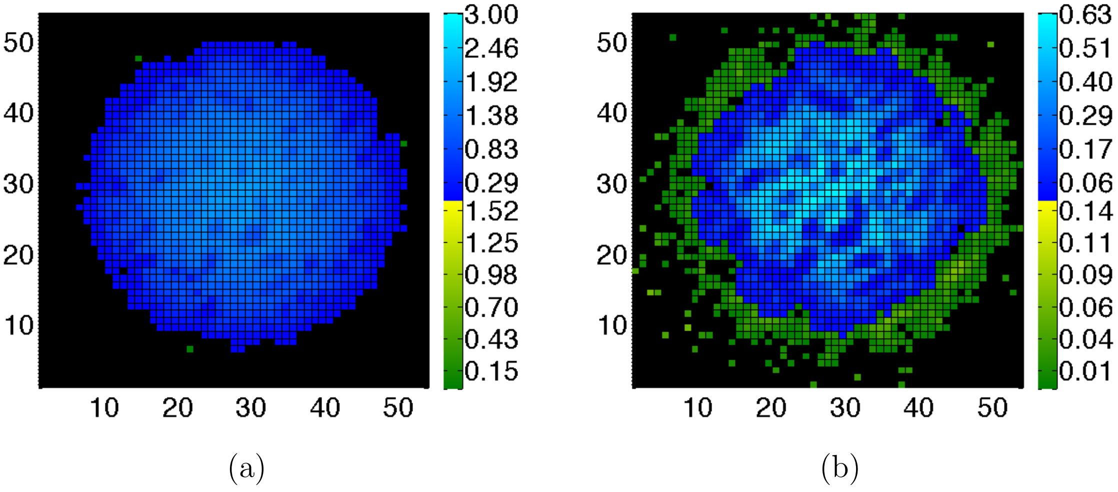

(a) (b)

Figure 8.14: Effects of trap curvature on the domain development. The system considered here corresponds to $s = 10\ E_R$ ($U/t = 14$) with (a) $N \sim 27000$ and $\omega = 67.5$ Hz (b) $N \sim 4800$ and $\omega = 30$ Hz.

domain. The exception is that the BG that is supposed to arise at the edge of the trap at low densities gets stabilized to a superfluid. This is a function of the trap curvature. Tests have shown that if the curvature is reduced the BG reappears. For instance consider Fig. (8.14), where a $s = 10\ E_R$ system at $\Delta/U = 0.18$ with $N \sim 4800$ (corresponding to a central $\mu/U = -0.25$) and trap frequency $\omega = 30$ Hz, is compared against another system at the same interaction and disorder strength but for a stronger trap of $\omega = 67.5$ Hz with $N \sim 27000$ particles. The system clearly has a BG present at the trap edge. Therefore for weaker confinement the system corresponds closely to the trap free phase diagram shown in Fig. (8.21). This is in important fact to be kept in mind when comparing the phase diagrams shown for $U/t < (U/t)_c$ in Fig. (8.21-8.22) and the threshold type of behavior shown in Fig. (8.12). It will be shown in the next chapter, with explicit comparisons with experiments that is a real effect.

$\Delta/U = 0.48$ shows a strong deviation from the LDA picture. Whereas the LDA suggests that a multilayered structure with concentric BG, SF and finally BG at the edge of the gas should develop, the exact picture is one in which the gas gets completely transformed to BG state. This is most likely because this point is located near a critical boundary and so critical fluctuations rapidly destroy the SF state. Finally the next two disorder points $\Delta/U = 0.72$ and 1.20 agree with the LDA and the gas is completely in the BG state. So apart from a suppression in the threshold value of Δ/U at which the BG transformation occurs, qualitatively speaking the LDA picture is able to address the domains that develop in this system.

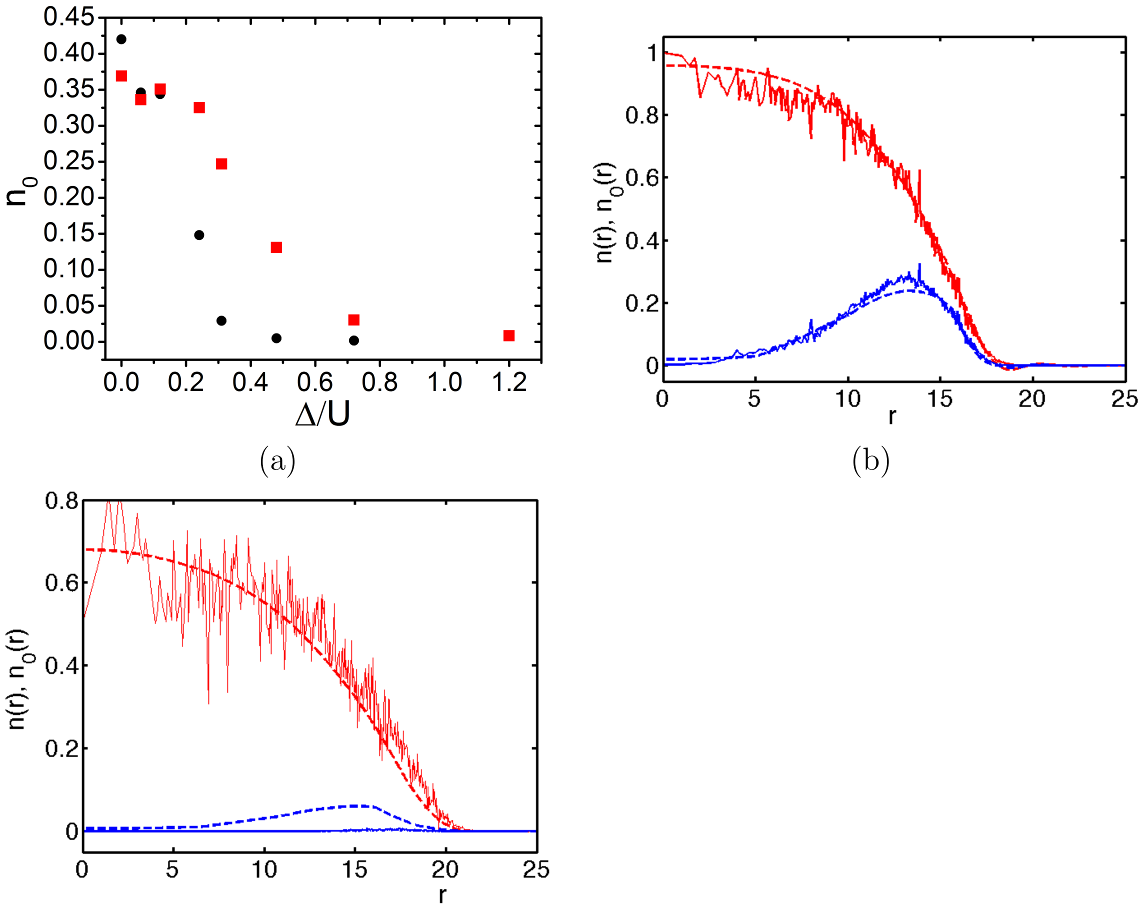

(a) (b)

(c)

Figure 8.15: (a) Comparisons of condensate fraction calculated using LDA (red squares) and phase diagrams from QMC and *ab initio* type of calculation involving the exact system (black dots). The system parameters are given by $s = 13.6\ E_R$ $(U/t = 40)$, trapping frequency $\omega = 50$ Hz and $N \sim 11500$. (b)-(c) Show typical density $n(r)$ (red) and condensate density $n_0(r)$ (blue) profiles generated using the LDA (dashed line) and *ab initio* calculations (solid line) for two disorder strengths: (b) $\Delta/U = 0.12$ (b) $\Delta/U = 0.48$

Quantitatively, however, comparisons with LDA will show large differences as Δ/U is increased. Consider the condensate fraction calculated using QMC calculations of the trap-free phase diagram together with the LDA for the trap and *ab initio* QMC calculations that take the full trap into consideration shown in Fig. (8.15a). As expected for low disorder strengths, the differences are not extreme but as Δ/U is increased there are large quantitative differences even though the qualitative picture remains the same. The LDA description cannot account for the expansion of the gas and the local texture of the disorder plays a crucial role in determining the way in which domains develop in the system.

Typical images of the density and condensate profiles are shown in Fig. (8.15b-c). The LDA images were generated by using the chemical potential dependence of the density and condensate fraction. As discussed before, the trap potential is interpreted as a local chemical potential shift ($\mu(r) = \Omega r^2$). The profiles are constructed together by stitching together the density and condensate values at the different $\mu(r)$ from the phase diagram generated using QMC. Global observables are obtained by a weighted sum of different radii. The weights correspond to the frequency of sites in the cubic lattice at a particular distance from the center of the trap. The *ab inito* profiles are constructed using the images shown in Fig. (8.4) and (8.5). The densities were averaged using the trap's spherical symmetry. The "noise" on the profiles is real arising due to this averaging procedure; recall that the system does not share the spherical symmetry of the trap. At low disorder strengths, the profiles seem to be in good agreement, and evidently the global condensate fraction measurements are also in good agreement. However, as disorder increases, the *ab initio* density profiles show that although they have the same shape as the LDA profile, there are large fluctuations. Concurrently, the condensate profiles do not agree, whereas the LDA picture suggests that there is a condensate, the *ab initio* results show that this is not possible. The implications of this study is that while the qualitative picture obtained from LDA is generally useful, it can have large quantitative discrepancies with the actual measures. So care must be taken while trying to use LDA type of descriptions for disordered systems.

8.4.5 Fate of the Re-entrant Superfluid

The discussion with regards to the LDA and trapped system suggests that trapped systems might have different properties and transition boundaries. This presents the question whether the re-entrant superfluid (RSF) state can arise in trapped systems. To recap - the RSF is a superfluid that arises in the unit filling regime for U/t that in the clean system corresponds to a MI state. This is an interesting state, because this is a disorder induced ordered state. As discussed in section 8.2, experiments done to date have not seen this state and it has been speculated that these are due to finite temperature of experiments [56, 116, 58]. From the full scale computations done with $s = 13.6$ it is very suggestive that the reason experiments are not able to see the RSF is because of the expansion of the gas due to disorder. Essentially the system follow the path shown in Fig. (8.3b), where increasing disorder only follows a path where the system changes from a SF to an IN. However, there still is a marked difference in the requisite disorder strength need for this transition. Unfortunately, much more controlled investigations are needed to understand the behavior of experiment, and there might be dynamical effects that have to be accounted for. Here,

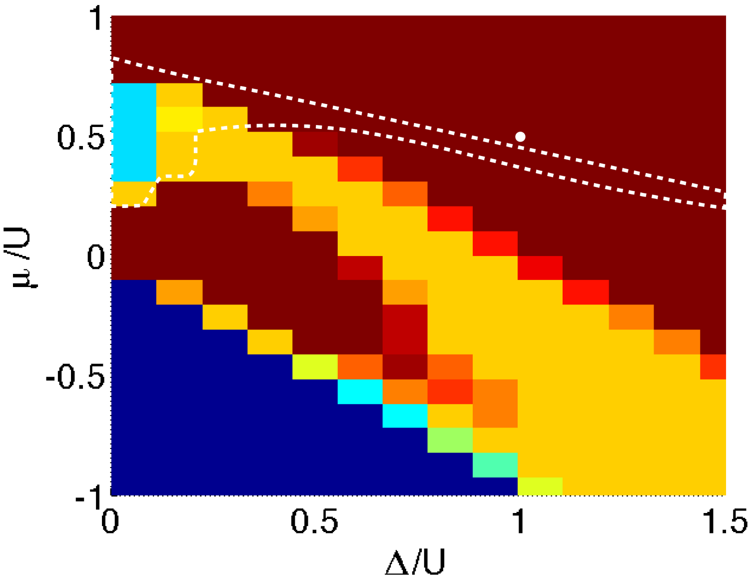

Figure 8.16: The phase diagram for $s = 13.6\ E_R$. The region marked by the white dashes corresponds to unit filling. Notice that the phase diagram clearly shows that the re-entrant superfluid state is possible. The white circle corresponds to $\mu/U = 0.5$, $\Delta/U = 1.0$ - parameters used for simulations presented here. The value corresponds to a slightly larger than the unit filling density. This is done to allow for the expansion of the gas in traps.

the question of the possibility of seeing an RSF in trapped systems will be resolved.

Firstly, consider the trap free phase diagram shown in Fig. (8.16). From the difference in the slope of the SF-BG phase boundary, the slope of the regime corresponding to the unit filling enclosed within the boundary marked with white dashes and the fact that the disordered gas expands with addition of disorder, it is evident that a fixed density trapped system that starts out with unit filling, will be able to see the RSF only if the trap is so weak that that path traced out lies within the boundaries sketched in the figure. Alternatively, the trap curvature needs to be adjusted so that the central part of the gas is always within the boundary shown in the figure. Additionally, the RSF is always supported by "regular" SF phases at lower and higher density. So whenever it arises in a trapped setting somehow it must be shown that there is a SF corresponding to a local density of ~ 1.0. This is an unnecessarily challenging problem, and may be impossible for current experiments to conclusively show in 3D. Nonetheless, simulations were undertaken to show that such a phenomena is indeed possible.

The simulations undertaken was again for a $s = 13.6\ E_R$ at $\Delta/U = 1$ system because the

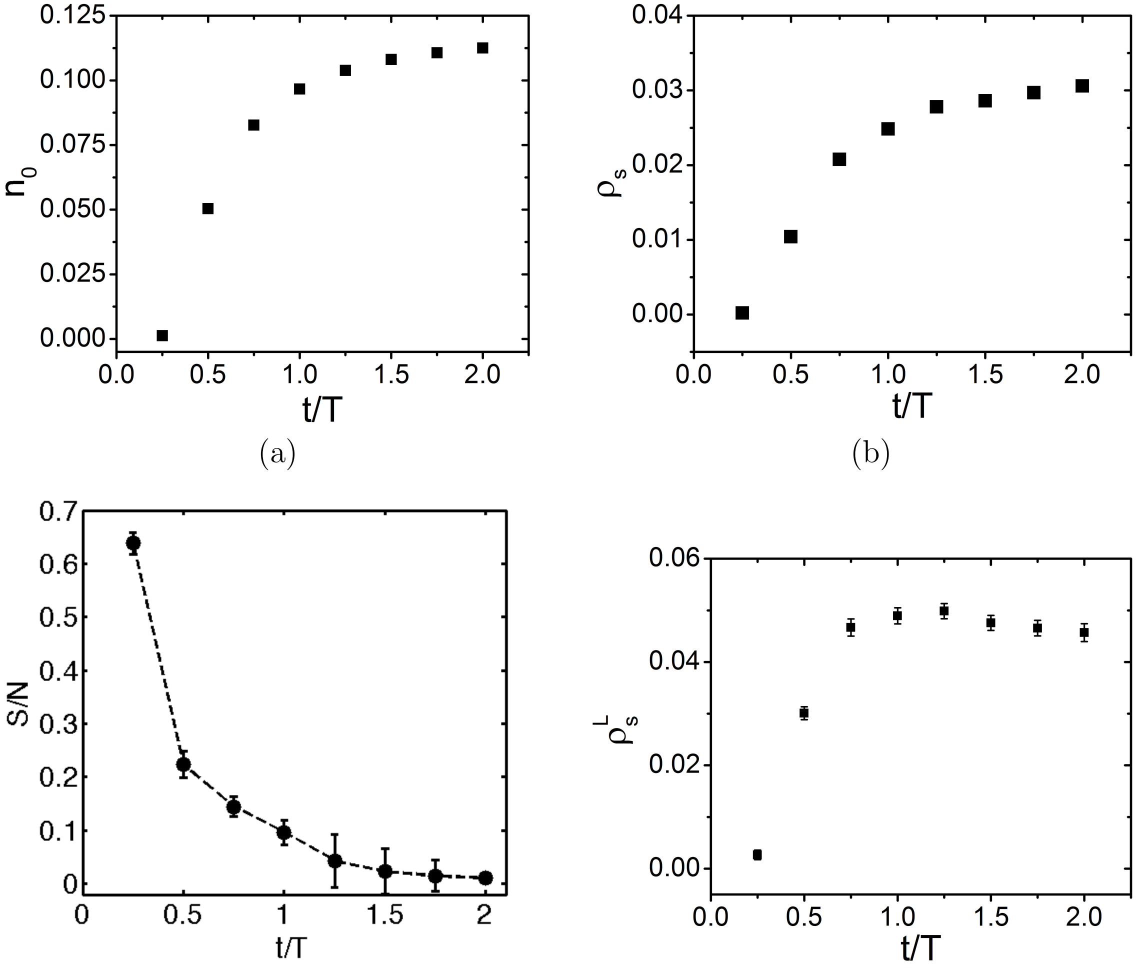

(a) (b) (c) (d)

Figure 8.17: Observables for a $s = 13.6\ E_R$ at $\Delta/U = 1$ system with $N \sim 28000$ particles. Here $t = 0.009\ E_R$ ($t = 1.5$ nK) and a trapping frequency of $\omega = 65$ Hz was used. (a) Global condensate fraction (b) Global superfluid fraction (c) Entropy per particle vs effective inverse temperature (t/T). The line is a guid to the eye. (d) Local superfluid fraction of the SF domain.

critical temperature of the SF decreases with the increase of U/t. This system is very easily accessible to experiments. A modest trapping frequency $\omega \sim 65$ Hz is sufficient, with the $N \sim 28000$. The central chemical potential is set to $\mu/U = 0.5$, which in the clean system would be in the middle of a MI dome. The full finite temperature behavior, all the way to the critical regime was studied. Global observables have been shown in Fig. (8.17a-b). The condensate fraction has been calculated from the ρ_1, and the superfluid fraction has been calculated from rotational formulation discussed earlier. For these disordered systems, the superflow is considerably lowered, but will always be finite if the condensate is present, as expected. Note that the critical temperature is around 6 nK. Using the fitting procedure discussed in Chapter 6 a crude estimate of the entropy per particle (S/N) vs t/T has been shown in Fig. (8.17c). This calculation is very hard for disordered system and requires a very large number of sweeps to get sufficient accuracy needed in the energy per particle to be fit correctly and then integrated. From this dependence, however, it seems that the critical temperature corresponds to $S/N \sim 0.65\ k_B$, which should be accessible to experiments. Using the domain identification protocol discussed above, the local superfluid fraction of the SF that develops at the center of the trap has been shown in Fig. (8.17d). The apparent dip in the local fraction at colder temperatures is not a numerical artifact originating in the domain threshold. Checks with different thresholds shows a persistence of this effect. Presumably this simply means a contraction of the condensate leading to a lower area subtended by the winding paths around the rotational axis, while the normal component remains relatively localized (or expansion of the normal component while the SF remains localized).

Slices of the density for different temperatures have been shown in the columns of Fig. (8.18). The domains were identified using the condensate shown in the second row. The on-site superfluid density is shown in the third row. The IN state is a BG at low temperatures but is transformed to a normal state via a cross-over. The precise way this happens has not been explored here since the main focus of this section is on identification of the RSF. It is evident from the last row of density and condensate profiles, that the central density fits the requisite criteria of central density $\langle n \rangle \sim 1.0$, and evidently there is a robust RSF present in the system. Note that for this part of the phase diagram a SF will never arise over a region with uniform density owing to fact that there will be large fluctuations in particle number over any region that has a SF. The last aspect is manifestly the reason behind the large compressibility of the SF.

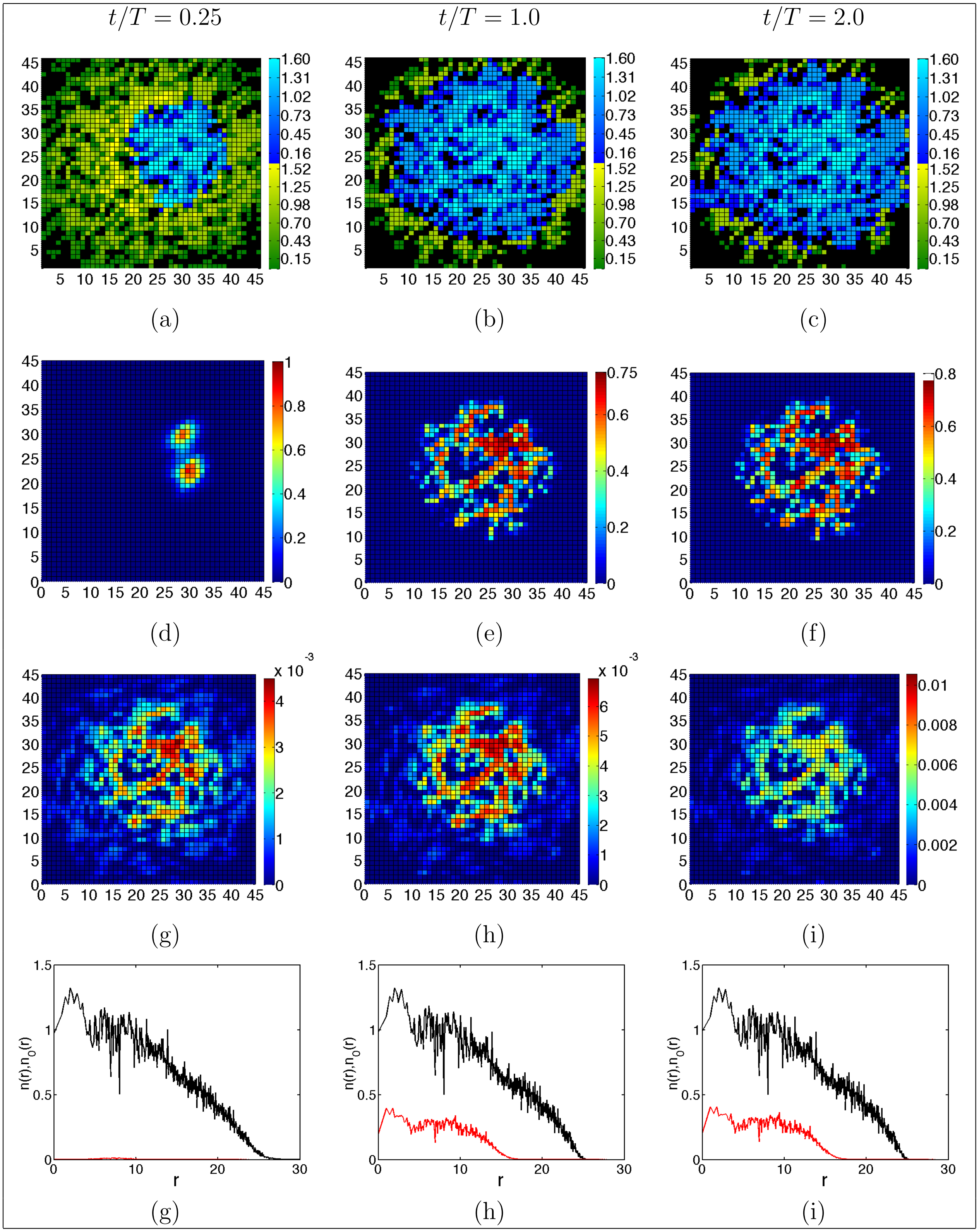

Figure 8.18: Slices of the density separated by domains (first row). The SF state is marked in blue and the IN state is in green. The onsite condensate density is shown in (second row) and the local superfluid density is in the (third row) for a $s = 13.6\ E_R$ system. The fourth row corresponds to density (black) and condensate density (red) profiles.

8.5 General Phase Diagram due to Speckle Disorder

In the sections above, a systematic description was give of the trapped gases in confined harmonic potentials. It was shown that although there are spectacular effects possible due to the trap and at a quantitative level there are differences with the trap free phase diagram, the latter still plays a very important role in guiding the behavior of such systems. As such it is pertinent to consider phase diagrams and observables that result for different parameters accessible to experiments. In this section, such diagrams are considered for a large range optical lattice depths $s = 8 - 18$ (E_R). The different observables are calculated and the corresponding phase diagrams are generated. The hope is that these diagrams will be of great qualitative use to experiments performed with traps and speckle fields in 3D – the only known system to date for which the disorder distributions can be reproduced exactly by theory. In the discussion that follows, the general effects of disorder averaging will be discussed first for a specific strongly correlated system as a way to gain qualitative insight into other parameters. The diagrams for other parameters have not been disorder averaged since they are only meant to guide experiments at a qualitative level.

8.5.1 Aspects of Disorder Averaging

In order to ascertain the properties of the phase diagram and the effects of disorder averaging in speckle disorder systems, 10 uncorrelated disorder samples were used to study a $s = 13.6$ system of size $L = 14^3$. The density, superfluid fraction and compressibility per particle were used to identify the different phases that result in these systems shown in Fig. (8.19). The phase were identified using the criteria discussed in Chapter 7, viz., the MI state is incompressible and devoid of any superfluid, the SF state has finite superfluid fraction and the BG is compressible but lacks any superfluid. These boundaries were determined using the criteria that the superfluid fraction must be larger than 0.1%, the compressibility needs to be within error bars of the MI compressibility which is close to zero at the temperatures used for these calculations $\beta t = 4.0$ (recall that the bandwidth in 3D is $12t$, so this is very close to the $T \to 0$ limit). Note that the raw non-interpolated data has been presented here. The jagged saw-tooth-like feature of the phase boundary appears since a finite grid size was used. There is also a small contribution here due to drifts of the Δ/U values for each sample. Unlike the box disorder case where U is fixed in simulations by hand, in the speckle disorder case the U values drift slightly. Here the average has been used. (Recall also that Δ is the disorder strength and not the bound for Speckle disorder.)

The main effect due to disorder averaging manifests as a blurring of the boundaries in

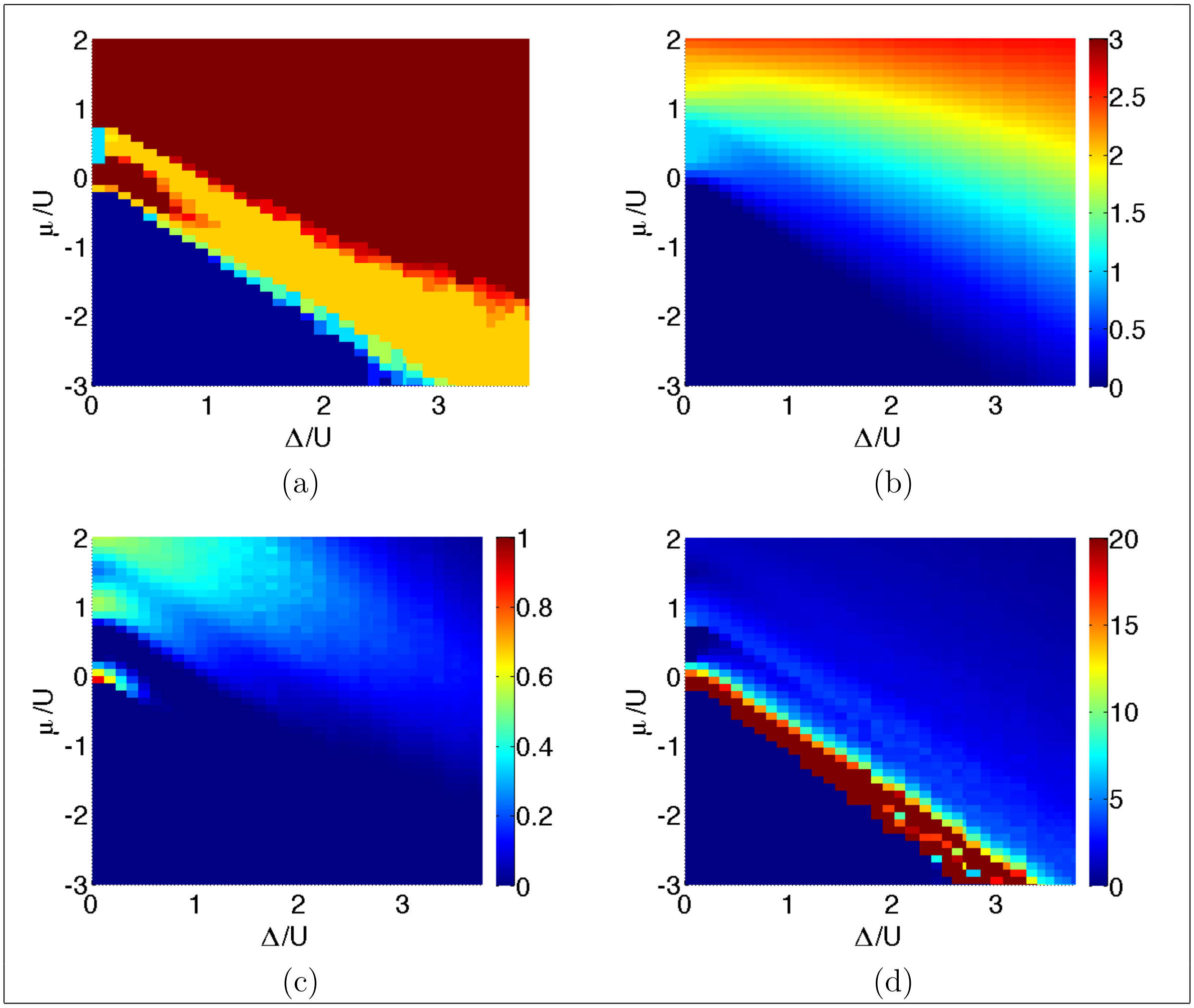

(a)

(b)

(c)

(d)

Figure 8.19: Phase diagram for $s = 13.6$ system. (a) Phase diagram where the phases are indicated by the coloring: SF (red), BG (yellow), MI (light blue) and Vacuum (dark blue). (b) Density, (c) Superfluid Fraction (d) Compressibility per particle

Fig. (8.19a). This is to be expected near the phase boundary, where the correlation length starts diverging and the observables become sensitive to the disorder distributions. These aspects were discussed already in Chapter 7 Section 7.1. In terms of the coloring scheme the SF-BG boundary has color mixtures from the BG and the SF phases. The blurring in blue at the BG-vacuum boundary is owing to the small density effects. A full finite size scaling would eliminate this effect. In this system where the Harris criteria is not met, the break down of self averaging is expected[108]; however, this has not been verified in this work since the computational effort is very large. It is also qualitatively evident even with these small samples that if there are any issues then they will be most to do with the phase boundaries.

In order to quantitatively study the standard deviation (and not the standard error)

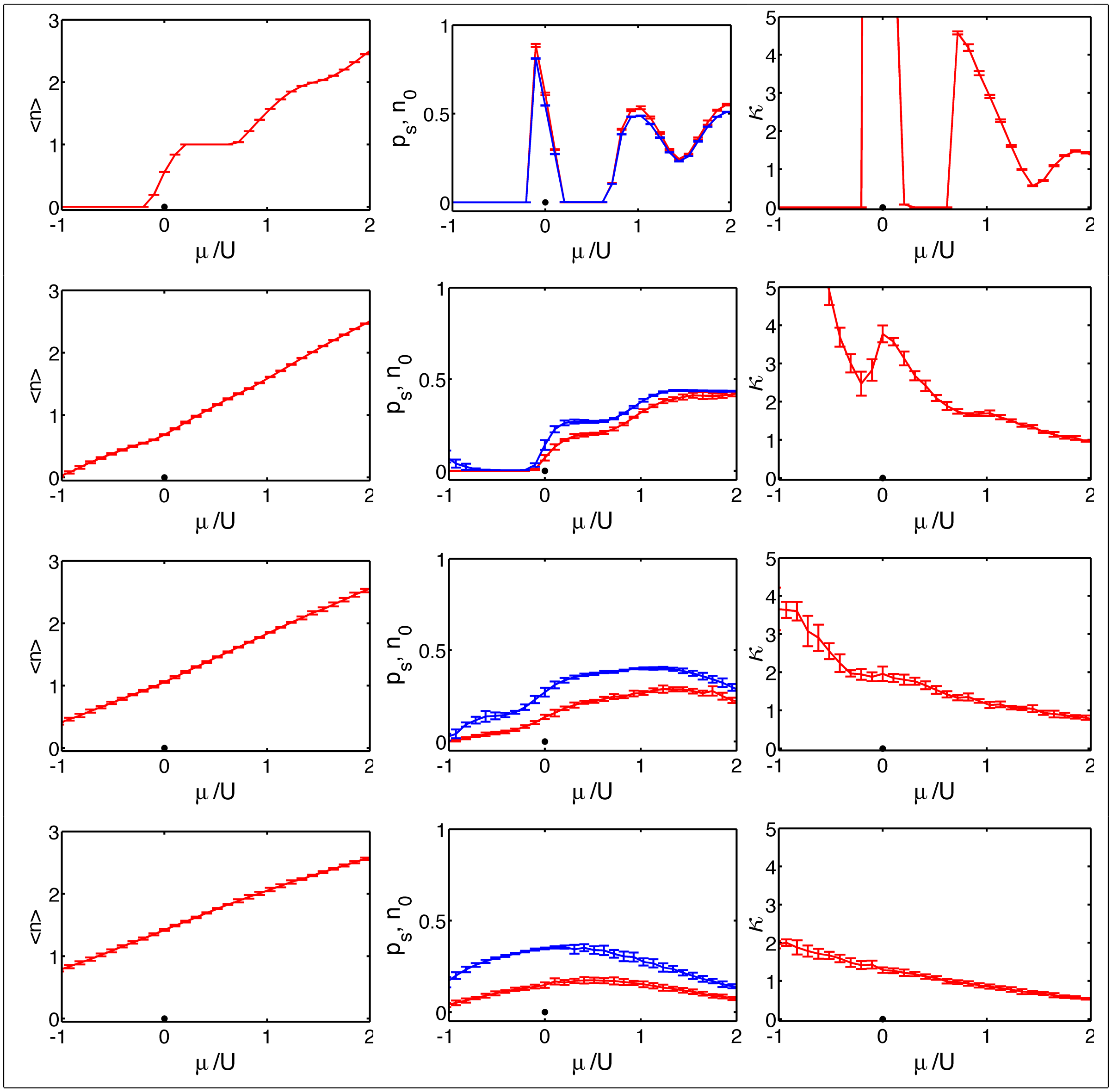

Figure 8.20: Slices taken through the phase diagram at $\Delta/U = 0.0$, 1.0, 2.0 and 3.0 (top to bottom) for different observables (left to right). Note that the condensate fraction (blue) has also been shown in addition to the superfluid fraction (red). Wherever n_0 is finite for $\rho_s = 0$, it is a local puddle and the density is very small. The error bars are the standard deviation due to disorder averaging.

of the different observables due to disorder averaging, slices at fixed disorder strengths of $\Delta/U = 0.0$, 1.0, 2.0 and 3.0 have been shown in Fig. (8.20) for the different observables. In addition to the superfluid fraction calculated from the winding number formulation, the condensate fraction has also been shown. A peculiar behavior in these disordered systems is that the ρ_s can be less than n_0, whereas in clean system generally the opposite holds. The disorder in the system is a hindrance to the flow of particles, and such the superflow is reduced. On the other hand in terms of static correlations the particles are able to maintain long range order more easily. At the $n \to 0$ edge of the phase boundary, there is large statistical fluctuations and should not be taken seriously. The error bars on these images are the standard deviation due to disorder averaging. They are quite small and grow near the critical regime.

This particular analysis reveals that for practical purposes disorder averaging may not be needed unless phases very close to the critical boundary is being assessed. As such full scale computations of a range of systems have been shown in the next set of figures. For each such figure, the phase diagram has been computed as in the case discussed here using the same thresholds. The behavior of the systems is best addressed in two categories: $U/t < (U/t)_c$ and $U/t > (U/t)_c$.

For $U/t < (U/t)_c$, the phase diagram looks remarkable similar for all cases presented here. Notably of-course, with the increase of interaction strength (U/t or s), the BG appears for lower Δ/U. Notice that there is a small region of BG separating the SF from the vacuum in all cases of disorder except for $\Delta/U = 0$. The few cases where it seems not to appear are due to binning and threshold related issues. Remarkably, the BG state appears to rapidly grow with disorder strengths, in a flaring out type of behavior prominent for $s = 10$, $s = 11$ and $s = 12$. It will be evident in the next chapter that experiments see a threshold type of behavior in the excitations produced by disorder quenching precisely because of this flaring out effect. Essentially what happens is that due to the trapping potential, experiments and QMC calculations in this regime do not see any of the BG at the edge of the gas for low Δ/U. However as Δ/U approaches this broader regime, the BG rapidly develops and the SF is no longer stablized by the confinement.

For $U/t > (U/t)_c$ the phase diagrams change considerably from the case above. There is a small SF region present for low Δ/U for all interaction strengths shown here, although it is almost completely gone for $s = 18$. Recall that for $s = 17.1$ the trap did not see any SF for $\Delta/U \sim 0.25$. The regime shrinks with increasing Δ/U. Notice that there is a RSF regime present for all commensurate fillings (only $n = 1$ and $n = 2$ is visible here) that also shrinks with increasing Δ/U. The MI state is plainly visible for the clean case and also marginally for low Δ/U. This is a finite size effect, indicating that experiments performed with currently accessible trapping frequencies, which controls the central number of sites over which the density remains smooth, might be able to see the presence of the MI at finite Δ/U.

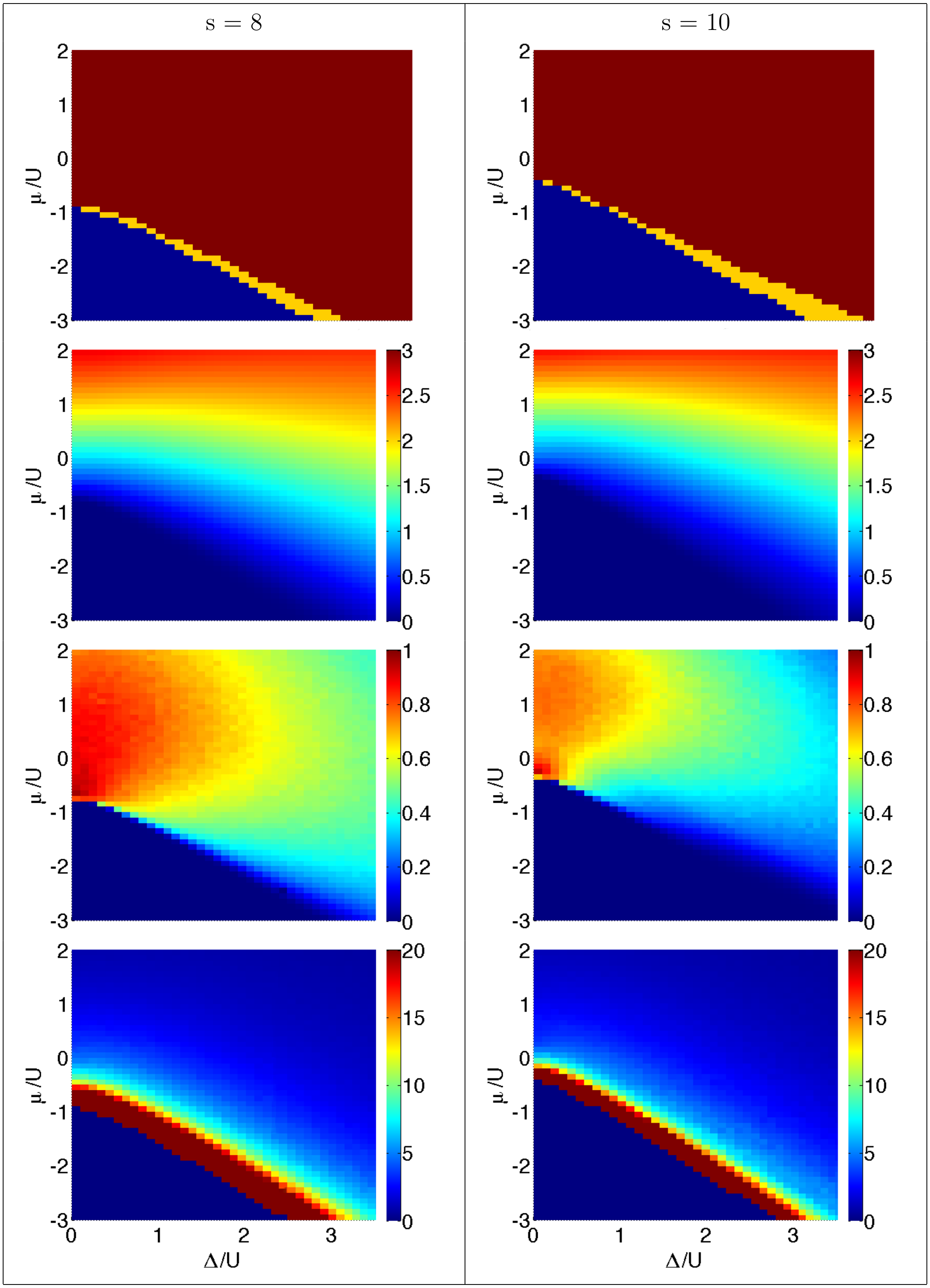

Figure 8.21: Top to bottom: Phases, density, superfluid fraction and compressibility.

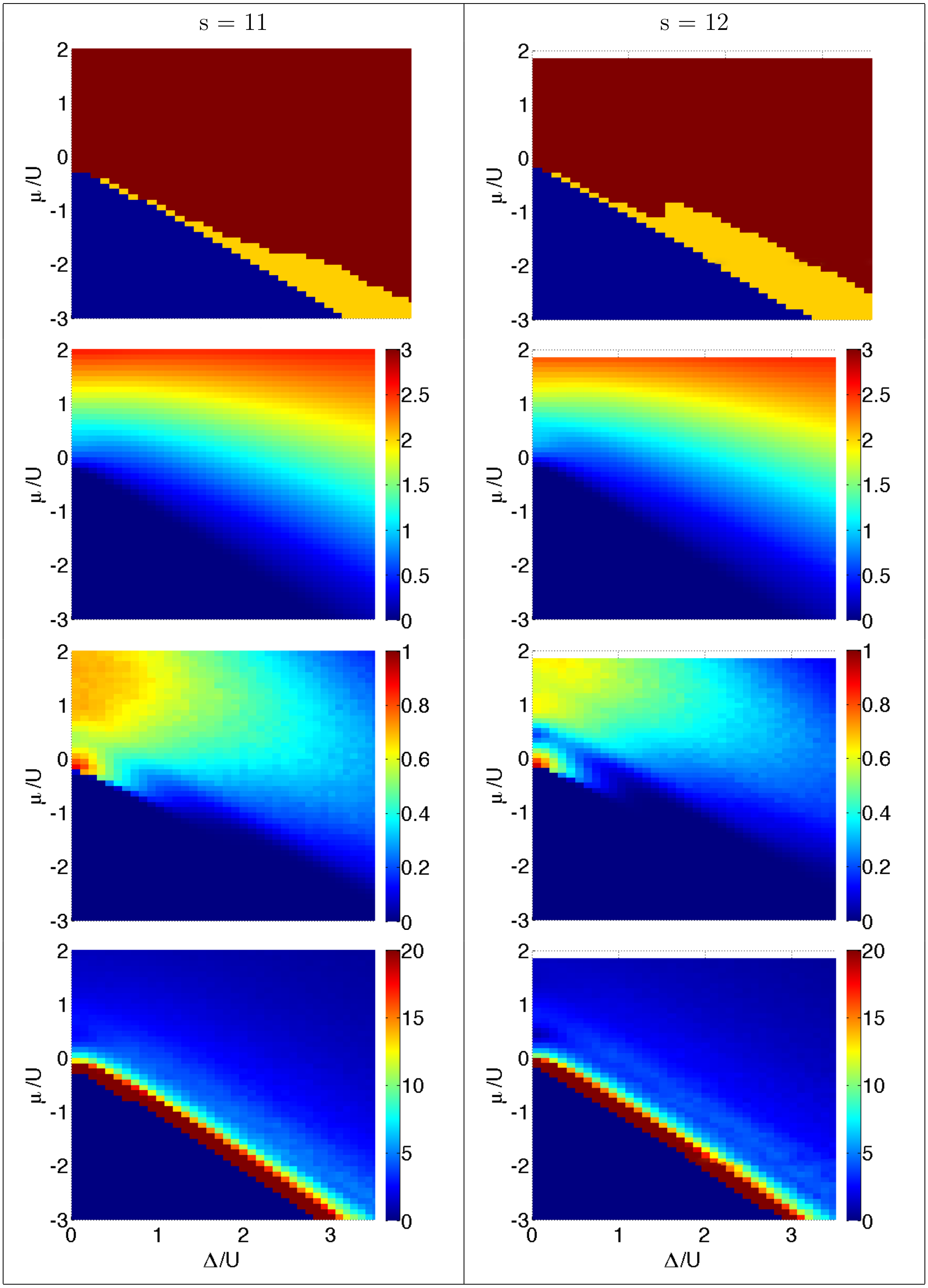

Figure 8.22: Top to bottom: Phases, density, superfluid fraction and compressibility.

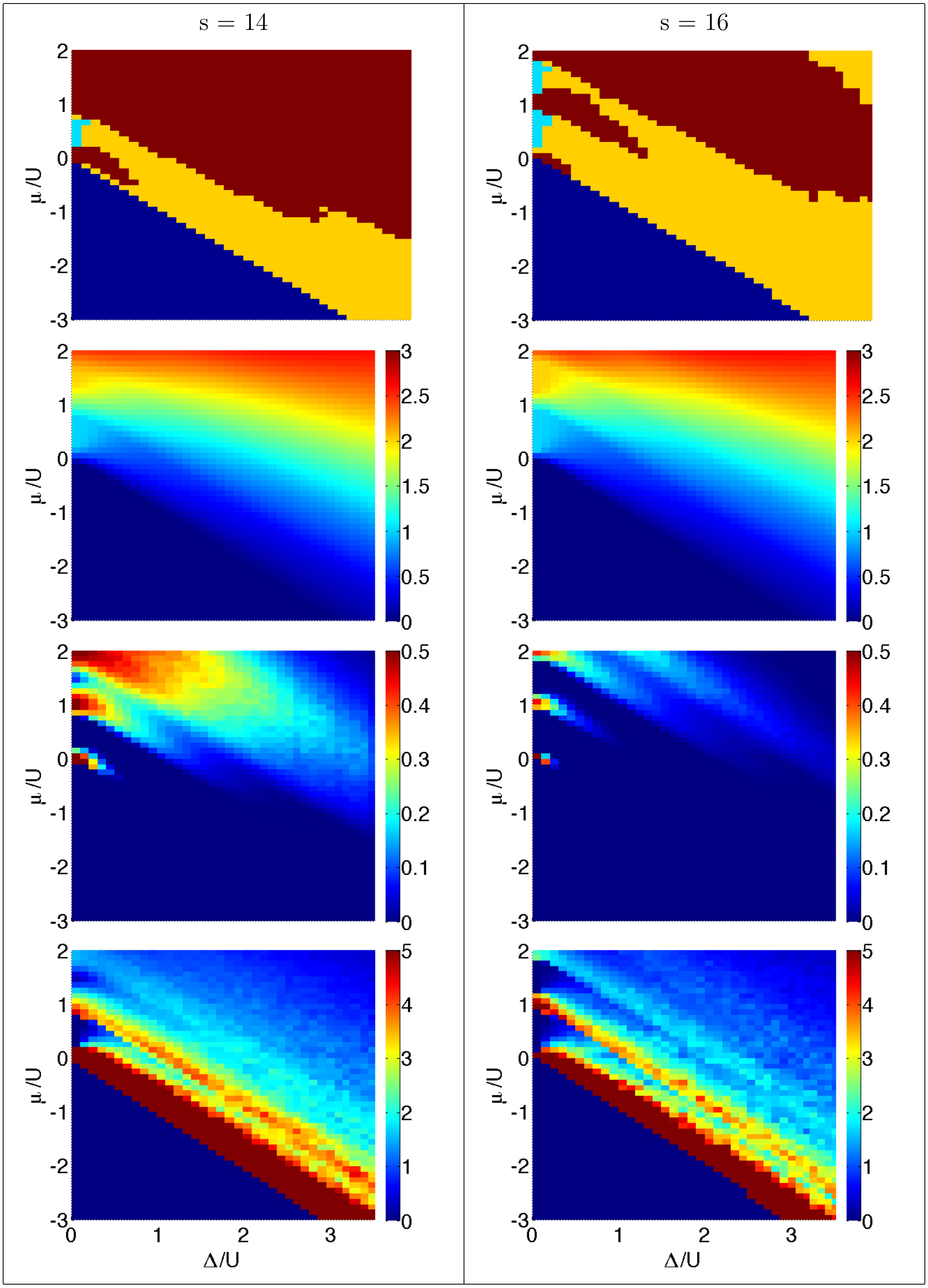

Figure 8.23: Top to bottom: Phases, density, superfluid fraction and compressibility.

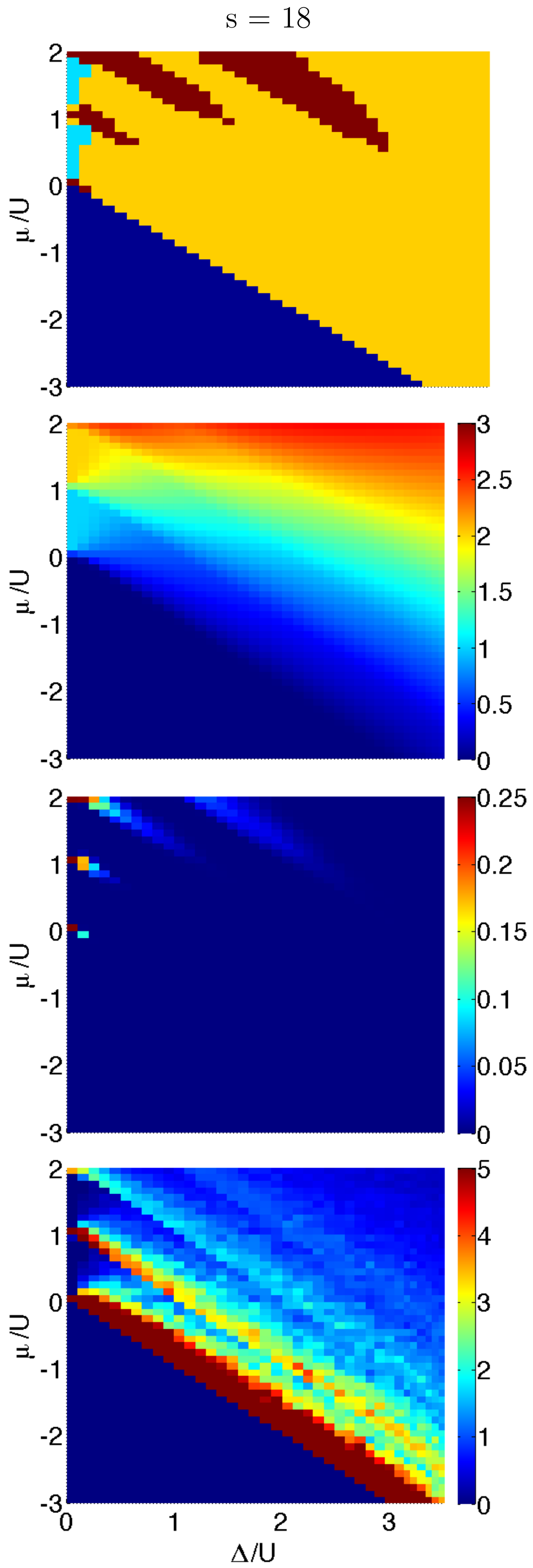

Figure 8.24: Top to bottom: Phases, density, superfluid fraction and compressibility.

8.5.2 Effects of Off-Diagonal Disorder

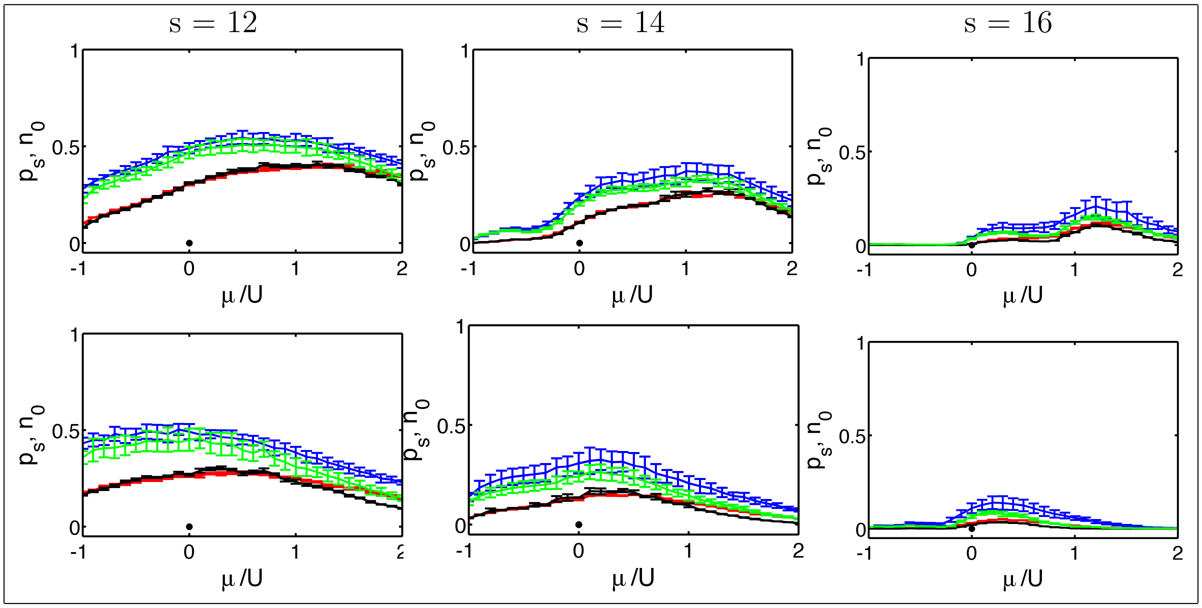

Figure 8.25: Comparisons of condensate and superfluid fraction for $\Delta/U = 2$ (top) and $\Delta/U = 3$ (bottom). The condensate fraction for simulations with (without) tunneling disorder is shown in blue (green). The superfluid fraction for simulations with (without) tunneling disorder is shown in red (black).

As a final consideration of this speckle disorder system, calculations were performed to establish the effects of tunneling disorder on the low temperature phase diagram of the system. Fig. (8.26-8.28) show the phase diagram constructed from the different observables as before. The disorder distributions are identical to the ones used for the phase diagrams generated earlier, only this time disorder in the tunneling term has been removed and set to the clean system value. It is evident from the figures that the overall phase diagrams look qualitatively identical to the diagrams with off-diagonal disorder. There seems to be some features for the $s = 16$ case for large disorder ($\Delta/U > 2.5$): the tunneling disorder seems to stabilize the SF state. Quantitatively, direct comparisons show that the only difference of note is in the condensate and superfluid fraction at large disorder strengths and it increases with interaction strength. Comparisons are shown in Fig. (8.25) for $s = 12$, 14 and 16. This is quite remarkable, because the distribution of the tunneling term has a significant tail (see Fig. 5.9). Apparently the superfluid is impervious to the connection strengths (designated by the hopping term t in the DBHM) even in the presence of large disorder, and stabilizes itself. The condensate does show small changes owing to the difference in static correlations. These are all low temperature results, the tunneling term might play more of a role at finite T, but this dependence has not been studied in this work, and will be pursued elsewhere.

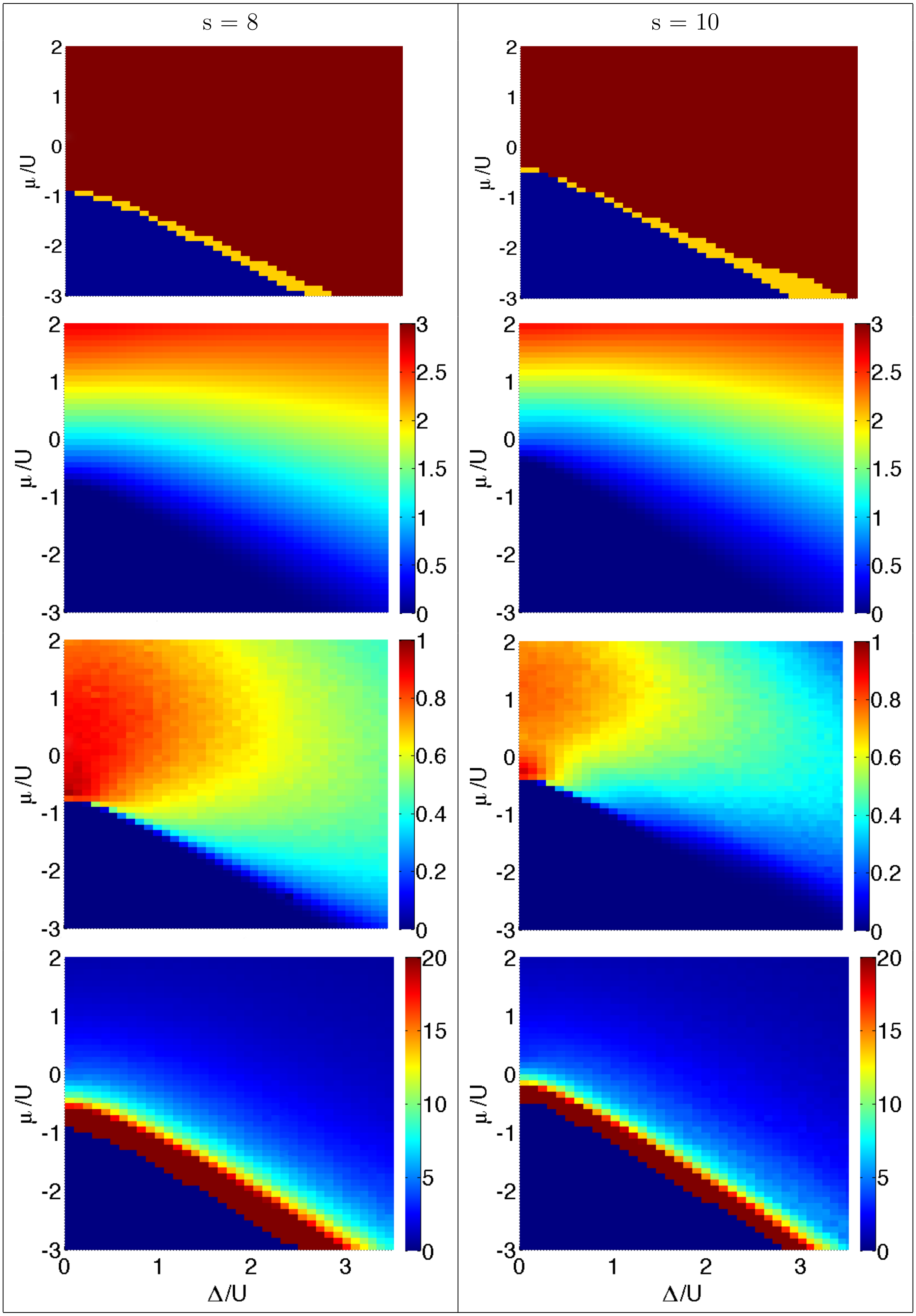

Figure 8.26: Top to bottom: Phases, density, superfluid fraction and compressibility.

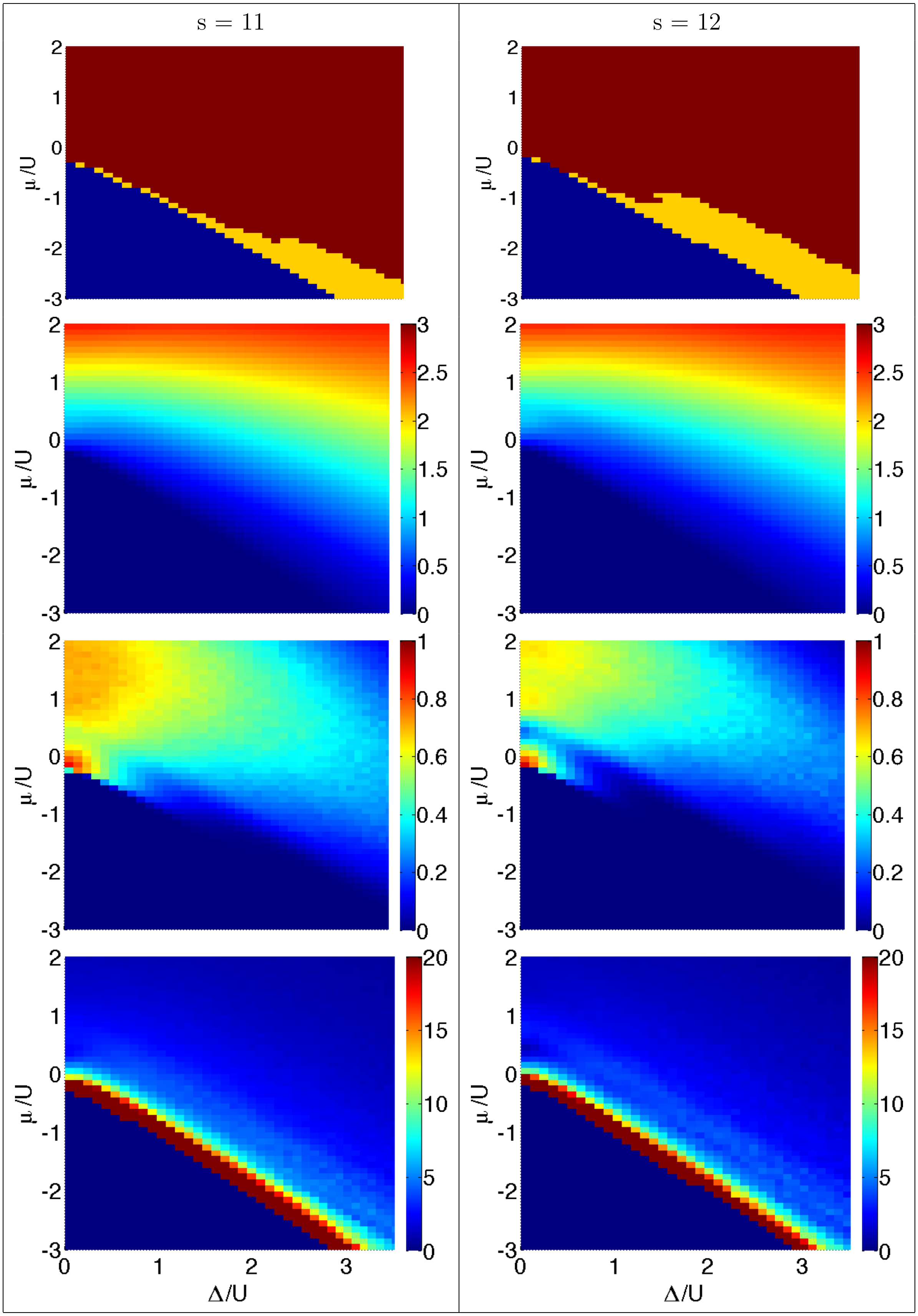

Figure 8.27: Top to bottom: Phases, density, superfluid fraction and compressibility.

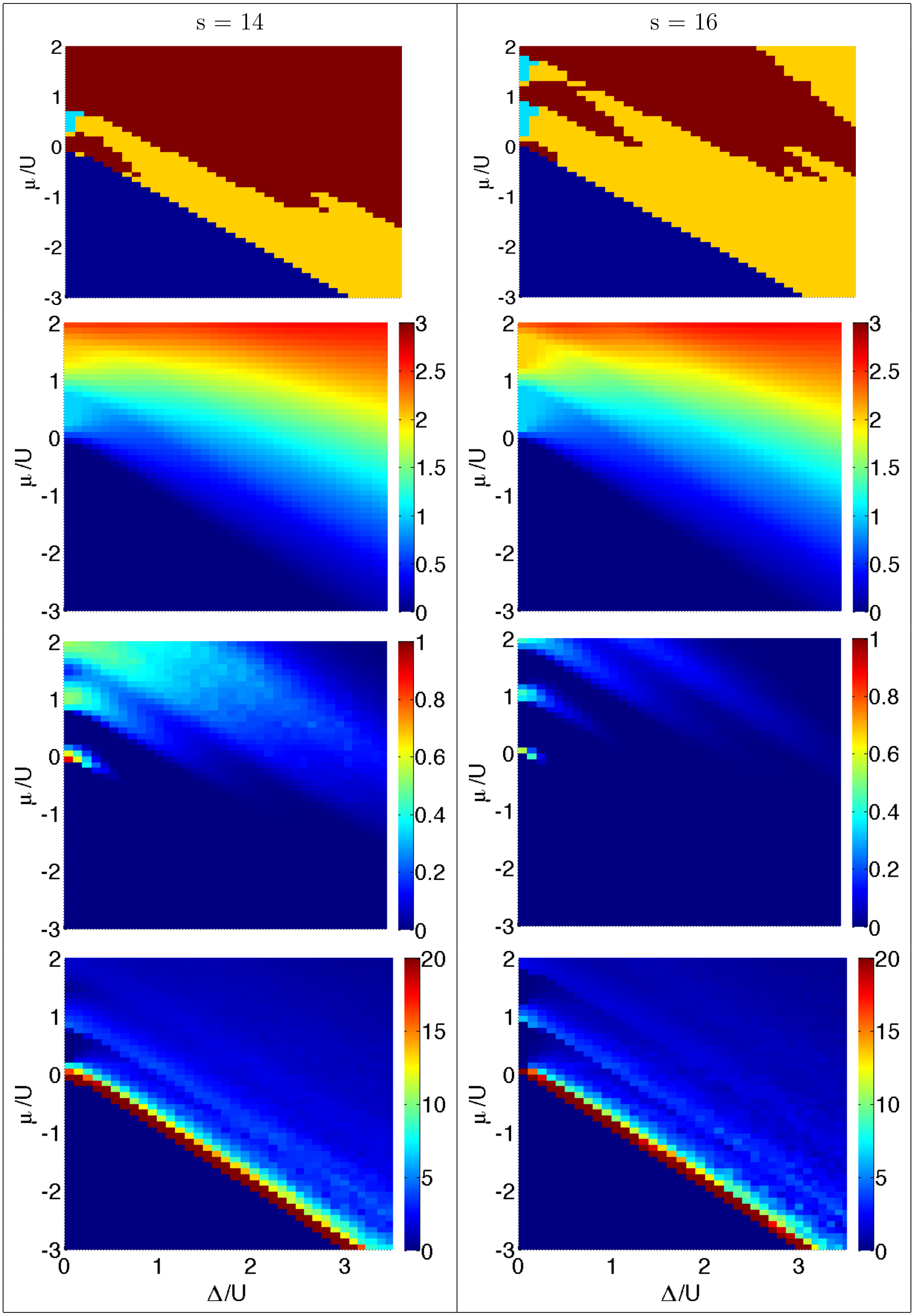

Figure 8.28: Top to bottom: Phases, density, superfluid fraction and compressibility.

8.6 Summary of Results

In conclusion, this chapter entailed the study of the properties of trapped optical lattice systems in the presence of speckle disorder. Through the analysis of strongly correlated systems on either side of the SF-MI critical phase boundary it was demonstrated that the domains that develop in these trapped systems correspond well to the phases of the untapped system. Using the largest eigenstate of the single-particle density matrix, the system naturally separates into the SF and IN domains. Furthermore, local measurements of the domain reveal that the IN can be made of either the MI state or the BG state. Mixtures of MI and BG cannot be discriminated since the the latter can always contain arbitrarily large MI domains owing to its Griffiths-phase type of property. Additionally, QMC simulations show that while the local density approximation is generally a good qualitative indicator of the structure of the domains that develop in trap systems, there can be strong violations. This is especially true in weak traps where the critical surface separating domains can strongly modify the way in which the system evolves as disorder is increased. Also, the LDA does not yield good quantitive agreement with *ab initio* calculations for observables when disorder strength is large. This arises due to the expansion of the gas that cannot be accounted by the LDA. An important case is $U/t < (U/t)_c$ systems that can exhibit threshold type of behavior where the BG develops at the outer ring of the gas only if sufficient disorder is present in the system. It is conclusively shown with simulations that this effect is purely due to the trap, and is not amenable to a LDA type of description. Whenever the BG exists, the single-particle eigenstates are highly localized with small but not insignificant (compared to normal gas) particle numbers. These are explicitly shown for a range of systems. The BG domain, thus, consists of localized quasi-condensed puddles that are uncorrelated so that global superfluidity is absent. This chapter also shows that the re-entrant superfluid phase is realizable in these trapped systems. Finite temperature calculations show that the critical temperature for an experimentally accessible system is ~ 6 nK, corresponding to an entropy per particle of $\sim 0.65\ k_B$, which is well within the cooling limits of experiments. The key feature of these trapped systems is that the gas expands due to disorder – a surprisingly simple property that has been overlooked in many studies to date. Finally, the effects of disorder averaging are discussed. In general, the quantitative departures in the observables are noticeable only near the critical boundaries between phases. Within individual phases such departures are small. Additionally, it is shown that at low temperatures tunneling disorder has almost no effect on the superfluid fraction. Amazingly the superfluid state remains robust and unchanged despite the presence of disorder in the links connecting different sites.

Chapter 9

Probing the Bose-Glass-Superfluid Transition

In this chapter, results from a collaborative enterprise between theory and experiment will discussed [31]. The objective was to probe the Bose-glass Superfluid phase transition using two independent tools. The hope was that the theoretical framework constructed so far with quantum Monte-Carlo (QMC) was sophisticated enough to account for most of the details that is needed for a quantitative comparison. On the experimental front, a quenching paradigm traditionally associated with classical systems was extended to quantum systems created with ultra cold atomic gases. It is immediately clear that the two approaches are radically different: QMC techniques probe the equilibrium properties of the system, whereas experimental techniques are dynamical in nature. However, it will be seen that, despite these radically different approaches, a remarkable agreement in the trapped phase diagram is obtained.

The dynamical measurements due to experiments will appear to fit the standard quantum Kibble-Zurek framework of excitation generation as the SF-BG phase boundary is crossed. However, an exploration of the timescales of relaxation will make it evident that things are not so simple, and the non-equilibrium paradigm traditionally associated with spin-glasses and quantum glasses might also apply.

9.1 Experimental Setup and Measurements

Details about the general experimental apparatus has been discussed in Chapter 8 section 8.1. For the measurements discussed here $(27 \pm 2) \times 10^3$ ^{87}Rb atoms are condensed to near absolute zero and confined in an optical dipole trap with geometric mean trap frequency

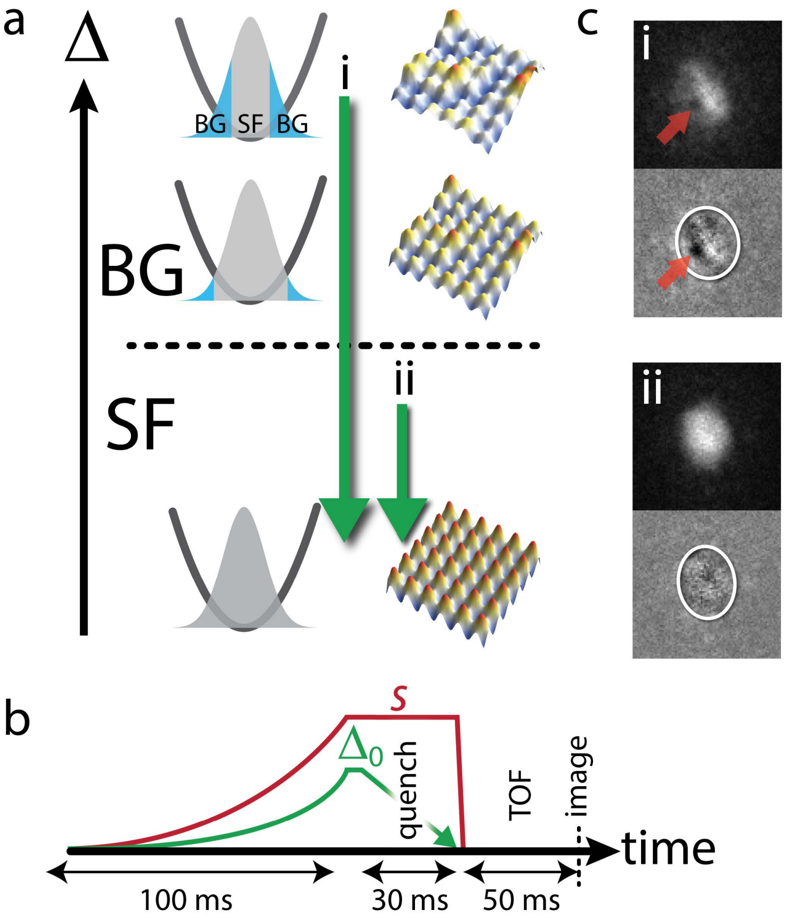

Figure 9.1: (a) Schematic phase diagram of the DBHM and quench. The gas is quenched from the BG to the SF regime by rapidly reducing (green arrow) the disorder strength Δ from Δ_0 to zero at fixed U/t, which is determined by the lattice potential depth s. Equilibrium configurations and the disordered lattice potential (false color) are shown at three values of Δ. For sufficiently high Δ, BG (blue) and SF (light gray) phases coexist in the trap. (b) Time sequence for the measurement. The lattice potential depth and disorder strength are shown using red and green lines. (c) Equilibration is disrupted during the quench and excitations are produced, which are measured in TOF images (grayscale). Images are shown for $\Delta_0 \sim 0.5\ E_R$ (top) and $\Delta_0 = 0$ (bottom) at $s = 12\ E_R$, along with the residual from a fit; the white ellipse on the residual marks the fitted TF radius. For sufficiently high disorder, excitations such as vortices are apparent (red arrow) after the quench, while smooth profiles are obtained at low Δ_0.

$\omega = 2\pi 53(3)$ Hz, without the lattice. The lattice potential is ramped on in 100 ms using an exponential function with a 200 ms time constant. For $s =$ 10-12 E_R, the extra confinement from the gaussian profile of the lattice beams increases the geometric mean trap frequency to approximately $\omega = 2\pi(69 \pm 4)$ Hz. The disorder potential is characterized by the strength Δ, its form and properties have been discussed in Chapter 5. Briefly, it introduces disorder in all terms of the Disordered Bose-Hubbard Hamiltonian (DBHM), given by 8.1 (See Chapter

8 for details). The experimental protocol used in these experiments, involve turning on the speckle field to the requisite initial disorder strength Δ_0, together with the beams that setup regular lattice. Following this, the disorder strength is linearly ramped from Δ_0 to zero in 30 ms. This is known as a quantum quench as it involves the changing of Hamiltonian parameters at ultra-low temperatures (more on this later). As per a regular time-of-flight (TOF) scheme, the next step is to snap-off all confining beams and fields and allow the gas to expand for 50 ms, after which it is imaged. The full measurement cycle is shown in Fig. (9.1b).

The essence of this protocol is rooted in the ideas of the quantum Kibble-Zurek (KZ) mechanism that predicts the creation of defects when a system is slowly quenched (compared to the relaxation time) from a disordered to an ordered state, across a second order phase transtion [129, 130, 131, 132, 133]. It actually goes further than this and, using critical scaling analysis, gives a quantitative account of the number of defects formed as a function of the quenching rate (see below for discussion). From the discussions in the previous chapter it is clear that for $(U/t) < (U/t)_c \equiv 29.34(2)$, i.e., for parameters of the system where in the clean system only a SF state is possible, the edge of the trapped gas undergoes a quantum phase transition to the BG state for sufficiently large Δ. For stronger disorder, the BG domain grows by encompassing more atoms and expanding in volume. Therefore, the expectation is that by a KZ like process, excitations should develop once the BG appears and grow as the BG domain grows. Such excitations are measured using TOF techniques: by imaging after a long (50 ms) period of free expansion, vortices and other excitations are transformed into modulations of the density profile and the measured optical depth (OD). These excitations are visible in the typical images shown in Fig. (9.1c and 9.2b). For low Δ the density profile after the quench and TOF is smooth, while for high Δ features consistent with vortices are present.

To characterize the quantity of excitation present after the quench, an observable of the form

$$\tilde{\chi}^2 = \sum_{ij} \frac{(\mathcal{O}_{ij} - f_{ij})^2}{f_{ij}} / \sum_{ij} \mathcal{O}_{ij}, \tag{9.1}$$

is used. Here $\mathcal{O}_{ij}$ is the measured OD at the pixel indexed by i and j within a mask set by a smooth fitting function f that is the combination of a Thomas-Fermi (TF) profile and a gaussian used to capture the SF momentum distribution. This method was previously utilized to observe the quantum KZ effect by measuring excitations generated via a quench between MI and SF states in a clean lattice [134]. Data for s = 11 ER and $\Delta \sim$ 0-1 E_R are shown in Fig. (9.2a). It is apparent that excitations are not generated by the quench until

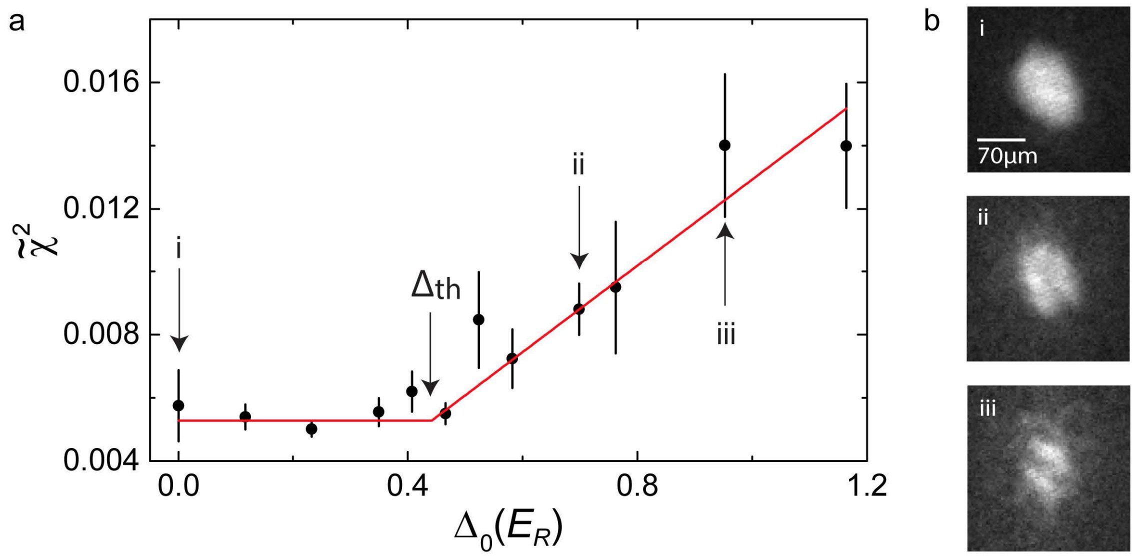

Figure 9.2: (a)-(b) Results of quench measurements. (a) The observed $\tilde{\chi}^2$ as Δ_0 is varied at $s = 11$ E_R and the piecewise linear fit (red line) used to extract the threshold disorder Δ_{th} are shown. The error bars show the standard error in the mean for the 6-12 measurements averaged at each Δ_0. TOF images obtained after the quench are shown for (i) $\Delta_0 = 0$, (ii) $\Delta_0 = 0.7$ and (iii) $\Delta_0 = 0.95$ E_R.

a threshold disorder strength is crossed, above which $\tilde{\chi}^2$ increases approximately linearly with Δ_0. Similar threshold behavior is observed for all lattice depths considered in this work ($s = 10$ - 12).

9.1.1 Determining Quench Time

The time variation of the spatially inhomogeneous disorder potential during the quench can cause excitations such as phonons, for example, by exceeding the local superfluid speed of sound [61]. To avoid complications from this type of effect, the associated timescale may be approximated using a simulation of the three-dimensional time-dependent Gross-Pitaevskii equation [135]. A disorder quench is simulated as in the experiment followed by 20 ms of free expansion. Because it is too computationally intensive to include the lattice, a trapped gas is simulated with the interaction strength adjusted to match the lattice system while coarse-graining over the lattice length scales [136]. Density distributions from these simulations were column integrated and analyzed using the $\tilde{\chi}^2$ measure of excitation, as with the experimental data. Results for $\Delta = 1$ E_R, the chemical potential determined by $\mu = m\omega r_i^2/2 + U\langle n\rangle/d^3$ (with U for s = 10 E_R), and a trap frequency set to match the experiment are shown in Fig. 1. An exponential fit yields a time constant of 9 ± 2 ms. Therefore a quench time of 30 ms is chosen in experiments to suppress excitations that arise only from the time variation of

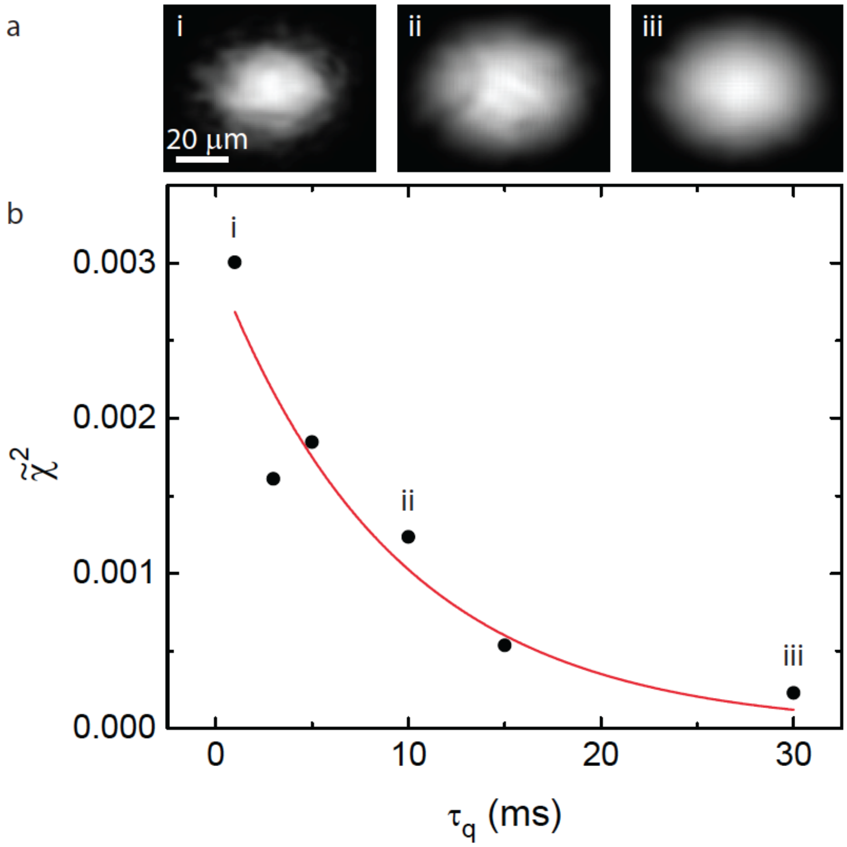

Figure 9.3: Time-dependent Gross Pitaevskii simulations including 20 ms of free expansion following the quench for different quench times τ_q (a) Simulated column density profiles for (i) $\tau_q = 1$, (ii) 10 and (iii) 30 ms. (b) Excitation strength $\tilde{\chi}^2$ as τ_q is varied. The solid line is a fit to an exponential decay.

the speckle potential. For $\tau_q = 30$ ms, the simulated $\tilde{\chi}^2$ is approximately 20 times smaller than in the experiment for similar Δ.

9.1.2 The Quantum Kibble-Zurek Mechanism

Since the main paradigm used to both motivate and describe experimental observations is the KZ process, it is worth briefly discussing its basic features. A full discussion is beyond the scope of this work, but there are many excellent references [129, 130, 131, 132, 133, 137]. The basic idea is to try to understand the out-of-equilibrium dynamics that is induced in a system as it changes from a (phase) disordered state to an ordered state across a continuous phase transition due to the "slow" quench of a parameter (say g) of the Hamiltonian (instead of the temperature traditionally associated with classical KZ mechanism). The time scales associated with such a quench is determined by considering the way the characteristic size of the domains in the disordered system change as the phase boundary is approached.[1]

In the disordered state, there a local domains with characteristic length scale $\xi << L$, the size of the system. The order parameter across different domains are uncorrelated such that for the full system there is no order. Only when the phase boundary is crossed at g_c do the domains coalesce via the spontaneous breaking of symmetry, so that the system has a finite order parameter. Now within the disordered state ($g > g_c$) the equilibration time τ_{eq} is comparable to the microscopic time scales of the system. Thus, the system rapidly equilibrates provided parameters are changed slower than the microscopic time scales of the system.

As the g approaches g_c, however, the ξ and τ_{eq} start to diverge and eventually during the ramp, at some value of g, the associated time take to equilibrate is larger than the time left to reach g_c. The KZ argument is that when this happens, the domain boundaries freeze – no further dynamic evolution is possible. These boundaries describe local topological defects in the system and appear as excitations once the phase boundary is crossed [137]. Eventually, they are expected to be reabsorbed into the system via heating, although this is still unclear [133].

It follows from this discussion, that the slower the quench, the closer to the system can get to the phase boundary without suffering from freeze out. However, even an infinitely slow quench will generate defects since the equilibration time diverges at the phase boundary. These ideas can put on a more quantitative footing using scaling arguments so that the number of topological defects can be related explicitly to the quenching rate of the system. It can be shown that the number of defects,

$$N(\hat{t}) \propto \tau_Q^{-d\nu/(1+\nu z)} \text{ at } \hat{t} \propto \tau_Q^{(\nu z)/(1+\nu z)}, \tag{9.2}$$

where, ν is the correlation length exponent, z is the dynamical critical exponent, d is the dimension of the system, τ_Q is the quenching time. If t is the time that parametrizes the quenching procedure $g(t) = g_c(1 - t/\tau_Q)$, then $\hat{t}$ is specific time for which the time needed for g to reach g_c is equal to the equilibration time τ_{eq}. Thus, $N(\hat{t})$ must be measured at the special instant $\hat{t}$ [133]. Notice that the key point here is that this entire quench is adiabatic up to $\hat{t}$ and the scaling arguments only hold for systems near equilibrium.

---

[1] Note that by disordered state, the symmetric state with no order parameter is present, is being implied. This is more general than the states that arise due to disorder

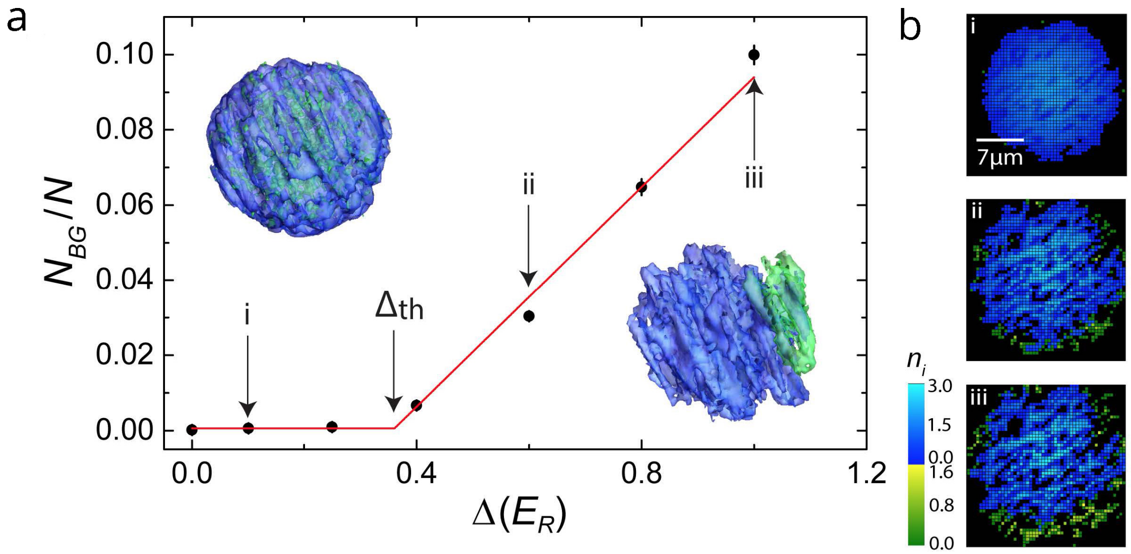

Figure 9.4: (a)-(b) Results from QMC simulations. (a) The upper bound N_{BG}/N on the BG fraction (strictly the insulator fraction, I_f) is shown as a function of Δ for s = 11 ER. The error bars show the standard error in the mean for the QMC statistical noise. The insets are three-dimensional contour plots of the highest (blue) and second highest (green) occupation eigenfunction of the single-particle density matrix for $\Delta = 0.05$ (upper left) and $\Delta = 1\ E_R$ (lower right). (b) Density slices through the trap center are shown for (i) $\Delta = 0.1$, (ii) $\Delta = 0.6$ and (iii) $\Delta = 1\ E_R$ (iii). The blue (green) regions are the SF (BG) domains, and the color bar shows the average number of particles on each site

9.2 QMC Results

In order to connect with the observed threshold behavior with SF-BG transition, exact QMC simulations of the equilibrium system were undertaken using the same trap and lattice parameters, atom number, and speckle disorder as in the experiment. The machinery needed to do this has been discussed in previous chapters. As discussed earlier, the way to distinguish between the two domains is via the eigenstates of the single-particle density matrix $\rho_1 = \sum_{ij}\langle \hat{b}_i^\dagger \hat{b}_j\rangle$. The largest mode for the entire regime of disorder parameters considered in these set of experiments will always correspond to a Bose-Einstein condensate (BEC). The spatial extent of the BEC is used to determine regions that are devoid of coherence. Such regions are also devoid of global superfluidity, i.e., the superfluid order parameter in this local insulting domain is zero.

For clean systems ($\Delta = 0$) and $U/t < (U/t)_c$ at ultra-low temperatures ($k_BT/12t << 1$), a single condensate extends throughout the system. As Δ is increased this behavior changes: the macroscopic condensate shrinks leaving behind regions devoid of coherence with it. Also, as discussed in the previous chapter, since the SF-BG transition is continuous there can be

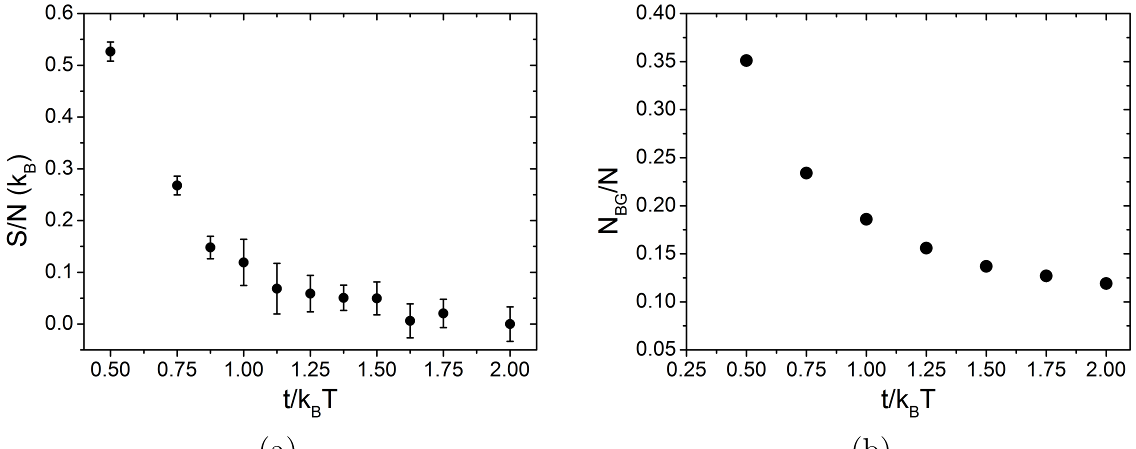

(a) (b)

Figure 9.5: (a) Shows the entropy per particle estimated from the energy per particle. A coarse upper bound of experiments is estimated to be $S/N \sim 0.4\ k_B$ (See text). (b) Shows the dependence of the Bose-glass fraction on temperature for $s = 12\ E_R$ and $\Delta = 1\ E_R$. The cross-over type of behavior and the saturation of the BG fraction as $T \to 0$ are evident.

no phase coexistence. Thus, the remaining region must strictly be insulating. To illustrate this behavior, the two highest eigenstates of ρ_1 for $s = 11\ E_R$ and $\Delta = 0.05, 1\ E_R$ are shown in Fig. (9.4c). At low Δ, all single-particle states are spatially overlapped with the SF domain, and the second largest state (or the first single-particle excited state) results from interaction-induced quantum depletion. For sufficiently high Δ, however, this extended state is replaced by a spatially localized mode that corresponds to a non-macroscopic and locally coherent superfluid puddle characteristic of the BG phase (see previous chapter for more discussion on the properties of the BG).

To compare with experimental measurements, the number of particles in the local region correspond to the insulator is measured (given by N_{bg}) and the BG fraction N_{bg}/N is computed, where N is the total number of particles. This estimate is strictly an upper bound at non-zero temperatures because thermal excitations are present. Typical behavior for N_{bg}/N at $s = 11\ E_R$ as Δ is varied is shown in Fig. (9.4b). Notice that, just like the behavior of the excitation measurement in experiments, N_{bg}/N is only non-zero above a threshold value of disorder above which it increases approximately linearly. Recall from the previous chapter that this threshold is purely a trap effect. If the curvature of the trap is reduced, the BG will appear continuously with the addition of disorder.

9.2.1 Effects of finite Temperature

The QMC simulations are carried out in the ultra-low temperature regime corresponding to $k_BT = t$. In contrast, the experiments access low but non-zero temperature. Understanding the impact of non-zero temperature on the quench measurement is complicated by the problem of precisely determining temperature in optical lattice experiments [102]. Therefore, a standard technique is used to estimate temperature in the lattice by assuming the entropy per particle (S/N) inferred from TOF measurements of condensate fraction in the trap is preserved during the lattice turn-on. QMC simulations are then applied to convert S/N to temperature in the disordered lattice. The highest interaction and disorder strengths accessed in this work ($s = 12$ and $\Delta = 1\ E_R$) is considered for the remainder of this section, where the maximal impact of non-zero temperature is expected.

The temperature is sufficiently low in the experiment so that only an upper bound on S/N can be determined. Based on an analysis of the imaging noise and images taken at short and long expansion times (i.e., low and high optical depth), the condensate fraction before turning on the lattice is estimated to be greater than 0.9. This lower limit implies on upper bound of 0.4 k_B per particle on S/N, according to a semi-ideal model [82]. Therefore $0.4\ k_B > S/N > 0\ k_B$ is estimated for the measurements presented in this work.

This entropy estimate from the experiment can be compared to the results of QMC simulations. Using the energy per particle (E/N) from QMC runs, the entropy per particle as a function of temperature is inferred. The results shown in Fig. (9.7a) were obtained by fitting E/N to a cubic spline for the sampled points. The ultra-low temperature behavior is obtained by fitting the low temperature points to a exponential function. The entropy per particle (S/N) is then obtained from E/N via integration. This procedure is similar to those used for clean systems [12].

Given the bounds from the experiment, estimates of the temperature is given by $T < 1.7t/kB$ for $s = 12$ and $\Delta = 1\ E_R$. A method for understanding how this non-zero T affects the quench measurements and determination of Δ_{th} is unavailable and beyond the scope of this work. To gauge the impact of nonzero T, equilibrium QMC simulations is used to calculate the dependence of N_{bg}/N on temperature. Fig. (9.7b) shows results for $s = 12$ and $\Delta = 1\ E_R$. The regime sampled by the experiment is thus close to the $T \to 0$ limit and is not dominated by thermal excitation. An insulating domain persists in the zero-temperature limit, and the localized states that arise in the BG domain are robust in the temperature regime sampled in the experiment.

9.2.2 Effects of Disorder Averaging

Experimentally, a systematic accounting of disorder averaging is intractable. However, over the course of experiments, there are small shifts in the focal point of the speckle light used to generate the disorder potential. In the presence of such shifts, no observable changes are found in the qualitative or quantitative behavior of the gas. Theoretically, disorder averaging is also extremely challenging for these large systems (60^3 lattice points with 27,000 particles; c.f. [116] with lattices of size 8^3-16^3 at unit filling for box-disorder systems). Discussions in the previous chapter point out that the effects of break down of self-averaging appear to be strong only near the critical point. So the only location of these effects are the SF-BG boundary between the domains which is a thin shell. A systematic sense of the uncertainty that results from using different disorder realizations is estimated by running simulations for 10 uncorrelated disorder potentials at $\Delta = 1\ E_R$ and $s = 12\ E_R$. These parameters, which correspond to the strongest interactions and disorder we have considered, are expected to exhibit the largest possible deviations. We find that disorder averaging introduces an uncertainty of $\sim 7\%$ to N_{bg}/N under these conditions. Thus, there is strong reasons to suspect that critical smoothing, discussed in the previous chapter, does indeed occur for trap curvatures $\omega = 2\pi(69 \pm 4)$ Hz.

9.2.3 Effects of Disorder Distribution

An intriguing question that comes to mind are the possible effects of disorder distributions in trapped systems. Towards this end, two systems at $s = 11\ E_R$ are simulated that are identical in all respects apart from the type of disorder distribution; one system uses has box disorder, while the other has speckle disorder. Note that the standard deviation of box disorder and speckle disorder are different. If the box disorder is characterized by the bound value Δ_{box} and the speckle field disorder amplitude is $\Delta_{speckle}$, then, in order to make them comparable, an appropriate choice is to adjust the bound and amplitude such that the standard deviation is equal. Consequently, if $\sigma_{box}(\delta\mu) = \sigma_{speckle}(\delta\mu)$, then $\Delta_{box} = \Delta_{speckle}\sqrt{3}$ must be used.

The resulting observables have been presented in Fig. (9.8a-d). It is evident that the box disorder system rapidly converts to a BG, while the speckle is much more stable. This is most likely due to the strong skewness in the speckle type of disorder. Recall that in this case most of the sites are at lower disorder values, while a few in the tails raise the overall standard deviation. Consequently, the condensate fraction and superfluid fraction is larger than the box disorder case. The local observables show that the threshold disorder needed to see the BG phase starts at much lower values for the box case (somewhere between

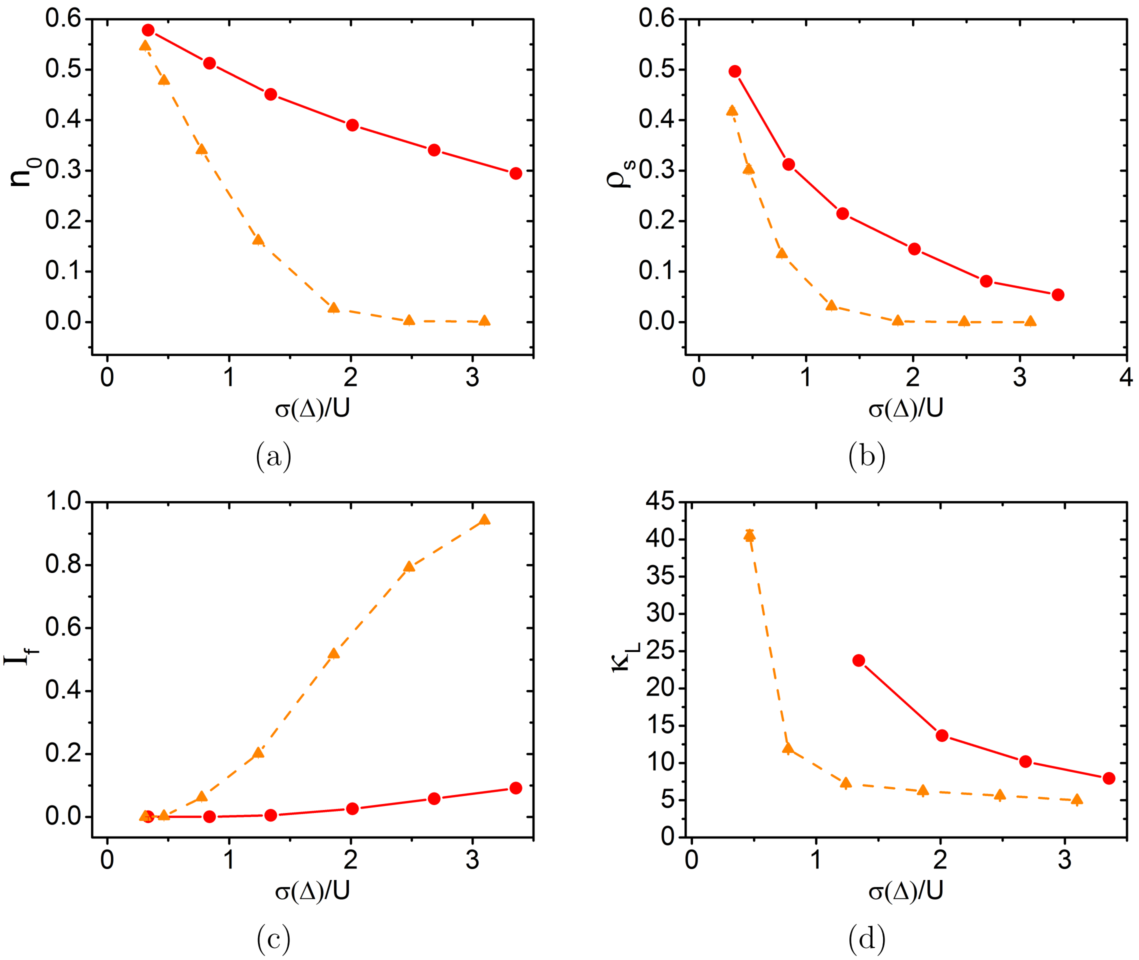

(a) (b) (c) (d)

Figure 9.6: Comparison of observables for box disorder (orange triangles and dashed line) and speckle disorder(red circles and solid line) for a $s = 12\ E_R$ system with $N \sim 28000$ particles and same trap curvature $\omega \sim 64$ Hz at scaled inverse temperature of $\beta t = 1.0$. (a)-(b) are global observables for the entire system (a) Condensate fraction (b) Superfluid fraction. (c)-(d) are local observables measured after the identification of domains. (c) Shows the insulator fraction (d) Shows the local compressibility per particle.

$\Delta/U = 0.31$ - 0.46 or $\Delta = 0.09$ to 0.137).

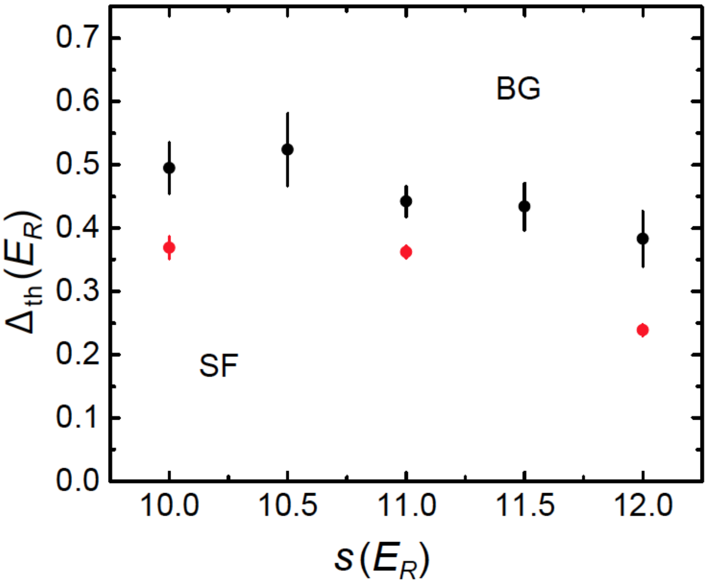

Figure 9.7: Phase boundary between the SF and BG regime for the trapped system. Every point is the result from a piece-wise linear fit to data at fixed s (such as shown in Fig. 9.2 and 9.4, and the error bars show the fit uncertainty. The black squares are the experimentally determined values of Δ_{th} from quench measurements and the red circles are the QMC simulation results.

9.3 Trapped Phase Diagram

The SF–BG phase diagram shown in Fig. (9.7) is constructed by estimating the threshold disorder Δ_{th} for generating excitations in the experiment and for BG to appear in QMC simulations using a piecewise-linear fit to data such as those shown in Fig. (9.4). The fitting function assumes constant behavior for disorder strengths less than Δ_{th}, and Δ_{th} and a slope are left as free parameters for disorder strengths greater than Δ_{th}. Several important features of the phase diagram are evident. The threshold disorder Δ_{th} is weakly dependent on s, and the QMC and experimental results agree within the 40% systematic uncertainty in Δ_0; there are additional systematic and statistical uncertainties arising from finite temperature and disorder averaging (the effect of the latter in minimal). This agreement demonstrates that the quench dynamics leading to production of excitations in this strongly disordered system is sensitive to the ultra-low temperature, (close to) ground-state equilibrium phase properties, and seems to supports the quantum KZ scenario. Furthermore, the observed threshold behavior cannot be explained by an LDA type of approach, which predicts that a BG appears for infinitesimal disorder. Finally, the decrease in Δ_{th} at higher s and smaller t/U, which cannot be accounted for by general single-site classical percolation mechanisms (see Chapter 7), implies that interactions facilitate the transition from SF to BG.

9.4 Dynamical Effects

From the considerations above it seems that the KZ mechanism is able to explain measurements from the quenching method employed in experiments. In essence, it suggests that the quench explores the near-equilibrium dynamics where so long as the time taken for local equilibrium to be reached is small compared to the time-scale associated with the quenching rate, no excitations are produced. As the phase boundary is approached, however, the local equilibration time diverges and local equilibrium is no longer possible. As such, the domains freeze out and appear as long lived topological excitations on the other side of the phase boundary. However, it turns out that this is not the complete picture. Two aspects of the experiment have actually not been addressed. The first one is to do with the initial state of the system during the turn on of the lattice and disorder speckle where an assumption was made about the adiabaticity in the loading of the disordered lattice from the trap. From considerations in Chapter 6, it has been explicitly seen that even for the simple case of the clean system, adiabaticity is not achieved during the load and leads to metastability of the condensate [12]. Therefore, it is unclear whether the initial state of the system in the disordered system corresponds to any state like the equilibrium BG. The second aspect pertains to the equilibration time-scales in the disordered BG phase as the system is quenched. Recall that the KZ mechanism relies on the maintenance of adiabaticity in the system as it is quenched, with possible exception only in the impulse regime near the equilibrium phase boundary.

The first question is an open one and is hard to address at the present moment. Unlike clean systems, no analytical theory such as the HFBP theory exists to lend insight into the relaxation processes. However, it can perhaps be addressed via the route used to explore the second question raised above. In the KZ scenario for clean systems, the amount of excitation and heat produced during a quantum quench typically displays power-law dependence on the quench time [138]. The knowledge of how this changes in disordered systems is limited to one-dimensional spin chains, which show logarithmic behavior [139, 140]. In the experiments considered here, the dependence of $\tilde{\chi}^2$ on the quench time τ_q when the SF-BG boundary is crossed is too weak to detect. Typical data are shown in Fig (9.8a) at $s = 10\ E_R$ for the SF domain at a disorder strength just below Δ_{th} ($\Delta_0 = 0.35\ E_R$) and for the BG regime ($\Delta_0 = 1\ E_R$).

To avoid complications from decay of excitations during the quench, the amount of excitation is determined by measuring the temperature (T) of the gas after allowing rethermal-

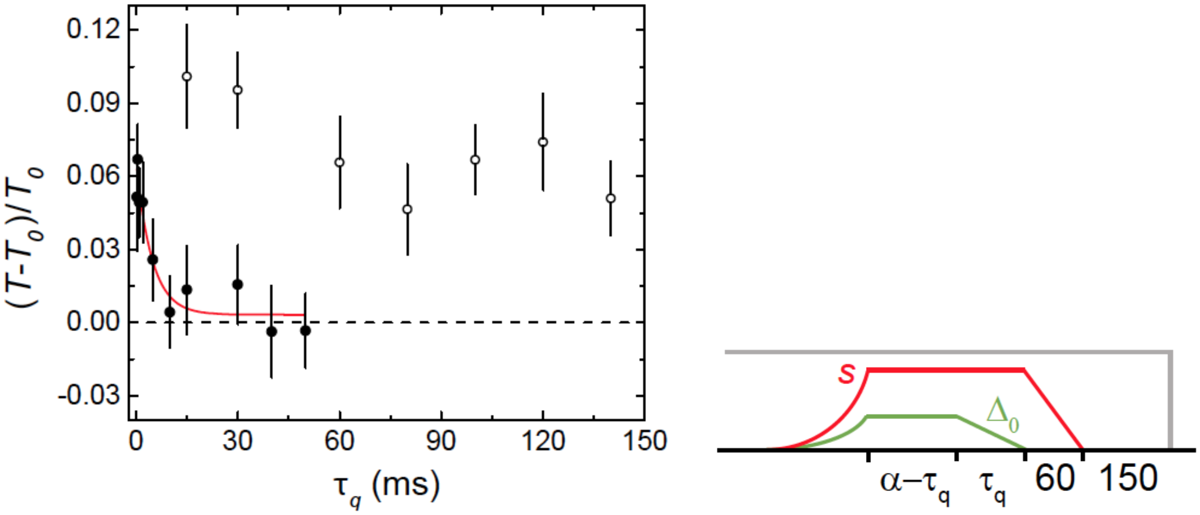

(a) (b)

Figure 9.8: (a) Fractional change in temperature of gas after quenches with different quench times τ_q. The filled circles are for the SF phase with $\Delta_0 = 0.35\ E_R$, which is smaller than the threshold disorder Δ_{th}. The open circles are for $\Delta_0 = 1\ E_R$, which is greater than Δ_{th} and corresponds to the BG regime. The error bars shown the standard error in the mean for the 8–15 measurements averaged for each point. The solid line is a fit to an exponential decay. (b) Timing used for dynamics measurement. The lattice potential (red) is on for a fixed time α, and the quench time τ_q of the disorder potential (green) is varied. After the quench, the lattice is ramped off in 60 ms, and the atoms are allowed to thermalize in the trap (gray) for 150 ms. For the data shown in (a), $\alpha = 45$ ms for $\Delta = 0.35\ E_R$, and $\alpha = 150$ ms for $\Delta = 1\ E_R$.

ization in the trap for 150 ms. This procedure entails the measurement of the condensate fraction using TOF imaging at the end of a slow turn-off of the lattice over 60 ms and 150 ms thermalization time in the trap. The procedure is shown in Fig. (9.8b). The condensate fraction is then inverted to T using the semi-ideal model. Note that exact temperature is not so important, what is relevant is the fractional deviation in the temperature $(T - T_0)/T_0$, shown in Fig. (9.8a), where T_0 is the temperature of the gas without disorder applied. This measure also normalizes heating from the lattice laser light. For the SF domain, a characteristic timescale for excitations to occur is evident. The data fit well to a decaying exponential function with a time constant 4.4 ± 1.6 ms. Quenches with τ_q much longer than this time do not produce excitation. In contrast, in the BG regime, an adiabatic timescale is absent for τ_q up to 140 ms, which is approximately an order of magnitude longer than the tunneling time $h/t \sim 15$ ms, which is the slowest microscopic timescale present in the DBHM Hamiltonian. Larger τ_q cannot be explored because heating from the lattice light results in a loss of the signal-to-noise ratio.

The emergence of an equilibration time much longer than microscopic timescales is reminiscent of glassy behavior in classical disordered systems [141]. Our understanding of dynamics in the DBHM for two and three dimensions is limited [142], since direct simulation is intractable for experimentally relevant numbers of particles. Whether the long timescale observed in the BG phase in this experiment is associated with critical phenomena or if is is connecting solely with disorder-induced glassiness is thus an open question. More work, such as measurements of how correlations change during the quench [143], is needed to clarify how the KZ scenario is altered by disorder.

9.5 Concluding Remarks

This chapter used two very different methods to probe the SF-BG phase boundary in the quantum disordered problem encapsulated by the the disordered Bose-Hubbard model. Within the systematic uncertainty in experiments, excellent agreement was obtained for the phase boundary corresponding to trapped systems. It was explicitly shown that the speckle distribution in an important contributor to the location of the boundary and additionally, the trap plays a vital role in explaining the threshold type of behavior seen in these finite size systems. However, there are also many puzzling aspects to this apparent agreement.

Despite the prevalence of disorder in quantum matter, little is known about how disorder influences non-equilibrium dynamics and affects the KZ paradigm in closed quantum systems [144]. Understanding dynamic and non-equilibrium properties of disordered quantum materials is of paramount importance to applications such as quantum annealing of disordered spin systems to benchmark adiabatic quantum computing [145]. It is unclear whether the KZ paradigm applies in these systems, since it requires adiabatic timescales during most of the quench. While it is clear that the BG domain does not relax even for time scales of an order of magnitude larger than the microscopic time scales, the relaxation time might still not correspond to the age of the system [141], i.e., the behavior might be entirely different from those expected in traditional glassy systems.

Unfortunately, quantum glasses is just as poorly understood. The little that is known is in the context of 1D disordered transverse field Ising model – one of the few examples of quantum glasses that are accessible to experiments and theory [146, 147]. However, there are reasons to suspect that the BG state is also in the same class of systems. Standard Monte-Carlo techniques exhibit the same problems of slowing down associated with classical glassy problems [59]. Although modern Monte-Carlo methods, such as the SSE algorithm that uses non-local forms of update used in this dissertation, essentially circumvents this problem [121], signatures of glassy behavior are actually still present. For instance the at a given U/t, as disorder is increased the operator string length in the SSE formalism (see Chapter 3) increases, indicating that essential dynamics that describe the state of the system take a long time to happen. Strictly speaking, the connection between slowing down in Markov processes, such as those describing QMC, and real-time dynamics is not at all obvious. In fact they may not be related at all. However, this is not what is being alluded to here. The configuration of the paths in the worldline picture does contain all the information that is pertinent to the equilibrium state – both dynamic and static. Thus, when the operator string length increases such that there are large sectors in imaginary time that are devoid of any kinetic hops then this does point to real features of the actual state. In essence, given that imaginary time is proportional to the propagation levels, the configuration space points out to the fact that the essential dynamics of the system take a long time to occur. Additionally the paths are strongly clustered with little or no exchanges taking place between different SF puddle areas. (More in-depth studies will need to be conducted to explore this connection more rigorously.)

It is, thus, quite remarkable that despite such glassy behavior the dynamical phase boundary accessed by experiments is (within error bars) coincidental with or, at the very least, close to the equilibrium phase diagram. There is no *a priori* reason to believe that the dynamical phase boundary has to be anywhere near the equilibrium boundary [141]. (In fact, there may not be any connection between the properties of the dynamical state and the equilibrium phases and, therefore, there may not even be a dynamical phase boundary!) In any event, future experiments will undoubtedly need to be able to measure unequal time correlators or time-dependent susceptibilities. These should reveal whether the phenomena in this type of quantum disordered system correspond to the typical phenomena seen in glassy systems, such as aging [141, 146].

In either case, whether it be in understanding quantum KZ mechanisms in the presence of disorder or quantum glassy phenomena, the DBHM might be one of the few 3D disordered systems that is accessible to both theory and experiment. The dissertation has developed tools that has revealed a broad range of equilibrium phenomena associated with this fascinating system. Hopefully, having demystified some of the essential equilibrium properties of such systems, deviations from it will lend insight into the dynamical aspects of the system.

Part IV

Appendix

Appendix A

The Density Matrix

The idea of the density matrix originates in the formulation of Quantum Statistics as a way of studying the general properties of a system as it evolves in time *independent* of the details of the initial conditions. Towards this end we think of an *ensemble* of $\mathscr{N}$ systems that subscribe to the same Hamiltonian $\hat{\mathscr{H}}$. At time t, let the state of any system k in the ensemble be given by $|\Psi^k(t)\rangle$. Then the evolution of the system must satisfy the Schrödinger equation:

$$\hat{\mathscr{H}}|\Psi^k(t)\rangle = i\hbar\frac{\partial|\Psi^k(t)\rangle}{\partial t} \tag{A.1}$$

Introducing a complete set of basis states $\{|\psi_n\rangle\}$ and time-dependent coefficients $a_n^k(t)$, we can express the state of a system as a liner superposition of weighted basis states:

$$|\Psi^k(t)\rangle = \sum_n a_n^k(t)|\phi_n\rangle \tag{A.2}$$

where

$$a_n^k(t) = \langle\phi_n|\Psi^k(t)\rangle, \tag{A.3}$$

represent the time varying *probability amplitudes* for a system to be in a particular state $|\phi_n\rangle$. It must satisfy $\sum_n |a_n^k(t)|^2 = 1$ for all k. We can reformulate Schrödinger equation in terms of the time-dependent coefficients, by inserting (A.2) into (A.1)

$$\begin{aligned} i\hbar\frac{da_n^k(t)}{dt} &= \langle\phi_n|\hat{\mathscr{H}}|\Psi^k(t)\rangle \\ &= \langle\phi_n|\hat{\mathscr{H}}\left\{\sum_m a_m^k(t)|\phi_m\rangle\right\} \\ &= \sum_m \langle\phi_n|\hat{\mathscr{H}}|\phi_m\rangle a_m^k(t) \\ &= \sum_m H_{nm}a_m^k(t) \qquad \text{(A.4)} \end{aligned}$$

Note that $\{a_m^k(t)\}$ are different for each system in the ensemble since they don't all necessarily have to start with the same initial conditions. Indeed, as we explained before we need a description for the system that averages over all such possible descriptions. Towards this end, we define the density operator $\hat{\rho}(t) \equiv \sum_{n,m}|n\rangle\rho_{nm}(t)\langle m|$, with matrix elements given by,

$$\rho_{mn}(t) \equiv \frac{1}{\mathscr{N}}\sum_{k=1}^{\mathscr{N}} a_m^k(t)a_n^{k*}(t). \qquad \text{(A.5)}$$

The evolution of the density matrix is then given by,

$$\begin{aligned} i\hbar\frac{d\rho_{nm}(t)}{dt} &= \frac{1}{\mathscr{N}}\sum_{k=1}^{\mathscr{N}}\left[i\hbar\left\{\frac{a_n^k(t)}{dt}a_m^{k*}(t) + a_n^k(t)\frac{a_m^{k*}(t)}{dt}\right\}\right] \\ &= \frac{1}{\mathscr{N}}\sum_{k=1}^{\mathscr{N}}\left[\sum_p H_{np}a_p^k(t)a_m^{k*}(t) - \sum_p a_n^k(t)a_p^{k*}(t)H_{mp}^*\right] \\ &= \sum_p \left(H_{np}\rho_{pm}(t) - \rho_{np}(t)H_{pm}\right) \\ &= (\hat{\mathscr{H}}\hat{\rho} - \hat{\rho}\hat{\mathscr{H}})_{nm} \qquad \text{(A.6)} \end{aligned}$$

where we have used the Hermitian property of the Hamiltonian $H_{mp}^* = H_{pm}$. Finally then,

$$i\hbar\frac{d\hat{\rho(t)}}{dt} = [\hat{\mathscr{H}}, \hat{\rho}] \qquad \text{(A.7)}$$

Measuring observables follow directly from the definitions above:

$$\begin{aligned}\langle G\rangle &= \frac{1}{\mathscr{N}}\sum_{k=1}^{\mathscr{N}}\langle\psi^k|G|\psi^k\rangle \\ &= \frac{1}{\mathscr{N}}\sum_{k=1}^{\mathscr{N}}\left[\sum_{m,n}a_n^{k*}a_m^k G_{nm}\right] \\ &= \sum_{m,n}\rho_{mn}G_{nm} = Tr(\hat{\rho}\hat{G}), \qquad \text{(A.8)}\end{aligned}$$

where $\hat{G} \equiv \sum_{nm}\langle\phi_n|\hat{G}|\phi_m\rangle$ and we require $Tr(\hat{\rho}) = 1$, otherwise we must normalize explicitly so that:

$$\langle\hat{G}\rangle = \frac{Tr(\hat{\rho}\hat{G})}{Tr(\hat{\rho})}. \qquad \text{(A.9)}$$

Appendix B

Property of Noisy Eigenvalue Problems

There exists a unitary transformation $\mathcal{U}$ That brings ρ_1 into diagonal form.

$$\tilde{M} = \mathcal{U}^T \left(\hat{\rho} + \bar{G}\right) \mathcal{U} = \hat{\rho}^D + \tilde{G} \tag{B.1}$$

where $\bar{G}$ is noise matrix with variance σ_G, $\hat{\rho}^D$ is the diagonalized Hermitian matrix, and $\tilde{G}$ is the transformed noise matrix.

If the noise is small, we can expand the characteristic equation of $\tilde{M}$ and keep terms up to fourth order in the noise,

$$\tilde{C}(x) \approx \prod_i (e_i - x)\left(1 + \mathcal{G}_1 + \mathcal{G}_2 + \mathcal{G}_3 + O(4)\right) \tag{B.2}$$

$$\mathcal{G}_1 = \sum_j \frac{\tilde{G}_{j,j}}{(e_j - x)} \tag{B.3}$$

$$\mathcal{G}_2 = \sum_{j<k} \frac{\mathrm{Det}\tilde{G}_{i,j}}{(e_j - x)(e_k - x)} \tag{B.4}$$

$$\mathcal{G}_3 = \sum_{j<k<l} \frac{\mathrm{Det}\tilde{G}_{i,j,k}}{(e_j - x)(e_k - x)(e_l - x)} \tag{B.5}$$

with e_i the ith eigenvalue of the exact Hermitian matrix, x is the eigenvalue we are solving for, and the determinants are of submatrices of the noise matrix (i.e $\mathrm{Det}\tilde{G}_{j,k} = \tilde{G}_{j,j}\tilde{G}_{k,k} - \tilde{G}_{j,k}\tilde{G}_{k,j}$).

When we expand x around an exact solution, $x = e_i + \Delta x$ and solve $\tilde{C}(x) = 0$ keeping terms of order zero in Δx and quadratic in the variance, we get an equation for the bias to third order in $(e_k - e_i)^{-1}$. Keeping the dominant terms gives the form of the bias as,

$$\Delta x \;=\; -\sum_{k \neq i} \frac{\tilde{G}_{i,k}\tilde{G}_{k,i}}{(e_k - e_i)} + \frac{(\mathrm{Det}\tilde{G}_{i,k})^2}{(e_k - e_i)^3}. \tag{B.6}$$

The first term is linear in the variance of the noise matrix elements and spreads the eigenvalue spectrum, the second term is quadratic in the noise term and compresses the spectrum. When the ρ_1 matrix is symmetrized the first term becomes much larger because $\tilde{G}_{i,k} = \tilde{G}_{k,i}$. When the noise in the matrix elements becomes sufficiently large the eigenvalue offsets are a small perturbation to the matrix and it obeys the same eigenvalue distribution as a gaussian random matrix.[1]

---

[1] These deviations were due to Jeremy McMinis [46].

Appendix C

Bogoliubov Transformation

The Bogoliubov transformation is concerned with diagonalizing Hamiltonians of the form:

$$\hat{H} = \epsilon_0(\hat{a}^\dagger \hat{a} + \hat{b}^\dagger \hat{b}) + \epsilon_1(\hat{a}^\dagger \hat{b}^\dagger + \hat{a}\hat{b}) \tag{C.1}$$

The transformation starts with casting the operators in the following form:

$$\begin{aligned} \hat{\alpha} &= u\hat{a} + v\hat{b}^\dagger \\ \hat{\beta} &= u\hat{b} + v\hat{a}^\dagger \end{aligned} \tag{C.2}$$

The inverse transformation is:

$$\begin{aligned} \hat{a} &= u\hat{\alpha} - v\hat{\beta}^\dagger \\ \hat{b} &= u\hat{\beta} - v\hat{\alpha}^\dagger. \end{aligned} \tag{C.3}$$

Using Bose commutation relations $[\hat{\alpha}, \hat{\alpha}^\dagger] = [\hat{\beta}, \hat{\beta}^\dagger] = 1$,

$$u^2 - v^2 = 1, \tag{C.4}$$

and the Hamiltonian gets transformed to:

$$\begin{aligned} \hat{H} = 2v^2\epsilon_0 - 2uv\epsilon_1 &+ [\epsilon_0(u^2 + v^2) - 2uv\epsilon_1](\hat{\alpha}^\dagger \hat{\alpha} + \hat{\beta}^\dagger \hat{\beta}) \\ &+ [\epsilon_1(u^2 + v^2) - 2uv\epsilon_0](\hat{\alpha}\hat{\beta} + \hat{\beta}^\dagger \hat{\alpha}^\dagger) \end{aligned} \tag{C.5}$$

The appropriate choice for u and v is given by:

$$\epsilon_1(u^2 + v^2) - 2uv\epsilon_0 = 0 \tag{C.6}$$

Let $u = \cosh(t)$, $v = \sinh(t)$, so that:

$$\begin{aligned} &\epsilon_1(\cosh^2(t) + \sinh^2(t)) - 2\epsilon_0 \sinh(t)\cosh(t) = 0 \\ &\implies \tanh(2t) = \frac{\epsilon_1}{\epsilon_0} \end{aligned} \tag{C.7}$$

Finally, with $\epsilon \equiv \sqrt{\epsilon_0^2 - \epsilon_1^2}$

$$\begin{aligned} u^2 &= \frac{1}{2}\left(\frac{\epsilon_0}{\epsilon} + 1\right) \\ v^2 &= \frac{1}{2}\left(\frac{\epsilon_0}{\epsilon} - 1\right) \end{aligned} \tag{C.8}$$

so that $u^2 + v^2 = \frac{\epsilon_0}{\epsilon}$ and $uv = \frac{1}{2}\frac{\epsilon_1}{\epsilon}$, and the Hamiltonian becomes:

$$\hat{H} = \epsilon\left(\hat{\alpha}^\dagger\hat{\alpha} + \hat{\beta}^\dagger\hat{\beta}\right) + \epsilon - \epsilon_0 \tag{C.9}$$

Generally particle number constraints require the conservation of:

$$\begin{aligned} \hat{a}^\dagger\hat{a} &= (u\hat{\alpha}^\dagger - v\hat{\beta})(u\hat{\alpha} - v\hat{\beta}^\dagger) \\ &= u^2\hat{\alpha}^\dagger\hat{\alpha} + v^2\hat{\beta}\hat{\beta}^\dagger - uv(\hat{\alpha}^\dagger\hat{\beta}^\dagger + \hat{\alpha}\hat{\beta}) \\ &= u^2\hat{\alpha}^\dagger\hat{\alpha} + v^2\hat{\beta}^\dagger\hat{\beta} + v^2 - uv(\hat{\alpha}^\dagger\hat{\beta}^\dagger + \hat{\alpha}\hat{\beta}) \end{aligned} \tag{C.10}$$

So that taking a weighted average due to the trace operation with a density matrix (say):

$$\langle\hat{a}^\dagger\hat{a}\rangle = u^2\langle\hat{\alpha}^\dagger\hat{\alpha}\rangle + v^2\langle\hat{\beta}^\dagger\hat{\beta}\rangle + v^2 - uv(\langle\hat{\alpha}^\dagger\hat{\beta}^\dagger\rangle + \langle\hat{\alpha}\hat{\beta}\rangle) \tag{C.11}$$

Appendix D

Bibliography

[1] M. H. Anderson, J. R. Ensher, M. R. Matthews, C. E. Wieman, and E. A. Cornell. Observation of bose-einstein condensation in a dilute atomic vapor. *Science*, 269(5221):198–201, 1995.

[2] K. B. Davis, M. O. Mewes, M. R. Andrews, N. J. van Druten, D. S. Durfee, D. M. Kurn, and W. Ketterle. Bose-einstein condensation in a gas of sodium atoms. *Phys. Rev. Lett.*, 75:3969–3973, Nov 1995.

[3] C. C. Bradley, C. A. Sackett, J. J. Tollett, and R. G. Hulet. Evidence of bose-einstein condensation in an atomic gas with attractive interactions. *Phys. Rev. Lett.*, 75:1687–1690, Aug 1995.

[4] B. DeMarco and D. S. Jin. Onset of fermi degeneracy in a trapped atomic gas. *Science*, 285(5434):1703–1706, 1999.

[5] B. DeMarco, S. B. Papp, and D. S. Jin. Pauli blocking of collisions in a quantum degenerate atomic fermi gas. *Phys. Rev. Lett.*, 86:5409–5412, Jun 2001.

[6] Andrew G. Truscott, Kevin E. Strecker, William I. McAlexander, Guthrie B. Partridge, and Randall G. Hulet. Observation of fermi pressure in a gas of trapped atoms. *Science*, 291(5513):2570–2572, 2001.

[7] Takeshi Fukuhara, Yosuke Takasu, Mitsutaka Kumakura, and Yoshiro Takahashi. Degenerate fermi gases of ytterbium. *Phys. Rev. Lett.*, 98:030401, Jan 2007.

[8] M Greiner, C A Regal, and D S Jin. Emergence of a molecular Bose–Einstein condensate from a Fermi gas. *Nature*, 426(6966):537–540, 2003.

[9] M Greiner, C Regal, and D Jin. Probing the Excitation Spectrum of a Fermi Gas in the BCS-BEC Crossover Regime. *Physical Review Letters*, 94(7):070403–4, February 2005.

[10] Markus Greiner, Olaf Mandel, Tilman Esslinger, Theodor W Hansch, and Immanuel Bloch. Quantum phase transition from a superfluid to a Mott insulator in a gas of ultracold atoms. *Nature*, 415(6867):39–44, 2002.

[11] L Fallani, J Lye, V Guarrera, C Fort, and M Inguscio. Ultracold Atoms in a Disordered Crystal of Light: Towards a Bose Glass. *Physical Review Letters*, 98(13):130404, March 2007.

[12] M McKay, U Ray, Stefan Natu, Philip Russ, David Ceperley, and Brian DeMarco. Metastable Bose-Einstein condensation in a strongly correlated optical lattice. *Physical Review A*, 00(003600):003600–12, February 2015.

[13] Y J Lin, K Jiménez-García, and I B Spielman. Spin-orbit-coupled Bose-Einstein condensates. *Nature*, 470(7336):83–86, February 2011.

[14] Kenneth Günter, Thilo Stöferle, Henning Moritz, Michael Köhl, and Tilman Esslinger. Bose-fermi mixtures in a three-dimensional optical lattice. *Phys. Rev. Lett.*, 96:180402, May 2006.

[15] Immanuel Bloch. Ultracold quantum gases in optical lattices. *Nature Physics*, 1(1):23–30, October 2005.

[16] Immanuel Bloch, Jean Dalibard, and Sylvain Nascimbène. Quantum simulations with ultracold quantum gases. *Nature Physics*, 8(4):267–276, April 2012.

[17] Georges Aad, T Abajyan, B Abbott, J Abdallah, S Abdel Khalek, AA Abdelalim, O Abdinov, R Aben, B Abi, M Abolins, et al. Observation of a new particle in the search for the standard model higgs boson with the atlas detector at the lhc. *Physics Letters B*, 716(1):1–29, 2012.

[18] David Griffiths. *Introduction to elementary particles.* John Wiley & Sons, 2008.

[19] Anthony James Leggett. *Quantum liquids: Bose condensation and Cooper pairing in condensed-matter systems.* Oxford University Press, 2006.

[20] J. Bardeen, L. N. Cooper, and J. R. Schrieffer. Theory of superconductivity. *Phys. Rev.*, 108:1175–1204, Dec 1957.

[21] S. Trotzky, L. Pollet, F. Gerbier, U. Schnorrberger, I. Bloch, N.V. Prokof'ev, B. Svistunov, and M. Troyer. Suppression of the critical temperature for superfluidity near the Mott transition. *Nature Physics*, 6:998, 2010.

[22] Elihu Abrahams. *50 years of Anderson Localization.* World Scientific, 2010.

[23] D M Basko, I L Aleiner, and B L Altshuler. Metal–insulator transition in a weakly interacting many-electron system with localized single-particle states. *Annals of Physics*, 321(5):1126–1205, May 2006.

[24] Arijeet Pal and David A Huse. Many-body localization phase transition. *Physical Review B*, 82(17):174411, November 2010.

[25] T. Vojta. Phases and phase transitions in disordered quantum systems. In A. Avella and F. Mancini, editors, *American Institute of Physics Conference Series*, volume 1550 of *American Institute of Physics Conference Series*, pages 188–247, August 2013.

[26] Matthew PA Fisher, Peter B Weichman, G Grinstein, and Daniel S Fisher. Boson localization and the superfluid-insulator transition. *Physical Review B*, 40(1):1–25, July 1989.

[27] Leonardo Fallani, Chiara Fort, and Massimo Inguscio. Bose–Einstein Condensates in Disordered Potentials. pages 119–160. Elsevier, 2008.

[28] Richard Phillips Feynman, Albert R Hibbs, and Daniel F Styer. *Quantum mechanics and path integrals: Emended edition.* Dover Publications, 2005.

[29] EL Pollock and DM Ceperley. Simulation of quantum many-body systems by path-integral methods. *Physical Review B*, 30(5):2555–2568, 1984.

[30] N. Goldenfeld. *Lectures on Phase Transitions and the Renormalization Group.* Frontiers in physics. Addison-Wesley, Advanced Book Program, 1992.

[31] C. Meldgin, U. Ray, P. Russ, D. Ceperley, and B. DeMarco. Probing the Bose-Glass–Superfluid Transition using Quantum Quenches of Disorder. *ArXiv e-prints*, February 2015.

[32] M.H. Kalos and P.A. Whitlock. *Monte Carlo Methods.* Wiley, 2008.

[33] E.J. Newman and G.T. Barkema. *Monte Carlo Methods in Statistical Physics.* Clarendon Press, 1999.

[34] Makoto Matsumoto and Takuji Nishimura. Mersenne twister: A 623-dimensionally equidistributed uniform pseudo-random number generator. *ACM Trans. Model. Comput. Simul.*, 8(1):3–30, January 1998.

[35] Nicholas Metropolis, Arianna W. Rosenbluth, Marshall N. Rosenbluth, Augusta H. Teller, and Edward Teller. Equation of state calculations by fast computing machines. *The Journal of Chemical Physics*, 21(6):1087–1092, 1953.

[36] Anders W. Sandvik. Stochastic series expansion method with operator-loop update. *Phys. Rev. B*, 59:R14157–R14160, Jun 1999.

[37] Olav F. Syljuåsen and Anders W. Sandvik. Quantum monte carlo with directed loops. *Phys. Rev. E*, 66:046701, Oct 2002.

[38] Matthias Troyer and Uwe-Jens Wiese. Computational Complexity and Fundamental Limitations to Fermionic Quantum Monte Carlo Simulations. *Physical Review Letters*, 94(17):170201, May 2005.

[39] Fabien Alet, Stefan Wessel, and Matthias Troyer. Generalized directed loop method for quantum monte carlo simulations. *Phys. Rev. E*, 71:036706, Mar 2005.

[40] E. L. Pollock and D. M. Ceperley. Path-integral computation of superfluid densities. *Phys. Rev. B*, 36:8343–8352, Dec 1987.

[41] V G Rousseau. Superfluid density in continuous and discrete spaces: Avoiding misconceptions. *Physical Review B*, 90(13):134503, October 2014.

[42] Yongkyung Kwon, Francesco Paesani, and K Whaley. Local superfluidity in inhomogeneous quantum fluids. *Physical Review B*, 74(17):174522, November 2006.

[43] Fabien Alet, Stefan Wessel, and Matthias Troyer. Generalized directed loop method for quantum Monte Carlo simulations. *Physical Review E*, 71(3):036706, March 2005.

[44] Oliver Penrose and Lars Onsager. Bose-einstein condensation and liquid helium. *Phys. Rev.*, 104:576–584, Nov 1956.

[45] David M. Ceperley. Path integrals in the theory of condensed helium. *Reviews of Modern Physics*, 67(2):279–355, 1995.

[46] Ushnish Ray, Fei Lin, Jeremy McMinis, and David M. Ceperley. Extracting the Condensate Fraction from the Single Particle Density Matrix. *Unpublished*, 2010.

[47] G. W. Stewart. *Matrix Algorithms Volume II: Eigensystems.* SIAM, 2001.

[48] Yang C. Lehoucq R. B., Sorensen D. C. Arpack users' guide: Solution of large scale eigenvalue problems with implicitly restarted arnoldi methods, 1997.

[49] David M. Ceperley and P. H. Acioli. . *Journal of Chemical Physics*, 100(8169), 1994.

[50] R.P. Feynman. *Statistical Mechanics: A Set Of Lectures.* Advanced Books Classics Series. Westview Press, 1998.

[51] S Q Zhou and D M Ceperley. Construction of localized wave functions for a disordered optical lattice and analysis of the resulting Hubbard model parameters. *Physical Review A*, 81(1):013402, January 2010.

[52] G. Grosso and G.P. Parravicini. *Solid State Physics.* Elsevier Science, 2013.

[53] G.D. Mahan. *Condensed Matter in a Nutshell.* In a Nutshell. Princeton University Press, 2011.

[54] R.M. Martin. *Electronic Structure: Basic Theory and Practical Methods.* Cambridge University Press, 2004.

[55] M.P. Marder. *Condensed Matter Physics.* Wiley, 2010.

[56] M Pasienski, D McKay, M White, and B DeMarco. A disordered insulator in an optical lattice. *Nature Physics*, 6(9):677–680, July 2010.

[57] L Pollet, N Prokof'ev, B Svistunov, and M Troyer. Absence of a Direct Superfluid to Mott Insulator Transition in Disordered Bose Systems. *Physical Review Letters*, 103(14):140402, September 2009.

[58] Ulf Bissbort, Ronny Thomale, and Walter Hofstetter. Stochastic mean-field theory: Method and application to the disordered Bose-Hubbard model at finite temperature and speckle disorder. *Physical Review A*, 81(6):063643, June 2010.

[59] Werner Krauth, Nandini Trivedi, and David Ceperley. Superfluid-insulator transition in disordered boson systems. *Phys. Rev. Lett.*, 67:2307–2310, Oct 1991.

[60] N.J. Higham. *Functions of Matrices: Theory and Computation.* Society for Industrial and Applied Mathematics, 2008.

[61] C.J. Pethick and H. Smith. *Bose-Einstein Condensation in Dilute Gases.* Cambridge University Press, 2008.

[62] X Zhang, C L Hung, S K Tung, and C Chin. Observation of Quantum Criticality with Ultracold Atoms in Optical Lattices. *Science*, 335(6072):1070–1072, March 2012.

[63] J. M. Deutsch. Quantum statistical mechanics in a closed system. *Phys. Rev. A*, 43:2046–2049, Feb 1991.

[64] Mark Srednicki. Chaos and quantum thermalization. *Physical Review E*, 50(2):888, 1994.

[65] Marcos Rigol, Vanja Dunjko, and Maxim Olshanii. Thermalization and its mechanism for generic isolated quantum systems. *Nature*, 481(7380):224–224, 2012.

[66] Ana Maria Rey, Keith Burnett, Robert Roth, Mark Edwards, Carl J Williams, and Charles W Clark. Bogoliubov approach to superfluidity of atoms in an optical lattice. *J. Phys. B*, 36:825, 2003.

[67] I.B. Spielman, W.D. Phillips, and J.V. Porto. Condensate fraction in a 2d Bose gas measured across the Mott-Insulator transition. *Phys. Rev. Lett.*, 100:120402, 2008.

[68] Christopher Gaul and Cord A Müller. Bogoliubov theory on the disordered lattice. *The European Physical Journal Special Topics*, 217(1):69–78, 2013.

[69] M. White, M. Pasienski, D. McKay, S. Q. Zhou, D. Ceperley, and B. DeMarco. Strongly interacting bosons in a disordered optical lattice. *Phys. Rev. Lett.*, 102:055301, Feb 2009.

[70] Henk TC Stoof, Koos B Gubbels, and Dennis BM Dickerscheid. *Ultracold quantum fields*, volume 1. Springer, 2009.

[71] G.-D. Lin, Wei Zhang, and L.-M. Duan. Characteristics of bose-einstein condensation in an optical lattice. *Phys. Rev. A*, 77:043626, Apr 2008.

[72] A. Griffin. Conserving and gapless approximations for an inhomogeneous bose gas at finite temperatures. *Phys. Rev. B*, 53:9341–9347, Apr 1996.

[73] Franco Dalfovo, Stefano Giorgini, Lev P Pitaevskii, and Sandro Stringari. Theory of Bose-Einstein condensation in trapped gases. *Reviews of Modern Physics*, 71(3):463–512, April 1999.

[74] Shunji Tsuchiya and Allan Griffin. Damping of bogoliubov excitations in optical lattices. *Phys. Rev. A*, 70:023611, Aug 2004.

[75] K. Sheshadri, H.R. Krishnamurthy, R. Pandit, and T.V. Ramakrishnan. Superfluid and insulating phases in an interacting-boson model: Mean-field theory and the rpa. *Europhys. Lett.*, 22:257, 1993.

[76] A.L. Fetter and J.D. Walecka. *Quantum theory of many-particle systems.* International series in pure and applied physics. McGraw-Hill, 1971.

[77] W. Yi, G.-D. Lin, and L.-M. Duan. Signal of bose-einstein condensation in an optical lattice at finite temperature. *Phys. Rev. A*, 76:031602, Sep 2007.

[78] Ana Maria Rey, Guido Pupillo, Charles W. Clark, and Carl J. Williams. Ultracold atoms confined in an optical lattice plus parabolic potential: A closed-form approach. *Phys. Rev. A*, 72:033616, Sep 2005.

[79] P Buonsante, V Penna, A Vezzani, and P Blakie. Mean-field phase diagram of cold lattice bosons in disordered potentials. *Physical Review A*, 76(1):011602, July 2007.

[80] M. R. White. Ultracold atoms in disordered optical lattice. 2009.

[81] J. Szczepkowski, R. Gartman, M. Witkowski, L. Tracewski, M. Zawada, and W. Gawlik. Analysis and calibration of absorptive images of Bose-Einstein condensate at nonzero temperatures. *Rev. Sci. Instrum.*, 80:053103, 2009.

[82] M. Naraschewski and D. M. Stamper-Kurn. Analytical description of a trapped semi-ideal bose gas at finite temperature. *Phys. Rev. A*, 58:2423–2426, Sep 1998.

[83] Stefan S. Natu, David C. McKay, Brian DeMarco, and Erich J. Mueller. Evolution of condensate fraction during rapid lattice ramps. *Phys. Rev. A*, 85:061601, Jun 2012.

[84] D. McKay, M. White, and B. DeMarco. Lattice thermodynamics for ultracold atoms. *Phys. Rev. A*, 79:063605, 2009.

[85] F. Gerbier, J. H. Thywissen, S. Richard, M. Hugbart, P. Bouyer, and A. Aspect. Experimental study of the thermodynamics of an interacting trapped Bose-Einstein condensed gas. *Phys. Rev. A*, 70:013607, 2004.

[86] B. D. Busch, Chien Liu, Z. Dutton, C. H. Behroozi, and L. Vestergaard Hau. Observation of interaction dynamics in finite-temperature Bose condensed atom clouds. *Europhys. Lett.*, 51:485, 2000.

[87] M Zawada, R Abdoul, J Chwedenczuk, R Gartman, J Szczepkowski, L Tracewski, M Witkowski, and W Gawlik. Free-fall expansion of finite-temperature Bose-Einstein condensed gas in the non-Thomas-Fermi regime. *J. Phys. B*, 41:241001, 2008.

[88] Joern N. Kupferschmidt and Erich J. Mueller. Role of interactions in time-of-flight expansion of atomic clouds from optical lattices. *Phys. Rev. A*, 82:023618, Aug 2010.

[89] F. Gerbier, S. Trotzky, S. Fölling, U. Schnorrberger, J. D. Thompson, A. Widera, I. Bloch, L. Pollet, M. Troyer, B. Capogrosso-Sansone, N. V. Prokof'ev, and B. V. Svistunov. Expansion of a quantum gas released from an optical lattice. *Phys. Rev. Lett.*, 101:155303, Oct 2008.

[90] Ushnish Ray and David M Ceperley. Revealing the condensate and noncondensate distributions in the inhomogeneous Bose-Hubbard model. *Physical Review A*, 87(5):051603, May 2013.

[91] V. A. Kashurnikov, N. V. Prokof'ev, and B. V. Svistunov. Revealing the superfluid˘mott-insulator transition in an optical lattice. *Phys. Rev. A*, 66:031601, Sep 2002.

[92] Stefan Wessel, Fabien Alet, Matthias Troyer, and G. George Batrouni. Quantum Monte Carlo simulations of confined bosonic atoms in optical lattices. *Phys. Rev. A*, 70:053615, 2004.

[93] Massimo Campostrini and Ettore Vicari. Critical Behavior and Scaling in Trapped Systems. *Physical Review Letters*, 102(24):240601, June 2009.

[94] B. Efron and R.J. Tibshirani. *An Introduction to the Bootstrap*. Chapman & Hall/CRC Monographs on Statistics & Applied Probability. Taylor & Francis, 1994.

[95] Markus Greiner, Immanuel Bloch, Olaf Mandel, Theodor W. Hänsch, and Tilman Esslinger. Exploring phase coherence in a 2d lattice of bose-einstein condensates. *Phys. Rev. Lett.*, 87:160405, 2001.

[96] Y. B. Band, Marek Trippenbach, J. P. Burke, and P. S. Julienne. Elastic scattering loss of atoms from colliding bose-einstein condensate wave packets. *Phys. Rev. Lett.*, 84:5462, 2000.

[97] Yasuyuki Kato, Qi Zhou, Naoki Kawashima, and Nandini Trivedi. Sharp peaks in the momentum distribution of bosons in optical lattices in the normal state. *Nature Physics*, 4:617, 2008.

[98] Roberto B. Diener, Qi Zhou, Hui Zhai, and Tin-Lun Ho. Criterion for bosonic superfluidity in an optical lattice. *Phys. Rev. Lett.*, 98:180404, 2007.

[99] Lode Pollet, Corinna Kollath, Kris Van Houcke, and Matthias Troyer. Temperature changes when adiabatically ramping up an optical lattice. *New. J. Phys.*, 10:065001, 2008.

[100] Fabrice Gerbier, Simon Fölling, Artur Widera, and Immanuel Bloch. Visibility of a Bose-condensed gas released from an optical lattice at finite temperatures. 2007.

[101] G.-D. Lin, Wei Zhang, and L.-M. Duan. Characteristics of Bose-Einstein condensation in an optical lattice. *Phys. Rev. A*, 77:043626, 2008.

[102] D C McKay and B DeMarco. Cooling in strongly correlated optical lattices: prospects and challenges. *Rep. Prog. Phys.*, 74(5):054401, 2011.

[103] Stefan S. Natu, Kaden R. A. Hazzard, and Erich J. Mueller. Local versus global equilibration near the bosonic mott-insulator˘superfluid transition. *Phys. Rev. Lett.*, 106:125301, Mar 2011.

[104] T Nikuni, E Zaremba, and A Griffin. Two-fluid dynamics for a Bose-Einstein condensate out of local equilibrium with the noncondensate. *Phys. Rev. Lett.*, 83(1):10–13, 1999.

[105] J. E. Williams and A. Griffin. Damping of condensate collective modes due to equilibration with the noncondensate. *Phys. Rev. A*, 63:023612, Jan 2001.

[106] Shunji Tsuchiya and Allan Griffin. Landau damping of bogoliubov excitations in two- and three-dimensional optical lattices at finite temperatures. *Phys. Rev. A*, 72:053621, Nov 2005.

[107] U Bissbort and W Hofstetter. Stochastic mean-field theory for the disordered Bose-Hubbard model. *EPL (Europhysics Letters)*, 86(5):50007, June 2009.

[108] A B Harris. Effect of random defects on the critical behaviour of ising models. *Journal of Physics C: Solid State Physics*, 7(9):1671, 1974.

[109] J T Chayes, L Chayes, Daniel S Fisher, and T Spencer. Finite-size scaling and correlation lengths for disordered systems. *Physical Review Letters*, 57(24):2999, 1986.

[110] Subir Sachdev. *Quantum Phase Transitions.* Cambridge University Press, second edition, 2011. Cambridge Books Online.

[111] W.D. McComb. *Renormalization Methods: A Guide For Beginners.* OUP Oxford, 2003.

[112] Thomas Vojta. Rare region effects at classical, quantum and nonequilibrium phase transitions. *Journal of Physics A: Mathematical and General*, 39(22):R143–R205, May 2006.

[113] Amnon Aharony and A Harris. Absence of Self-Averaging and Universal Fluctuations in Random Systems near Critical Points. *Physical Review Letters*, 77(18):3700–3703, 1996.

[114] Shai Wiseman and Eytan Domany. Finite-Size Scaling and Lack of Self-Averaging in Critical Disordered Systems. *Physical Review Letters*, 81(1):22–25, July 1998.

[115] Zhiyuan Yao, Karine P C da Costa, Mikhail Kiselev, and Nikolay Prokof'ev. Critical Exponents of the Superfluid–Bose-Glass Transition in Three Dimensions. *Physical Review Letters*, 112(22):225301, June 2014.

[116] V Gurarie, L Pollet, N V Prokof'Ev, B V Svistunov, and M Troyer. Phase diagram of the disordered Bose-Hubbard model. *Physical Review B*, 80(21):214519, December 2009.

[117] D. Stauffer and A. Aharony. *Introduction To Percolation Theory.* Taylor & Francis, 1994.

[118] M. J. Pasienski. Disordered insulator in an optical lattice. 2011.

[119] A E Niederle and H Rieger. Superfluid clusters, percolation and phase transitions in the disordered, two-dimensional Bose–Hubbard model. *New Journal of Physics*, 15(7):075029–26, July 2013.

[120] Ş. G. Söyler, M. Kiselev, N. V. Prokof'ev, and B. V. Svistunov. Phase diagram of the commensurate two-dimensional disordered bose-hubbard model. *Phys. Rev. Lett.*, 107:185301, Oct 2011.

[121] Lode Pollet. A review of Monte Carlo simulations for the Bose-Hubbard model with diagonal disorder. *arXiv.org*, July 2013.

[122] Christophe Mora and Yvan Castin. Extension of Bogoliubov theory to quasicondensates. *Physical Review A*, 67(5):053615, May 2003.

[123] Yancheng Wang, Wenan Guo, and Anders W Sandvik. Anomalous quantum glass of bosons in a random potential in two dimensions. *arXiv.org*, page 3213, October 2014.

[124] Geoffroy J Aubry, Fabien Bonnet, Mathieu Melich, Laurent Guyon, Panayotis Spathis, Florence Despetis, and Pierre-Etienne Wolf. Condensation of Helium in Aerogel and Athermal Dynamics of the Random-Field Ising Model. *Physical Review Letters*, 113(8):085301–5, August 2014.

[125] J. I. A. Li, A. M. Zimmerman, C. A. Collett, W. J. Gannon, and W. P. Halperin. The superfluid glass phase of He3-A. *Nature Physics*, pages 1–5, January 2013.

[126] Omid Nohadani, Stefan Wessel, and Stephan Haas. Bose-Glass Phases in Disordered Quantum Magnets. *Physical Review Letters*, 95(22):227201, November 2005.

[127] B Capogrosso-Sansone, N Prokof'ev, and B Svistunov. Phase diagram and thermodynamics of the three-dimensional Bose-Hubbard model. *Physical Review B*, 75(13):134302, April 2007.

[128] Lode Pollet, Nikolay Prokof'ev, and Boris Svistunov. Comment on "Direct Mapping of the Finite Temperature Phase Diagram of Strongly Correlated Quantum Models". *Physical Review Letters*, 105(19):199601–1, November 2010.

[129] T W B Kibble. Topology of cosmic domains and strings. *Journal of Physics A: Mathematical and General*, 9(8):1387, 1976.

[130] WH Zurek. Cosmological experiments in superfluid helium? *Nature*, 317(6037):505–508, 1985.

[131] Wojciech Zurek, Uwe Dorner, and Peter Zoller. Dynamics of a Quantum Phase Transition. *Physical Review Letters*, 95(10):105701–4, September 2005.

[132] Anatoli Polkovnikov. Universal adiabatic dynamics in the vicinity of a quantum critical point. *Physical Review B*, 72(16):161201–4, October 2005.

[133] Giulio Biroli, Leticia F Cugliandolo, and Alberto Sicilia. Kibble-Zurek mechanism and infinitely slow annealing through critical points. *Physical Review E*, 81(5):50101, May 2010.

[134] David Chen, Matthew White, Cecilia Borries, and Brian DeMarco. Quantum Quench of an Atomic Mott Insulator. *Physical Review Letters*, 106(23):235304, June 2011.

[135] W. Bao, S. Jin, and P. Markowich. *Siam J. Sci. Comput.*, 25(1):27–64, 2003.

[136] M. Greiner. Ultracold quantum gases in three-dimensional optical lattice potentials, ph.d. thesis. 2003.

[137] Anatoli Polkovnikov, Krishnendu Sengupta, Alessandro Silva, and Mukund Vengalattore. *Colloquium* : Nonequilibrium dynamics of closed interacting quantum systems. *Rev. Mod. Phys.*, 83:863–883, Aug 2011.

[138] Jacek Dziarmaga. Dynamics of a quantum phase transition and relaxation to a steady state. *Advances in Physics*, 59(6):1063–1189, 2010.

[139] Tommaso Caneva, Rosario Fazio, and Giuseppe Santoro. Adiabatic quantum dynamics of a random Ising chain across its quantum critical point. *Physical Review B*, 76(14):144427, October 2007.

[140] Jacek Dziarmaga. Dynamics of a quantum phase transition in the random ising model: Logarithmic dependence of the defect density on the transition rate. *Phys. Rev. B*, 74:064416, Aug 2006.

[141] J P Bouchaud, L F Cugliandolo, J Kurchan, and M Mezard. Out of equilibrium dynamics in spin-glasses and other glassy systems, 1998 Spin Glasses and Random Fields ed AP Young.

[142] Chien-Hung Lin, Rajdeep Sensarma, K. Sengupta, and S. Das Sarma. Quantum dynamics of disordered bosons in an optical lattice. *Phys. Rev. B*, 86:214207, Dec 2012.

[143] N Navon, A L Gaunt, R P Smith, and Z Hadzibabic. Critical dynamics of spontaneous symmetry breaking in a homogeneous Bose gas. *Science*, 347(6218):167–170, 2015.

[144] J Eisert, M Friesdorf, and Christian Gogolin. Quantum many-body systems out of equilibrium. *Nature Physics*, 11(2):124–130, 2015.

[145] Giuseppe E Santoro, Roman Martoňák, Erio Tosatti, and Roberto Car. Theory of quantum annealing of an ising spin glass. *Science*, 295(5564):2427–2430, 2002.

[146] J Brooke, D Bitko, T F, Rosenbaum, and G Aeppli. Quantum Annealing of a Disordered Magnet. *Science*, 284(5415):779–781, April 1999.

[147] Arnab Das and Bikas Chakrabarti. Colloquium: Quantum annealing and analog quantum computation. *Reviews of Modern Physics*, 80(3):1061–1081, September 2008.